Ultrafast photodynamics in condensed phase: ClF, Cl_2 and I_2 in solid rare gases

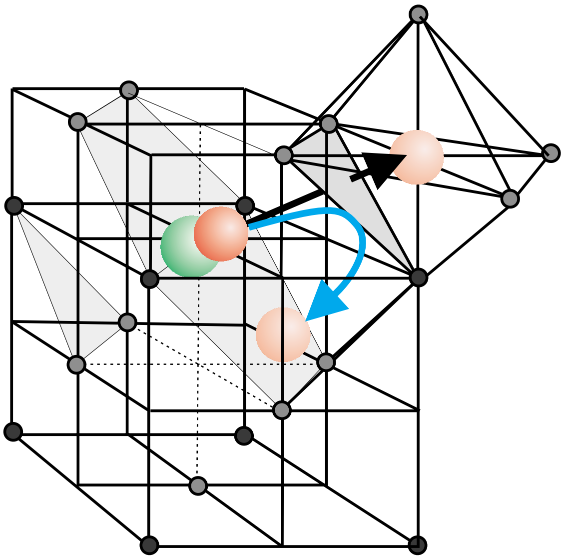

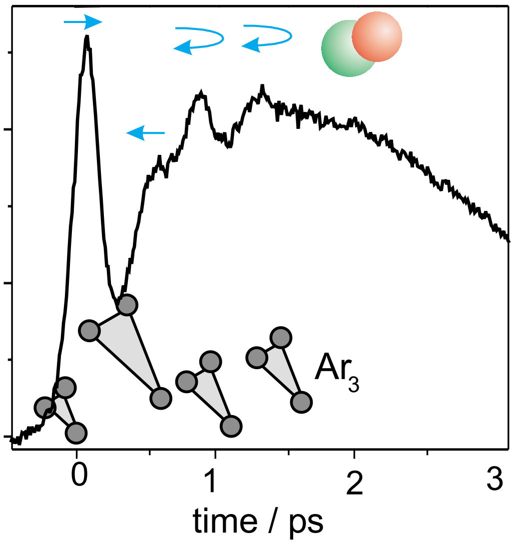

Dissertation by
Matias Bargheer
Physics Department
Freie Universität Berlin
2002

Ultraschnelle Photodynamik in kondensierter Phase: ClF, Cl_2 and I_2 in Edelgasfestkörpern

im Fachbereich Physik
der Freien Universität Berlin
eingereichte Dissertation

Matias Bargheer
Mai 2002

Disputationstermin: 17.7. 2002

Erstgutachter: Prof. Dr. N. Schwentner

Zweitgutachter: Prof. Dr. L. Wöste

Abstract

This thesis is part of a project that deals with photochemistry in the condensed phase and is embedded in the collaborative research center ”Analysis and Control of Ultrafast Photoinduced Reactions” (SfB 450). Halogens and interhalogens ($I_{2,}$ Cl_2 and ClF) in rare gases solids are investigated as model systems by femtosecond-pump-probe spectroscopy.

Coherent wave packet dynamics of I_2 with a period of $T \sim 350$ fs can be observed for more than 10 picoseconds after photoexcitation, despite the strong interactions of the molecule near the dissociation limit with the crystalline Kr matrix. With this system, a novel evaluation scheme for pump-probe spectra is developed and tested, which permits the construction of effective one dimensional potentials of excited electronic states (B and E). An average trajectory of I_2 is measured to visualize the dissipative wave packet dynamics, and vibrational relaxation rates are determined from different signatures of the pump-probe spectra. Near the minimum of the potential, the energy loss is less than 1% per period, but it grows beyond 50% above the gas phase dissociation limit.

The molecules ClF and Cl_2 are examined in Ar and Kr matrices with pump-probe spectroscopy for the first time. The wave packet dynamics of an F fragment that exits the solvent cage is observed in real time. The time for direct cage exit is measured to be $t_{exit} = 250$ fs. Besides the dissociation, the competing recombination of the molecular fragments displays rich dynamics. Above the dissociation limit, the ClF molecule loses more than 35% of its kinetic energy in the first period, whereas the rate slows down to 0.1% near the minimum of the potential. Experimental results evidence a strong coupling of singlet and triplet states, which forces the molecule to recombine into the lowest electronically excited states. Although the spin-orbit coupling of the light atoms Cl and F is weak, the spin-flip occurs in less than $t_f = 500$ fs. Wave packet dynamics persist despite these strong interactions. The scattering of fragments by the cage is compared for molecules with similar electronic states but different isolation geometries in the lattice. A photoselected orientation of the ClF bond in the isotropic Ar cage (single substitutional) is destroyed within $\tau_d = 1.2$ ps, whereas I_2 remains aligned in the fixed cylindrical Kr cage (double substitutional). In co-doped $ClF/Cl_2/Ar$ matrices, the ratio of excited Cl^+Cl^- vs. Cl^+F^- is controlled with a contrast of $1:250$, using a double-pulse sequence.

The systematic variation of pump and probe wavelength allows for a definite interpretation of the experiments without the aid of calculations, which makes the results particularly valuable for the comparison to the simulations which are simultaneously developed within the SfB 450.

In advance, the spectroscopy of ClF in Ar and Kr was clarified and dissociation yields were measured. Two NOPAs were constructed to provide tunable fs-pulses. The commercial design was improved to double their efficiency. In addition, the implementation of a flexible variant of the FROG technique permits the characterization of the pulse duration and phase of fs-pulses from the IR to the UV.

Kurzfassung

Diese Arbeit ist in einem Projekt entstanden, das sich mit Fragestellungen der Photochemie in der kondensierten Phase beschäftigt und in den Sonderforschungsbereich SfB 450, ”Analyse und Steuerung ultraschneller photoinduzierter Reaktionen” eingebettet ist. Als Modellsysteme werden Halogene und Interhalogene (I_2, Cl_2 und ClF) in Edelgasfestkörpern mit Femtosekunden-Pump-Probe Spektroskopie untersucht.

Trotz der starken Wechselwirkung des I_2-Moleküls nahe der Dissoziationsgrenze mit der kristallinen Kr-Matrix bleibt eine kohärente Wellenpaketdynamik mit einer Periode von $T \sim 350$ fs über 10 Picosekunden nach der Photoanregung erhalten. Für die Auswertung der Pump-Probe Spektren wird an diesem System ein neues Schema entwickelt und erprobt, das die Konstruktion effektiver eindimensionaler Potentiale von angeregten elektronischen Zuständen (B und E) gestattet. Die dissipative Wellenpaketdynamik des Moleküls wird an einer gemessenen Trajektorie sichtbar gemacht, und verschiedene Signaturen der Ultrakurzzeitspektren die-nen der Bestimmung von Schwingungsrelaxationsraten. In der Nähe des Potentialminimums beträgt die Energieabgabe weniger als 1% pro Periode, steigt aber im Bereich der Gasphasendissoziationsgrenze auf Werte über 50% an.

Zum ersten Mal werden die Moleküle ClF und Cl_2 in Ar- und Kr-Matrix mittels Pump-Probe Spektroskopie untersucht. Für ClF in Kr wird die Wellenpaketdynamik beim Austritt eines Fragmentes (F) aus dem Umgebungskäfig zeitaufgelöst beobachtet. Die gemessene Zeit für den direkten Käfigaustritt beträgt $t_{exit} = 250$ fs. In Konkurrenz zur Dissoziation steht die Rekombination der Molekülfragmente, die eine reichhaltige Dynamik aufweist. Oberhalb der Dissoziationsgrenze verliert ClF über 35% der kinetischen Energie in der ersten Periode, während die Rate im Potentialminimum auf 0,1% pro Schwingung sinkt. Die experimentellen Ergebnisse belegen eine starke nicht-adiabatische Kopplung von Singulett- und Triplettzuständen, die das Molekül sehr schnell in die niedrigsten elektronisch angeregten Zustände relaxieren läßt. Das Umklappen des Spins erfolgt in weniger als $t_f = 500$ fs, obwohl die Spin-Bahn-Kopplung bei leichten Atomen wie Cl und F schwach ist. Trotz dieser starken Wechselwirkungen ist eine Wellenpaketdynamik zu beobachten. Das Streuverhalten der Fragmente am Käfig von geometrisch unterschiedlich eingebauten Molekülen mit ähnlichen elektronischen Zuständen wird verglichen. Wenige Stöße der Fragmente mit dem isotropen Ar-Käfig (einfach substituiert) zerstören eine photoselektierte Ausrichtung der ClF-Bindung innerhalb von $\tau_d = 1,2$ ps, während I_2 in seinem zylindrischen Kr-Käfig (zweifach substituiert) starr ausgerichtet bleibt. In gemischt dotierten $Cl_2/ClF/Ar$-Matrizen läßt sich mit einer Doppelpulsfolge das Verhältnis von angeregtem Cl^+Cl^- gegenüber Cl^+F^- und deren Fluoreszenz mit einem Kontrast von über 1:250 steuern.

Durch systematische Variation der Wellenlängen von Pump- und Probe-Pulsen wird mit den Experimenten eine eindeutige Interpretation erarbeitet, ohne dabei auf Rechnungen zurückzugreifen. Die Ergebnisse sind deshalb besonders geeignet für den Vergleich mit den im SfB 450 parallel laufenden Simulationen.

Die Spektroskopie von ClF in Ar und Kr sowie die Bestimmung der Dissoziationsausbeuten stellen wichtige Vorarbeiten dar. Der Aufbau von zwei neuen NOPAs zur Erzeugung der fs-Pulse resultierte in einer Verdopplung der Effizienz gegenüber dem kommerziellen Gerät. Zudem wurde eine flexible Variante der FROG-Technik implementiert, mit der sich fs-Pulse vom infraroten bis zum ultravioletten Spektralbereich bezüglich ihrer Pulsdauer und Phase charakterisieren lassen.

Contents

List of Tables

Abbreviations

Ti:Sa - titanium doped sapphire
SHG - second harmonic generation
(PG)-FROG - (polarization gate)-frequency resolved optical gating
NOPA - non-collinear optical parametric amplifier
LIF - laser induced fluorescence
CARS - Coherent anti-Stokes Raman scattering
DIM - diatomics in molecules
DIIS - diatomics in ionic systems
CI - configuration interaction
MD - molecular dynamics
PES - potential energy surface
RKR - Rydberg-Klein-Rees
fs - femtosecond $(10^{-15}s)$
ps - picosecond $(10^{-12}s)$
a_0 - Bohr radius 5.292x10^{-11} m

List of Figures

Chapter 1

Introduction

This thesis presents a contribution to ultrafast photodynamics of molecules in the condensed phase, which is a blooming branch of femtochemistry. The making and breaking of molecular bonds is the essence of chemistry, and these elementary steps occur on the ultrafast time scale of molecular vibrations (tens of femtoseconds, 1 fs = 10^{-15} s). In 1999 Achmed Zewail received the Nobel Prize in Chemistry for his fundamental contributions to the new field called femtochemistry, and its growth is documented in many recent proceedings [1–9]. The research in this field aims at an understanding of chemical reaction dynamics on a molecular level, in order to conceive new ways of controlling chemical processes [10–20], and this thesis is embedded in the special research project ”Analysis and Control of ultrafast photoinduced reactions”[1]. Various groups investigate increasingly complex systems, from isolated molecules in the gas phase (e.g. in molecular beams), over small molecules in liquids, up to large biomolecules in their native protein environment.

Research subject

The diatomic molecules ClF, Cl_2 and I_2 isolated in the solid rare gases Ar and Kr, which are investigated here, present conceptionally simple model systems. They show typical manybody or condensed phase properties such as dissipation, decoherence and nonadiabatic coupling; however, at a level of complexity which today can be handled theoretically. *Although the theory of the ultrafast dynamics of diatomic halogens in rare gases is well established, experimental data on the femtosecond timescale in these systems are scarce.* They are restricted to the large and heavy I_2 molecule in rare gases, and until now experimental pump-probe spectra with rather limited wavelength variation are analyzed via simulations [21–33]. In this thesis, the method of fs-pump-probe spectroscopy is used systematically to characterize the relevant ultrafast processes. It is especially well suited to study reactions of molecules in condensed phase environments, since conventional frequency domain spectra in the dissociation continuum are structureless and the solvent induces dynamical and structural broadening in the bound region, as well. The pump pulse triggers the dynamics, and the probe pulse records snapshots of the ultrafast processes at times set by the time delay between the two pulses. The laser induced fluorescence (LIF) is the recorded signal. The time resolution in such measurements is limited by the pulse duration. Pump and probe pulses use spectroscopic characteristics of the molecules to select reactants, products and electronic states; the LIF is an additional fingerprint of the molecules. Recent progress in the generation of tunable fs-laser-pulses promotes spectroscopically adapted fs-pump-probe experiments [34, 35]. Two improved non-collinear optical parametric amplifiers (NOPAs) are constructed to provide fs-pulses in a wide wavelength range and the short pulse duration is optimized in situ with a versatile implementation of the frequency-resolved optical gating (FROG) technique.

The goal of this thesis is to generate systematic sets of experimental data, which allow an extraction of the relevant information without the aid of simulations in order to provide an independent

---

[1] Funded by the ”Deutsche Forschungsgemeinschaft” via SfB 450.

check that may validate the theoretical formalism and calibrate simulation parameters. The experimental study includes the two limiting cases of the large and heavy halogen I_2 in Kr and the small and light interhalogen ClF in Ar and Kr. Some results on the intermediate Cl_2 are also presented. The electronic structure of halogens and interhalogens is very similar. The basic differences determining the dynamics are the size and mass of the constituents. The I_2 molecule is fixed in the axial geometry of the double substitutional site. ClF is embedded in a nearly spherical cage. The reactive F fragment can move around the Cl atom within the matrix cage or even leave the first solvent shell to be trapped as a radical or to form a new molecule.

Since the research project aims at photochemical reactions, the focus of the investigations lies on strong interactions of the molecules with their solvent environment, which cannot be regarded simply as a perturbation of an isolated molecule. Therefore, the experiments involve excitation close to or above the gas phase dissociation limit. A wide range of phenomena typical for condensed phase photodynamics is extracted directly from the spectra and compared to detailed molecular dynamics simulations from the literature and cooperation partners. The results of the pump-probe experiments are presented in chapter 6. The discussion in chapter 7 comprises the following ultrafast processes:

- the dynamic cage effect (ch. 7.1)
- energy dissipation with a detailed account of the fragment-cage dynamics (ch. 7.3)
- maintenance of vibrational coherence despite strong dissipation (ch. 7.9)
- ultrafast reorientation of the molecular bond (ch. 7.5)
- non-adiabatic transitions including ultrafast solvent-induced spin-flip (ch. 7.6) and
- ultrafast dissociation versus recombination of the fragments (ch. 7.7). Finally,
- control of the yield of Cl^+Cl^- vs. Cl^+F^- formation is demonstrated (ch. 7.8).

Before the ultrafast photodynamics of the ClF molecule are analyzed, important properties of the molecule ClF have to be investigated. The experimental results are presented in chapter 4 and discussed in chapter 5 with respect to

- spectroscopy of ClF in Ar and Kr (ch. 5.1 and 5.2) and
- photodissociation yield of ClF in Ar and Kr (ch. 5.4).

As an introduction to the system diatomics in solid rare gases, chapter 2.1 summarizes the early work on classical molecular dynamics simulations of I_2/Kr and F_2/Ar, which provides an intuitive picture of the microscopic dynamics. Although the classical trajectories already show many of the dynamical processes of interest, a semiclassical extension that allows the description of nonadiabatic transitions between electronic states is inevitable. A basic description of wave packets is introduced as well. The concept pursued in this thesis is to extract information directly from the measured spectra without the aid of simulations. A theoretical background on typical phenomena in the condensed phase (matrix) is prepared in chapter 2.2 in order to provide heuristic arguments for the discussion of the condensed phase spectroscopy and dynamics. It includes the cage effect, cage exit and nuclear rearrangements, as well as excimers, ionic states and polarization effects. Chapter 2.3 discusses the method of fs-pump-probe spectroscopy with laser induced fluorescence (LIF) detection, with an emphasis on the specialties that occur in the condensed phase. It is the main experimental method employed in the thesis (part II). Chapter 2.4 provides the literature on the ClF molecule, since this thesis presents the first account of excited electronic states of ClF in condensed media and for the first time fs-spectroscopy is applied to $ClF.$

The experimental setup is described in chapter 3. Besides the preparation of the corrosive gas ClF in solid rare gas samples, the generation and characterization of tunable ultraviolet femtosecond pulses was implemented. The pulses are generated by frequency doubling the visible output of a non-collinear optical parametric amplifier (NOPA), and one of the major technical advances in this thesis was to double the efficiency of the NOPAs (chapter 3.4). A versatile variant of the frequency-resolved optical gating (FROG) technique was developed to measure the UV pulses in situ, i.e. on the substrate, together with the pump-probe scan.

Motivation of the model system

Several groups advance theories that allow a description of molecular dynamics and reactions in inert rare gases (Rg) as a model solvent [36–38]. In experiments and theory, this conceptionally simple modular construction set, consisting of Rg solvent atoms and various solute molecules, allows isolation of the species of interest and the investigation of the molecule-solvent interaction. Structural properties of the model solvent can be varied from gas [39,40], over clusters [41] and liquids [42–44], to solids [41,45,46]. Parameters like the polarizability and lattice constants change from Ne to Xe. The investigation of cold and ordered samples, i.e. the solid rare gas matrices examined in this thesis, simplifies the theoretical description, since thermal averaging is reduced and the initial geometry is well defined. Historically, the study of halogen-rare-gas excimers and exciplexes in theory [47–51] and experiment [52–57] has focused considerable attention on diatomic halogens in $Rg,$ resulting in precise potential energy surfaces. Both classical and detailed non-adiabatic molecular dynamics simulations of I_2 [58–66] and F_2 [67–73] in Rg were recently published.

On the experimental side, matrix isolation spectroscopy of various molecules and even highly reactive radicals in solid rare gas matrices has generated a large pool of spectroscopic knowledge of isolated species [74–78], and a recent review [36] summarizes the aspects of particular importance to this thesis. The spectroscopy of I_2 [79,80] and F_2 [81–84] in Rg is well established; however, molecular states of F_2 lie unfavorably far in the ultraviolet. Considering the photodynamics, I and F represent two extrema. Static experiments on photodissociation prove that for $I_2,$ the cage effect is complete and all fragments geminately recombine [85], whereas F atoms show high cage exit probability [53,86,87] and mobility [88] in Rg matrices. Even the penetration depth in layered rare gas samples was measured [89,90]. In this thesis, the interhalogen ClF was preferred to the halogen F_2 for spectroscopic reasons, although the spectroscopy had to be established first (chapter 4). All other F containing interhalogens are unstable against disproportionation to XY_3 and therefore more difficult to handle [91]. ClF is expected to display a wide range of interesting dynamics, and it offers the perspective to finally control a photochemical reaction in the condensed phase model-environment of solid rare gases. The F fragments not only form excimers and exciplexes like KrF and Kr_2F with the matrix atoms, but also triatomic molecules like $ClXeF,$ $FXeF$ and $FKrF,$ which are bound in the ground state [92–95]. The first Ar containing molecule, $HArF,$ was found only two years ago [96] and the new rare gas containing molecule $ClKrF$ is predicted to be stable [97].

The theoretical description of ultrafast processes in the condensed phase is also a subject of active research, and dihalogens in rare gas matrix provide tractable model systems. According to the Fourier transformation, the ultrafast timescale is connected to broad spectra [98], which results in the excitation of wave packets synthesized from a coherent superposition of states [99,100]. The full quantum mechanical description can only be carried through for small systems with a few degrees of freedom. Large molecules and condensed phase systems have many degrees of freedom. Reduced dimensionality approaches and a wealth of semi-classical methods are investigated to tackle the challenges [99]. Semi-classical descriptions receive their justification from the spatial localization of the wave packets that persists on the femtosecond timescale. The motion of classical particles is approximated by wave packets, as stated in Ehrenfest's correspondence principle [101]. In order to break a molecular bond, enough energy must be localized in this region. The coupling to other degrees of freedom leads to rapid dissipation of energy in the condensed phase or equivalently to Intramolecular Vibrational Redistribution (IVR) in larger molecules, counteracting this localization of energy [6]. Semi-classical theories describe the motion and interaction of the nuclei in great detail, and refinements for the quantum effects of delocalization, tunneling and interference can be made [102,103].

The presence of the solvent fluctuations that randomly change the dynamics of the solute molecule destroys the quantum coherences, and it is an open question how coherence in the condensed phase is accessible to external control. Another important complication originates from the coupling of different electronic states, which must be incorporated into theories, since most chemical reactions involve excited electronic states. These non-adiabatic effects receive increasing attention as computer power allows the treatment of the interplay of electronic and nuclear motion in complex systems [99]. To test the predictions of these advanced theoretical treatments, it is necessary to derive the relevant information from systematic experiments as it will be shown here. The close collaborations with the theory groups of Prof. J. Manz and Prof. R.B. Gerber within the SfB450 is mutually stimulating for experiment and theory of the model system diatomics in condensed rare gases.

Chapter 2

Conceptual framework and summary of literature

The first part of this chapter gives a short introduction to the molecular dynamics simulations of halogens in rare gas solids based on a classical picture of the system. A semiclassical extension to this theory is presented which provides the most detailed description of the dynamical system at present.
The literature will be summarized with the focus on the special systems, that are experimentally examined with femtosecond pulses for the first time in this thesis, ClF *and* Cl_2 *in* Ar *and* Kr *matrices. The introduction to fs-pump-probe spectroscopy is given with an emphasis on dissipative systems. A nearly complete summary of the literature concerning the spectroscopy of the molecule* ClF *is given.*

2.1 Simulations of ultrafast dynamics in condensed phase

2.1.1 Classical molecular dynamics: I_2/Kr and F_2/Ar

The early classical molecular dynamics simulations of I_2/Kr and F_2/Ar already demonstrate many of the important dynamical effects discussed in this thesis. The simulations start with a box of approx. 500 rare gas (Rg) atoms in a closest packed geometry (face centered cubic - fcc), with a halogen molecule (Y_2) in the center of the box. A small molecule like F_2 occupies only one lattice site (substitutional) of the solid and large molecules like I_2 occupy two lattice sites (double substitutional). The forces between two rare gas atoms ($Rg - Rg$) and between halogen and rare gas $Y - Rg$ are of the van-der-Waals type, with strong repulsion at short distances and weak attraction, i.e. nearly a system of hard spheres. For the molecular $Y - Y$ interaction, a Morse potential is used and potentials are assumed to be pairwise additive. In this classical system, the dynamics correspond to three dimensional billiards.

To describe the photodynamics of the molecules, first the initial conditions have to be found. The system is equilibrated at a specified temperature with the molecule in its ground state X. The initial configurations are then randomly sampled under the condition that the molecular bond distance R fulfills the Franck resonance condition [104] with the excited electronic state within the energy bandwidth of the pump pulse. The trajectories are then started for each of the initial conditions by switching the molecular potential from the ground state (X) to the excited state. Since the system is entirely classical, the positions and momenta of all particles can be calculated for each time step by numerical propagation of Hamilton's equations.

Classical trajectories for I_2/Kr from ref. [26]

First consider the photodynamics of the large and heavy I_2 molecule, excited to its A state[1] above the gas phase dissociation limit, in the center of a box of Kr atoms [26]. Fig. 2.1a shows the bond distance R_{I-I} as a function of time t for a set of trajectories. All trajectories start well localized at

---

[1] A is the lowest optically accessible state of I_2 with a shallow potential (weak binding).

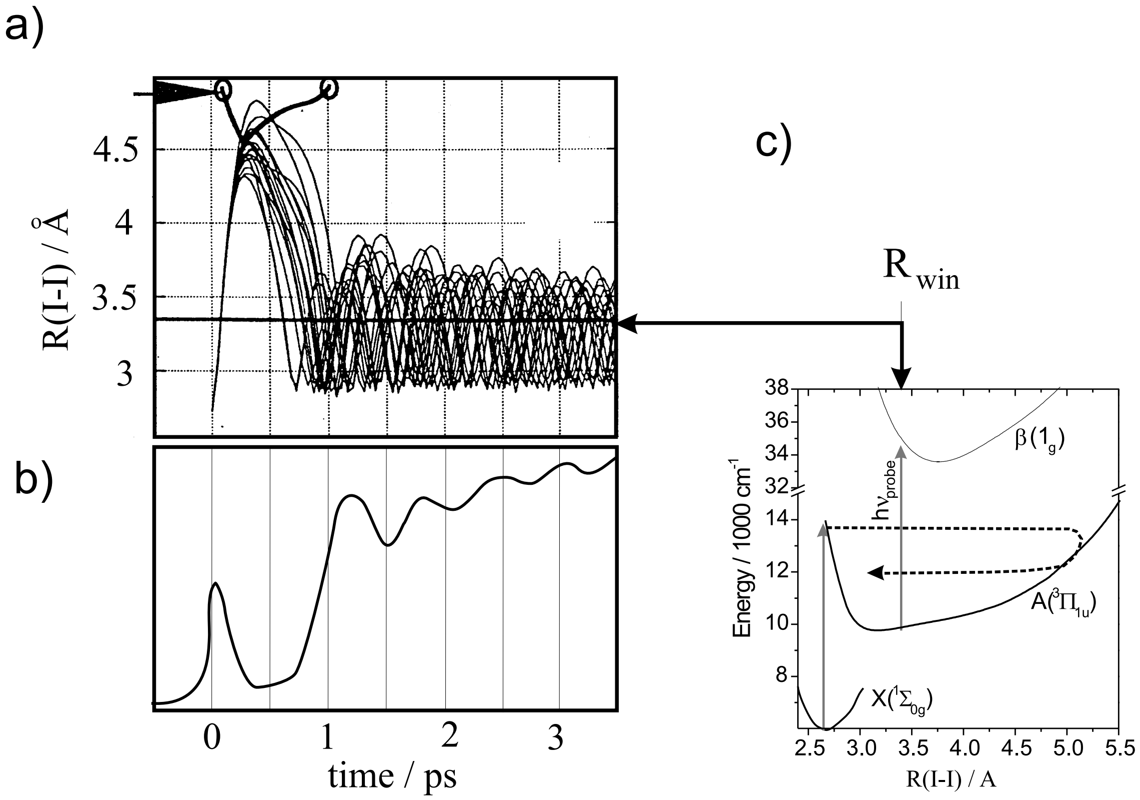

Figure 2.1: a) Bond distance R_{I-I} as a function of time from classical trajectory calculations of I_2/Kr. Each line corresponds to one trajectory for a given initial condition. b) Experimental pump-probe spectrum for $\lambda_{pump} = 704$ nm and $\lambda_{probe} = 352$ nm. c) Potential energy diagram of I_2 with probe window at R_{win} from the A state to the ion-pair states, which connects the trajectories with the observed signal [26].

$R_{I-I} = 0.266$ nm. The bond stretches to 0.45 nm within 300 fs, and here the I atoms encounter the Kr cage atoms, suddenly stopping the dissociative motion. In all trajectories, the I atoms are forced to recombine within 1 ps and subsequently oscillate around the new equilibrium bond length near 0.33 nm. The slightly different initial conditions, i.e. positions and momenta of the two I atoms and all Kr atoms, prepare different scattering parameters, yielding a very broad distribution of recombining trajectories. The strong energy loss in the first collision can is evident from the reduced amplitude of the $I - I$ oscillations in the molecular potential.

Fig. 2.1c depicts the potential diagram which connects the simulated trajectories with the observed signal in a pump-probe spectrum in panel b). The energy $h\nu$ of the probe pulse specifies the probe window R_{win} by the Franck-Condon resonance (*chapter 2.9*) to a higher lying state. The intensity of the fluorescence from this state is proportional to the number of trajectories in the probe window during the time interval of the probe pulse. A high velocity of the trajectories decreases the signal, because the trajectory spends less time in the probe window.

Fig. 2.2 shows the ensemble averaged total energy of I_2 for the trajectories from Fig. 2.1a. A rapid loss of 2000 cm^{-1} within the first ps, induced by the first strong fragment-cage collisions after dissociation, is followed by a slow exponential decay for the vibrational relaxation after recombination in the A state.

In *chapter 7.3.1* an $I - I$ trajectory vibrationally relaxing in the B state will be derived from the pump-probe spectra and *chapter 7.4.2* presents the corresponding relaxation rates. The energy loss in the A state is discussed in *chapter 7.4.3*.

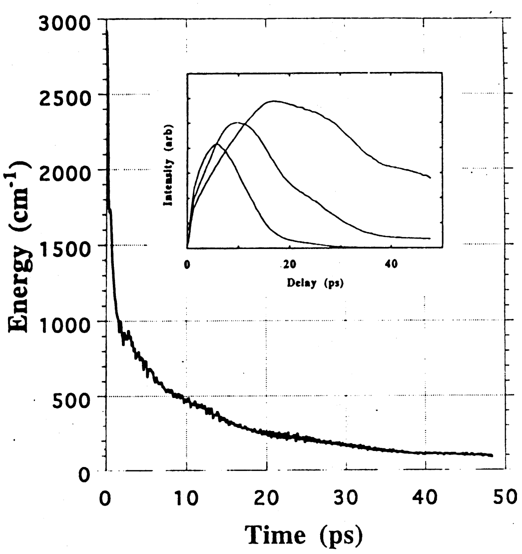

Figure 2.2: Ensemble averaged total energy of I_2 as a function of time [26]. An initial rapid loss is followed by a slow exponential decay with time constant 12 ps. The inset shows the pump-probe spectra calculated from the same ensemble for three different window locations a) 0.35 nm, b) 0.34 nm and c) 0.33 nm. The smaller R_{win} is located deeper in the potential and sees the population for longer times.

Classical trajectories for F_2/Ar from ref. [67]

While even at high excess energies, the I atoms are always confined to the initial cage in a Kr solid, the observed behavior for F_2 in Ar solids is entirely different. Classical trajectory calculations [67] on F_2/Ar predict that F atoms leave the cage around the F_2 molecule, formed by the first Ar shell. This cage exit is observed in 55% of trajectories already at an excess energy $E_{excess} = 1$ eV of the molecule above its gas phase dissociation limit. Fig. 2.3a) shows a typical trajectory for excitation of F_2 in the $^1\Pi$ state[2] with $E_{excess} = 1$ eV. The trajectory shows asymmetric cage exit, i.e. one F atom (1) leaves the original cage and the other one (2) resides on the initial substitutional site. Panel a) shows the distance of both atoms to their initial position as a function of time. Fragment 1 encounters an Ar atom after 500 fs which forces the F atom to stay in the original cage. After approx. 1 ps, the F atom suddenly hops out of the cage and is trapped in the nearest interstitial site[3] (cf. Fig. 2.5c). Fragment 2, in contrast, is confined to the original substitutional site. Panel b) displays the kinetic energies of the two particles. The kinetic energy of both particles is rapidly lost, however, after 1 ps atom 1 picks up 0.1 eV of kinetic energy after overcoming the barrier for dissociation. Again, this energy is quickly dissipated in the final (interstitial) site.

The probability for cage exit increases with the excitation energy. For excess energies higher than 1 eV the symmetric cage exit dominates (both fragments leave the cage). The initial configuration plays an important role, and at low temperatures (4 K) the $F - F$ atom is initially aligned with both F atoms pointing at triangular windows of the cage (cf. Fig. 2.5c), which again favors cage exit.

The small size of the F fragments determines the recombination dynamics, as well. The molecular $F - F$ bond may be rapidly tilted by scattering off the cage atoms, as is observed in the trajectory plotted in Fig. 2.4. In contrast, the $I - I$ bond orientation is sterically fixed by the solid Kr lattice.

The fs-pump-probe spectra of ClF in Ar will display the recombination dynamics *(chapter 7.3.2)*, the energy loss by vibrational relaxation *(chapter 7.4.3)*, the tilting of the $Cl - F$ bond *(chapter 7.5.3)* and the cage exit of F fragments (*chapter 7.7*).

---

[2] The lowest allowed transition from the ground state of the F_2 molecule is to the $^1\Pi$ state, which is purely repulsive.

[3] interstitial = opposite of substitutional = between the atoms of a complete lattice

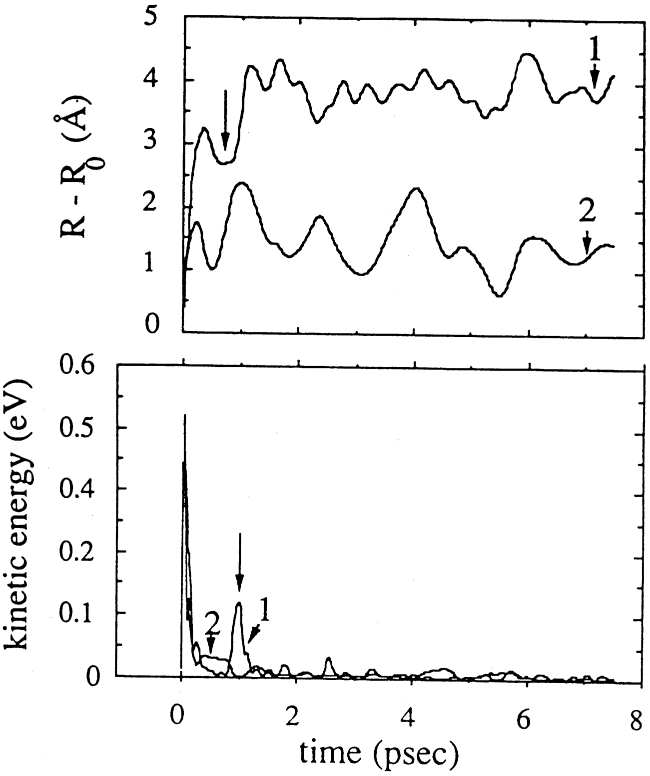

Figure 2.3: a) Distance of the two F fragments to their initial position as a function of time from classical trajectory simulations on F_2/Ar photodissociation. A single trajectory is shown that shows asymmetric cage exit. b) Corresponding kinetic energies of the two F fragments as a function of time [67].

2.1.2 Coupling of electronic and nuclear motion

The classical molecular dynamics (MD) on a single electronic potential energy surface deliver many details of the photodynamical processes, which can be described by classical quantities of the nuclei, such as position, momentum, kinetic energy, bond-direction and cage exit probability. The processes will be described correctly as long as only one electronic state is involved in the dynamics (weak electronic coupling). Recombination to the ground state or other bound electronic states alter the dynamics and compete with the cage exit. Changes of electronic state decrease the probability of cage exit, especially, if repulsive states are initially excited.

Transitions among coupled electronic states of a molecule give rise to non-adiabatic dynamics, i.e. coupled motion of electronic and nuclear degrees of freedom. The adiabatic approximation (Born-Oppenheimer approximation) assumes that the motion of electrons is much faster than the motion of nuclei. As a consequence, the electron configuration should instantaneously adjust to the position of the nuclei. The electronic state determines the dynamics, since it sets the forces on the nuclei as the gradient of the potential energy. The nuclear motion in turn influences the coupling of electronic states, i.e. the probability for changing the occupation of the electronic states. In the semi-classical Landau-Zener picture[4], the transition probability w depends on the velocity v of the trajectory $w = 1 - \exp(-A/v)$. Thus, nuclear and electronic degrees of freedom are coupled.

Non-adiabatic coupling arises from the anisotropic interaction energy of the open shell fragments (P-orbitals) with a rare gas atom, as well. It is given by $U^{DIM}(r_i,\gamma_i) = V_0(r_i) + V_2(r_i)P_2(\cos\gamma_i)$, where V_o is the isotropic part of the interaction potential and V_2, together with the second Legendre polynomial, describes the angular dependence of the asymmetric part [107]. This interaction, based

---

[4] The constant A in the exponential is given as $A = 2\pi V_x^2/(\hbar|F_2 - F_1|)$, where V_x^2 is the coupling matrix element of the two states and $|F_2 - F_1|$ is the difference of the forces according to the two potential surfaces at the crossing [105, 106].

In a quantum mechanical picture, the overlap of the vibrational wave functions determines the transition probability. The vibrational states are the solutions of Schrödinger's equation for the nuclear motion.

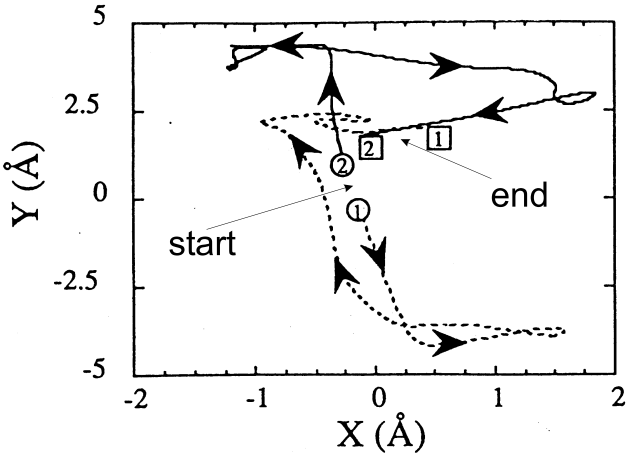

Figure 2.4: Nonreactive trajectory of both F fragments (1 and 2) in two cartesian coordinates [67]. The initial positions are denoted as circles, the final positions after 3.5 ps as squares. At the end of this recombination dynamics, the $F-F$ bond is tilted by 90°.

on electrostatic and empirical considerations, is clearly not of the Born-Oppenheimer type. It explicitly depends on an electronic degree of freedom, the orbital angle γ_i. Pictorially speaking, the lobes of the electronic orbitals are attached to the nucleus and may be tilted by the dynamical interaction with the electron clouds of the rare gas atoms. An adiabatic vs. nonadiabatic treatment of the problem is compared in ref. [69, 70].

2.1.3 DIM and DIIS treatment for potential energy surfaces

To handle nonadiabatic processes, first, an efficient calculation of the electronic surfaces is needed that can be included in dynamical simulations. The diatomics-in-molecules (DIM) method is a semi-empirical approach developed by Ellison [108] for computing potential energy surfaces (PES) of polyatomic systems from diatomic potentials. A detailed explanation of this method is exemplified in the system I_2/Rg [63–65]. It is an extension of the simple approach of adding up pair potentials presented in chapter 2.2.4, that also accounts for the proper symmetrization of the electronic wave functions. The molecular interactions, e.g. of Cl with F will distort the electron distribution of these atoms, and thus the interaction with the surrounding Ar atoms is altered, too. The idea is to cast the total Hamiltonian into a form which contains only Hamiltonians of all possible diatomic and monatomic constituents, but no interaction operators. Thereby, experimental diatomic and monatomic energies can be taken as the eigenenergies after diagonalization of the matrix. DIM uses the pair potentials as a starting point, and it is not surprising that it works best for weakly bound molecular states, since for these the deformation of the electronic clouds is weak [109].

For halogens and interhalogens a total number of 36 valence states has to be taken into account, because 13 of the 23 electronic states have $\Omega \neq 0$ and are doubly degenerate. The surrounding rare gas atoms break the symmetry of the molecular states of $F-F$ or $Cl-F$, and the direction – not only the absolute value of the projection of the angular momentum – enters into the potential energy. For a detailed modeling, spin-orbit interaction must be taken into account. It was shown that spin-non-conserving transitions play a crucial role in the dynamics [71] (*chapter 7.6*).

The diatomics-in-ionic-systems (DIIS) method is a variant of the DIM method that also accounts for the coupling of electron-transfer (ion-pair) states with neutral valence states. It has been pioneered by Last and George [110, 111] for Cl/Xe and successfully applied by Batista and Coker for I_2/Kr.

For a detailed explanation of the DIM and DIIS method, the reader is referred to the literature cited above and to ref. [112].

2.1.4 Non-adiabatic molecular dynamics (DIM - trajectories)

A very fruitful way of treating molecular dynamics on several electronic surfaces semiclassically, is the ”surface hopping” method developed by Tully and co-workers, which treats nuclear motions classically and the electronic degrees of freedom quantum-mechanically [113, 114]. Criteria based on the time dependence of the electronic wave functions are used in an algorithm that decides when the ”hopping” to another electronic state takes place.

DIM-trajectory simulations combine the calculation of electronic PES by the DIM method with the semi-classical surface-hopping technique [63–65, 71]. In each time step, the Hamiltonian is diagonalized in the electron coordinates, and the eigenvalues yield the energies of all electronic states for the specific nuclear configuration at time t. The new potential delivers the forces on the nuclear degrees of freedom for the next time step. The nuclei are treated classically, and the position of all particles is known for all times. It is common to plot the position of the relevant particles for individual trajectories and to display the eigenvalues of the Hamiltonian, i.e. the potential energy for all electronic states as a function of time (e.g. Fig. 7.19).

The zero-point motion of the atoms must be added artificially to the initial conditions in an appropriate way. The classical approximation is especially good if the atoms are either heavy or hot. The spreading of the wave packet will be discussed in the following chapter, and it will enter in the discussion of the ClF wave packets *(chapter 7.3.2)*. There are several ways to incorporate wave properties of matter in MD trajectory simulations [102, 103].

DIM trajectories for I_2/Kr

It is well known that the bound B state of I_2 is coupled to repulsive electronic states. This predissociation is strongly enhanced in condensed phase and the major aim of the DIM studies was to quantitatively simulate the corresponding nonadiabatic dynamics. The predissociation of I_2 will not be considered in this thesis, since in solid Kr it takes place on a timescale of 10 ps [115, 116]. The discussion will focus on the description of the early B state dynamics itself and the strong interaction with the Kr environment. A one dimensional representation of the multidimensional potential will be constructed from the experiment, and the discussion in *chapter 7.1* will show that an average over potential energies from many DIM trajectories is desirable for comparison. An ensemble average, together with a width of the distribution for the classical quantities, would display an intuitive semiclassical picture of a wave packet smeared out in phase space. *Fig. 7.7b* demonstrates the discussed effects for a trajectory of I_2/Ar, but for a quantitative evaluation, simulations of the system I_2/Kr are needed.

DIM trajectories for F_2/Rg

The nonadiabatic simulations of the dynamics of F_2 in Rg add several very interesting predictions to the classical results. Ref. [71] presents simulations of the non-adiabatic dynamics of F_2 in an Ar_{54} cluster after excitation to the singlet $^1\Pi$ state. The main result is the ultrafast transition to the weakly bound $^3\Pi$ states, involving an ultrafast spin-flip, that will be discussed in *chapter 7.6*. The dissociation quantum efficiency is lower in the nonadiabatic simulations, and ref. [71] emphasizes the importance of delayed cage exit at low excitation energies, i.e. the process displayed in Fig. 2.3. The F atom first kicks the argon atoms, and can only exit after the cage has opened after approx. 1 ps. In the MD simulations of F in Kr it was observed, that the kinetic energy of the nuclei can be transferred to electronic potential energy, which reduces the probability to overcome the potential barriers [69, 70].

2.1.5 Wave packets

This chapter is a quick reminder of some important features of wave packets. For further reading consider refs. [117] and [118].

Wave packets are a coherent superposition of several eigenstates of a quantum system. The excitation of a diatomic molecule with a sufficiently short fs-pump-pulse prepares a coherent superposition of vibrational levels with the time dependent wave function $\psi(R,t)$, where R is the bond length and t is time. If the square of the wave function $|\psi(R,t)|^2$ is localized in the coordinate R, this is called a wave packet. The spatial width of the wave packet corresponds to the uncertainty for a measurement of the bond distance, i.e. the location of the constituent atoms is smeared out.

In the cold rare gas matrix, initially the vibrational ground state is populated, and the wave function is a Gaussian. A short laser pulse projects this Gaussian wave function onto the excited state surface, and in the linear approximation of the excite state potential its shape remains Gaussian [117].

The spatial and energetic width of the I_2 wave packet is examined in *chapter 7.2* and the dispersion of the $Cl-F$ wave packet is discussed in *chapter 7.3.2*.

Dynamics and spreading of the wave packet

The wave packet obeys Schrödinger's equation $i\hbar\frac{\partial}{\partial t}\Psi\left(R,t\right)=\left(\frac{p^2}{2m}+U\left(R\right)\right)\Psi\left(R,t\right)$ in the potential $U(R)$. With Ehrenfest's theorems [101], it is transformed into the differential equations for the expectation values $\langle R\rangle$ for space and $\langle p\rangle$ for momentum.

$$\frac{\partial}{\partial t}\left\langle R\right\rangle=\frac{\langle p\rangle}{m};\frac{\partial}{\partial t}\left\langle p\right\rangle=-\left\langle\nabla U\left(R\right)\right\rangle \tag{2.1}$$

They govern the classical trajectory of the wave packet. For some potentials the expectation value of the gradient of the potential is equal to the gradient of the potential at the expectation value $\langle R\rangle$, i.e. $\left\langle\nabla U\left(R\right)\right\rangle=\nabla_{\langle R\rangle}U\left(\langle R\rangle\right)$. Then eq. 2.1 are the classical Hamilton equations for the expectation value $\langle R\rangle$. This is true for all linear and quadratic potentials and Ehrenfest's description of the wave packet motion becomes exact.

$$\langle\partial U(R)/\partial R\rangle=\left\langle\partial R^2/\partial R\right\rangle\overset{!}{=}\langle 2R\rangle\overset{!}{=}\partial\left\langle R\right\rangle^2/\partial\left\langle R\right\rangle=\partial U\left(\langle R\rangle\right)/\partial\left\langle R\right\rangle.$$

The classical equations are approximated by eq. 2.1 if the wave packet is well localized and the potential is nearly constant within the spread of the wave packet ($\nabla U\left(R\right)\approx\nabla U\left(r\right)|_{r=\langle R\rangle}$). Then the constant gradient of the potential can be taken out of the integral.

$$\left\langle\nabla U\left(R\right)\right\rangle=\int\Psi^*\left[\nabla U\left(R\right)\right]\Psi dR\approx\nabla_{\langle R\rangle}U\left(\langle R\rangle\right). \tag{2.2}$$

Under the influence of the potential, the width ΔR of the packet changes in time, and this is called dispersion[5]. For a freely propagating Gaussian ($U=const.$) in a constant potential, the width changes according to $\Delta R(t)=\sqrt{R^2-\langle R\rangle^2}=\sigma\sqrt{1+t^2\left(\hbar/2m\sigma^2\right)^2}$, with $\sigma=\Delta R(0)$. For large t, the width grows linearly with time according to $\Delta R(t)/\sigma=t\frac{\hbar}{2m\sigma^2}$. Consider excitation to the repulsive ClF potential surface with a bandwidth of 500 cm^{-1}. The spatial width of the wave packet excited by this pulse is $\sigma=0.008$ nm. A freely propagating ClF wave packet (taking the ClF potential as flat) with this width and reduced mass $m=12.3$ amu would double after $t=4m\sigma^2/\hbar=50$ fs. For an I_2 wave packet with the same initial spacial width but with reduced mass $m=127$ amu the time increases to 500 fs.

The harmonic potential is the only case where wave packets do not disperse and keep their shape. If a Gaussian ground state wave packet is transferred to a potential with the same shape, the wave packet will oscillate without changing shape (coherent state). If the new potential is flatter, but still harmonic, the wave packet will get broader near the minimum and return to its original shape at the

---

[5] Unfortunately sometimes also the word "dephasing" is used, but this is an ambiguous term as discussed in chapter 2.3.3.

turning point. If the potential is steeper, the wave packet is focused near the minimum, however in the same way in each period [117].

The dynamics in a more realistic, anharmonic Morse potential is similar. The laser pulse prepares the wave packet at its turning point in the Morse oscillator. In diatomic molecules the excited states are in general more weakly bound, and thus, the sharp Gaussian ground state wave packet broadens near the minimum of the excited state but gets sharper at the outer turning point. The anharmonicity changes the shape of the wave packet from period to period by dispersion. The dispersion of the wave packet may be pre-compensated by chirping the pump pulse, i.e. exciting the slower moving components first [19, 31, 32]. For this pre-compensation no discrete structure of vibrational levels is needed. Also classical particles in an anharmonic potential have different round-trip times. When the slower particles are started first, the faster ones can catch up with them, and all particles will be focused (piled up) after a certain time. In this sense the effect is classical.

When the wave packet is prepared with a transform limited (not chirped) pulse, it will spread out. After some time determined by the vibrational frequency and anharmonicity of the potential, the wave packet displays so-called partial and complete revivals (rephasing) and the dynamics start all over again. For the revivals a discrete structure of energy levels is needed and the effect is thus quantum mechanical. Consider for example three levels, with different round-trip times $T - \Delta T$, T and $T + \Delta T$. After a (large) number N of round-trips, $N\Delta T = T$ and the levels are back "in phase". For a higher number of excited levels, this is only a partial revival and the complete rephasing is even later. In the B state of I_2 this time is on the order of 50 ps. In the condensed phase considered here, the "rephasing time" due to the anharmonicity is long compared to the timescale for the destruction of the phases by random scattering off the bath atoms, and this process was never observed. From a different viewpoint, the fluctuating environment smears out the vibrational level structure, which destroys the coherence. The measured data are analyzed with respect to vibrational coherence in *chapter 7.9*.

Classical oscillation in a Morse potential

For heavy molecules like I_2 the classical approximation is good since the large mass prevents a fast spreading of the wave function. Morse potentials are close approximations to realistic molecular potentials $V(R) = D_e\left(1 - e^{-\beta_m(R-R_e)}\right)^2$. In *chapter 5.3*, a Morse-like extrapolation is used to construct an effective one dimensional potential for I_2/Kr. The classical vibrational frequency of a Morse oscillator is

$$\nu_{morse}(E) = \omega_e\sqrt{1 - \frac{E}{D_e}}, \tag{2.3}$$

with the harmonic frequency $\omega_e = \beta_m\sqrt{2D_e/m}$. D_e is the dissociation energy and m the reduced mass. ω_e is a frequency (not angular frequency) but is usually measured in wavenumbers (cm^{-1}) like the energies E and D_e. The anharmonicity $\omega_e x_e = \frac{1}{2}\nu\, d\nu/dE$ of the Morse potential is constant, independent of E.

$$\frac{d\nu_{morse}}{dE} = -\frac{\omega_e}{2D_e}\left(1 - \frac{E}{D_e}\right)^{-\frac{1}{2}} = -\frac{\omega_e^2}{2D_e\nu_{morse}} \tag{2.4}$$

If a wave packet is excited with a spectral bandwidth of ΔE and without chirp, it will disperse due to the anharmonicity $\omega_e x_e$. The wave packet will be smeared out after n periods, when the differences of vibrational frequencies $\Delta\nu_{morse}$ have accumulated $n\Delta\nu_{morse} = \nu_{morse}$. Here $\Delta\nu_{morse}$ is defined as the frequency difference at the full width half maximum of the excitation pulse ΔE.

$$n = \frac{\nu_{morse}^2}{2\Delta E\omega_e x_e} \tag{2.5}$$

A larger anharmonicity $\omega_e x_e$ and a broader excitation spectrum ΔE lead to a faster dispersion of the wave packet. As an example consider a wave packet on ClF/Ar near the dissociation limit, where

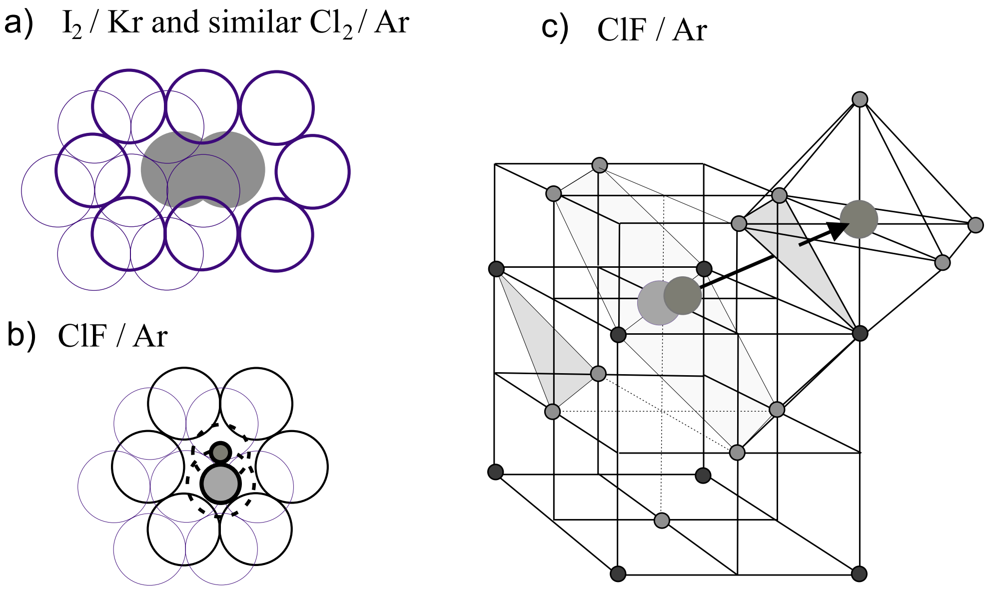

a) I_2 / Kr and similar Cl_2 / Ar

b) ClF / Ar

c) ClF / Ar

Figure 2.5: a) I_2/Kr matrix. Atoms are indicated with their van-der-Waals radii. I_2 occupies a double substitutional site in the fcc lattice. The situation for Cl_2/Ar is similar. b) ClF is isolated on a substitutional site of the Ar lattice. The van-der-Waals radii of Cl and F are indicated as dashed lines. The shaded cores are the atomic radii. c) ClF in the three dimensional fcc lattice. The F atom is pointing at a triangular window of three Ar atoms. The arrow indicates the direct flight to a nearest interstitial site with octahedral (O_h) symmetry.

the round-trip time is ~ 400 fs (equivalent to 83 cm^{-1}). The anharmonicity of the B state of ClF is $\omega_e x_e = 8.6$ cm^{-1}. A a spectral bandwidth of 300 cm^{-1}, equivalent to a 110 fs excitation pulse, will prepare a wave packet that is dispersed after less than 2 periods ($n = 1.3$).

2.2 Matrix effects and fundamentals

The rare gas matrix – like all solvents – changes the spectroscopy of the isolated molecules in several ways. The electronic polarizability of the medium induces solvational shifts of the electronic states and the nuclear rearrangement of the solvent atoms changes the forces of the solvent cage on the molecule. Within the framework of the DIM and DIIS method (cf. chapter 2.1.3) both effects are treated with good accuracy. This chapter introduces the microscopic physical effects as a basis for the interpretation of the experiments and also for the discussion on the sophisticated simulations using DIM trajectories.

2.2.1 The cage effect and isolation of diatomics in solid rare gases

At low temperatures, rare gases condense into solids, forming an fcc lattice [119]. Molecular and atomic impurities that are co-deposited with the rare gas are usually isolated on single or double substitutional sites of this lattice, depending on their size [6].

When generally speaking, in a condensed phase or in a dense gas, reactant species are in proximity to one another, and are caged in by surrounding molecules, e.g. of the solvent, they may undergo a set of collisions known as encounters; the term ”cage effect”, also known as Franck-Rabinowitch effect, is then applied. In this thesis, the ”cage effect” describes the effect of the rare gas matrix on the dissociation of the isolated diatomics under investigation [36]. The caging is perfect for sterical reasons in the case of I_2 and Cl_2 in solid rare gases, i.e. the dissociation efficiency upon excitation is negligible. On the other hand, small molecules like F_2 and HCl show high probabilities for cage

---

[6] For certain diatomic impurities an hcp structure is preferred and bigger molecules are isolated in larger vacancies [119].

exit. The light atomic fragments are mobile and may even migrate through the matrix over several nanometers [89, 120]. The onset of thermal mobility of F fragments is 15 K in solid Kr and 25 K in solid Ar [81].

In a potential diagram, the cage effect bends up the potential surfaces when the reactant species approach the cage (cf. Fig. 2.6). A higher potential barrier decreases the cage exit probability, and when the barrier is much[7] higher than the energy of the fragments the cage effect becomes perfect. The origin of the dramatically different cage exit probabilities of I vs. F fragments is pictured in Fig. 2.5. Panels a and b show the individual atoms with their van-der-Waals radii. I_2 in Kr [25] and Cl_2 in Ar [37] occupy double substitutional sites of the fcc-lattice (Fig. 2.5a). Therefore, the fragments undergo head-on collisions with nearest neighbors upon dissociation. Moreover, the I fragments are too big to fit through the spaces between Kr atoms in the lattice. ClF and F_2 in on the other hand, isolate on single substitutional sites. The F fragments point at a triangular window of the fcc-lattice [53] and may exit the cage along the path indicated by the arrow in Fig. 2.5c. It is obvious that the sphere with the van-der-Waals radius of an F atom would not fit through lattice spacing between van–der-Waals Ar spheres that are touching (cf. Tab. 5.3). In reality, the F atoms are able to migrate in solid rare gases, indicating that the picture of F atoms as spheres is too simplified. The open shell fragments have the symmetry of P-orbitals. The electron cloud of the F radicals, which is responsible for the repulsive interaction with the filled electronic shells of the rare gas atoms has less repulsion in the direction of the singly filled P-orbital [68].

Fig. 2.5c displays the situation in three dimensions. ClF is surrounded by its twelve nearest neighbors, and its bond is pointing at the triangular windows (gray shaded areas). The question of whether ClF is fixed in space as indicated in Fig. 2.5c was addressed in a preliminary calculation. ClF is allowed to move, and the first Ar shell is relaxed to find the minimum energy configuration for fixed rotation angle of ClF. The energy is calculated by adding pair-potentials for $Ar-Ar$ [67], $Ar-Cl$ [56], $Ar-F$ [57] and ClF in the ground state [121]. As a result the minimum energy configuration was confirmed to be the one with the Cl and F atoms pointing at opposite triangles of Ar, as indicated in Fig. 2.5c. A barrier of 30 cm^{-1} for adiabatic rotation is obtained, i.e. for rotation of ClF when the Ar atoms have enough time to rearrange to the lowest energy configuration. The full DIM calculation is currently performed in by M. Schröder[8].

2.2.2 Cage exit and isolated F radicals

The dissociation of F_2 and subsequent trapping of F radicals in matrices has been intensively investigated in experiment and theory. A comparison of adiabatic vs. non adiabatic treatment of the P-orbital dynamics in molecular dynamics simulations of F in Kr is discussed in refs. [69, 70]. They start from the radiative dissociation of the $Kr_2^+F^-$ exciplex. The fluorescence terminates on a potential surface which provides the Kr atoms with 0.4 eV kinetic energy each and the F fragment with 0.2 eV. After 4 ps the F fragments are stabilized either on an octahedral O_h or a tetrahedral T_d site.

Experiments with dissociation of F_2 in various rare gas matrices were reported [67, 81, 83, 87, 89, 90, 120]. Absorption and emission spectra for F_2/Kr are reproduced and discussed in the respective chapters in Part I of this thesis. Since F_2 is prepared on a single substitutional site, after dissociation the F fragments can occupy - in addition to the O_h or T_d sites - a substitutional site in the lattice. Since Cl mobility is sterically forbidden in matrices, the Cl radical will stay on the original substitutional site after dissociation of ClF. The F atom must accordingly take one of the interstitial sites.

---

[7] A small tunneling rate may survive, if the barrier is only slightly higher.

[8] Group of Prof. Manz, Theoretische Chemie, Freie Universität Berlin

2.2.3 Electronic polarization

The Onsager model [110, 111, 122] predicts the inductive shift of electronic states as the inductive energy of a molecular dipole $\mu = er$ in a spherical cavity with diameter d in a dielectric with the dielectric constant ε:

$$\Delta E = \frac{1}{4\pi\varepsilon_0}\frac{8(\varepsilon - 1)\mu^2}{(2\varepsilon + 1)d^3} \tag{2.6}$$

For the valence states μ is approximately constant. The minimum of the potential energy curve, $T_e,$ is a linear function of $(\varepsilon - 1)/(2\varepsilon + 1)$ [79] and electronic states can be assigned accordingly. The dipole moment μ increases on going from valence to ionic states, and the shift can be quite large for the respective transitions[9]. These shifts due to electronic polarization enter into the discussion in *chapter 5.2* and suggest that the valence states remain unshifted in absorption. The shift in the difference potentials for ClF (*chapter 5.3.1*) is attributed to lowering of the energy of the ionic states.

2.2.4 Nuclear rearrangements

The matrix structurally constrains the molecule, leading to shifts of absorptions and emissions. In a simplified approach, depicted in Fig. 2.6, the potential surfaces can be calculated by adding up pair potentials, e.g. between $Cl - F,$ $Cl - Rg$ and $F - Rg.$ This is fundamental to understanding the meaning of the effective 1-D potential derived in *chapter 7.1*. The following description exemplifies the ”dynamical” potential that results from the additive pair potential approach, used in the molecular dynamics simulations discussed above (chapter 2.1). For the LIF emission a complementary description in a configuration coordinate model is used. Both treatments neglect the electronic effects (i.e. polarization, inductive forces and electronic wave functions) described above.

Model for the dynamic cage

In a system with several coordinates, the one dimensional potential in the coordinate relevant for pump-probe spectra is dynamically changed by the other coordinates. This phenomenon is analyzed in the following. Classical molecular dynamics simulations work with additive pair potentials, i.e. each particle feels the potentials of all other particles. Thus the total potential energy that governs the motion of a diatomic molecule in the matrix is the sum of the molecular potential energy V_{mol} and the energy of the cage potential V_{cage}. The van-der-Waals potential between Rg cage and the molecular fragment X has a shallow minimum and a strong repulsion (Lennard-Jones)[10].

Fig. 2.6 shows the potential energy surfaces of iodine for the three relevant electronic states; the ground state $X,$ the B state, in which the observed dynamics take place, and the E state for the probe transition. They are shown for the gas phase as a thin dash-dotted line. In addition, each state is shown with the potentials imposed by a *static* cage onto the molecular coordinate $R.$ To demonstrate the effect, it suffices to consider an $I - I$ molecule with two Kr atoms in a linear configuration as indicated in Fig. 2.6 (top). The dotted lines, as an example, are calculated as follows. The molecule is in the ground vibrational state of the X state, and the molecular bond is fixed at the corresponding equilibrium position $R_{eq}(X).$ Then the Kr atoms move into the minimum energy configuration, which is given by the van-der-Waals $I - Kr$ distance, i.e. by the shallow minimum of the Lennard-Jones potential. Then the Kr atoms are fixed in this configuration, and the $I - I$ bond is elongated and the total potential energy is calculated as the sum of the $I - I$ and $I - Kr$ potential.

---

[9] In a second order approximation, the diameter d of the cavity also changes due to rearrangement of the matrix atoms.

[10] This minimum corresponds to what is sometimes called the dispersive forces as opposed to inductive forces, which are induced by a static dipole (e.g. ionic states) on the dielectric. If the weak attraction is neglected, exponential repulsion due to Pauli repulsion of the electronic clouds works fine. These potentials have very short range, rendering a summation over nearest neighbors a good approximation.

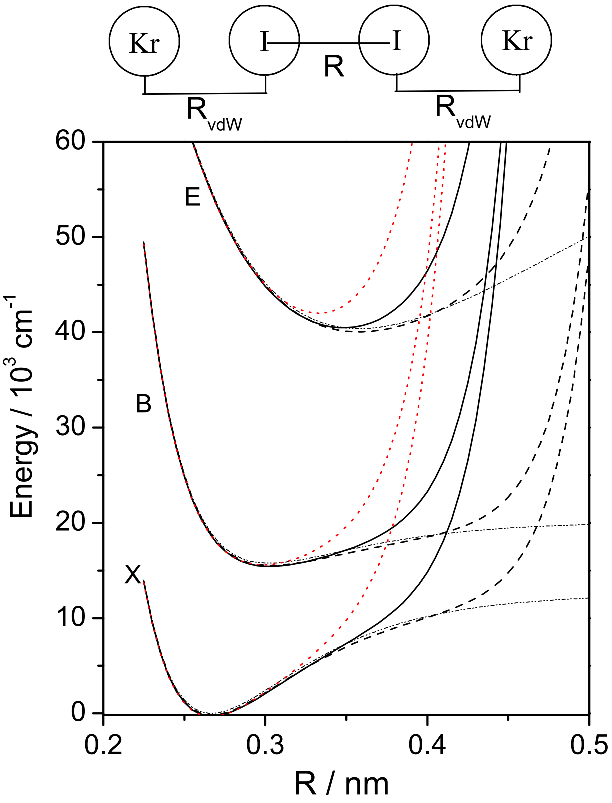

Figure 2.6: a) I_2 molecule with bond distance R and two adjacent Kr atoms at the van-der-Waals distance R_{vdW}. b) Potential energy surface for the ground state X and the excited states B and E. The gas phase I_2 potential is represented by the dash-dotted line. The other curves are additive pair potentials including the two adjacent Kr atoms fixed at the van-der-Waals distance after they have relaxed around the X state equilibrium (dotted), the B state (solid) and the E state (dashed).

The potential bends up at large R, since the I atoms feel the strong repulsion from the fixed Kr. This is a simple account of the cage effect. The solid line is calculated accordingly, now with the Kr atoms fixed in the configuration for the equilibrium position of the B state $R_{eq}(B)$ and the dashed line for the E state configuration. The cage moves outward as the $I-Kr$ repulsion shifts the Kr atoms further away.

As far as molecular dynamics are concerned, the effect of the surrounding matrix can be exemplified in Fig. 2.6 in the following way. Consider the three B state surfaces for the different matrix configurations. In a pump-probe experiment, the pump pulse at $h\nu_{pump}$ prepares the wave packet in the B state in the configuration indicated by the dashed potential for the ground state equilibrium. When the vibrational ($I-I$) wave packet moves outwards to larger R, the matrix cannot stay fixed, but has to respond to the repulsive $I-Kr$ forces. During outward motion, the potential will smoothly change from the dotted to the solid to the dashed shape, and during the inward motion the reverse. Therefore, the effective one dimensional potential, that will be experimentally derived in chapter 7.1.2, looks like an intermediate between the three potentials. Such a potential has up to now not been presented explicitly and instead only potentials for fixed cage geometries are given in the literature, although it would be very helpful for discussions of pump-probe spectra. One way to accomplish this task is proposed in chapter 7.3.1.

It is also instructive to discuss the frequency domain spectroscopy in this picture. If an absorption spectrum is recorded for a molecule in the X state, the Born-Oppenheimer approximation says that the nuclear coordinates will not change in the electronic transition. Therefore, the matrix induces a blue shift in the sense that the minima of the B and E states, $T_e(B)$ and $T_e(E)$, are shifted up due to the repulsion from the Lennard-Jones potential at large R. This effect is clearly visible only for the E state (compare the minima of the dotted and dash-dotted lines). A weak blue shift in absorption with respect to the gas phase is actually seen in the light rare gases, like Ne, where the

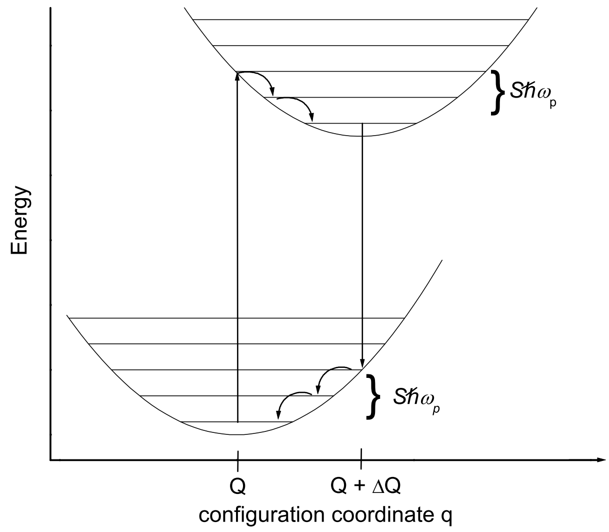

Figure 2.7: Potential energy for two different electronic states in the configuration coordinate model. In the harmonic approximation the potential energy is a parabola with equilibrium position Q for the lower electronic state and $Q + \Delta Q$ for the excited state.

electronic polarization shift to the red is weak [74]. For ionic states the red shift due to polarization overcompensates this weak blue shift.

Note that in the present approximation, all electronic states feel the same $I - Kr$ pair-potential, and for the molecular dynamics calculations, the difference potential ΔV is identical to the gas phase. In different electronic states of a diatomic, the electron clouds have different shapes and this alters the pair interactions to the surrounding atoms. These effects are in part accounted for with the DIM method, but they are small. Comparison of the DIM calculation on I_2/Kr with I_2 gas phase potentials yields variations < 100 cm^{-1} among valence states and < 400 cm^{-1} between ion-pair and valence states.

Electron phonon coupling

The fluorescence from ionic states is the recorded signal in all pump-probe spectra of this thesis. For a proper assignment, their spectroscopy is discussed in *chapter 5.2*. These spectra are usually very broad and red shifted, and the underlying mechanism is discussed in the following. Details are given in refs. [123], [124] and [125].

In the ionic states, the molecular bond is extended compared to the valence states. The strong red shift in emission results from the rearrangement of the rare gas lattice around the larger electronic cloud. To describe the rearrangement of many atoms in a convenient way, a configuration coordinate q is introduced.. It q may be thought of as the size of the cage, for example. In the harmonic approximation, the rare gas matrix forms a parabolic potential (Fig. 2.7) around the molecule in the ground state, $V_g = \frac{1}{2}M\omega_p^2 q^2$, with equally spaced eigenvalues $n\hbar\omega_p$, which are the characteristic phonons of the host lattice (and thus vibrations of the cage). In the excited electronic state of the molecule, e.g. the ionic states, the lattice rearranges around the extended electron cloud. This corresponds to a parabola displaced by $\Delta Q,$ i.e. the equilibrium position in the configuration coordinate is larger. In the crudest approximation, the form of the parabola is not changed, implying that the phonon frequency ω_p is kept constant.

In this model the Stokes shift between absorption and emission is $E_s = 2S\hbar\omega_p$ [124, 125]. S is the mean number of phonons emitted during the absorption and the emission [126], and thus a measure of the electron-phonon coupling strength. The creation of phonons is indicated in Fig. 2.7 as the small arrows. S is called the Huang-Rhys phonon coupling constant which is connected to the parabolic potential by the ratio $S\hbar\omega_p = \frac{1}{2}M\omega_p^2\Delta Q^2$. The intensity I of these phonon assisted transitions is described by a Poisson distribution [127] $I(\hbar\omega_{zp} - n\hbar\omega_{ph}) = e^{-S}S^n/n!$, where $\hbar\omega_{zp}$ is the zero phonon line energy of the electronic transition. This is a consequence of the Franck-Condon overlap of the vibrational wave functions in the two displaced harmonic oscillators [124]. In the strong-coupling limit $(S \gg 1)$, the line shape is Gaussian with the width $H = 2.36\sqrt{S}\hbar\omega_p$. For Cl_2 in Ar it was demonstrated in excitation spectra, that the electron-phonon coupling gradually increases on exciting higher and higher in the part of the anharmonic molecular potential, where the molecular frequency drops below the Debeye frequency of the lattice [128].

2.2.5 Matrix shifts

For different electronic states, molecules and matrices general predictions cannot be made, because the inductive, dispersive and geometrical shifts compete [125, 129, 130]. A collection of shifts for many diatomics in rare gases is given in ref. [74]. The transitions from the ground state to valence states are usually only weakly shifted by 1 to 2 %, since they occur in the Frank-Condon region, where the influence of the matrix is weak. The results on ClF in Ar and Kr presented in *chapter 5.1* lie in the same trend.

For ionic states the strong red shift in absorption is mainly due to the polarization effect, that is described by eq. 2.6. In emission, the rearrangement of the matrix cage yields an additional Stokes shift. Moreover, nonradiative coupling among the ionic states can yield additional red shifts between absorption and emission, when the population relaxes to a lower lying electronic state. Often the coupling is very strong among closely spaced states in the ionic manifold, and the emission usually originates from the lowest state of the ionic manifold.

For completeness: Rydberg states of molecules and atoms are blue shifted in condensed rare gases, since the large Rydberg-electron cloud is repelled by the filled electron shells of the rare gases according to Pauli's exclusion principle. This effect often leads to a deperturbation of the ionic states [131], which in the gas phase strongly couple to the Rydberg states, forming double-well potentials.

2.2.6 Excimers and exciplexes

Excimers are diatomic molecules (dimers) that are bound only in the excited state. Exciplexes are analogous polyatomic molecules (complexes). In the case of rare-gas-halogen molecules, the ground state is only weakly bound (~ 100 cm^{-1} $\sim 1/80$ eV) by van-der-Waals forces, whereas the excited state is ionic and lends its binding energy (several eV) from Coulomb's law. As a typical example consider the potential of KrF is displayed in Fig. 5.5.

These species are largely used in excimer lasers, as they cover a wide range of UV wavelengths and have very large gain [52]. Inversion is easily achieved, since the molecule is not bound in the ground state. Rare gas halides play an important role in the understanding of the chemical bond and are well characterized. Anisotropic potential energy parameters for the diatomics like ArF and $KrCl$ have been derived from molecular beam scattering experiments [56, 57] and ab initio calculations [50, 51]. Triatomic species like Ar_2F and Kr_2F have been calculated ab initio [47–49] and observed in emission in the gas-phase [55] and in rare gas matrices [53, 54] (cf. Fig 4.6).

For pump-probe spectroscopy KrF is an interesting candidate since its absorption is in the near UV. Absorption and excitation spectra of the excimers in Ar and Kr matrices were measured by several groups [82, 88, 132]. The spectra of KrF in Ar agree in all publications and display a well resolved vibrational structure from the levels in the ionic states. The spectra for KrF in Kr are contradictory. While the authors in ref. [132] reported a broad band around 260 nm, a narrow and strong absorption at 275 nm attributed to $Kr_6^+F^-$ dominates the excitation spectrum of ref. [88]. Bressler [82] measured the excitation spectrum and reports both structures, but with a strong yet unexplained dependence on the history of the sample. A series of absorption spectra in *chapter 4.2.4* will clarify the origin of the disagreement and *chapter 4.3.3* offers an explanation.

atom	Cl	F	Ar	Kr	Xe
E^+	12.97	17.42	15.76	14.00	12.13
E^-	3.62	3.40			

Table 2.1: Ionization potentials E^+ and electron affinities E^- of halogens and rare gases

2.2.7 Molecular ion-pair versus excimer states in condensed rare gas

Ionic states involve transferring one electron from one atom to another, and sometimes charge delocalization among several atoms. Let Rg denote rare gas atoms and X and Y halogen atoms. Within this thesis two different ionic species are important. The molecular ion-pair states solvated in rare gas X^+Y^-/Rg or excimers and exciplexes $Y^-Rg_n^+$ with a neutral X nearby. Which of the possible charge distributions is actually taken, depends on the interplay of ionization energy E^+, electron affinity E^- and the polarization energy E_μ of the formed molecular dipole in the dielectric, the energy for charge delocalization E_{del}, as well as the distance-dependent coulomb energy $E_C(R)$ and the ”Pauli repulsion” $E_P(R)$ between different atomic orbitals. It is a challenge to accurately model the different species and even more difficult to simulate the dynamics among different species. For some special cases ionic potentials have been calculated in the DIIS formalism [64, 110, 111]. It is considered as an important task for the theoretical collaborations to investigate these states for the F and Cl atoms in rare gases.

Until this is accomplished, the potentials calculated and/or measured in the gas phase have to suffice, and plausibility arguments account for the surrounding matrix and the solvent shift. As an example that will be needed later, consider the formation of Cl^+F^-/Rg vs. $Rg^+F^-\ \ Cl$. The bond distance of all involved ionic species is approx. 0.25 nm and thus the energy gain in the interplay of E_C and E_P as well as the polarization energy E_μ is approximately equal for both charge distributions. The electron affinity $E^-(F)$ enters equally in both species, and for the moment charge delocalization is ignored. Then the decisive quantity is the ionization potential E^+, which is lower for Cl than for Ar and Kr [11]. In argon the difference in $E^+ = 2.79$ eV (Tab. 2.1). Hence the ionic state Cl^+F^- is observed in argon (*chapter 4.2.1*). Of course, the Ar^+F^- states will be formed, if after dissociation Cl is not near F. The expected formation of Ar^+F^- and Kr^+F^- species in matrices upon F_2 excitation was observed [81, 88]. For Kr and Cl the difference in E^+ is only 1.03 eV. The delocalization of the positive charge among several rare gas atoms cannot be neglected anymore, since the energy is lowered by approx. 1 eV, when $Kr^+F^- \rightarrow Kr_2^+F^-$ [47–49]. The decision whether Cl^+F^-/Kr is stable against formation of $Cl + Kr_2^+F^-$ cannot be made on these grounds (*cf. chapter 5.2.2*).

DIM calculations on these exciplexes [47–49] show that the distance between the Rg atoms in the minimum energy configuration of these exciplexes is much smaller (0.25 nm) than the corresponding $Kr-Kr$ van-der-Waals distances in the matrix. Comparison to the diatomic energies of KrF reveals that the energy of charge delocalization between two Kr atoms is gained only after the bond has shrunk [50, 51]. Therefore, in excitation usually only diatomic exciplexes are important. In emission the $Rg_2^+X^-$ exciplex is observed [81, 88][12].

---

[11] Only Xe has an even lower ionization energy and therefore the Xe excimers can be used for detection in the OODR experiments [133] (Tab. 2.1). Xe^+Cl^- was also found to exist in matrices [132].

[12] In the ionic states of halogens X^+Y^-, the molecular bond is extended and the rare gas atoms approach the halogen more closely, so that the fluorescence leading to the repulsive halogen-rare gas potential is dramatically red-shifted, as discussed in the preceding chapters. For this reason the states are sometimes assigned as $X^+(Y^-Rg)$ instead of $(X^+Y^-)Rg$ [134]. The ionic species denoted by $(X_2)^-Rg_n^+$ are higher in energy for the relevant molecules in this thesis, since $E^+(Cl) < E^+(Kr)$.

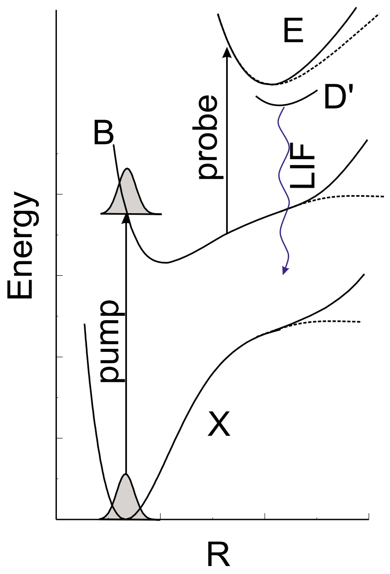

Figure 2.8: Scheme of pump-probe spectroscopy. The dashed lines indicate the gas phase potentials and the solid lines mimic the potentials including the solvent cage effect. The pump pulse prepares a wave packet from a coherent superposition of vibrational levels in the excited electronic state B. The probe pulse promotes the wave packet to the final state E in the ionic manifold, when the packet is in the probe window. After nonradiative relaxation within the ionic manifold, the fluorescence from the D' state is recorded.

2.3 Femtosecond pump-probe spectroscopy

2.3.1 Method

Femtosecond pump-probe spectroscopy is a method to follow ultrafast dynamical processes on the timescale of the pulse duration. The pump pulse starts the dynamics and the probe pulse takes a snapshot of one of the system's properties after a delay time t. The signal can be absorption, or diffraction of the probe photon, or generation of secondaries like fluorescence, photoelectron spectra etc. The signal is recorded as a function of time delay.

In the context of this thesis, femtosecond pump-probe spectroscopy more specifically refers to the process depicted in Fig. 2.8. A fs-pump pulse is absorbed by a molecular system and starts the wave packet dynamics on the excited electronic state, e.g. the B state. The wave packet moves in the potential and when it passes the probe window after the delay time t between pump and probe pulse, it is excited to the E state. The delay time t is varied continuously on the femtosecond timescale. Nonradiative relaxation within the ionic manifold to the D' state results in fluorescence emission (LIF) on the nanosecond timescale[13]. The intensity of the fluorescence as a function of delay time t shows, when the wave packet passes the probe window. In the absence of saturation it is proportional to the intensities of the pump and the probe pulse. The dashed lines in Fig. 2.8 indicate the potentials of the molecules in the gas phase, and the solid curves include the forces from the solvent cage.

The closer analysis of the method needed in the analysis of the spectra requires a more detailed description. The pump pulse creates a wave packet by coherently exciting a superposition of several vibrational states around E_{pump} in an excited electronic state. In the case of a dissociative potential, the continuum of states is coherently excited. The wave packet evolves under the influence of the excited state Hamiltonian. By Ehrenfest's theorems, the expectation values for position and momentum of the wave function satisfy the classical equations of motion (chapter 2.1.5), approximating the motion of a classical particle in a potential, as long as the wave packet is localized. (cf. Fig. 2.9a).

The probe pulse promotes the wave packet to the E state, if the resonance conditions, i.e. energy and momentum conservation, are fulfilled. This is the case when the wave packet is at a probe window position R_{win}, where the difference potential ΔV equals the probe photon energy $h\nu_{probe}$. This condition follows from the Franck-Condon approximation, which is based on a negligible change of the momentum of the wave packet due to the photon [104,135]. Classical momentum conservation

---

[13] The fluorescence terminates on several electronic states that are allowed for the dipole transition.

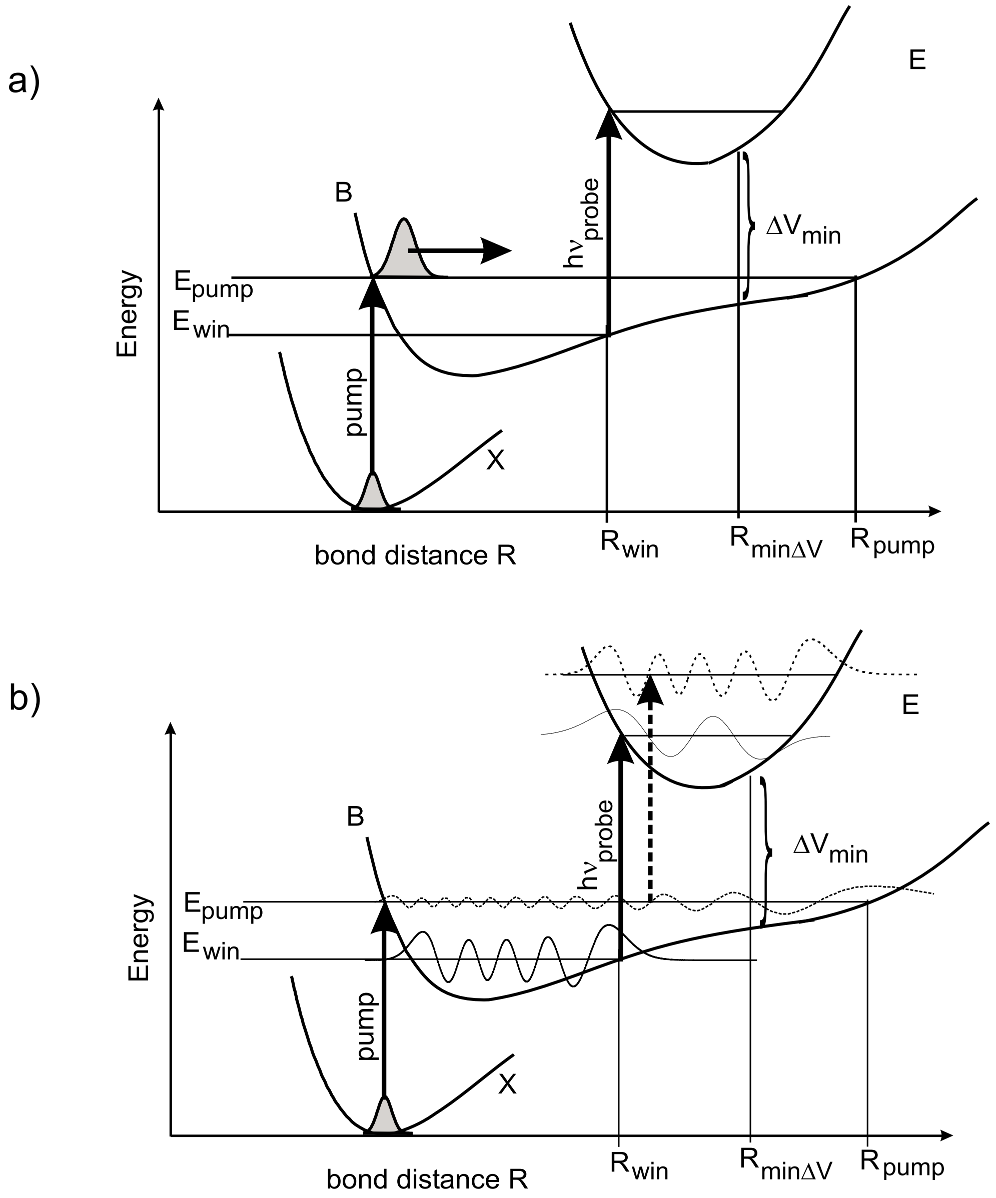

Figure 2.9: Scheme of pump-probe spectroscopy in systems with dissipation. a) The pump pulse prepares a wave packet around E_{pump} in the excited electronic state B. The outer turning point of the wave packet with the initial energy is R_{pump}. The probe pulse promotes the wave packet to the final state E, if the wave packet is at the position of the probe window at R_{win}. The condition for the probe window is that the difference potential $\Delta V = E_E - E_B$ matches the energy of the probe photon $h\nu_{probe}$. The minimum of the difference potential $\Delta V_{\min}$ is located at $R_{\min \Delta V}$. The observed pump-probe signal decreases with the velocity, at which the wave packet passes the probe window. At the energy E_{pump} the signal is low. When the wave packet is relaxed to E_{win}, it has zero velocity in the probe window, and the signal is high. b) Same potential diagram including one of the vibrational wave function excited by the pump pulse. It is connected to the vibrational wave function (dashed) in the E state by the probe energy $h\nu_{probe}$ (dashed). The overlap of the wave functions is poor (weak signal). The vibrational wave function at the energy of the probe window E_{win} (solid arrow) has a large overlap to the corresponding wave function in the E state (solid).

requires that the kinetic energy of the wave packet remains unchanged after the electronic transition. The conservation of total energy therefore implies $h\nu_{probe} = \Delta V(R) = V_E(R) - V_B(R)$. A detailed investigation of the classical expression shows that the pump-probe signal is inversely proportional to the velocity[14] v of the wave packet at the probe window R_{win} [45].

The classical argument of momentum conservation is reflected in a quantum description by the overlap integral (Franck-Condon factors) of the nuclear (vibrational) wave functions, corresponding to the vibrational eigenstates that are coherently coupled in the wave packet (cf. Fig. 2.9b). A wave function oscillating quickly with R, corresponds to large kinetic energy (large velocity v) and a slowly varying wave function means small kinetic energy. The overlap of slowly varying wave functions in the initial and final state is large, and the overlap of a fast oscillation with a slowly varying function is close to zero. Two oscillating functions may have appreciable overlap. The overlap of the two wave functions connected with the solid arrow (probe) is large, because the large antinodes overlap and the oscillations do not. This is always the case, if the probe window energy E_{win} is at the energy of the probed level, i.e. the wave packet is probed at the turning point.

In order to deduce information on the dynamics from the pump-probe spectra, the potential, and especially the difference potential ΔV, for the probe transition must be known. As a first approximation, the difference potential is identical to the gas phase in the cases examined here, since the interaction energy of the rare gas atoms with the molecule is similar for all electronic states. This approximation is quite accurate according to the discussion in chapter 2.2.4. In *chapter 7.1* it will be demonstrated, that information from a series of pump-probe spectra can be used to construct a potential energy surface in advance and subsequently extract the dynamics.

2.3.2 The threshold for the probe transition

The probe transition in pump-probe spectroscopy deserves a closer inspection. For a quick discussion consider Fig. 2.9b. It is obvious that no probe absorption will take place if $h\nu_{pump} + h\nu_{probe} < \min E$, i.e. the energy of the vibrational level in the B state prepared by the pump pulse plus the probe energy is smaller than the minimum of the E state. Now let the pump pulse excite vibrational levels around E_{pump} in the B state, above the level needed to reach the region of the lowest probe window at $R_{\min \Delta V}$ (minimum of the difference potential ΔV). Although excited state absorptions with $\min E - E_{pump} < h\nu_{probe} < \min \Delta V$ are energetically allowed, the Franck-Condon overlaps are very small. The high vibrational levels in the B state have fast oscillations with R. The low vibrational levels in E, that could be accessed from the energetics $\min E - E_{pump} < h\nu_{probe}$, vary slowly with R, yielding a poor overlap for all probe energies $h\nu_{probe} < \min \Delta V$ (cf. Fig. 2.9b, dashed wave functions and dashed arrow). This small overlap corresponds to momentum conservation in the wave packet language. The longest probe wavelength that transfers appreciable population to the higher lying E state is given by $h\nu_{\min} = \min \Delta V$. It is determined by the difference potential ΔV and *not* by the difference between the pump energy and the minimum of the final state[15]. This will be used in *chapter 7.1.3* to construct the E state of I_2/Kr.

In order to measure the threshold of the probe transition, i.e. the minimum of ΔV, in the condensed phase, the molecule can be excited with any energy above $E_B(R_{\min \Delta V})$, above the window for the minimum of ΔV. Vibrational relaxation successively populates lower and lower vibrational levels until this level is reached. As long as $h\nu_{probe} < \min \Delta V$, there will be no signal. The resonance is reached for $h\nu_{probe} = \min \Delta V$. This method is applied to obtain the correct vertical shifts of the difference potentials ΔV of ClF and Cl_2 in Ar (*chapter 5.3.1*).

---

[14] The expression $1/v$ diverges for a wave packet at the turning point and the quantum mechanical expression is needed.

[15] This is the classical result derived above from the Franck-Condon principle. Only a minor correction has to be made to obtain the correct quantum mechanical result, that accounts for the zero-point energy of the zeroeth vibrational level in the E state and the fact that some overlap is already obtained for levels in B that are slightly above $E_{\min \Delta V}$.

2.3.3 Condensed phase pump-probe spectroscopy

In the gas phase, time and frequency domain spectra of a molecule are connected by a Fourier transformation. The information delivered by the two methods is mathematically equivalent. It was exemplified for I_2 that the Fourier transform of a fs-pump-probe spectrum shows the individual vibrational and rotational levels excited by the pump pulse [39]. For a high resolution in the frequency domain, a long pump-probe transient has to be recorded over several 100 ps. In systems with population- and energy-relaxation processes or collision induced decoherence, the oscillations in fs-pump-probe spectra may not live long enough to resolve individual vibrational and rotational levels. This is the case in the system of diatomics in rare gases investigated here. Since the pump pulse excites several vibrational levels, the vibrational frequency measured in a pump-probe spectrum depends on the relative weight with which the individual vibrational levels are probed, i.e. on the probe-wavelength. This effect is experimentally demonstrated very clearly for the first time within this thesis (chapter 7.1.2). It has been noticed previously in classical MD simulations but reported without further discussion [27]. In frequency domain spectra the relaxation processes lead to a broadening of the absorption band, which washes out the relevant structure [29, 62, 100]. This makes fs-pump-probe spectroscopy the method of choice in dissipative systems, since it can beat the timescale of the relevant relaxation processes.

The presence of the solvent or bath changes the pump-probe spectra in several ways. First of all, it induces dissipation and the molecule loses energy (*vibrational energy relaxation, chapter 7.1*). In an anharmonic potential, this changes the vibrational frequency in the course of time (*chapter 7.4.2*). It also changes the envelope of the pump-probe spectrum (*chapter 7.4.1 and 7.4.3*). Often the solvent influences the coupling of electronic states and thus the population relaxation to lower states [42, 43, 66, 115]. The dramatic effect of solvent-induced spin-flip is discussed in *chapter 7.6*. Decoherence, i.e. loss of coherence, is an important issue in the condensed phase. The consequence of decoherence for pump-probe spectra is the loss of modulation depth. Random scattering events of the molecule with the solvent destroy the phase relationship and thus the wave packet. It is important to notice that not only this random dephasing decreases the modulation depth, but also the dispersion of the wave packet due to the anharmonicity of the potential (see above). The decay of this modulation can originate from dispersion (anharmonicity) and decoherence (random collisions) and hence the two processes are often mixed up and called ”dephasing” [16]. This situation is complicated by the additional ensemble effect that leads to ”inhomogeneous broadening” of the spectral lines and is often also referred to as ”dephasing”. In principle, the contribution from dispersion can be distinguished from the other processes, because the dispersion on the anharmonic potential can be pre-compensated by chirping the pump pulse, i.e. by negative optical dispersion introduced in the pump-pulse. A short discussion on coherence vs. dephasing in the measured spectra can be found in *chapter 7.9*.

It should be mentioned that LIF detection in pump-probe spectroscopy has the advantage in condensed phases that this method probes the population of the excited state in the coordinate of the probe transition. The observed fluorescence signal is proportional to the population in the final state after both pulses, and measures the diagonal elements of the density matrix in the excited state. The method of coherent anti-Stokes Raman scattering (CARS), for example, measures coherences, i.e. off-diagonal elements. Moreover, CARS requires an electronic coherence, which decays rapidly in condensed phases (~ 100 fs) and damps out the oscillations [58, 62, 136]. The LIF technique allows the observation of oscillations due to vibrational coherence, even if electronic dephasing is very fast.

---

[16] It is unfortunate that in the most widely used theoretical framework, especially for MD in the liquid phase, all quantities are expressed as correlation functions, which do not distinguish decoherence and dispersion. For the calculation of the pump-probe spectrum, this correlation function is the overlap of the ground state Gaussian with the excited state wave packet.

2.3.4 Selection rules

In light diatomic molecules like ClF the angular-momenta are coupled according to Hund's case a, and the following selection rules hold [137]: $\Delta S = 0$, $\Delta\Sigma = 0$, $\Delta\Lambda = 0, \pm 1$ and from $\Sigma + \Lambda = \Omega$ it follows that $\Delta\Lambda = \Delta\Omega$. Therefore a transition $^1\Sigma_0 \rightarrow ^1 \Pi_1$ is allowed, whereas $^3\Pi_0 \rightarrow ^3 \Pi_1$ is forbidden. Optical transitions between singlet and triplet states are spin-forbidden (spin selection rule: $\Delta S = 0$), transitions with $\Delta\Omega = \pm 2$ are dipole-forbidden and originate from the quadrupole-interaction with the light field. The transition $X(^1\Sigma_0) \rightarrow B(^3\Pi_0)$ is spin-forbidden $(\Delta S = 1)$,but the selection rule is weakened by the spin-orbit interaction[17]. In the heavy I_2 molecule the angular momenta are coupled according to Hund's case c, and only the selection rule $\Delta\Omega = 0, \pm 1$ remains [137].

The selection rules are reflected in the transition moments that have been calculated by A.B. Alekseyev (cf. Fig 5.6) and in part published in ref. [121]. They will be used in *chapter 5.3.1*. Transitions between valence and ion-pair states are governed by the propensity rule $\Delta\Omega = 0$, since they involve transferring an electron from one atom to another. To accomplish this, an electric field in the direction of the electron transfer is needed. In a diatomic the transition is parallel to the molecular axis, i.e. $\Delta\Omega = 0$. The electronic states in Fig. 2.11 and 4.1 have been labeled according to their quantum number Ω for that reason. This propensity rule is valid also for I_2.

The following considerations on polarization are important for the polarization selective pump-probe spectroscopy discussed in *chapter 7.5*. In analogy to the Zeemann effect in atoms, where m_j is the projection of the angular momentum j on the axis of symmetry dictated by the magnetic field, Ω is the projection of the electronic molecular angular momentum J on the internuclear axis. For observation transverse to the symmetry axis, $\Delta m_j = 0$ and $\Delta\Omega = 0$ correspond to polarization parallel to this axis and $\Delta m_j = \pm 1$ and $\Delta\Omega = \pm 1$ to perpendicular polarization. For longitudinal observation, only $\Delta m_j = \pm 1$ and $\Delta\Omega = \pm 1$ exist, since the polarization is perpendicular to the symmetry axis [138]. The difference for the molecule from the Zeemann analogy is that, for the Stark effect induced by the internuclear electric field, the emitted light is not circularly polarized, since the effect of the electric field is the same for electrons with $m_j = \pm 1$ [139]. The interplay of polarization and selection rules gives rise to the method of photoselection [140]. Electronic excitation with polarized light prepares a distribution of excited-state molecules aligned with the light polarization $(\Delta\Omega = 0)$ or perpendicular to it $(\Delta\Omega = \pm 1)$ (cf. chapter 2.3.5)

2.3.5 Polarization dependent pump-probe spectra

This chapter provides the intensity ratios for the LIF expected in polarization sensitive pump-probe spectra that were taken for the analysis of angular reorientation in *chapter 7.5*. Electronic transitions in molecules have a transition dipole moment with magnitude and direction. The transition dipole matrix element $| < \Phi_i|\overrightarrow{E} \cdot \overrightarrow{\mu}|\Phi_f > |^2$, which determines the intensity of absorbed or emitted light, is proportional to the square of the scalar product $\overrightarrow{E} \cdot \overrightarrow{\mu}$, where $\overrightarrow{\mu}$ is the transition dipole and $\overrightarrow{E}$ is the electric field. If a sample of randomly oriented molecules is excited with linearly polarized light, an ensemble of molecules is selected that have the transition dipole aligned with the polarization (photoselection [138, 140]). The analytic form of the dipole distribution is $\cos^2\theta$ (Fig. 2.10b), where θ is the angle between the electric field $\overrightarrow{E}$ and the transition dipole $\overrightarrow{\mu}$ [138].

If the transition dipole moment in a diatomic molecule is directed along the internuclear axis, the transition is called parallel $(\Delta\Omega = 0)$, otherwise perpendicular $(\Delta\Omega = \pm 1)$ (cf. chapter 2.3.4). A parallel transition yields an ensemble of molecules with an alignment of the axes that is identical to the distribution of dipoles (Fig. 2.10b). A perpendicular transition selects an ensemble of molecules

---

[17] Since $\Delta\Lambda = 1$ it follows from $\Delta\Omega = 0, \pm 1$ that the transition is to the $\Omega = 0 + \Delta\Lambda \pm \Delta\Sigma = 0$ state (unlike $X^1\Sigma_0 \rightarrow ^1 \Pi_1$).

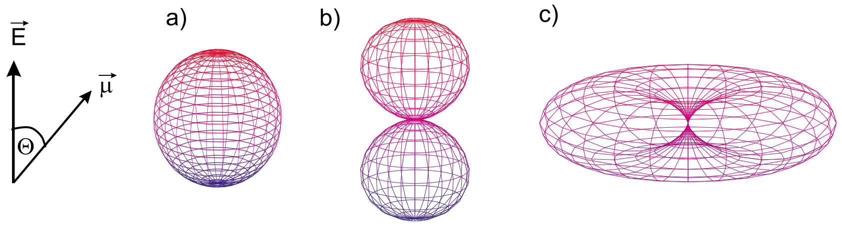

Figure 2.10: Distributions of the molecular ensemble, a) sphere for a randomly distributed ensemble, b) ensemble selected with polarized light in a parallel ($\Delta\Omega = 0$) transition, c) ensemble selected with polarized light in a perpendicular ($\Delta\Omega = \pm 1$) transition.

with the axis perpendicular to the $\cos^2\theta$ distribution, i.e. a toroidal ensemble of molecules, $\sin^2\theta$ (Fig. 2.10c).

If the molecules do not rotate or librate, they will fluoresce with a well defined polarization, i.e. they emit a photon with polarization along the transition dipole for emission[18]. This is used in fluorescence depolarization spectroscopy to determine the angular motion of molecules on the timescale of the fluorescence lifetime by recording the fluorescence anisotropy as a function of time.

This thesis deals with the polarization dependence[19] of the photons absorbed and emitted in forward direction. The photoselected anisotropy is detected with a polarization analyzer or, equivalently, by another interaction with a polarized photon[20]. For general theory on polarization dependent spectroscopy the reader is referred to ref. [141].

For convenience, Tab. 2.3.5 collects the possibilities for two or three interactions of a molecular ensemble with a light field that are relevant to the pump-probe experiments presented in this thesis. The transition dipole moment $\overrightarrow{\mu}$ of the pump transition can be parallel (Fig. 2.10b, $\cos^2\Theta$) or perpendicular (Fig. 2.10c, $\sin^2\Theta$) to the molecular axis. This is indicated by the lobe ”8” and the torus ”◎” in the first column of Tab. 2.3.5. The probe transition and the fluorescence are parallel transitions ($\Delta\Omega = 0$) in all cases examined here, since they have charge transfer character (cf. chapter 2.3.4). The polarization of the probe pulse is fixed ($\|$, column three), e.g. parallel to the optical table. The pump pulse has perpendicular ($\perp$) or parallel ($\|$) polarization with respect to the probe pulse, or the distribution is randomized (o). Column four specifies whether no polarization analyzer is used (”O”) or whether it is perpendicular $\perp$ or parallel $\|$ to both pulses.

A quick graphical explanation for the expected intensity ratios that are collected in the last column can be given as follows. Since all photons propagate in the forward direction, each interaction of the transition dipole with a light field (emission or absorption) mathematically corresponds to calculating the overlap of the three distributions in Fig. 2.10, when their volumes are normalized to 1. The distribution b) has to be rotated by 90° when calculating the overlap for perpendicular $\perp$ photoselection or LIF analyzer. Alternatively the values can be looked up in ref. [141].

Experiments are often carried out in the magic angle configuration, with the two relevant polarizations at an angle of 54°. At this angle the signal is independent of the orientation of transition dipoles [142].

---

[18] In the diatomic molecules examined here, the transition dipole in emission has the same direction as in absorption.

[19] Dipole radiation is anisotropic both with respect to the direction of the emitted or absorbed photon and to their polarization. A dipole emits and absorbs radiation with a toroidal intensity distribution for the direction of the emitted light as shown in Fig. 2.10c (theory of Hertz oscillator), and the polarization has a $\cos^2\Theta$ distribution (Fig. 2.10b). Thus, the anisotropy after polarized excitation can be simply recorded by comparing the emission in forward direction with the one in the direction of the exciting polarization.

[20] A polarization analyser selects the emitted photons with the right polarization in emission and an incoming photon is polarized before the interaction.

transition dipole for pump	photo-selection	probe transition	LIF analyzer	intensity
parallel 8	$\parallel$	$\parallel$	O	$I_{\parallel} = 3/5 = 0.6$
parallel 8	$\perp$	$\parallel$	O	$I_{\perp} = 1/5 = 0.2$
parallel 8	o	$\parallel$	O	$I_d = 1/3 \approx 0.33$
parallel 8	$\parallel$	$\parallel$	$\parallel$	$I_{LIF\parallel} = 5/35$
parallel 8	$\parallel$	$\parallel$	$\perp$	$I_{LIF\perp} = 1/35$
perpendicular ◎	$\parallel$	$\parallel$	O	$1/5 = 0.2$
perpendicular ◎	$\perp$	$\parallel$	O	$2/5 = 0.4$

Table 2.2: Intensity ratios observed for spectroscopy with polarized light. Pump and probe pulse are collinear and the fluorescence is observed in the forward direction. The first column denotes whether the electronic transition is parallel 8 ($\Delta\Omega = 0$) or perpendicular ◎ ($\Delta\Omega = 1$). The second column specifies the photoselection of the originally isotropic ensemble by the pump pulse, with polarization parallel $\|$ or perpendicular $\perp$ to the probe polarization, which is kept fixed (third column). o indicates an isotropic (depolarized) ensemble. The fourth column specifies the polarization of the fluorescence detection with respect to the probe. O indicates no polarization analyzer. The abbrevations $I_{\|}$, $I_{\perp}$, I_d, $I_{LIF\|}$ and $I_{LIF\perp}$ together with the respective intensity ratios are given in the last column.

2.3.6 I_2 in Kr as the model system to advance fs-pump-probe spectroscopy in the condensed phase

One part of this thesis is dedicated to pump-probe spectroscopy on I_2 in Kr matrices. This system is particularly well studied and characterized. Its heavy mass makes I_2 a convenient molecule for fs-pump-probe studies. The focus of the part of the thesis concerning I_2 is to test the power of the ultrafast spectroscopic tool and to learn how detailed information on molecular dynamics can be extracted from the spectra without the help of simulations. This chapter gives a concise introduction to the relevant previous work on I_2.

A series of pioneering publications by the Zewail group [42–44] investigated the influence of rare gas environments on the free molecule, in clusters and in the gas phase for increasing rare gas pressures up to liquid phase densities. The observed number of oscillations decreases with increasing rare gas density and this was in part attributed to a rapid loss of B state population due to predissociation, i.e. nonadiabatic transitions to a dissociative state. Surprisingly strongly modulated wave packet oscillations extending up to several ps with up to 20 periods were observed in the ordered crystalline phase of Ar, Kr and Xe matrices in the Apkarian group. A wealth of information on energy relaxation and predissociation dynamics induced by the cage was derived from the experimental data in combination with classical trajectory calculations [21, 23, 25–29, 45, 58, 62]. Semiclassical calculations on DIM surfaces [63–65] corroborate essential features. Focusing of wave packets in the B state of I_2 in Kr after several ps was achieved by linearly chirped pump pulses [31, 32].

Absorption and emission spectra of I_2/Kr are well known. In this thesis the B state is excited in the Franck-Condon region from 570 to 480 nm, the $B \to E$ transition is used as the probe and the $D' \to A'$ transition at 420 nm is monitored together with $\beta \to A$ for the pump-probe spectra [80, 115]. The B state in matrices shows a peculiarity. While the vibrational dynamics in pump-probe spectra are well resolved it is not possible to derive the essential spectroscopic constants like T_e, ω_e and $\omega_e x_e$ from absorption spectra because only a structureless Franck-Condon envelope is observed. This is explained by long lasting $I - I$ correlation functions and quickly damped I_2-matrix and matrix-matrix correlation functions [62].

This situation provides a challenge and a test bed to derive the spectroscopic properties from fs-pump-probe spectra. While for free molecules it was especially demonstrated in the I_2 case [39] that the Fourier transformation of fs and ps data is equivalent to analyzing rotationally resolved vibrational progressions [143], this method requires modifications for the strong interactions in condensed phases which in many cases lead to fast vibrational relaxation. A wave packet started at high vibrational levels falls down within a few oscillations in the potential well, thus passing quickly through regions of rather different frequencies, prohibiting a standard Fourier transformation.

For this case it was shown [32, 144] that by following the decrease in duration of the vibrational periods along the time course of a pump probe spectrum and by systematically varying the pump photon energy, i.e. the starting point in the potential well, it is possible to derive both the spectroscopic constants and the vibrational relaxation rates.

This thesis works out the concept in more detail, and shows especially that accurate spectroscopic constants also require a systematic variation of the probe photon energy (*chapter 7.2*). The determination of vibrational relaxation rates relies on the anharmonicity, which becomes small near the bottom of a bound potential energy surface. The periods have to be measured more and more accurately with decreasing anharmonicity and energy relaxation rate. An improved B state potential energy surface up to the dissociation limit is derived that includes the dynamics of the solvent cage. This potential is an effective 1-D-potential that should be observed in DIM-trajectory calculations, if the energy is averaged over all trajectories, as detailed in *chapter 7.3.1*. Shifting the spatial position of the probe window near the dissociation limit directly yields snapshots of an experimental $R(t)$ trajectory at large elongation R of the $I - I$ bond. The trajectories and the derived kinetic energies display the details of the caging of the I atoms by the matrix atoms.

2.4 The molecule chlorine monofluoride (ClF)

The spectroscopy of F_2 in rare gases shows that electronic transitions in this system lie unfavorably far[21] in the UV, rendering femtosecond pump-probe experiments difficult. The ClF molecule possesses the interesting F fragment which is mobile in matrices, but has advantageous spectroscopic properties as will be shown in this thesis.

2.4.1 Chemical and physical properties

The ClF molecule is the lightest interhalogen, with atomic masses $m(Cl) = 35$ amu and $m(F) = 19$ amu. The colorless gas is used in chemical industry as a strong fluorinating agent and is sold commercially in large quantities but also in $1\ l$ bottles with a purity of 99%[22]. The melting point of ClF is $T = 117.55$ K and the boiling point is $T = 173.15$ K. In contact with water it decomposes to hydrofluoric and hydrochloric acid (HF and HCl). ClF is formed at 250°C in the presence of copper as a catalyst by the reaction sequence $Cl_2 + 3F_2 \rightarrow 2ClF_3$ followed by $ClF_3 + Cl_2 \rightarrow 3ClF$ [91]. The molecule is stable at room temperature against decay into $Cl_2 + F_2$ and a slight excess of Cl_2 prevents the disproportionation $3ClF \rightarrow Cl_2 + ClF_3$. Therefore, most of the 1% impurity in the gas used is Cl_2.

2.4.2 Spectroscopy and potential

Despite the stability and commercial availability only little spectroscopic information on gas phase ClF was available before V. A. Alekseev *et al.* investigated this molecule using optical-optical double resonance (OODR) spectroscopy [133, 145–148]. Merging their experimental work with the recent configuration interaction (CI) calculations by A. B. Alekseyev *et al.* [121] has resulted in very accurate potential surfaces for gas-phase ClF (see Fig. 2.11).

---

[21] Especially the probe to the ionic states would be 4.45 eV further to the UV, due to the higher ionization potential of F compared to Cl (cf. Tab. 2.1).

[22] Sold by ABCR GmbH & Co KG, Hansastr. 29c, 76189 Karlsruhe, Germany.

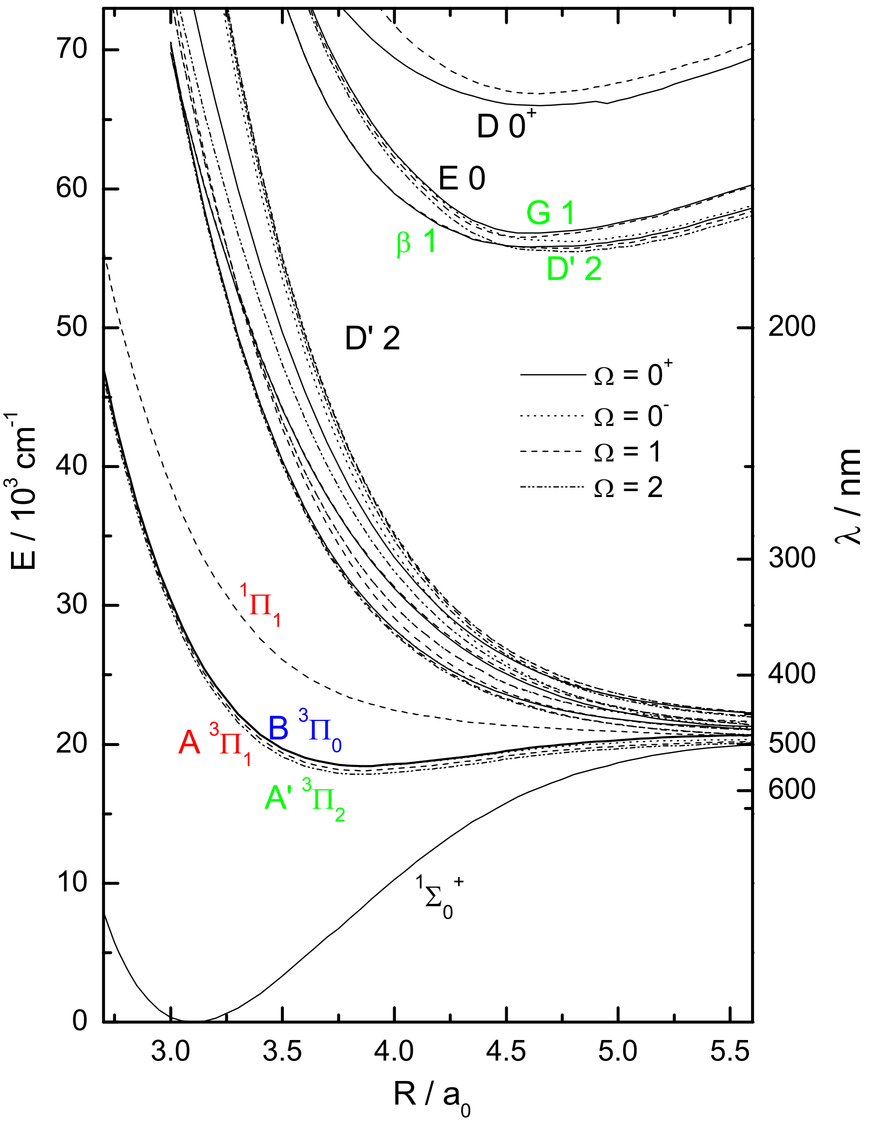

Figure 2.11: Potential of ClF from ref. [121]. The line structure represents the quantum number $\Omega = 0^+$ (solid), $\Omega = 0^-$ (dotted), $\Omega = 1$ dashed and $\Omega = 2$ (dash-dot).

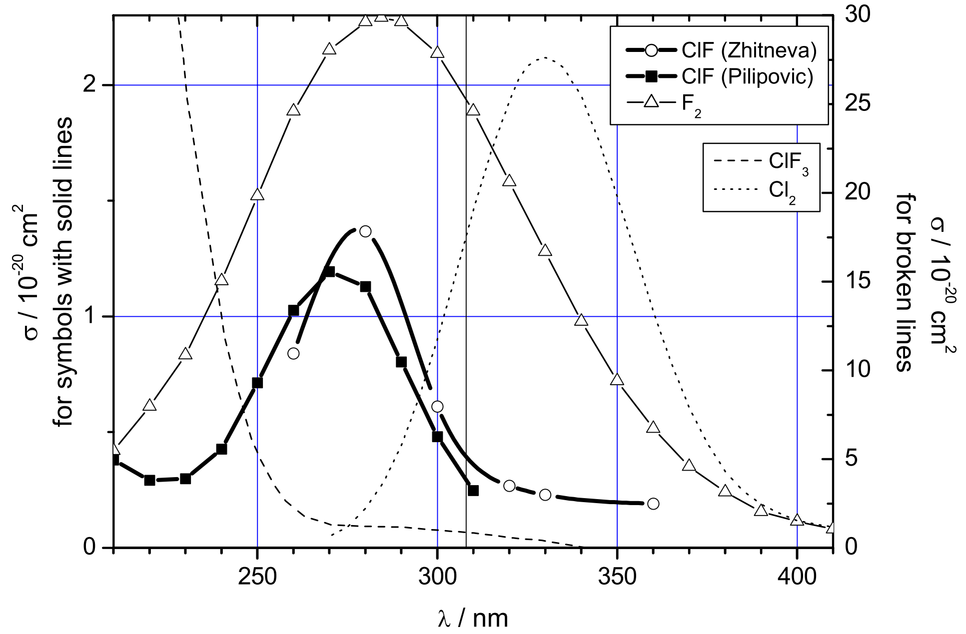

Figure 2.12: Absorptions of ClF, Cl_2, F_2 and ClF_3. The scale on the left hand side is for solid lines with symbols, ClF (open circles after Zhitneva [150]), ClF (solid sqares after Pilipovich [149]) and F_2 (open triangles [151,152]). The scale on the right hand side is for the stronger absorbing molecules Cl_2 (dotted [153]) and ClF_3 (dashed [154]).

Electronic absorption spectra in the dissociation continuum of ClF are given in ref. [149, 150] for the range from 190 to 360 nm and reproduced in Fig. 2.12. The maximum of the absorption is around 270 to 280 nm with a weak cross section of $\sigma = 1.36 \times 10^{-20}$ cm^{-2} (ref. [150], open circles) or $\sigma = 1.21 \times 10^{-20}$ cm^{-2} (ref. [149], solid squares).

In a third paper [155] the absorption band at 270 nm is shifted to 250 nm and stronger by a factor of 8, probably due to a Xe impurity. A comparison to a calculated absorption spectrum gives confidence in the above mentioned spectra (cf. Fig. 5.2). The separation from impurities Cl_2, F_2 and ClF_3 is difficult according to Fig. 2.12. Despite the weak absorption in the bound state $B(^3\Pi_0)$, a laser excitation spectrum has been reported by I. S. McDermid [156] and references for the pioneering work on the ClF molecule are given therein. The spectroscopic data for the ground state obtained by various methods are collected in Ref. [157] and reproduced in Tab. 5.1. The relative absorption cross sections ($\sigma \sim \mu^2$) for the B and $^1\Pi$ state can be estimated from the transition moments μ that were kindly provided by A.B. Alekseyev [158]. The ratio of the respective maxima yields $\sigma(X \rightarrow^1 \Pi_1)/\sigma(X \rightarrow B(^3\Pi_0) = 50$ (cf. discussion in chapter 5.1.2).

The value for the fundamental frequency $\nu_{0\rightarrow 1}$ of the ground state is taken from IR absorption data [159] that have been reinvestigated by J. A. Coxon [160]. The ground state vibrational progression characterized by the frequency ω_e and anharmonicity $\omega_e x_e$ are derived from electronic absorption and emission data of the $X \leftrightarrow B$ transition [157].

Several articles concerning IR and Raman spectra of ClF in condensed media have been published. The first [161] was on ClF in solid Ar and N_2. L. Andrews reported more details on infrared spectra of ClF in rare gas matrices at a dilution of 1:50 [162]. In addition to the slightly shifted ground state vibrational frequencies of 770.2 cm^{-1} and 762.7 cm^{-1} for the two isotopes (in Ar) additional peaks were observed and attributed to dimers and higher clusters. The frequency of a matrix-isolated ClF-monomer is shifted to the red by approximately 3 cm^{-1} in Ar and 10 cm^{-1} in Kr as compared to the gas phase values [157]. Similar red shifts have been reported for ClF in liquid Ar (5 cm^{-1}), O_2(6 cm^{-1}) and N_2 (8 cm^{-1}) [163].

Spectroscopy on the ionic states is performed by the OODR technique [133, 145–148] and the emission $D' \rightarrow A'$ has been used to construct a laser at $\lambda = 284.4$ nm [164–166]. Absorption spectra for the lowest Rydberg states [167] of ClF (140 - 129 nm) can be compared to calculations [168].

Several publications report very precise experimental [169, 170] and theoretical [109] studies of the ground state of the triatomic van-der-Waals complex $ArClF$, showing deviations of the potential from simply adding pair-potentials, and reveal three-body effects. The effects are quite small but may play a role in the initial alignment of the ClF molecule in the Ar matrix (see end of chapter 2.2.1).

2.4.3 Photochemistry of ClF

Few experiments on the photochemistry of ClF in the gas phase have been reported. Photodissociation of ClF_3 yields F and Cl atoms [171] and the photolytic reaction $3ClF \rightarrow Cl_2 + ClF_3$ was investigated by Zhitneva [150]. Two-photon laser assisted reactions with Xe produce the excimers $XeCl$ and XeF [155, 172] and these species are used in the OODR experiments to detect the formation of the ion-pair states of ClF [133, 145–148].

Two reviews on photochemistry in matrices deal especially with the reactions of F fragments in Ar and Kr [36, 86]. In an early matrix study the $F - Cl - F$ radical was investigated in solid nitrogen, since it is interesting for chemical structure considerations of a 21 electron system [173–175]. Complexes and photoreactions of ClF with metal atoms [176], with hydrogen [177] and with oxygen were studied by IR spectroscopy and UV absorption [178].

2.4.4 Stable triatomic rare gas halides in the ground state

Some rare gas halide trimers of the form RgX_2 form stable molecules. XeF_2 is a white powder at room temperature. KrF_2 is calculated [179] to be stable by 0.39 eV and the experimental value is 1.01 eV [92–94]. It has been observed in matrices by IR and Raman spectroscopy as well as the molecule $ClXeF$ [95]. The same experiments that tried to prepare $ClKrF$ did not have a positive result, although the species is predicted to be stable [97]. The linear molecule Kr_2F was observed by ESR spectroscopy [180]. These molecules may be important in future experiments, when the fs-control of photochemical reactions is pursued further.

2.4.5 Electronic states of interhalogens: ClF

Halogen and interhalogen molecules exhibit a simple electronic structure. The constituent atoms have a single p-hole in the outer shell, giving rise to states which are equivalent to those from only one outer shell electron. The orbital diagram for ClF is shown in Fig. 2.13. The F atom has higher electron affinity and thus the binding molecular orbitals σ and π have higher probability near the F atom, whereas the antibinding orbitals are closer to Cl. [181]. In the correlation diagram the interhalogens are close to the separated atom model [137, 139].

The electronic *states* of a molecule, e.g. Σ, Π, Δ, result from occupying the molecular orbitals with electrons. The ground state $X(^1\Sigma_0)$ of ClF is a singlet state, because all spins are paired up when the five p electrons of F and Cl occupy the lowest possible molecular orbitals as shown in Fig. 2.13. The symmetry Σ comes from the unoccupied σ^* orbital. The lowest valence states are $1^3\Pi$ and $1^1\Pi$. They originate from an excitation $\pi^* \rightarrow \sigma^*$, thus the total orbital angular momentum of

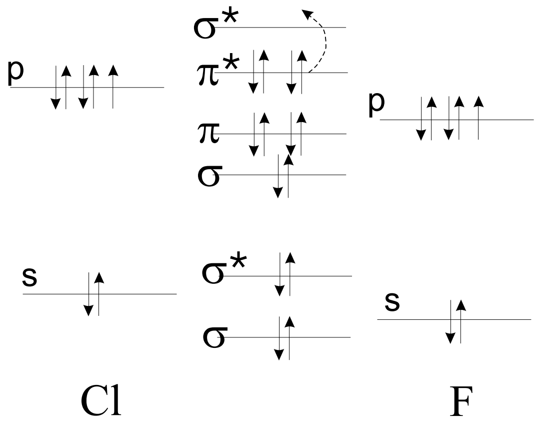

Figure 2.13: Orbital diagram of ClF. The atomic s and p orbitals of Cl and F are occupied with seven electrons each. In the ground state all molecular orbitals, except the antibinding σ^* are occupied with a pair of electrons. The excitation of one electron from π^* to σ^*, indicated by the dashed arrow, gives rise to the lowest lying excited states.

the unoccupied orbitals is $\Lambda = 1 + 0$. The two spins can be either parallel or antiparallel (triplet or singlet)[23].

The following paragraphs summarize and extend the discussion of the orbital character of the different states from the recent publication on CI calculations on ClF by A. B. Alekseyev *et al.* [121]. Potential curves are given for all 23 valence states and 9 ion-pair states. In the Franck Condon region, the most stable electronic configuration is the $\sigma^2\pi^4\pi^{*4}$ closed-shell species, which produces the strongly bound $X(^1\Sigma_0)$ ground state. The σ orbital has binding character, while its counterpart, the lowest-lying unoccupied σ^* orbital, is antibinding . In the Franck Condon region, the π and π^* orbitals are also binding and antibinding , respectively, though much more weakly so in comparison with the σ and σ^* MOs. They become nearly lone-pair $p_{x,y}$ orbitals localized on the F and Cl atoms at intermediate distances larger than 4.0 a_o. The ground state dissociation energy can be estimated from the calculated energy value at a large ClF separation, $r = 20.0\ a_0$, which gives $D_e = 20878$ cm^{-1} $= 2.589$ eV. The upper limit derived in experimental studies from the predissociation of the B state [156, 182] caused by the interaction with a repulsive 0^+ state is $D_0 < 21126 \pm 6$ cm^{-1}.

All other eleven valence states result from the π^*, π or $\sigma \longrightarrow \sigma^*$ excitations relative to the $\sigma^2\pi^4\pi^{*4}$ ground state configuration. The lowest two ClF excited states are $1^3\Pi$ and $1^1\Pi$ ($\sigma^2\pi^4\pi^{*3}\sigma^*$ in the Franck-Condon region), which correspond to the $\pi^* \longrightarrow \sigma^*$ transition with the lowest excitation energy (Fig. 2.13). The $1^3\Pi$ multiplet is the only ClF excited state which is bound, by approximately 2700 cm^{-1} without spin-orbit coupling, and is characterized by a much larger equilibrium distance, 3.9 a_o vs. 3.07 a_o for $X(^1\Sigma_0)$. It is worth noting that at a bond length of 3.9 a_o the π and π^* MOs are almost completely localized on the F and Cl atoms, respectively, and thus have nonbinding character. This means that the $1^3\Pi$ state arises from excitation out of the nonbinding π^* to the antibinding σ^* orbital, which explains its much smaller binding energy relative to the ground state. The $\sigma^2\pi^4\pi^{*3}\sigma^*$ configuration dominates the 1 $^3\Pi$ state up to its equilibrium distance, where contributions from the $\sigma^2\pi^3\pi^{*4}\sigma^*$ ˜18.0% and $\sigma^1\pi^4\pi^{*3}\sigma^{*2}$ ˜28% configurations also become important, with their influence quickly increasing at longer distances. The same type of behavior is also characteristic for the $1^1\Pi$ state, for which the exchange of leading configurations happens at slightly shorter distances. This state has a flat potential curve, with a very shallow minimum of approximately 100 cm^{-1} depth at 6.5 a_o.

When the molecular bond is broken in these lowest electronically excited states, the atomic fragments dissociate into ^2P states. Since the F has higher electronegativity the σ^* hole stays with the F, as this corresponds to lower energy than the π^* hole, which stays at the Cl. Geometrically, the singly occupied atomic P orbitals are oriented as shown in Fig. 2.14. At large internuclear distances

---

[23] The 1 before $^1\Pi$ is the principal quantum number and counts the number of nodal planes in the wave function. 1 corresponds to one nodal plane at infinity (ref. [137] p. 326).

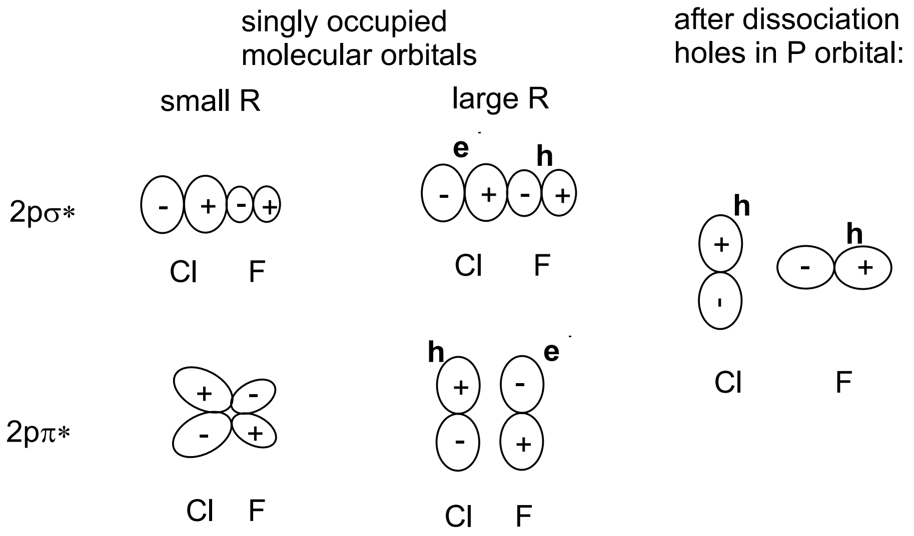

Figure 2.14: Molecular orbitals for dissociation in the first excited state manifold of ClF. The two antibinding singly occupied molecular orbitals of ClF tranform to atomic orbitals localized on Cl and F. The $p\pi^*$ orbital is a lone pair already for $R > 3.9\ a_0$. Since F has higher electronegativity, the hole (h) in the highest molecular orbital σ^* stays with F during dissociation. The singly occupied P-orbital on the F atom is accordingly oriented parallel to the direction of motion. The Cl is left with the hole in an orbital perpendicular to this direction.

$R > 3.9$ a$_0$, the molecular π orbitals already resemble lone-pair $p_{x,y}$ orbitals. The singly occupied P orbital of the F atom ($2p\sigma^*$) points in the direction of the dissociative motion, whereas the Cl orbital is perpendicular to it ($2p\pi^*$). After dissociation, the Cl and F radical are left with seven electrons in the outer shell, each. The singly occupied P orbitals on Cl and F, i.e. the ones which are left with a hole, are oriented perpendicular and parallel to their direction of motion, respectively. This will influence the encounters with the solvent atoms, and the picture helps to visualize the processes in the scattering and spin-flip dynamics in *chapters 7.5.3* and *7.6*.

There is a large gap in the ClF electronic spectrum, up to an excitation energy of approximately 55 800 cm^{-1}, at which the first two of the ion-pair states, $3^3\Pi(\sigma^2\pi^4\pi^{*3}\sigma^*)$ and 2 $^3\Sigma^-$ $(\sigma^2\pi^4\pi^{*2}\sigma^{*2})$, appear. They converge to $Cl^+(^1P) + F^-(^1S)$ of the separated atoms. Both of them are strongly bound, mainly due to the $Cl^+ - F^-$ electrostatic interaction, which explains their long equilibrium distances with respect to the ClF ground state. The transitions to these states are used to monitor the recombination dynamics of ClF/Ar, and the shifted difference potentials to the valence states are given in *chapter 5.3.1*. The highest-lying states considered in ref. [121] are the singlet ion-pair states $^1\Sigma^+$, $^1\Pi$ and $^1\Delta$, all converging to the $Cl^+(^1D) + F^-(^1S)$ dissociation limit. They have very similar potential curves with approximately 10000 cm^{-1} higher excitation energies and will not be excited in this thesis, however, will be important to study $^1\Pi$ state dynamics more closely, which lead to rapid spin-flip (*chapter 7.6*).

Chapter 3

Experimental setup

This chapter introduces the reader to the setup used in the experiments. The important and unique aspects of the setup are described. The chapter on generation and characterization of light pulses is extended, since the NOPA and FROG setups used, were in part developed within the thesis work. For the theoretical background on nonlinear optics the reader is referred to the literature on the special subjects. Some footnotes are included to give helpful hints to those who work with this or similar systems in the future.

3.1 Ultrahigh vacuum (UHV) setup and cryostat

The set-up comprises a mixing chamber (I) and a sample chamber (II) made from stainless steel (see Fig. 3.1). The vacuum is established by turbo molecular pumps with rotary pumps for the pre-vacuum. The background pressures are 10^{-6} and 10^{-8} mbar, respectively. Pressure reduction valves connect the mixing chamber with the high-pressure bottles with high purity gases, Ar (200 bar, 99.9999%), Kr (200 bar, 99.998%), ClF (30 bar, 99% from ABCR) and Cl_2 (30 bar, 99%). All gases are used without further purification although in the future it may be desirable to purify the ClF. This has not been tried yet, because the chemical equilibria mentioned in chapter 2.4.1 may again lead to Cl_2 formation. A needle valve controls the gas flux from the mixing chamber to the sample chamber.

The sample chamber is equipped with two CaF_2 substrates that are thermally contacted with two independent sample holders, made from copper. One is attached to a flow cryostat, the other to a closed-cycle cryostat. In most experiments the flow cryostat is employed, since it can cool the sample down to 4 K. The temperature is checked with a Si-diode from Cryophysics. The two samples are thermally insulated from each other. They can be moved with the x-y-z manipulator holding the flow cryostat. The cycle cryostat is connected to the sample holder with flexible copper wires from the side, which limits the temperature to 20K[1]. This setup allows switching between the cycle cryostat for long term experiments and the He-flow cryostat without opening the vacuum chamber.

A similar setup with a closed cycle cryostat is used for the preparation of I_2 in Kr matrices [32, 144] from the vapor pressure above a solid I_2 crystal (99,999% from Sigma Aldrich) and Kr (99,998% from Linde). The background pressures were 10^{-6} mbar in the mixing chamber[2] and $5{\cdot}10^{-9}$ mbar in the sample chamber. This low background pressure allows the samples to be kept for several days without noticeable changes.

---

[1] This can be improved with a refurbished cycle cryostat.

[2] 10^{-6} mbar can be achieved by applying the turbo molecular pump but usually the 10^{-2} mbar produced with the rotary pump are sufficient, since I_2 fluorescence is much stronger than that from all impurities. It was tested that the results are not affected by the impurities. Most of the molecules expected to be present in the background gas are not resonant with the used laser pulses.

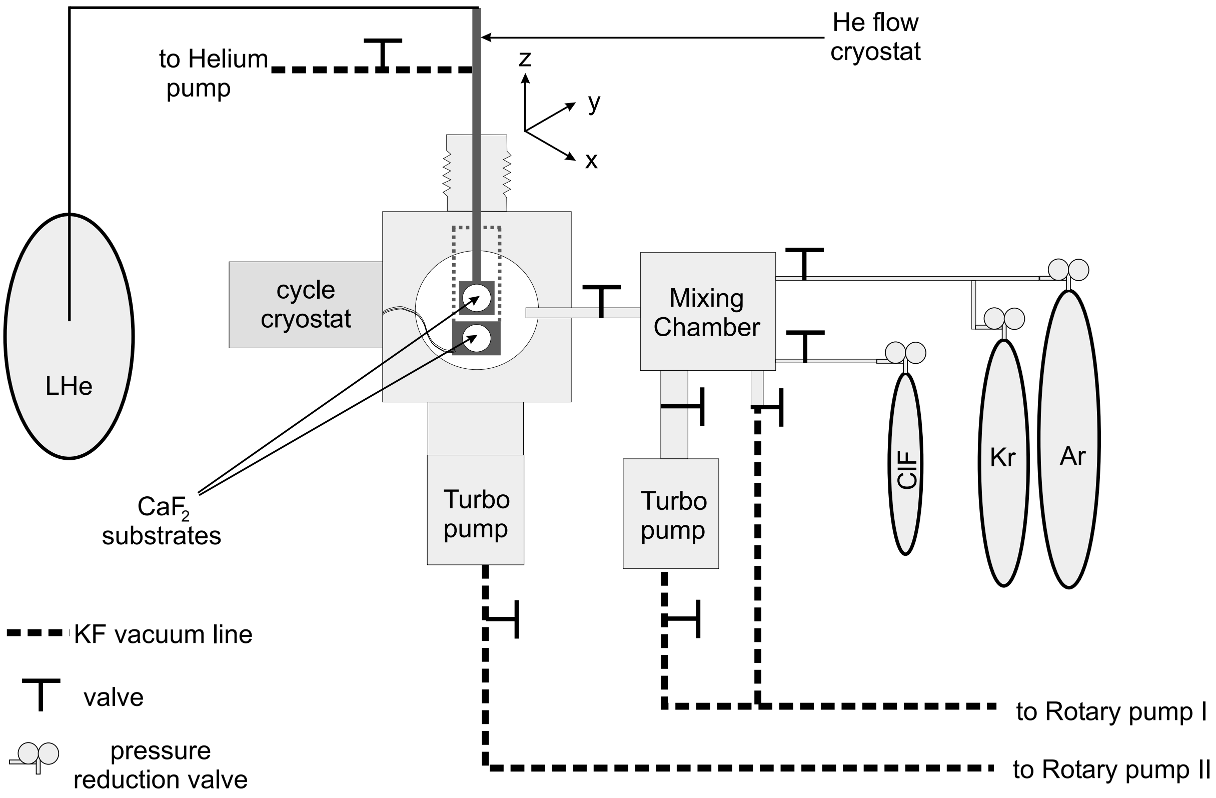

Figure 3.1: The sample chamber contains the two CaF_2 substrates, which can be moved with the x-y-z stage. The He-flow cryostat cools the upper substrate, while the lower substrate is connected to a cycle cryostat with flexible copper wires. The gas mixture (prepared in the mixing chamber) is sprayed onto the samples through the thin tube, which connects the two chambers. A top view of the geometry of the substrate, the thin tube and the laser beams is shown in Fig. 3.5. Besides the three connections to the ClF, Ar and Kr gas bottles, there are two more (not shown) to attach Xe and Cl_2 bottles.

3.2 Sample preparation

The mixing chamber is kept permanently passivated with ClF. Before diluting 1 mbar ClF with the rare gas at ratios ranging from 1:500 to 1:100,000 the mixing chamber is evacuated to a pressure of approx. 10^{-6} mbar. The mixture is introduced into the sample chamber (background pressure in the sample chamber is 10^{-8} mbar) through a stainless steel valve with a thin tube attached to it and sprayed onto a 1 mm thick CaF_2 substrate. The geometry for the crystal growth is depicted in Fig. 3.5. The tube is at the same height as the laser beams. Thus the sample does not have to be moved after preparation. Rare gas films of typically 100 μm thickness are grown in 30 min, which has been verified by counting interference fringes of a HeNe laser. The quality of the films is judged by eye and by the scattering of UV pulses. The deposition conditions (rate and temperature) have been optimized to generate transparent and only weakly scattering films. The rate is controlled with the needle valve and checked with the ionization manometer, which reads 10^{-5} mbar during deposition, reflecting the dynamical equilibrium with the cryostat and the turbo pump. The temperature is set to 15 K for Ar and 20 K for Kr matrices. The temperature of the samples must subsequently be changed quite slowly to avoid cracks in the film due to thermal expansion or contraction. If the samples are deposited more rapidly or at lower temperatures, this usually leads to scattering films with many cracks. Higher temperatures have the disadvantage of promoting the formation of molecular dimers and higher clusters.

Most of the experiments on Cl_2 were conducted in the ClF/Ar or ClF/Kr samples. The 1% content of Cl_2 in the ClF gas is sufficient, since the absorption cross section for Cl_2 is much larger (cf. Fig. 2.12). To check the assignment of the bands and dynamics to Cl_2, pure Cl_2/Ar samples were grown at similarly low concentration from 1:10 000 to 1:100 000. For this purpose, gas from a high pressure bottle with 1:100 Cl_2/Ar was diluted with Ar.

The I_2/Kr samples consisting of 30 μm thick clear crack-free films of Kr doped with I_2 in a ratio of 1500 : 1 were prepared in the same way at 20 K as described in refs. [32, 144].

3.3 Laser system

A commercial regeneratively amplified Ti:Sa laser, (CPA 2001 from Clark-MXR) is the basis of all fs pulses used in this work. It delivers pulses at 775 nm with a pulse duration of 150 fs at 1 kHz repetition rate and with a typical pulse energy of 750 μJ. This laser is seeded with a frequency doubled Erbium fiber laser pumped with telecom diode arrays. It is a turn key system but has the disadvantage that the wavelength cannot be tuned. All tunable radiation is generated by subsequent nonlinear processes. Fig. 3.2 shows the setup in a block diagram.

At the moment four non-collinear optical parametric amplifiers (NOPAs) are pumped in parallel. The remaining fraction of fundamental laser light is used for second harmonic generation (SHG) and for white light generation in another experiment. This extremely flexible setup was made possible by a great increase of NOPA efficiency achieved in this thesis (chapter 3.4). The chirp of the fundamental at 775 nm is adjusted to produce a high conversion efficiency in all four NOPAs at the same time. The pulses are slightly negatively pre-chirped (blue components first) when leaving the CPA 2001, since there is some dispersive material before the NOPAs.

3.4 New NOPA design

The first NOPA [183] setup goes back to 1997 and since then many groups improved various parameters [34, 35, 184, 185]. The major advantage of the new design presented in this thesis is that the efficiency of the process is doubled while excellent pulse stability and temporal characteristics are maintained for the same output power. In this way the NOPAs are now pumped with pulse energies of only 0.11 mJ. The commercial regeneratively amplified Ti:Sa laser delivers approximately 0.7-0.8 mJ and up to six of these devices can be pumped in parallel, while retaining some excess of pump-power e.g. for SHG. In addition, the new NOPA is much more compact (300 x 600 mm instead of 600 x 1200).

The wavelengths of the NOPA are readily tuned, rendering this device a very versatile spectroscopic tool. It is tunable from 460 to 720 nm, and it delivers 10 μJ pulse energy around 550 nm, thus providing an excellent overall efficiency of about 10 %. The used pulse length was typically 30 fs and with an optimized alignment pulses shorter than 20 fs can be obtained [35]. If one aims at records concerning pulse duration < 20 fs, the spectral bandwidth of the NOPA becomes very broad. These pulses are less useful for the spectroscopic applications of this thesis.

3.4.1 NOPA setup

The non-collinearly pumped optical parametric amplifiers (NOPA) in Fig. 3.3 closely follows the original design developed in the group of Riedle [183]. The pump light (110 μJ of the CPA output) is mildly focused with a 2 m lens, approx. 1 m before the NOPA (not shown in Fig. 3.3)[3]. A fraction of 4% is reflected off the beamsplitter (BS), focused with a 30 mm lens (L1) into a 1mm thick sapphire plate and a second 3 mm quartz lens (L2) collects the divergent white light, generated in the sapphire (Saph), and mildly focuses it into the NOPA BBO. This beam is kept parallel to the

---

[3] Alternatively a telescope setup that produces the same convergence can be used.

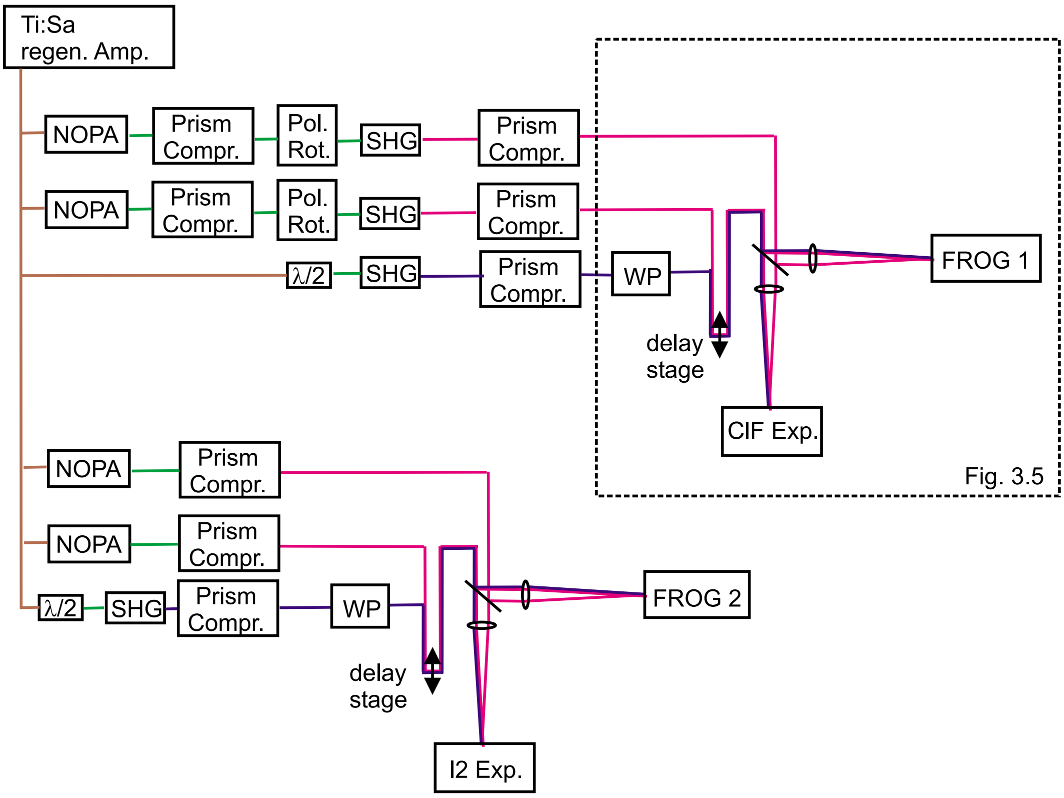

Figure 3.2: Block diagram of the laser system. The pulses are produced in the commercial regeneratively amplified Ti:Sa and split in two equal parts, one for the ClF experiment (upper part of the diagram) and one for the I_2 experiment (lower part). For the ClF experiment, there are two equal optical paths. They start with a NOPA (Fig. 3.3) to generate tunable fs pulses in the visible spectral region, pass an SF10 prism compressor and a polarization rotation stage (Pol. Rot.). The second harmonic (SHG for UV pulses) is generated and the pulses are recompressed in a quartz prism compressor, before they are directed to the sample. The polarization of the third part of the Ti:Sa output is rotated in a $\lambda/2$ waveplate. The SHG is generated and compressed in another quartz prism line. The waveplate (WP) rotates the polarization subsequently for FROG and polarization sensitive pump-probe experiments. Details of the setup in the dashed box are shown in Fig. 3.5. The setup for the I_2 experiment is similar, except that the SHG stages are missing, since the visible output of the NOPA is used.

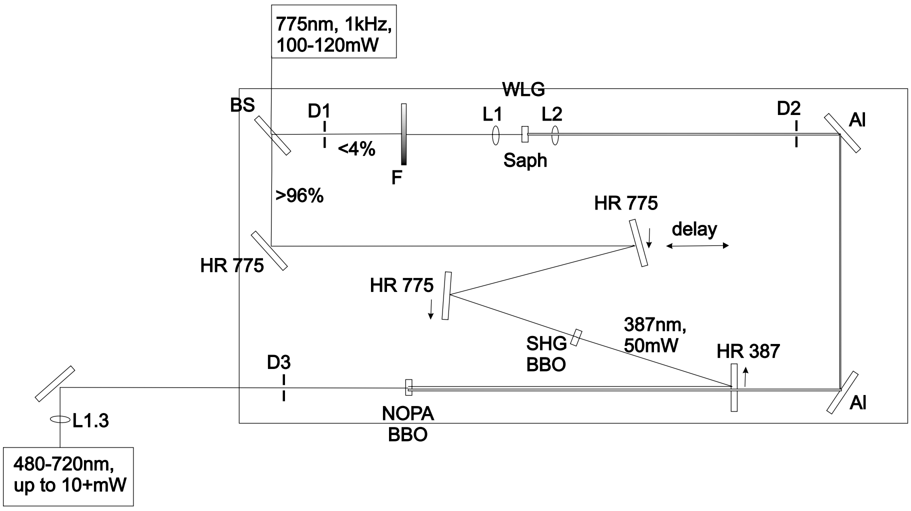

Figure 3.3: New design of the non-collinear optical parametric amplifier (NOPA). See text for an explanation.

table and aluminum mirrors are used to provide high reflectivity in the blue spectral region [4]. Three HR 775 mirrors direct the remaining 96 % of the pump light to the mirror HR 387, which is placed ~ 30 mm below the white light beam. The arrows on the mirrors indicate where the beam is lowered. The SHG BBO (1 mm thick, 5 x 5 mm cross section) is placed in the convergent beam at the position where the second harmonic efficiency (SHG) is maximal (~ 60 cm in front of the focus of the 2 m lens)[5]. The SHG efficiency is $\sim 40\%$. The plane HR 387 mirror directs the SHG beam upwards, through the NOPA BBO (2 mm thick, 5 x 5 mm), which should be placed at the position where the NOPA efficiency is optimal (~ 10 cm in front of the focus of the 387 nm beam).

The original design (commercially available from Clark) differs from the optimized setup described above. A 1 m lens in front of the NOPA reduces the beam size. The actual focusing of the 387 nm light is accomplished by a spherical focusing mirror (HR 387) with a focal length of 250 mm, which produces a hard focus just before the NOPA BBO. The SHG BBO is larger (10 x 10 mm) and the beam size on this crystal is larger, which reduces the conversion efficiency. The major improvement of the overall performance in the new design lies in the focusing conditions in the NOPA BBO, since the wave fronts of the white light and the pump light are matched better for the weak convergence induced by the lens.

3.4.2 Adjustment of the main parameters

Several parameters can be optimized to obtain pulses with specific characteristics. The wavelength tuning is accomplished by tilting the NOPA BBO and adjusting the time delay ($\leftrightarrow$ of HR775 in Fig. 3.3) between white light and 387 nm pump light. Since the white light is positively chirped by the dispersive components, the red components come first, and the temporal overlap with the pump pulse has to be adjusted accordingly. Tilting the NOPA BBO changes the phase matching condition (Fig. 3.4) for the NOPA process (pump $\rightarrow$ signal + idler).

The spectral width of the pulses can be influenced with the chirp of the white light and the height, at which the pump beam hits the HR 387 mirror. Additional dispersive material introduced into the white light beam induces higher positive chirp, which reduces the amplified bandwidth, because not all spectral components temporally overlap with the pump light. The position of the beam on HR 387

---

[4] Reflection on silver mirrors is weak below 450 nm.

[5] At this point the beam has just the size of the cheaper 5 x 5 mm BBO crystals. In the commercial NOPA setup 10 x 10 mm crystals have to be used.

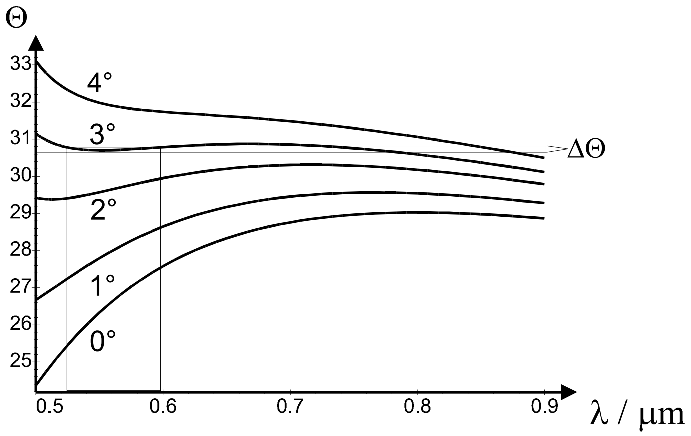

Figure 3.4: Phasematching angle Θ for different non-collinear angle α = 0, 1, 2, 3 and 4° versus output wavelength in a NOPA pumped at λ_{pump} = 387 nm. The angle α is measured inside the BBO.

changes the non-collinear angle α. Fig. 3.4 shows the phase matching angle Θ as a function of the output wavelength λ for different non-collinear angles α [144, 185]. The 2 mm thick BBO supports a certain range of angles $\Delta\Theta$ which have a phase mismatch of less than Δk, where Δk is the argument in the sinc function [186]. Shifting the range $\Delta\Theta$ around Θ up and down in Fig. 3.4 is equivalent to tilting the NOPA BBO. In order to support a large bandwidth $\Delta\lambda$ with the phasematching condition, the proper angle α must be chosen, for which the function $\Theta(\lambda)$ is flat enough do be inside the variance $\Delta\Theta$. For the example depicted in Fig. 3.4, a range $\Delta\lambda = 500$ - 600 nm will be amplified. If the phase matching angle Θ does not vary over a wide range of wavelengths λ, not only the phase velocity ω_0/k_0, but also the group velocity $d\omega/dk$ is matched[6] [183]. This implies that the signal and idler pulses co-propagate through the BBO at the same speed. Therefore, the temporal broadening is minimal yielding short pulses and the efficiency of the process is increased. The non-collinear angle α not only accomplishes this group-velocity matching but also, by coincidence, the spatial walkoff of the pump and signal beam is minimized, again for the sake of efficiency in this geometry. Note that there are two symmetric geometries that realize an angle Θ of the optical axis with the pump beam. In the right configuration the angle of the optical crystal axis to the white light is larger than Θ [35].

A very sensitive parameter, as far as efficiency is concerned, is the white light generation. The beam must be optimized in order to produce a spherical and homogeneous beam profile. The intensity is adjusted with the tunable neutral density filter F in Fig. 3.3 in such a way that the white light is well (but not far) above the threshold for optimal focusing. Sometimes it is easier to use the diaphragm D1 to cut a homogeneous and spherical beam out of the 4% fundamental. For a good alignment of the NOPA, the entire intensity in the ring of parametric fluorescence generated in the NOPA BBO has to collapse into the white light beam to produce a single intense laser beam.

3.5 Generation of tunable UV femtosecond pulses

3.5.1 Pump pulses at 387 nm

The second harmonic (SHG) at 387 nm (fundamental 775 nm) is widely used throughout this work. It is produced in a 1 mm thick BBO crystal by focusing 15 % of the Ti:Sa output with a 300 mm lens and positioning the BBO approx. 5 cm before the focus. These pulses attain the theoretical limit of pulse duration dictated by the pump pulse: $\tau = 150/\sqrt{2}$ fs ≈ 110 fs after compression, which is measured in a FROG autocorrelation (Fig. 3.5). The pulses are compressed in a quartz prism compressor. The efficiency of the SHG is approx. 30 %, yielding pulse energies of 34 μJ.

---

[6] Recall the dispersion relation $k^2(\omega) = \omega^2 n^2(\omega)/c^2$.

3.5.2 Pump and probe pulses from 240 - 360 nm

The NOPA output is frequency-doubled in a 100 μm thick BBO crystal to the range from 240 to 360 nm with pulse energies of about 1 μJ. The BBO is placed very close to the focal spot of a 300 mm lens. The bandwidth of the resulting UV pulses is limited to approx. 2 nm by the bandwidth of the SHG in the BBO crystal with thickness 100 μm. The intensity of the SHG is $I_{SHG} \sim L^2 \sin c^2(\Delta kL/2)$ [98, 186]. To compress the NOPA pulses, SF10 prisms were preferred, since quartz compressors would increase the beam length by 1.5 m. For compression of the UV pulses, however, quartz prisms must be used. The spectral profile is close to Gaussian and from the Fourier transformation of the 2 nm bandwidth at 270 nm, a pulse duration of 60 fs is expected. This has been verified by a PG-FROG in CaF_2 with the 387 nm pulse as the gate (cf. chapter 3.7). UV pulses as short as 30 fs have recently been achieved in the Riedle group [187], using thinner BBO crystals. This has not been implemented during this work, since the conversion efficiency is reduced. In addition, the increased spectral bandwidth limits the time resolution in the pump probe spectra, if the potentials are strongly anharmonic. The large variation in the shape of the pump-probe spectra in Fig. 6.8 upon tuning the probe wavelength by only 2 nm indicates that spectrally broader pulses would smear out the spectra. Moreover, the time resolution in the B state spectra is limited by the pulse duration of the 387 nm pulse. In the future, however, it will be worthwhile to generate shorter pulses for experiments with $^1\Pi$ excitation, i.e. when the second harmonic of the NOPA can be used for pump and probe pulses[7].

3.6 Pump-probe and FROG setup

Fig. 3.5 shows the multi-purpose optical setup, which is used to characterize all femtosecond pulses and to perform the pump-probe experiments. In addition, the time zero, i.e. the time coincidence $\Delta t = 0$ of pump and probe on the sample, can be measured with this setup. First the upper half of the setup is described. The three boxes labeled SHG of NOPA1, SHG of NOPA2 and SHG of Ti:Sa indicate the three independent UV pulses described above, each after running through the UV prism-compressors mentioned in Fig. 3.2. In the following they are referred to as λ_{N1}, λ_{N2} and λ_{Ti}. Note that all pulses are polarized parallel (↔) to the optical table, since this allows the prism compressors to run in Brewster angle configuration, which minimizes the reflection losses and in addition improves the degree of linear polarization. If the beams are properly aligned, i.e. are parallel to the optical table, no additional polarizer is needed to improve the polarization[8]. On the dichroic mirror DM, which is a high reflector for 387 nm on a quartz substrate, the beams λ_{N1} and λ_{Ti} are overlapped and they co-propagate subsequently. The beamsplitter BS is mounted in a flip-holder and is inserted for pulse characterization with autocorrelation FROG. The retroreflector (R) is mounted on a delay stage that can be moved with a computer-controlled stepping motor with 1 step corresponding to 1 μm, i.e. 0.66 fs (the beam travels additional 2 μm when the mirror is displaced by 1 μm). The beam λ_{N2} tightly passes mirror M1, and the beams are aligned in such a way that λ_{N2} propagates parallel to the two other beams at a distance of approx. 8 mm. If the waveplate WP is inserted into the setup, it rotates the polarization of λ_{N1} or λ_{Ti}. The flip-mirror FM determines, whether the pulses continue to the external FROG setup in the dotted frame or to the sample chamber where the FROG can be measured ”in situ” and where the pump-probe experiments are executed. The identical quartz lenses L$_1$ and L$_2$ have a focal length of 100 mm and a copy of the entrance window of the sample chamber provides the same dispersion in the external FROG setup.

---

[7] Then quarz prisms will have to be used to compress the NOPA light. Otherwise higher order chirp will limit the pulse duration.

[8] If the beam is reflected up and down, i.e. not symmetrical with respect to the polarization vector, metal mirrors induce elliptical polarization.

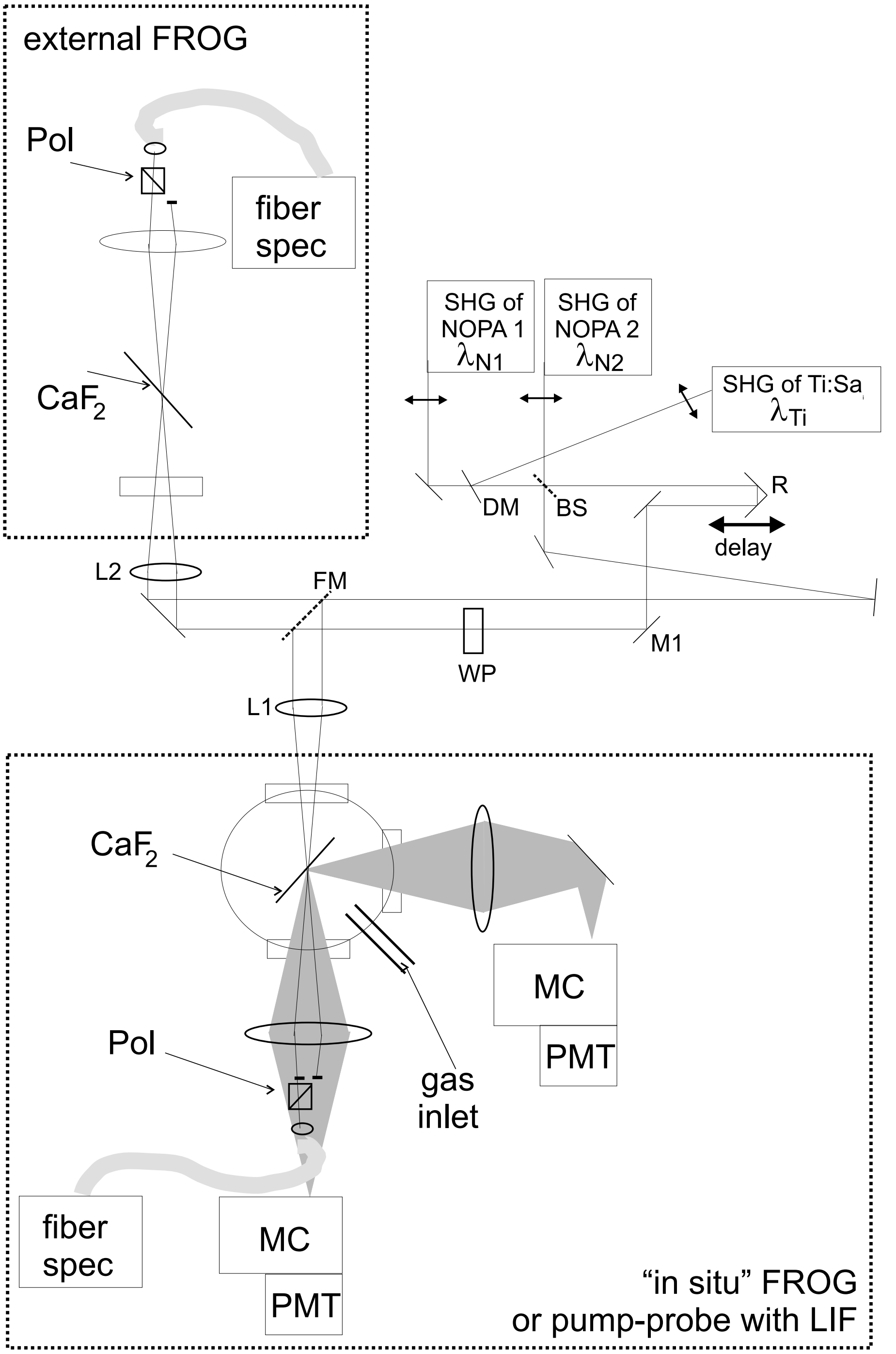

Figure 3.5: Combined pump-probe and FROG setup. Frame external FROG: A signal and a gate beam are focused on the CaF_2 substrate. The signal beam passes the polarization analyzer (Pol) and is spectrally resolved in the fiber optic spectrometer (fiber spec.). Without frame: Three horizontally polarized beams, λ_{N1}, λ_{N2} and λ_{Ti} are provided (see Fig. 3.2). The beam splitter BS and the mirror FM are mounted on flip-holders. BS is only introduced for FROG autocorrelations. FM is flipped out of the laser beams to run the external FROG. Frame "in situ" FROG: identical setup as for external FROG. Here the CaF_2 substrate is in the center of the sample chamber, and the fluorescence can be detected in the forward direction and at 90° with a monochromator (MC) and a photomultiplier tube (PMT). The polarizer (Pol) and the fiber spectrometer for the FROG have to be removed, when fluorescence in the forward direction is recorded. The gas inlet shows the thin tube for the doped rare gas used to grow the samples on the CaF_2 substrate.

3.7 Pulse characterization and determination of time zero

The pulses are characterized by the Polarization-Gating Frequency Resolved Optical Gating technique [188, 189] (PG-FROG). The setup implemented in this thesis allows the characterization of fs pulses from IR to UV (Fig. 3.5). It owes its flexibility to the use of a fiber optic spectrometer as a wavelength resolving detector. The visible pulses from the NOPAs, the Ti:Sa fundamental and its second harmonic are measured by autocorrelation, i.e. the pulses are split into two copies at the beamsplitter BS, one pulse serving as the ”signal” beam and one as the ”gate” [190]. The pulses are delayed with the same stage as in the pump-probe experiments and focused onto the 1 mm thick CaF_2 substrate (nonlinear FROG medium) in the sample chamber or alternatively on an equivalent CaF_2 outside[9]. The frequency doubled NOPA pulses are too weak to characterize them by autocorrelation. For them cross-correlation with a well characterized and strong 387 nm pulse is used by flipping the beamsplitter BS down. The duration of the 387 nm pulse limits the time resolution of the FROG cross correlation[10]. In all FROG measurements the ”signal” pulse is linearly polarized, passes a polarization analyzer POL after the FROG medium and is focused into the fiber optic spectrometer (cf. chapter 3.8). The $\lambda/2$ waveplate (WP) turns the linear polarization of the gate pulse to approx. 45° with respect to the signal pulse. If the pulses overlap in space and time inside the FROG medium, the nonlinear susceptibility $\chi^{(3)}$ induces polarization components in the signal beam that pass the polarization analyzer (POL). The intensity of these components, $I_{FROG} \sim I_{signal} I_{gate}^2$ is proportional to the intensity of the ”signal” pulse I_{signal} and to the square of the intensity of the gate I_{gate}. By scanning the delay between signal and gate, a two dimensional FROG trace is generated that shows the intensity of the pulse as a function of frequency and time. The chirp (frequency modulation) of the pulse can be read directly from the FROG trace [32, 144, 190]. In this thesis only transform limited pulses are used; however, this setup allows the characterization of shaped pulses in future experiments.

The time zero of the pump-probe experiment is given as the center of the cross correlation, i.e. the projection of the FROG trace onto the time axis. When the cross correlation FROG is measured in the sample chamber, a pump-probe spectrum can be taken in the same scan, when the LIF is collected at 90° (see below). This allows a very precise measurement of the time zero in the pump-probe spectra with an uncertainty of $\Delta t = \pm 20$ fs. In the experiments involving two frequency doubled NOPA pulses, the time zero must be inferred from the pump-probe spectrum itself. This is usually not difficult, since for equal pump and probe wavelength the spectrum is symmetric and for different wavelengths a minimum is clearly visible.

3.8 Fluorescence detection

The lower portion of Fig. 3.5 shows the sample chamber with the setup for fluorescence detection. The laser beams are focused onto the rare gas sample on top of the CaF_2 substrate, which can be rotated and is usually kept tilted at 45°. In this configuration, the fluorescence can be detected simultaneously in the forward direction and perpendicular to the incoming beams to reduce stray light.[11]

In one set of experiments, the fluorescence is excited with a $XeCl$ excimer laser at 308 nm (typical parameters: pulse duration $\Delta t = 10$ ns, repetition rate 10 Hz, pulse energy $W = 200$ μJ, focus

---

[9] To find the signal it is helpful to first find the spacial overlap with a pinhole. In some cases a 1 mm sapphire window is used, but the FROG signal often saturates even on the thin 300 μm sapphire window.

[10] If UV pulses as short as 30 fs are to be characterized, one will have to resort to other techniques like downconversion in very thin BBO crystals. The 775 nm pulse cannot be used because of the large group velocity difference to the UV pulses.

[11] It turns out in the experiments that all fluorescence bands of ClF/Ar are isotropic and unpolarized. This reflects the fact that the molecules undergo strongly hindered rotation within the fluorescence lifetime or that they are randomly tilted after scattering events. A different situation is met in the case of I_2/Kr and Cl_2/Ar, which are sterically fixed. Here the fluorescence is emitted with polarization parallel to the exciting polarization ($\Delta\Omega = 0$), implying emission with a dipole characteristic.

diameter $d = 2$ mm). The corresponding mirrors and the lens are not shown in Fig. 3.5, but beam propagates in the direction of the shown laser beams. This yields the valence band emission $A' \to X$. The ion-pair emission $D' \to A'$ is accessed by excitation with two photons, e.g. by using higher repetition rate or tighter focusing. The tunable fs laser pulses from two frequency doubled NOPAs (λ_{N1} and λ_{N2}) are used alternatively to produce the A' and D' emission or the excimer emission of Kr_2F. The second harmonic at 387 nm of the Ti:Sa regenerative amplifier system accesses only the valence states of ClF, also generating the A' emission.

For frequency domain spectroscopy, the fluorescence from the sample is collimated with a 100 mm fused silica lens onto a fiber optic spectrometer (fiber spec)[12]. It has a resolution of 0.7 nm for the large wavelength range from $\lambda = 350$ to 1050 nm and of 0.3 nm for the range extending from 200 to 530 nm. The integration time is 50 ms. For decay time measurements, the time window is delayed with respect to excitation. Contributions on shorter time scales are checked using either a CCD camera with a time resolution of 1 μs, or a photomultiplier tube (PMT) behind a monochromator (MC). Two monochromators (MC) with PMTs are used in pump-probe experiments to record different fluorescence bands simultaneously. One of the monochromators can be scanned with an electronic control unit. The UV fluorescence spectra were taken with this setup. For very strong emissions the fiber optic spectrometer can also be used.

For I_2 in Kr, the sample is perpendicular to the incoming beams and the fluorescence is detected in the forward direction using a combination of color glass filters and a monochromator before the photomultiplier. The fluorescence around 420 nm consists of two contributions [80] belonging to the $D' \to A'$ and the $\beta \to A$ or $\delta \to A$ transitions and both bands were detected together. The details can be found in the two respective diploma theses [116, 144].

3.9 Pump-probe setup

For time domain spectra, the fluorescence is collimated onto two monochromators with photomultiplier tubes, one in forward direction and one perpendicular to the laser beams, in order to monitor two bands at the same time. The photo current is amplified by the factor 100 and 1000, respectively, before it is integrated in a box car. The analog box car output is digitized with a DAC card and fed into the computer. One data point in a pump-probe spectrum is typically an average over 1000-8000 laser pulses, depending on the noise level and the time constraints due to bleaching of the sample. The setup is also used to measure time domain spectra with the full wavelength information of the fiber spectrometer when the intensity of the fluorescence is strong enough. Then the setup resembles the setup for FROG measurements but without the polarization analyzer POL (chapter 3.7). The fluorescence, instead of the ”signal” pulse, is focused into the fiber optic spectrometer.

Pump and probe pulse are delayed with respect to each other on a delay stage which can be moved by a computer controlled stepping motor (Fig. 3.5). For the ClF and Cl_2 spectra, the pump pulse was either the second harmonic of the Ti:Sa at 387 nm or a frequency doubled NOPA (240 - 330 nm). The second frequency doubled NOPA served as the probe pulse. For I_2 experiments two NOPA pulses were used after pulse compression in a quartz prism sequence.

In the pump-probe spectra that involve probing KrF, there is a large delay-independent background, since vibrationally relaxed KrF is also probed. Therefore a software ”lock-in” technique was implemented; a synchronized light beam chopper (model 221 from HMS Elektronik) blocks every second pump pulse. The computer then subtracts the signals with probe pulses only from the ones with pump and probe pulse. This method greatly improves the signal to noise ratio. Some comments on the ”lock-in” signal and its interpretation are given in the Appendix. This technique will be useful

---

[12] The SD2000 fiber optic spectrometer from Ocean Optics is also used for the FROG measurements. For the spectroscopy the polarization analyzer POL is removed.

in future experiments, whenever an unwanted, delay-independent signal from metastable states (e.g. A' state of ClF) exists.

Part I

Spectroscopy and Photodissociation of ClF in Ar and Kr

Before femtosecond pump-probe experiments on a new molecular system can be performed, the spectroscopy of the constituent molecules has to be clarified. This chapter provides the first spectroscopic account of excited electronic states of ClF *in the condensed phase. The absorption of* ClF *should be known for the choice of the pump pulses. The selection of the probe pulses in recombination dynamics requires the knowledge of the excited state absorption of* ClF*. The absorption of* F *radicals in* Kr *is needed to monitor the cage exit dynamics of the* F *fragment. The fluorescence bands after pump-probe excitation are recorded to provide an assignment of the* LIF *measured in the pump-probe spectra. The main motivation for the choice of* ClF *is to investigate the competing dissociation and recombination processes in the condensed phase. The expected cage exit of* F *atoms is essential, and therefore also the photodissociation yield is examined here.*

Chapter 4

Spectroscopic results

4.1 Valence states of ClF

The valence states are accessed by single photon excitation either with an excimer laser (308 nm), with the second harmonic of the Ti:Sa (387 nm) or the tunable NOPA (330 - 250 nm).

4.1.1 Absorption

Absorption spectra of the rare gas films were taken with the white light continuum of a Xe arc lamp, focused onto the ClF/Ar sample and afterwards collimated on the fiber optic spectrometer. The broad absorption of ClF was too weak to distinguish it from the scattered light that increases towards the UV. As the UV light dissociates ClF, a change in optical density of the sample is observed, which is probably due to absorption at 320 nm from the ClF_2 species generated [173], or due to bleaching of the Cl_2 absorption at 330 nm (Fig. 2.12). Since the absorption of ClF in rare gas matrix could not be determined experimentally, the gas phase absorption is compared to calculations in chapter 5.1.2.

4.1.2 Emission from valence states

Excitation of ClF in Ar with a concentration of 1:1000 at 290 nm into the repulsive $^1\Pi_1$ state ($h\nu_1$ in Fig. 4.1) leads to a fluorescence spectrum shown in Fig. 4.2a. The vibrational progression with 9 peaks ranging from 600 to 950 nm indicates recombination within the cage and emission from the bound $^3\Pi$ states. The corresponding spin-flip occurs within less than 500 fs (cf. chapter 7.6). Only one progression is observed in the spectrum, suggesting that vibrational relaxation is completed within the radiative lifetime. Indeed, the assignment in the discussion (Sect. 5.1) shows that the spectrum corresponds to transitions from $v' = 0$ in the A' state to a series of v'' levels in the electronic ground state ($h\nu_2$ in Fig. 4.1). Increasing the ClF concentration from dilutions of 1:20000 up to 1:1000 results in an approximately linear increase of the fluorescence intensity and leaves the spectrum unchanged. It is therefore attributed to ClF monomers. A significant contribution from a broad background, probably originating from dimers and higher clusters, is observed only at concentrations as high as 1:500.

Changing the excitation wavelength to 308 nm yields spectrum b) in Fig. 4.2 which contains the same progression as for 290 nm but with a superimposed sequence of sharper lines. The additional lines were previously identified as the $A'\,(v' = 0) \rightarrow X\,(v'')$ vibrational progression of Cl_2 [191]. In the gas phase, the absorption cross section of Cl_2 exceeds that of ClF by a factor of 60 at 308 nm (Fig. 2.12). The rather similar intensities of the Cl_2 and ClF emissions in Fig. 4.2b are consistent with the specified 1% Cl_2 impurity content in the sample gas. At 290 nm the absorption cross sections become equal and so the Cl_2 lines are not visible in Fig. 4.2a. The Cl_2 emission lines are sharper than the ClF lines and the triplet structure due to the isotope splitting of Cl_2 [191] is well resolved. Thus the width of the ClF lines is not limited by the experimental resolution. There is no systematic trend of the bandwidths with v''; the line shape is predominantly Gaussian and the width (fwhm) obtained from the Gaussian fit is included in Tab. 4.1.

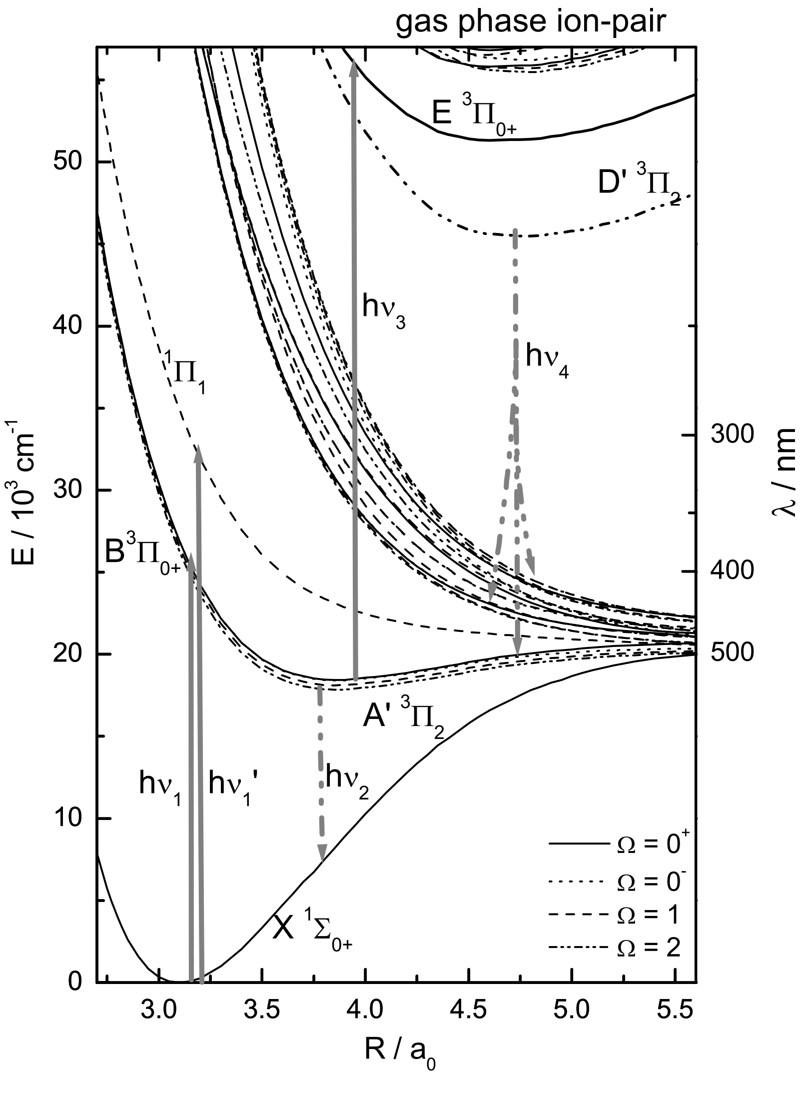

Figure 4.1: Potential diagram of ClF from ref. [121]. The line style indicates the Ω quantum number. All valence states are unshifted and the gas phase ion-pair energies are indicated on the top border of the plot. The E state is indicated with the shift in absorption (4500 cm^{-1}) and the emitting D' state with the shift in emission (10000 cm^{-1}). $h\nu_1$ and $h\nu_1'$ indicate the absorption to the B and $^1\Pi$ state that result in the emission band $A' \rightarrow X$ ($h\nu_2$). The excited state absorption $h\nu_3$ to the E state induces the emission band from D' with three contributions.

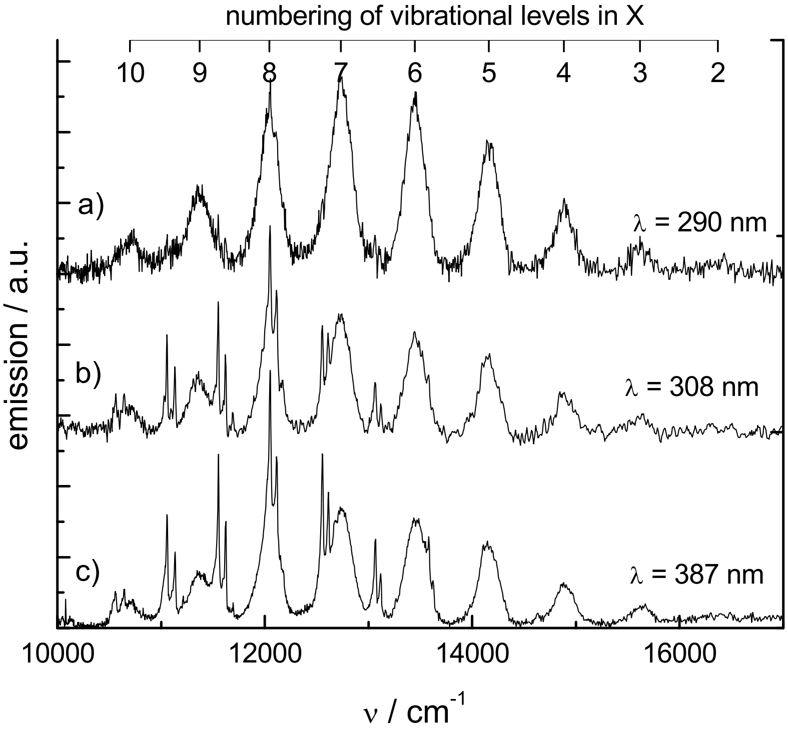

Figure 4.2: Vibrational progression of the $A' \rightarrow X$ fluorescence of ClF in Ar for different excitation wavelengths: $\lambda_{ex} = 290$ nm (a), 308 nm (b) and 387 nm (c). The numbers indicate the vibrational quantum number v'' in the X state (see chapter 5.1.1). The sharp peaks in the spectra for $\lambda_{ex} = 308$ nm and 387 nm are zero-phonon lines for the three isotopomers of Cl_2.

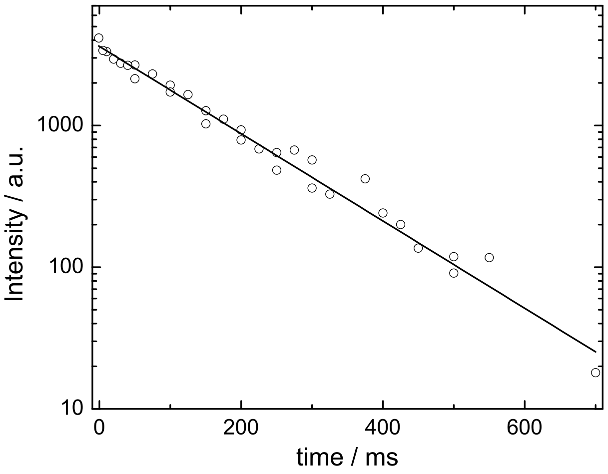

Figure 4.3: Intensity of the ClF fluorescence between 14,000 cm^{-1} and 15,100cm^{-1} as a function of time (see Fig. 4.2) after excitation at 308 nm. The solid line is an exponential fit to the data which yields the lifetime $\tau = 141 \pm 6$ ms.

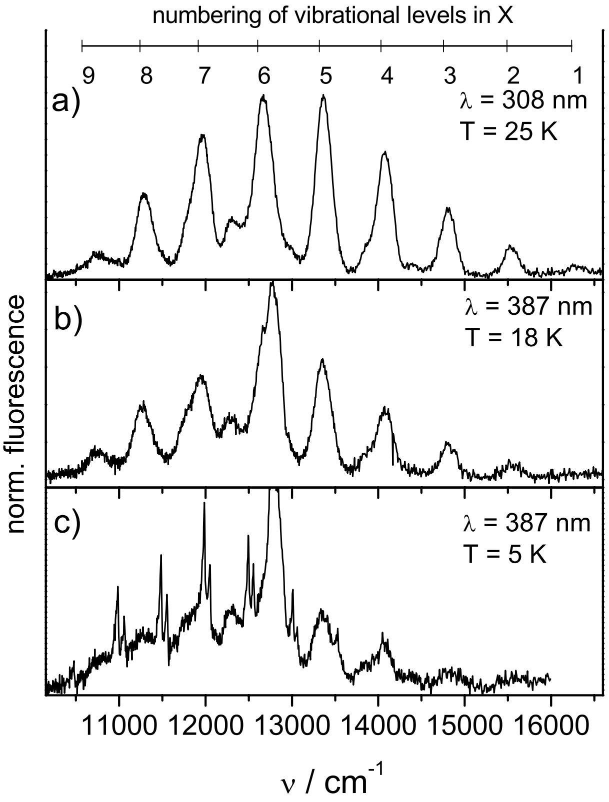

Figure 4.4: Vibrational progression of the $A' \rightarrow X$ fluorescence of ClF in Kr for different excitation wavelength. The sharp peaks in the spectrum for $\lambda_{ex} = 387$ nm at 5 K are zero-phonon lines for the three isotopomeres of $Cl_{2.}$ a) $\lambda_{ex} = 387$ nm, $T = 5$ K, b) $\lambda_{ex} = 387$ nm, $T = 18$ K and c) $\lambda_{ex} = 308$ nm, $T = 25$ K.

With 387 nm radiation from the frequency doubled Ti:Sa laser the $B(^3\Pi_0)$ state of ClF ($h\nu_1'$ in Fig. 4.1) is excited. The same ClF fluorescence band is observed as with 308 nm excitation (cf. Fig. 4.2c), but the relative intensities compared to the Cl_2 lines are changed. Nonradiative relaxation populates the same excited state in ClF in the end, independent of the electronic valence state that is excited (cf. chapter 7.6).

The fluorescence lifetime has been measured by delaying the 50 ms integration window of the fiber spectrometer with respect to the excimer laser pulse. Fig. 4.3 shows a semi-logarithmic plot of the intensity of the two ClF bands between 14000 and 15100 cm^{-1}. In this range no contributions from Cl_2 spoil the spectra. The exponential fit yields a lifetime of 141 ± 6 ms. No significant contributions on shorter time scales could be found with the CCD camera, which has 1 μs time resolution. An additional quickly decaying component is observed for high concentrations only and attributed to Cl_2 containing dimers, since the fluorescence spectrum has the vibrational pattern of Cl_2 without isotopic splitting.

A similar but slightly red-shifted progression is observed in Kr matrix (Fig. 4.4) and the maxima of the transition energies in both matrices are listed in Tab. 4.1.

4.2 Ionic states of ClF, Cl_2 and excimers

To access the ionic states or the excimers, two photon excitation is needed. This is accomplished by tight focusing of the excimer laser or by a double-pulse sequence of femtosecond pulses with appropriate time delay.

4.2.1 Emission from Cl^+F^-

The tightly focused excimer laser excitation at 308 nm results in an additional fluorescence band around 420 nm (Fig. 4.5). Its structure and short wavelength are incompatible with emission from

	Ar		Kr	
v''	$\nu\,(v'')$	$\Delta\nu$	$\nu\,(v'')$	$\Delta\nu$
0				
1			16298	351
2	16368	250	15543	358
3	15619	240	14808	282
4	14883	257	14081	271
5	14159	225	13367	256
6	13446	233	12666	298
7	12735	250	11975	290
8	12044	232	11304	266
9	11371	282	10696	380
10	10701	274		

Table 4.1: Observed positions ν and widths (fwhm) $\Delta\nu$ in the emission from valence states to the ground state. All values are in cm^{-1}.

valence states since the only bound valence state would emit in the red range. The band can be decomposed into four contributions with Gaussian shapes and equal widths as shown in Fig. 4.5 and discussed in Sect. 5.2. The emission from valence states shown in Fig. 4.2 slowly bleaches with irradiation due to permanent ClF dissociation (see chapter 5.4). The three bands around 420 nm, except the fourth peak at 20,000 cm^{-1}, show exactly the same bleaching behavior as the red fluorescence band. Since the red bands unambiguously belong to ClF, the same holds true for the three blue emission bands, which must result from excitation of higher-lying ionic states. The ionic manifold can only be excited by a two-photon absorption of ClF ($h\nu_1$ and $h\nu_3$ in Fig. 4.1) and it is the only one in reach for two photons at 308 nm. This assignment is confirmed by the quadratic dependence of the emission intensity on the incident laser pulse energy. The fluorescence lifetime is measured with a combination of filters and a photomultiplier to be 50 ns. A lower bound for the gas-phase lifetime of $\tau = 15$ ns attributed to the D' state is given by the laser emission [165] with 3.3 bar buffer-gas pressure and a similar lifetime has been estimated from OODR experiments [147]. However a longer lifetime may be observed, when the D'-state is populated via the longer-lived $^3\Sigma^-$-state, which is excited in the present experiment. This has been detailed for the case of Cl_2 [166,192]. In the condensed phase nonradiative electronic and vibrational relaxation within the ionic manifold is generally fast compared to the radiative decay. Therefore, the emission is attributed to dipole-allowed transitions from the lowest ionic state, $D'(^3\Pi_2)$ to the lower lying valence states ($h\nu_4$ in Fig. 4.1).

4.2.2 Emission from $Kr_2^+F^-$ exciplex and Cl^+Cl^-/Ar

The emissions reported in this chapter have already been observed and published. The aim of this spectroscopic study is to show how they can be excited with two femtosecond pulses, that will be used in pump-probe spectra.

$Kr_2^+F^-$ emission

The only excimer emission that could be exploited for pump-probe spectroscopy in this thesis originates from $Kr_2^+F^-$ and is displayed in Fig. 4.6a as the noisy line. This emission, centered around 460 nm, was previously assigned in ref. [54] and reproduced in Prof. Schwentner's group [82, 193]. Fig. 5.3 confirms that the $Kr_2^+F^-$ emission is observed in the present experiments. It is produced by two pulse excitation with $\lambda_{diss} = 387$ nm and $\lambda_{probe} = 270$ nm. The noisy line is the signal of a sample irradiated with λ_{diss} and λ_{probe} for 3 minutes to generate F by ClF dissociation and excite the KrF excimer. The spectrum of a virgin sample without F radicals is subtracted (not shown). The emission grows and saturates with irradiation time (cf. chapter 4.3.3). The shape of the emission is independent of the degree of ClF decomposition and only $\lambda_{probe} = 270$ nm is needed to excite the

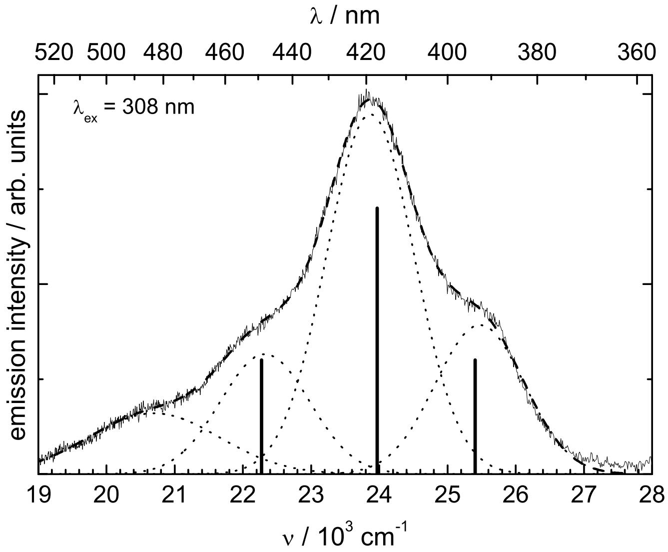

Figure 4.5: Fluorescence spectrum of the D' emission in Ar after two-photon excitation at $\lambda_{ex} = 308$ nm. The experimental spectrum (solid line) is fitted by four Gaussian functions whose superposition (dashed line) give excellent agreement with the measurement. The individual peaks are plotted as dotted lines. The vertical bars indicate the line positions calculated from the calculated gas-phase potentials [121] assuming a shifted D' state but unchanged valence states.

fluorescence after the sample was irradiated. This substantiates the assignment to a product of the dissociation. Since Cl containing products can be ruled out (see chapter 5.2.2), it must be assigned to a KrF species. The spectra can be fitted with two Gaussians centered around $\lambda_1 = 441$ nm and $\lambda_2 = 481.5$ nm. Fig. 4.6a displays the fit to the noisy line as thick dashed lines.

Fig. 4.6b collects spectra which represent the emissions that contribute to pump-probe signals that monitor the cage exit dynamics (chapter 7.7). They are the difference of the spectra taken for time delays between pump and probe of $\Delta t = 0$ ps (dashed), $\Delta t = 1.5$ ps (dotted) and $\Delta t = 100$ ps (solid), respectively, minus the spectrum recorded for $\Delta t = -1.5$ ps (not shown). These spectra correspond to three measured intensities in the pump-probe spectra in Fig. 6.13a. The differences are only 10% of the entire recorded signal (noisy line), and the spectra in Fig. 4.6b have been smoothed. The noisy line in panel a) thus represents the spectrum of all the KrF species that accumulated during the experiment and do not undergo recombination to ClF (see below). The 10% variation measures how this population of F atoms changes with the time delay of the pump-probe sequence on a timescale of ps. In the first 1.5 ps, the spectra differ mainly in the intensity of the Gaussian at 441 nm. After that, both bands are reduced by the same amount.

Fig. 4.7 shows a comparison of the $Kr_2^+F^-$ emissions for the accumulated populations created with $\lambda_{pump} = 387$ nm and $\lambda_{probe} = 270$ nm (thick lines) versus $\lambda_{probe} = 278$ nm (thin lines) in a temperature cycle. In both cases the sample is irradiated until the saturation of the emission growth is reached. While the signal intensity of the emission excited with $\lambda_{probe} = 270$ nm is halved upon raising the temperature from 4.5 K to 11 K and again from 11 K to 27 K. The intensity with $\lambda_{probe} = 278$ nm is reduced by a factor 5 from 4.5 K to 11 K and then halved for a further increase to 27 K. When the temperature is reduced to the initial 4.5 K, the intensity for $\lambda_{probe} = 278$ nm excitation recovers entirely. It does not recover instantaneously, but on the order of 20 seconds which is much faster than the initial growth saturating after ~200 seconds. For $\lambda_{probe} = 270$ nm the emission only grows back to 75% of the initial value.

This behavior indicates that $\lambda_{probe} = 278$ nm probes F atoms in such sites in the Kr lattice which do not recombine to ClF by annealing. Warming up the sample leaves the F atoms very near the site, where they have been trapped after dissociation. On the other hand, $\lambda_{probe} = 270$ nm probes F atoms that can disappear from their site by thermal migration.

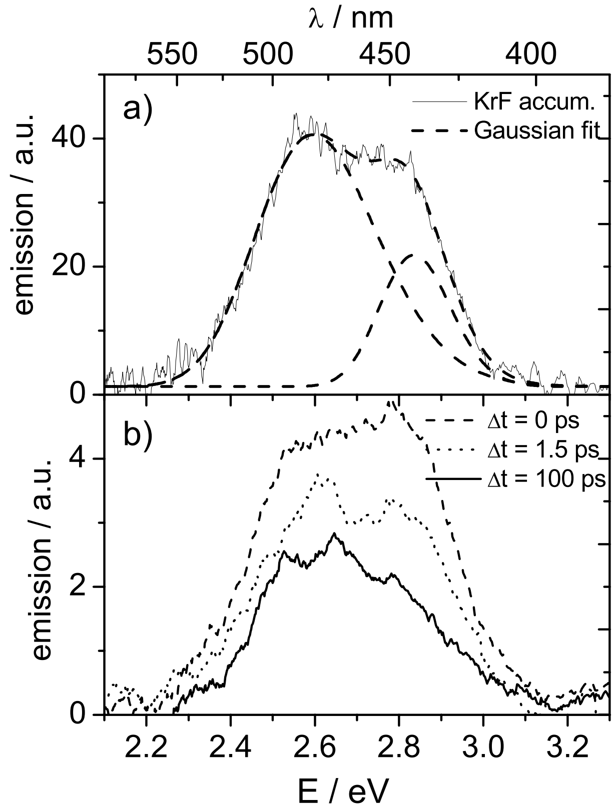

Figure 4.6: a) $Kr_2^+F^-$ emission from the accumulated population, excited with a double pulse sequence of 387 + 270 nm, is shown as a noisy line and fitted with the sum of two Gaussians centered at 441 and 481.5 nm. b) The spectra show the change of the fluorescence band for excitation with time delay $\Delta t = 0$ (dash) 1.5 (dotted) and 100 ps (solid) with respect to excitation with $\Delta t = -1.5$ ps.

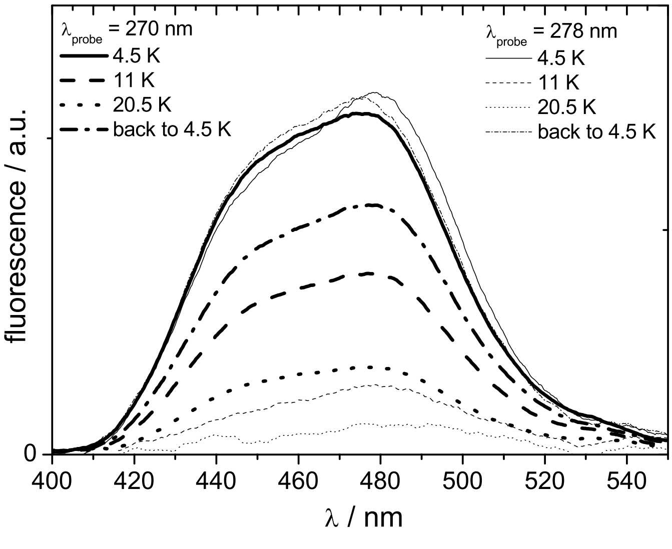

Figure 4.7: $Kr_2^+F^-$ emission from the accumulated population excited with a double pulse sequence of $\lambda_{pump} = 387$ nm and $\lambda_{probe} = 270$ nm (thick lines) vs. $\lambda_{probe} = 278$ nm (thin lines). Starting from 4.5 K (solid) the temperature is decreased to 11 K (dashed) and 20.5 K (dotted). Subsequently, the temperature is lowered again to 4.5 K. While the spectrum for $\lambda_{probe} = 278$ nm gains back the full intensity, 25% are lost for $\lambda_{probe} = 270$ nm. Note that the temperature dependence for $\lambda_{probe} = 278$ nm is much stronger.

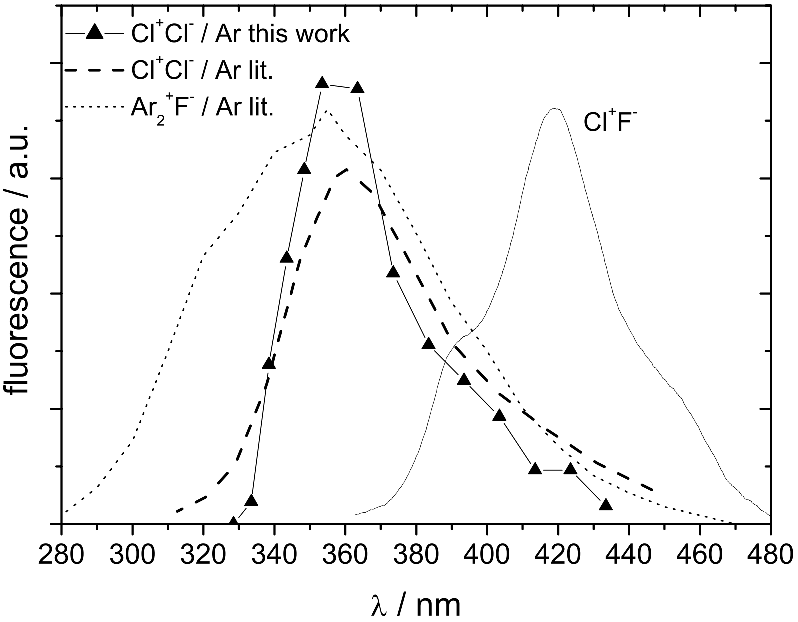

Figure 4.8: The solid triangles show the fluorescence spectrum measured after two pulse excitation with $\lambda_{pump} = 290$ nm and $\lambda_{probe} = 280$ nm. It is attributed to the D' emission of Cl^+Cl^-/Ar (thick dashed [134, 194]). It is observed in pure Cl_2/Ar matrices as well as in ClF/Ar samples due to the 1% Cl_2 content. For comparison the dotted line shows the $Ar_2^+F^-$ emission [81, 83]. The solid line reproduces the Cl^+F^- emission from Fig. 4.5.

$Ar_2^+F^-$ vs. Cl^+Cl^-/Ar emission

The analog emission in Ar matrices, i.e. fluorescence from $Ar_2^+F^-$, is reproduced in Fig. 4.8 from ref. [81] as the dotted line. It is centered around 355 nm and was excited by 193 nm pulses after dissociation of F_2 in Ar. An excitation spectrum of the $Ar_2^+F^-$ emission in ref. [83] shows a threshold of the absorption at 6 eV, corresponding to 208 nm.

In this thesis, a very similar emission is produced by excitation with a 290 nm + 280 nm pulse sequence and is plotted in Fig. 4.8 as solid triangles. The same emission can be produced by 387 nm + 280 nm excitation, but then the stray light from the 387 nm pulses spoils the spectra. In ref. [195] it was attributed to the $Ar_2^+F^-$ emission, and the surprisingly low excitation threshold of 286 nm was argued to be conceivable for hot F atoms. A large energy of 1.3 eV would be gained in the ionic state of Ar^+F^- upon compression of the $Ar - F$ bond from 0.35 to 0.24 nm [51] (cf. the corresponding KrF potential in Fig. 5.5). However, this argument neglects that even in the largest interstitial site the ArF bond is already compressed to 0.29 nm and the energy gain can only be half as high.

An intriguingly similar emission at 360 nm was reported for Cl^+Cl^-/Ar and it is reproduced in Fig. 4.8 as a dashed line [134, 194]. The agreement with the curve measured in this thesis (triangles) is good but not perfect. Therefore this new assignment was confirmed by preparing pure Cl_2/Ar samples. The same emission is observed, corroborating the assignment to Cl^+Cl^-/Ar. In the ClF doped samples this emission originates from the 1% content of Cl_2 in the ClF gas. It is observed with similar intensity as the Cl^+F^- emission, since the first step in the pump-probe sequence is the much stronger Cl_2 absorption shown in 2.12. Fig. 5.7 demonstrates that the absorption threshold of

286 nm observed in this thesis is consistent with the calculated potential surface of Cl_2, when the ionic state is red shifted as for ClF/Ar.

4.2.3 Excited state absorption of ClF and Cl_2

To locate the energy of the ionic states Cl^+F^- in absorption, two-photon excitation was performed with tunable radiation from the frequency doubled NOPAs (chapter 3.5.2). Since the minima of the ionic states are significantly displaced with respect to the bound valence states A', A and B, as shown in Fig. 2.11, vertical excitation of a vibrationally relaxed population in the bound valence states with 308 nm would not reach the minimum of any ionic state. However, frequency-doubled pulses from the Ti:Sa laser at $\lambda_{pump} = 387$ nm and 110 fs duration excite ClF into the B state somewhat above the dissociation limit ($h\nu_1'$ in Fig. 4.1). A time-correlated second UV pulse (probe) from a frequency-doubled NOPA excites the population from the triplet valence states into the ionic triplet states, provided as the probe-photon energy is larger than the minimum of the difference potential ΔV between the triplet valence and ionic states. The resonance condition [23, 45] for the probe photon is determined by the difference potential ΔV only and not by adding the energies of the pump and the probe photons (cf. chapter 2.3.2). The NOPA probe wavelength is tuned while recording the blue emission intensity at 420 nm. The onset of the blue emission is found at a probe wavelength of 322 nm, or $\Delta V = 31055$ cm^{-1}. The lowest transition allowed by the selection rules connects the $B(^3\Pi_0)$ state to the $E(^3\Pi_0)$ state. Comparing the measured ΔV with the gas phase value, and allowing for a vertical shift of the calculated potentials [121] in the matrix due to polarization, a red-shift of 4500 cm^{-1} is derived, i.e. $T_e\,(E)_{abs} = 51321$ cm^{-1}. Assuming an equal vertical shift also for the lowest ionic state, i.e. the D' state (Fig. 4.1), the energy minimum for the ionic manifold is 50750 cm^{-1} or 6.29 eV which is included in Tab. 5.1 as $T_e\,(D')_{abs}$.

The same strategy is pursued for Cl_2/Ar. The sample is pumped with the 387 nm pulse. The emission from Cl^+Cl^-/Ar at 360 nm is monitored while tuning the time-delayed UV pulse. The onset of the excitation spectrum is found at 286 nm. With the same arguments as above, the minimum of the E state of Cl_2 in Ar is red shifted by 3758 cm^{-1} to $T_e(E) = 38723$ cm^{-1}.

4.2.4 Absorption of KrF

The excimer absorption that leads to the above mentioned $Kr_2^+F^-$ emission is presented in Fig. 4.9b. It is recorded by measuring the transmission of a ClF/Kr sample at various temperatures with the white light spectrum of a focused Xe arc lamp. The white light dissociates ClF and detects the absorption of KrF simultaneously. The ratio of the transmission before and after bleaching the sample with the white light yields the plotted spectra. For each temperature a fresh spot on the sample was selected and irradiated for 5 min. The thick solid line shows another spectrum at 4 K, which was taken after 30 min irradiation.. The comparison in 4.9a to the excitation spectra of the $Kr_2^+F^-$ emission reported in refs. [82, 193] and [88] demonstrates the assignment to the KrF absorption, which yields the emission at 460 nm (Fig. 4.6).

While the excitation spectrum reported by Apkarian for $T = 12$ K (thick line in panel a), excited with frequency-doubled dye laser, resembles the cold spectrum which was irradiated for 25 min (thick line in panel b), the spectrum due to Bressler (thick dashed line panel a), excited with synchrotron radiation, resembles the one taken at 27 K with only 5 min irradiation. Another absorption spectrum of KrF/Kr at 22 K is available in the literature [132], and it shows a similarly broad absorption peaking at 265 nm.

In summary, the KrF absorption, that generates the $Kr_2^+F^-$ emission, depends on temperature and on irradiation time (photon flux). High temperatures and low photon flux preferentially produce a broad absorption in the range 250 - 270 nm. Cold temperatures together with long irradiation time or high photon flux create a narrow absorption centered at 275 nm.

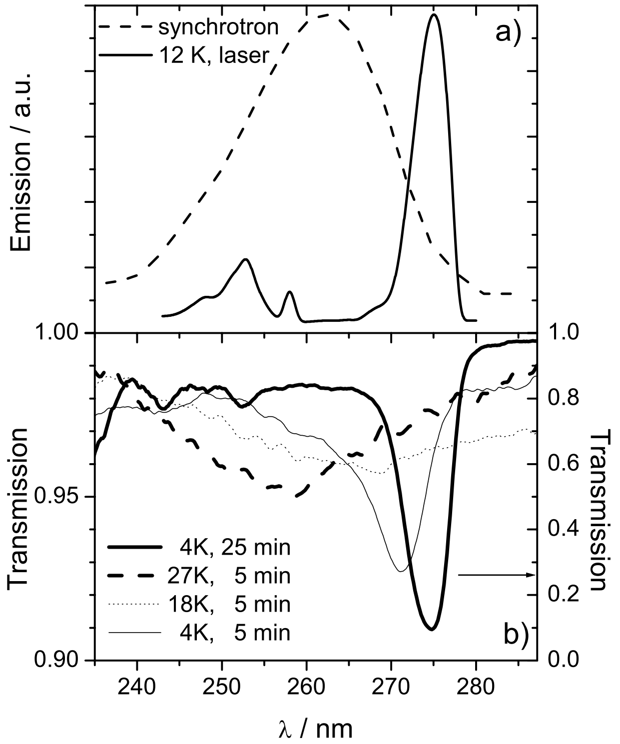

Figure 4.9: a) Excitation spectra of KrF measured by detection of the $Kr_2^+F^-$ emission. The solid line is reproduced from ref. [54] (laser excitation at 12 K) and the dashed line from ref. [82, 193] (synchrotron excitation, no temperature given). b) The transmission of ClF doped Kr samples measured in this thesis shows the absorption at 275 nm after 30 min irradiation at 4 K (thick solid line, right hand scale). The left hand scale is for 5 min irradiation. 27 K (thick dashed) yields an absorption similar to the dashed excitation in panel a). 18 K (thin dotted) and 4 K (thin solid) result in intermediate absorption bands.

4.3 Photobleaching of ClF in Ar and Kr

To prepare for pump-probe investigations on the cage exit dynamics of the F atom, experiments concerning the dissociation quantum efficiencies ϕ and their dependence on the kinetic energy of the F atom and the sample temperature are also carried out. These static measurements are partly performed with a $XeCl$ excimer laser and yield permanent dissociation efficiencies, i.e. the probability that an initially excited molecule will permanently dissociate and not recombine. The fluorescence signal, which is indicative of the remaining ClF concentration, changes on a timescale of seconds to minutes, depending on the photon flux. In contrast, fs-pump-probe experiments and molecular dynamics simulation only follow the processes over several ps. Thus processes like diffusion, occurring on longer timescales, are not included in fs experiments and simulations. In this chapter the permanent dissociation efficiency is measured, which is naturally smaller than dissociation efficiencies determined on the ps-timescale.

4.3.1 Bleaching of ClF/Ar

Excitation at 308 nm into the repulsive $^1\Pi_1$ state leads to permanent dissociation of ClF. This is monitored by the red fluorescence bands attributed to $A' \rightarrow X$ emission of ClF (see Sect. 5.1), which is proportional to the remaining ClF concentration. The decay of this red emission versus irradiation at 308 nm is shown in Fig. 4.10 for ClF in Ar (1:50,000) at a matrix temperature of 5 K. An exponential decay with 15% offset perfectly fits the measured trace. The reason for the offset cannot be unambiguously assigned. While there may be a weak background fluorescence from impurities like Cl_2, it is most likely due to reformation of ClF induced by secondary photodissociation of species that are formed by the migrating F atoms, such as F_2, ClF_2, ClF_3 etc.

A concentration study was performed to clarify the influence of secondary reactions. For the range of concentrations from 1:1,500 to 1:100,000, plotted in Fig. 4.11, the decay is only slightly slower for lower concentrations. For the discussion of the photodissociation quantum yield (chapter 5.4.1)

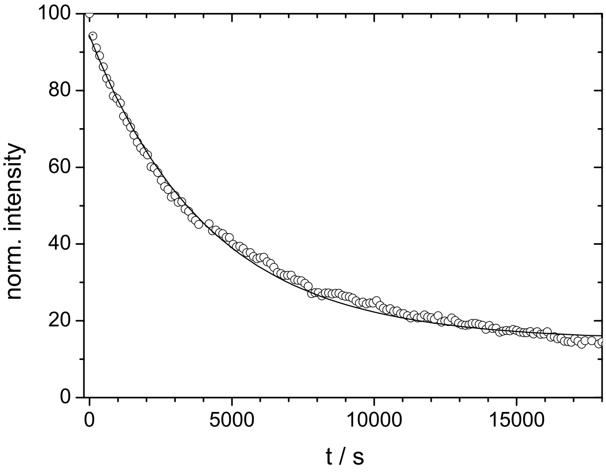

Figure 4.10: Intensity of the $A' \rightarrow X$ emission versus irradiation time at constant intensity for excitation of ClF in Ar (1:50,000) at 308 nm and 5 K. This intensity is a measure of the ClF concentration remaining in the sample. The solid line is an exponential fit to the experimental points with a background of 15%.

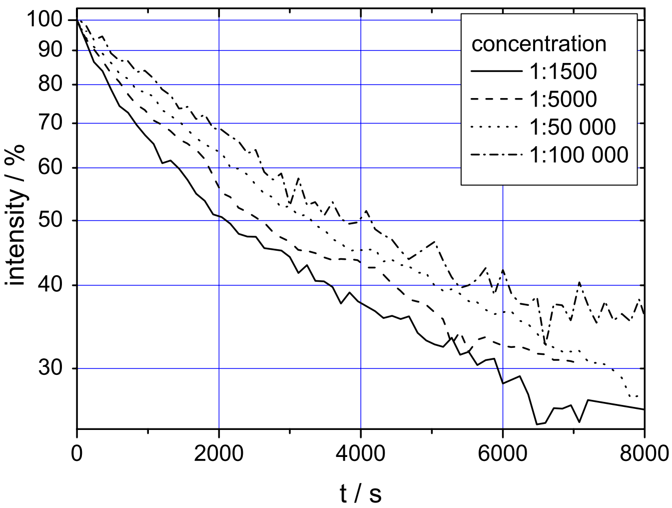

Figure 4.11: Intensity of the $A' \rightarrow X$ emission on a logarithmic scale versus irradiation time at constant intensity for excitation of ClF in Ar at 308 nm and 5 K. The concentration is varied from 1:1500 to 1:100000. Higher concentrations yield a faster initial decay and a stronger deviation from exponential decay.

the main (i.e. early) part of the decay curves is fitted with single exponentials. The resulting decay constants k allow the calculation of the dissociation cross section $\sigma\phi_d = k/I$, where I is the photon flux and $\sigma\phi_d$ is the product of the absorption cross section σ and the permanent dissociation efficiency ϕ_d. The lowest concentration (1:100,000) at 5 K yields the dissociation cross section $(\sigma\phi_d)_{308} = 1.5 \times 10^{-22}$ cm^2, which increases by a factor of 1.7 in going to a concentration of 1:1,500. Increasing the temperature of the matrix to 19 K (still below the thermal mobility of F in argon) enlarges the dissociation efficiency at 308 nm by 14%.

Excitation of ClF at 308 nm prepares the F atom with a substantial kinetic energy of $E_{kin} = 0.9$ eV. The gas phase dissociation energy of 20930 cm^{-1} corresponds to 478 nm. A wavelength of 387 nm from the frequency-doubled Ti:Sa laser yields $E_{kin} = 0.4$ eV. Once more a significant bleaching is observed. From a single-exponential fit the dissociation cross section $(\sigma\phi_d)_{387} = 2.1 \times 10^{-23}$ cm^2 is obtained at a concentration of 1:20,000.

The bleaching of ClF (Fig. 4.10) clearly demonstrates permanent dissociation of ClF and therefore also the mobility of the F fragment in Ar matrices. As mentioned above, the offset and the deviation of the decay curves in Fig. 4.11 from a single-exponential, indicate back reaction or other secondary reactions (see chapter 5.4). Such reactions will in general lead to a faster decrease for

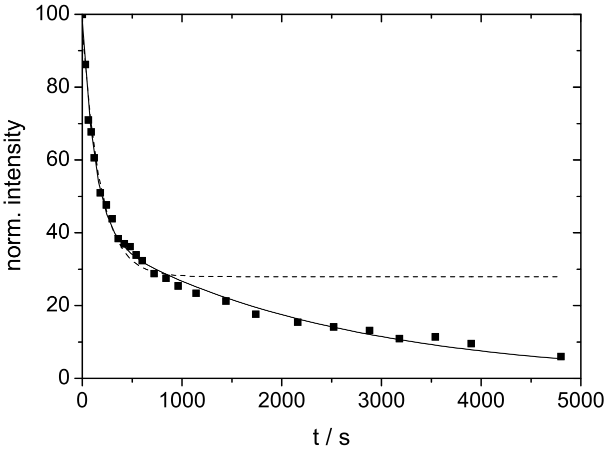

Figure 4.12: Intensity of the $A' \rightarrow X$ emission versus irradiation time at constant intensity for excitation of ClF in Kr at 308 nm and 28 K at a concentration of 1:5000. The dashed line is a single exponential fit with 28 % background. The solid line is a double exponential fit without background.

early times since rate constants add up, whereas at later times the slope might be smaller due to back reactions of newly formed species. This behavior is observed in the concentration study in Fig. 4.11, which shows a faster decay in the beginning for higher concentrations. Also optically thick samples will result in non-exponential decay and a constant offset for long times.

The concentration and the thickness d of the samples were lowered as much as possible to ensure optically thin and clear samples and to reduce secondary reactions while maintaining a reasonable signal-to-noise ratio. However, even at the lowest concentrations of 1:100,000 ($d = 50$ μm) used here, the decay deviates from a single exponential or shows an offset. The slopes at early and late times (or low and high doses) give limits to the true dissociation rate. At a concentration of 1:50,000 the early slope is 2.5×10^{-4} s^{-1} and the slope for long bleaching times is 0.75×10^{-4} s^{-1}. At an intensity $I = 1.4 \times 10^{18}$ photons·s^{-1}·cm^{-2} these slopes result in values of $(\sigma\phi_d)_{308} = 1.8 \times 10^{-22}$ cm^2 and 6.3×10^{-23} cm^2 for short and long bleaching times, respectively. The value from a single-exponential fit lies in between at 1.6×10^{-22} cm^2.

4.3.2 Bleaching of ClF in Kr

A similar bleaching study for ClF/Kr at 28 K and 308 nm for a concentration of 1 : 5000 is shown in Fig. 4.12. The deviation from exponential decay is even stronger. A single exponential fit to the early decay with 28 % background (dashed line) yields a close approximation. The resulting dissociation cross section is $(\sigma\phi_d)_{308} = 1.3 \times 10^{-21}$ cm^2. However, only a double exponential fit without offset (solid line) reproduces the entire curve. From the faster initial decay the cross section $(\sigma\phi_d)_{308} = 1.8 \times 10^{-21}$ cm^2 is obtained. This dissociation cross section is an order of magnitude larger than the one observed in Ar. Also, the dissociation cross sections for 387 nm excitation, $(\sigma\phi_d)_{387}$, are a factor 10 larger in Kr than in Ar (see Tab. 5.4). The next chapter will show that in Kr not only photoexcitation of the molecules formed after dissociation such as F_2, ClF_2 and ClF_3 leads to mobilization of F fragments, but also the excitation of the KrF exciplex.

In Kr the F atoms become thermally mobile at 15 K [81]. A large mobility is also seen in experiments with tightly focused lasers as they are used for the fs-pump-probe experiments. A pulse at 387 nm dissociates ClF in Kr in a spot of 100 μm diameter and a probe pulse at 270 nm is spatially overlapped to produce the $Kr_2^+F^-$ emission (Fig. 4.6) by exciting the F fragments in Kr. The emission rapidly grows as ClF is dissociated. After some time, however, it saturates and slowly decays. This already indicates, that F atoms are either trapped by impurities to form a molecule, which are not re-exited, or the F atoms leave the irradiated volume. In a warm sample (~ 25 K) the latter process is clearly proved to give a large contribution to the signal decay. When the sample is

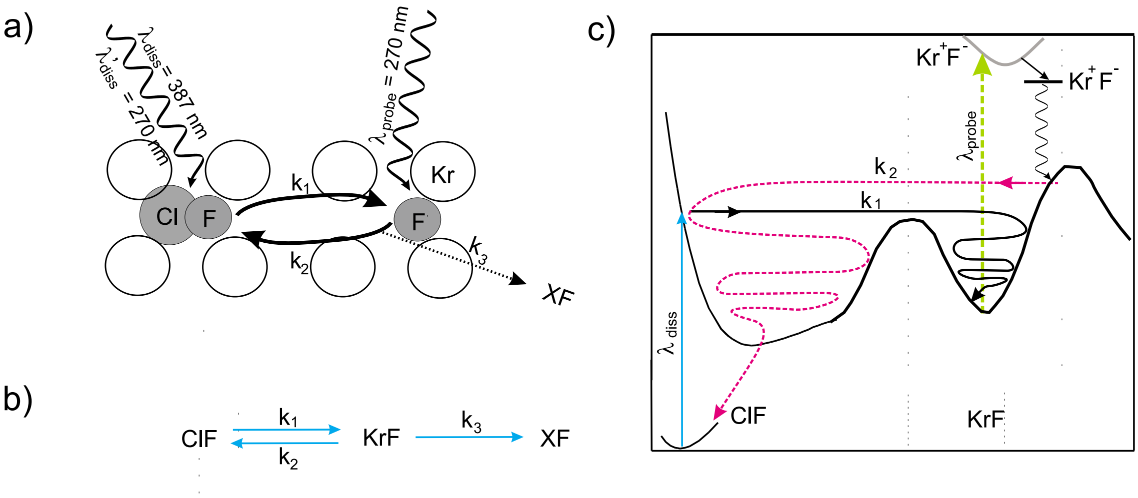

Figure 4.13: a) Scheme depicting the reversible shutteling of F atoms from Cl to Kr. $\lambda_{diss} = 387$ nm and $\lambda'_{diss} = 270$ nm dissociate ClF, leading to KrF species with a rate constant k_1. $\lambda_{probe} = 270$ nm drives the recombination to ClF with the rate constant k_2 by inducing the radiative dissociation of $Kr_2^+F^-$ (see text). The rate k_3 collects all processes that remove F from this reversible process. b) Rate model. c) Reversible photo process from ClF to KrF in a potential diagram (see text).

moved after long irradiation of a 100 μm large spot, the $Kr_2^+F^-$ fluorescence rises considerably just next to the focus, while it decreases to zero on a fresh spot. This clearly indicates that the F atoms are transported in the solid over macroscopic distances on the order of tens of micrometers by repeated re-excitation.

4.3.3 Control of dissociation vs. recombination of ClF in Kr

The configuration with two pulses, a dissociation pulse at $\lambda_{diss} = 387$ nm and a probe pulse at $\lambda_{probe} = 270$ nm is used for further investigations. The latter pulse contributes to the dissociation of ClF via the $^1\Pi_1$ state and is referred to as $\lambda'_{diss} = 270$ nm. More importantly, the probe pulse at $\lambda_{probe} = 270$ nm produces the emission from the $Kr_2^+F^-$ exciplex, which terminates on a repulsive KrF potential and provides the F fragments with substantial kinetic energy (radiative dissociation of $Kr_2^+F^-$), driving the recombination of F fragments with the immobile Cl radicals. Fig. 4.13a summarizes these processes schematically. Both $\lambda_{diss} = 387$ nm and $\lambda'_{diss} = 270$ nm dissociate ClF and lead to a KrF configuration with a rate constant k_1. $\lambda_{probe} = 270$ nm produces the $Kr_2^+F^-$ emission, which is observed in the experiments and leads to reformation of ClF with the rate constant k_2. A constant k_3 collects all processes that remove F atoms from this reversible process, e.g. by promoting F out of the laser focus. Fig. 4.13b restates this rate model. A schematic representation of the reversible process is shown in the potential diagram in Fig. 4.13c. Starting from the ground state of ClF, λ_{diss} dissociates the molecule and the F fragment must overcome the cage barrier. When it is cooled down in the Kr cage, λ_{probe} excites the ion-pair state Kr^+F^-. After rearrangement in the ionic manifold the $Kr_2^+F^-$ exciplex fluoresces (wavy arrow). The emission terminates on a repulsive KrF surface and the F fragments can overcome the barrier in the other direction to finally recombine to ClF.

Fig. 4.14a shows the $Kr_2^+F^-$ emission as a function of irradiation time in seconds for a Kr matrix doped with ClF at a concentration of 1:1000. In the first 400 s only the 270 nm laser is present, and thus responsible both for the dissociation λ'_{diss} and the probing λ_{probe}, which also drives recombination. The concentration of F fragments, i.e. KrF species, grows until it reaches a saturation value, which corresponds to an equilibrium of ClF dissociation versus recombination ($\lambda'_{diss} + \lambda_{probe}$). This

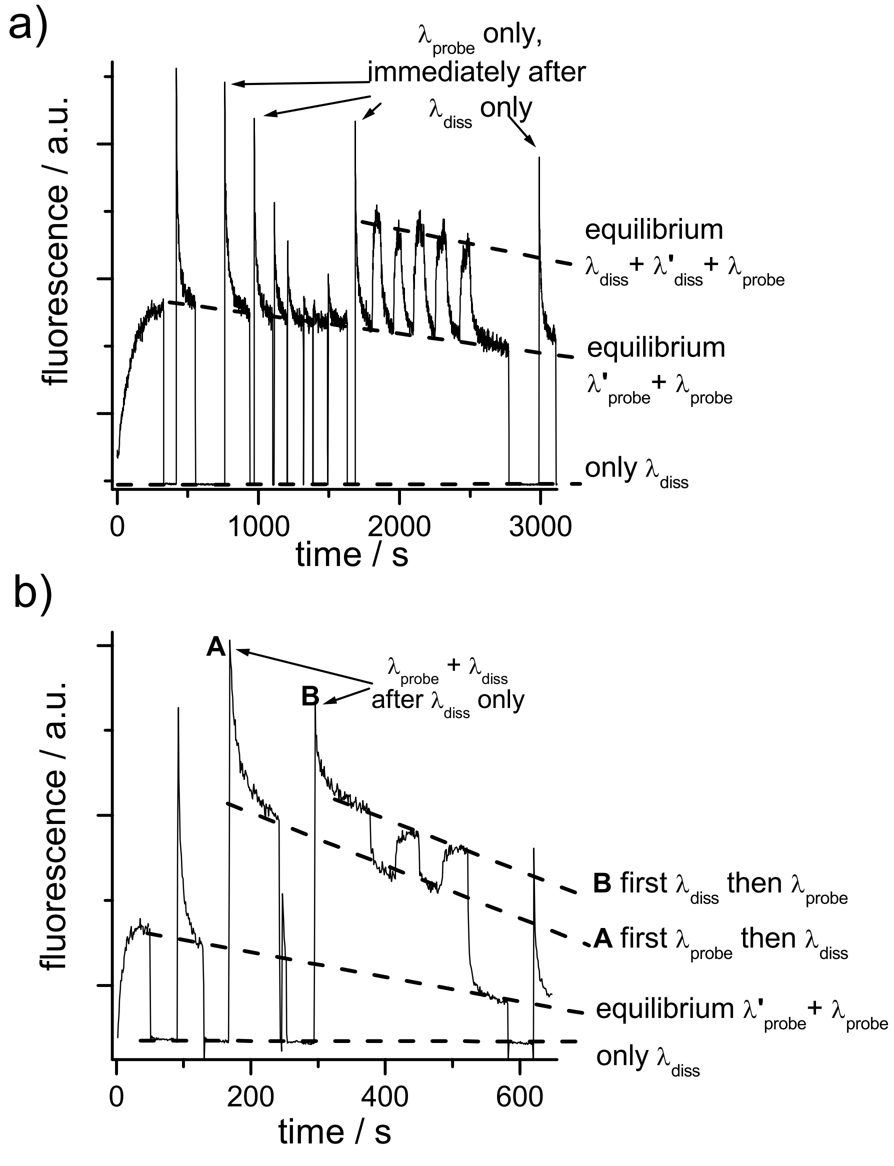

Figure 4.14: Concentration of F fragments measured via the $Kr_2^+F^-$ emission as a function of irradiation time with $\lambda_{diss} = 387$ nm and/or $\lambda_{probe} = 270$ nm (see text). The temperature is 4 K. Panel a) demonstrates how the photochemical equilibrium is shifted towards ClF by applying λ_{probe} and towards KrF with λ_{diss}. Panel b) demonstrates the effect of the time delay between λ_{diss} and λ_{probe} (see text).

equilibrium, indicated by the dashed line ($\lambda'_{diss} + \lambda_{probe}$), slowly decays in the course of the experiment according to the rate k_3. XF indicates the F fragments that leave the focus or that react to ClF_2 etc. The initial exponential growth curve can be fitted to determine the quantum efficiency (see chapter 5.4.1).

The dissociation laser $\lambda_{diss} = 387$ nm does not produce the excimer. When the signal in Fig. 4.14a drops to zero only the dissociation laser λ_{diss} is present and the second laser λ_{probe} is blocked. From 400 s to 1700 s, the sample is irradiated alternatingly with the dissociation laser only ($\lambda_{diss} \rightarrow$ no signal) and then with the probe laser only ($\lambda_{probe} \rightarrow$ spike). Obviously, after 400 s not all ClF molecules were dissociated in the equilibrium of $\lambda'_{diss} = \lambda_{probe} = 270$ nm, although the exponential growth converges. The dissociation pulse $\lambda_{diss} = 387$ nm can double the number of F fragments, depending on the time period used for dissociation.

From 1700 to 2500 s, λ_{probe} probes the sample continuously and λ_{diss} is switched on and of in addition. This switches the F fragment concentration from the equilibrium value for ($\lambda'_{diss} + \lambda_{probe}$) to a new equilibrium for both lasers ($\lambda_{diss} + \lambda'_{diss} + \lambda_{probe}$). The fluorescence is proportional to the number of F radicals. Approximately 30% of the F atoms are shuttled from Cl to Kr and back by switching λ_{diss} on and off, as can be estimated from the difference of the equilibria in Fig. 4.14a.

Fig. 4.14b shows a similar experiment, with higher laser intensity to demonstrate a more sophisticated effect. Again, in the first 50 s, the equilibrium concentration of F atoms for irradiation with $\lambda'_{diss} = \lambda_{probe} = 270$ nm is produced. The first spike at 90 s is generated in the same way as the first in peak in panel a) between 400 s and 1700 s. For the next two spikes at 170 s and 300 s, λ_{probe} is incident together with the dissociation laser λ_{diss} and the only difference is the time sequence between λ_{diss} and λ_{probe}. In sequence A λ_{probe} comes 1 ps before λ_{diss} and in sequence B λ_{probe} comes 100 fs after λ_{diss}[1]. From 400 s to 580 s, the time delay is switched four times and the fluorescence changes accordingly between the equilibria A and B, indicated on the right side of Fig. 4.14b. This peculiar behavior demonstrates a change of the equilibrium concentration of F radicals with time delay between λ_{diss} and λ_{probe}, which is discussed in chapter 5.4.2.

---

[1] Note that the repetition rate of both lasers is 1 kHz, i.e. the next sequence is 1 ms apart.

Chapter 5

Discussion of spectroscopy

5.1 Ground and valence states of ClF

5.1.1 Emission from valence states of ClF (measure of concentration)

The ClF spectra in Fig. 4.2 correspond to vibrational progressions ν'' in the electronic ground state according to the spectroscopic evidence. The energy differences ΔG of successive maxima from Tab. 4.1 are shown in Fig. 5.1 versus ν'' in a Birge-Sponer plot and compared with the IR fundamental frequency $\nu_{0\rightarrow1}$ from Ref. [162]. The ΔG values follow the linear regression within the experimental uncertainty given by line broadening. The slopes yield values for the anharmonicity $\omega_e x_e$ in Ar and Kr of 5.77 ± 0.3 cm^{-1} and 6.37 ± 0.15 cm^{-1}, respectively. Thus the anharmonicity increases by 9% (Ar) and by 20% (Kr) compared with the gas phase. The assignment of ν'' to the maxima is chosen in order to obtain extrapolated values for $\nu_{0\rightarrow1}$ in agreement with the one measured in IR absorption [162]. This results in an assignment of the progression for Ar to $\nu'' = 2 - 10$ whereas for Kr the assignment is shifted by one to $\nu'' = 1 - 9$. From the linear regression the harmonic frequencies ω_e for the electronic ground state are derived and compared with the gas phase values in Tab. 5.1.

The fundamental frequencies $\nu_{0\rightarrow1}$ show the typical red shift in the matrix [128, 196–199]. For ClF in Ar the shift of $\nu_{0\rightarrow1}$ is small and less than 0.5% [162] which is consistent with the present data within the experimental error. The value for the matrix shift derived for Kr in this work is larger (1.2%) and agrees once more with Ref. [162]. The main source for the shift is the higher anharmonicity in the matrix. This increase of the anharmonicity of matrix-isolated ClF compared

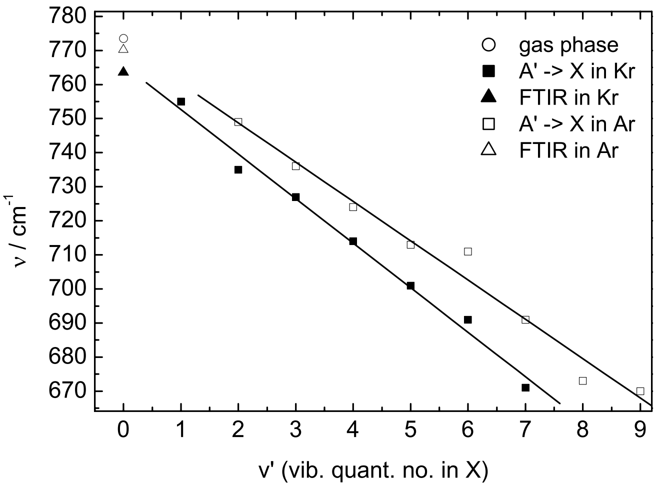

Figure 5.1: Birge-Sponer plot for the $A' \rightarrow X$ transition of ClF in Ar (solid squares) and Kr (open squares). The solid lines are linear regressions to the experimental data. Solid and open triangles indicate the frequencies [162] of the vibrational transition $0 \rightarrow 1$ of ^{35}ClF for Ar and Kr, respectively. The open circle is the corresponding gas-phase value.

Parameter	gas phase	Ar matrix		Kr matrix		Units
	Ref. [157]	Ref. [162]	this work	Ref. [162]	this work	
$\omega_e(X)$	783.2 ± 0.3		783.5 ± 2.5		777.2 ± 1.5	cm^{-1}
$\omega_e x_e(X)$	5.3 ± 0.1^b		5.77 ± 0.3		6.37 ± 0.15	cm^{-1}
$\nu_{0\to1}(^{35}ClF)$	773.8	770.2	771.8 ± 2.5	763.6	764.5 ± 2	cm^{-1}
$\nu_{0\to1}(^{37}ClF)$	766.6	762.7		756.5		cm^{-1}
$T_e(A')$	18257^a		18111.8 ± 7		17269.1 ± 3.5	cm^{-1}
$T_e(D')_{abs}$	55253		50750 ± 400			cm^{-1}
$T_e(D')_{em}$	55253		45270 ± 20			cm^{-1}

a) Ref. [145], b) A value of $\omega_e x_e = 4.8$ cm^{-1} is obtained if higher order terms are included.

Table 5.1: Potential parameters for ClF in the gas phase and in rare gas matrices. The gas phase values are for ^{35}ClF unless stated otherwise. Line broadening effects cover the isotope splitting in electronic transitions.

to the gas phase indicates that the cage atoms do not lead to a stiffening of the potential around the equilibrium distance but instead the polarizability weakens the $Cl-F$ binding, especially in Kr. A stiffening as observed in the case of I_2 (cf. chapter 7.1.2 and ref. [200]) will occur for larger $Cl-F$ elongations (not accessed by the $A' \rightarrow X$ emission), where the barrier induced by the repulsive forces from the cage atoms comes into play.

The linewidths of the individual vibrational transitions are given in Table 4.1. The average linewidths of the bands are $H = 250$ cm^{-1} for argon and $H = 306$ cm^{-1} for krypton and there is no trend with increasing vibrational number. A similar linewidth of 260 cm^{-1} has been found for IF isolated in Ar [198].

The electronic energy T_e of the upper, emitting electronic state is obtained from the measured peak positions and the linear regression in Fig. 5.1. The emitting state is assigned to $A'\,(^3\Pi_2)$, because of the extremely long radiative lifetime of $\tau = 141 \pm 6$ ms. It fits well into the trend of other halogens and interhalogens [198], which reflects the fact that selection rules become stricter for lighter molecules. All $^3\Pi \rightarrow X\ (^1\Sigma_0)$ transitions are spin forbidden and the $A'\,(^3\Pi_2) \rightarrow X$ transition is additionally forbidden by the angular momentum selection rule $\Delta\Omega = 0, \pm 1$. The lifetimes for transitions from $A\,(^3\Pi_1)$ and $B\,(^3\Pi_0)$ are known to be in the μs range for other interhalogens [198]. Having assigned the emitting state to A', its electronic energy $T_e(A')$ is calculated (cf. Tab. 5.1) using the known harmonic frequency of the A' state in the gas phase $\omega_e(A') = 363.5$ cm^{-1} [145]. The rather small red shift of the A' state from the gas phase to the Ar solid is typical for valence states (1-2%) [74, 79]. The increase of the red shift from 150 cm^{-1} in Ar to 990 cm^{-1} in Kr reflects the larger inductive and dispersive forces [129] discussed in chapter 2.2. The shift of 5.4% in Kr is large for a valence state. Shifts of the same order were observed for some fluorine-containing diatomics [74] e.g. KrF [193] and XeF [201] isolated in Ar.

5.1.2 Absorption (pump pulse)

The absorption of ClF in matrices could not be measured and the reported gas phase values (Fig. 2.12) have to be used. Since the shift of the $A' \rightarrow X$ emission is only 1% in Ar, a negligible shift is expected for the valence states in absorption, and for all results in this thesis unshifted valence states are taken. A value for the absorption cross section at 308 nm is interpolated from the data in Ref. [150]. From ref. [149] a value of 3.9×10^{-21} cm^2 is obtained, which is slightly higher than the value of 3.0×10^{-21} cm^{-2}. The intermediate value of $\sigma_{308} = 3.5 \times 10^{-21}$ cm^2, which should be accurate to within $\pm 25\%$, is listed in Tab. 5.4.

To check the consistency of the absorption data from the literature with the calculated potential surfaces, the ground state wave function is projected in Fig. 5.2 onto the repulsive limbs of the two

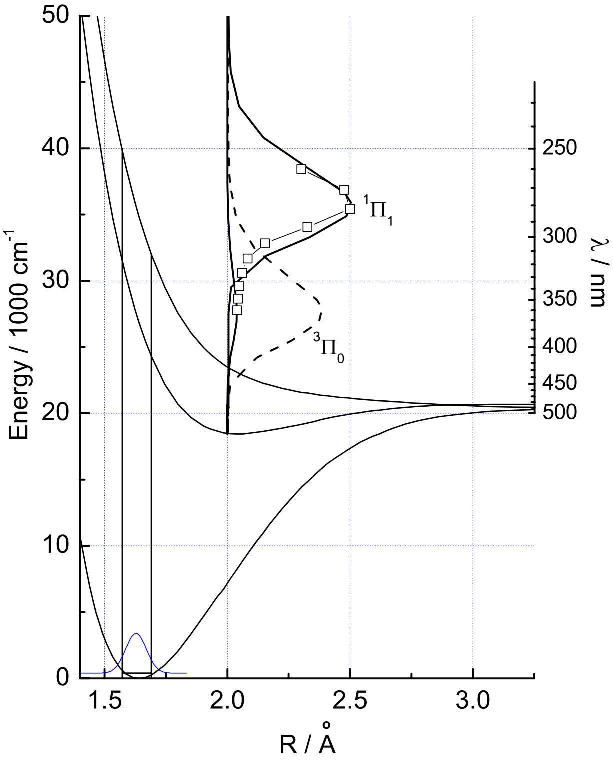

Figure 5.2: Absorption bands calculated from the projection of the ground state Gaussian onto the repulsive limbs of the $^1\Pi$ (solid) and $^3\Pi_0$ state (dashed). The open squares reproduce the absorption of ClF measured in ref. [150].

valence states [121] allowed by the $\Delta\Omega$ selection rule. Obviously, the $^1\Pi$ state gives rise to the strong absorption observed in ref. [150] that is reproduced in Fig. 5.2 as open squares. The transition to $B(^3\Pi_0)$ is spin-forbidden and very weak. The shoulder in the poor experimental absorption spectra may be due to the weak absorption to the B state. The long known and well resolved discrete B state spectra in the bound region [156] and the OODR experiments [133] demonstrate that the absorption in the Franck-Condon region is strong enough to record pump-probe spectra. No published values for the absorption cross section at 387 nm are available. An approximate relative intensity of the B state vs. $^1\Pi_1$ absorption is derived from the intensity ratios of the $A' \rightarrow X$ fluorescence bands of ClF and Cl_2 within the same spectra, upon irradiation at 308 nm (Fig. 4.2b) and 387 nm (Fig. 4.2a). The known absorption for Cl_2 [153] is thus used for calibration. The ratio of the absorption cross sections of ClF of $\sigma_{308}/\sigma_{387} \approx 8$ is obtained with a rather large uncertainty and the calculated B state absorption in Fig. 5.2 is scaled accordingly (cf. Tab. 5.4: $\sigma_{387} \approx 4.5 \times 10^{-22}$ cm^2).

5.2 Ionic states of ClF, Cl_2 and excimers

5.2.1 Emission from ionic states of Cl^+F^- (LIF)

The three dominant emission bands in Fig. 4.5 were already assigned with spectroscopic arguments to allowed transitions from the vibrationally relaxed ionic state $D'\,(^3\Pi_2)$ to valence states. From the large manifold of 16 valence states only $A'(1^3\Pi_2)$, the $2(^3\Pi_2)$ and the $2\,(^3\Delta_2)$ give rise transitions allowed by the selection rules $\Delta S = 0$ and $\Delta\Omega = 0$. Therefore the spectrum in Fig. 4.5 between 21,000 cm^{-1} and 27,000 cm^{-1} is approximated by three Gaussians. A fourth Gaussian takes into account the wing around 20,000 cm^{-1} which does not bleach with irradiation dose as the others do and is thus of different and yet unidentified origin. It will not be considered in this thesis.

The fit of the experimental spectrum in Fig. 4.5 was done without using spectroscopic information. The energy and equilibrium distance of the emitting ionic state is derived from the fitted peaks. The

Peak	Position	Width	Assignment
1	25474 ± 14	1536 ± 20	$D' \rightarrow A'\ {}^3\Pi_2$
2	23869 ± 6	1521 ± 21	$D' \rightarrow 2\ ({}^3\Pi_2)$
3	22322 ± 19	1539 ± 55	$D' \rightarrow 2\ ({}^3\Delta_2)$
4	20699 ± 57	2256 ± 74	unknown

Table 5.2: Positions and widths (fwhm) for the D' emission of ClF in Ar onto valence states obtained by fitting the measured fluorescence band by four Gaussian peaks. The assignment is discussed in the text. All values are in units of cm^{-1}.

fit results in three bands with equal widths of 1530 cm^{-1} and an approximately equal spacing of 1575 cm^{-1} (Tab. 5.2). In calculated potential energy curves for gas phase ClF [121] the bond distance $R \approx 5.1$ a$_0$ produces the calculated spacings between the three valence states $A'(1^3\Pi_2)$, $2(^3\Pi_2)$, and $2\,(^3\Delta_2)$. Since the population in the ionic state has relaxed into the vibrational ground state of the lowest ionic state, D', this value of R gives the equilibrium position R_{eq} of the D' state in the matrix. It is significantly expanded compared to the gas phase value $R_{eq} = 4.85$ a$_0$, indicating the strong solvation of the ionic states. According to the potentials [121], a smaller value for R would result in a larger spacing of the three bands than the one observed. The spacing of the valence states is not expected to be changed significantly in the matrix.

Using the measured transition energies and the gas phase valence band energies, the electronic energy of the emitting state is $T_e\,(D')_{em} = 45270 \pm 20$ cm^{-1}. This yields a red shift of about 10,000 cm^{-1} compared to the gas phase. Such a strong shift both in energy and equilibrium position is large but not exceptional, because it reflects the energy gain in solvation of the ionic dipole [202] and the Franck-Condon factors in the configuration coordinate after rearrangement of the Ar-lattice (Fig. 2.7). A comparable shift of 11200 cm^{-1} has been observed for Cl_2/Ar [134]. Larger molecules undergo weaker shifts (2100 cm^{-1} for IBr/Ar [196] and 2900 cm^{-1} for I_2/Ar [79]), which may be explained by the semi-empirical formula eq. 2.6 for the solvation-shift.

The onset of two-photon excitation (see chapter 4.2.3) yields a value of $T_e\,(D')_{abs} = 50750$ cm^{-1} in absorption which represents a red shift of 4500 cm^{-1} compared to the gas phase [121] and is due to electronic polarization (chapter 2.2.3). The value is comparable to shifts in absorption from valence to ionic states in other molecules [130]. The further red shift of 5500 cm^{-1} from $T_e\,(D')_{abs}$ to the value in emission $T_e\,(D')_{em}$ corresponds to a Stokes shift E_s caused by the lattice rearrangement. The Stokes shift E_s and the line width H are used in a configuration coordinate model for the rearrangement to give an approximation for the Huang-Rhys phonon coupling constant S (chapter 2.2.4). From the experimental values for E_s, a large coupling constant $S = 40$ is derived, assuming a typical phonon energy $\hbar\omega_p = 69$ cm^{-1} in argon crystals. In this approximation, the electron-phonon coupling accounts for a linewidth of $H = 1030$ cm^{-1}, which is smaller than the observed one. Note however, that the measured linewidth is expected to be broader, since the projection of the wave function from the vibrational ground state of D' onto the valence states yields a bandwidth of 500 cm^{-1}. A Gaussian superposition accounts for a width of 1145 cm^{-1} which is still too small. Higher than linear order of coupling can explain the difference, but since the linewidth in absorption is not available, further improvement is not pursued. The value of $S = 40$ indicates a strong coupling corresponding to a significant lattice rearrangement and an average of generated phonons on the order of 40 in an absorption or emission event. The phonon coupling dominates the line broadening, leading to equal widths in all three transitions.

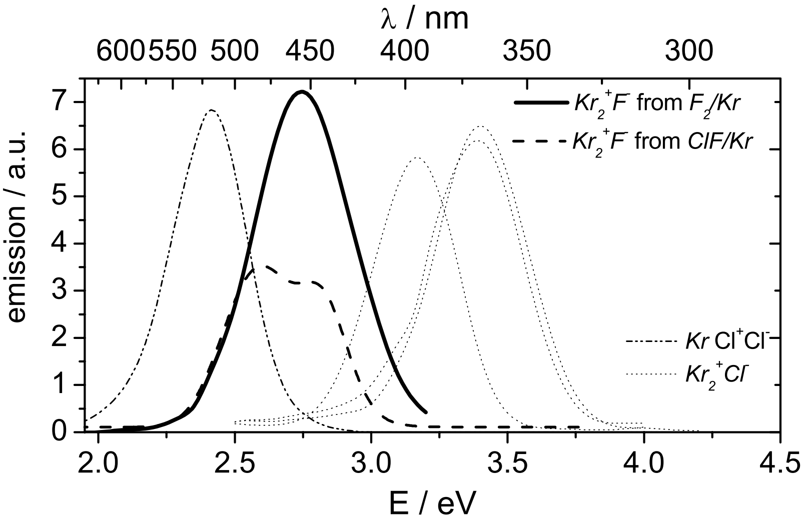

Figure 5.3: $Kr_2^+F^-$ emission measured in this thesis by dissociating ClF (thick dash) compared to the same emission after F_2 dissociation in Kr (thick solid [82, 193]) and to the emissions from $KrCl$ (three dashed curves for different sites [194]) and $KrCl_2^-$ (dash-dot [194]).

5.2.2 Identification of $Kr_2^+F^-$ emission (LIF)

The $Kr_2^+F^-$ emission recorded in this thesis by dissociation of ClF in Kr at $\lambda_{diss} = 387$ nm and probing the F fragments with $\lambda_{probe} = 270$ nm is reproduced in Fig. 5.3 as a thick dashed line (Gaussian fit from Fig. 4.6). It is compared to the same emission for F_2 in Kr [82] (thick solid line), to Cl^+Cl^-/Kr (dash-dotted) and to Cl atoms in different lattice sites (three dotted curves) [194]. Only the $Kr_2^+F^-$ emission after F_2 dissociation is comparable. Since the emission grows with sample irradiation, the nearby $KrCl_2$ emission cannot be a candidate.

As a check, two $Kr_2^+F^-$ emission bands taken from literature were fitted with the same Gaussian functions in Fig. 5.4, with their amplitudes and widths as the only adjustable parameters. Good agreement with the spectrum reported by Bressler [82, 193] (open squares, excited with 260 nm) is obtained, when the weight of the Gaussian at 441 nm is approximately doubled. For the spectrum recorded in Apkarian's group [54] (open circles, excited at 248 nm), it must be almost quadrupled. Until now, the broad spectra were interpreted as the vertical transition to the repulsive $Kr - Kr$ surface [54, 69]. As the emission observed in this thesis clearly consists of two bands and the spectra reported for different excitation wavelengths are shifted with respect to each other, an explanation involving two different lattice sites, which lead to different fluorescence spectra, seems natural.

The two bands most probably originate from different positions of the emitting $Kr_2^+F^-$ exciplex in the Kr lattice. A longer emission wavelength is expected in a tight geometry and the 480 nm band is therefore assigned to fluorescence on interstitial sites, i.e. Kr^+F^- is excited while F is on an interstitial site. During the formation of the $Kr_2^+F^-$ exciplex the $Kr - Kr$ bond is contracted by 44% [47] and this complex fluoresces in the tight geometry. The 441 nm band is favored by excitation of substitutionally isolated F atoms. After formation of the $Kr_2^+F^-$ exciplex, the geometry is less constrained due to the vacancy of the substitutional site. This explains why the 441 nm band dominates in F_2 doped samples, since F atoms may occupy both substitutional and interstitial sites. Dissociation of ClF, in contrast, produces mostly interstitial F fragments, because the substitutional

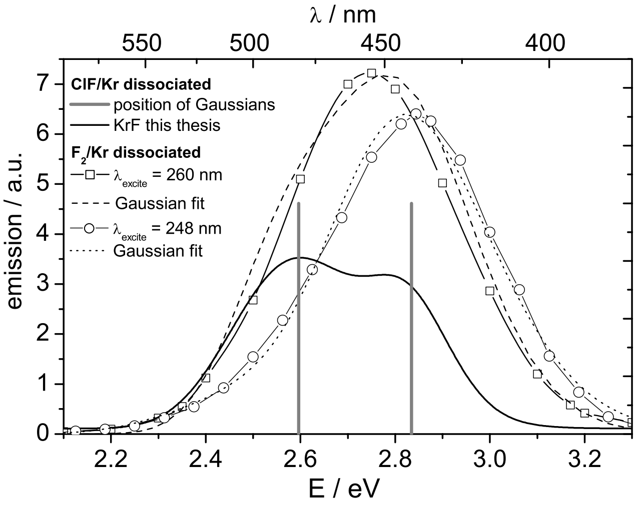

Figure 5.4: The Gaussian fit to the $Kr_2^+F^-$ emission (thick dashed) measured in this thesis after ClF dissociation and excitation at 270 nm is reproduced from Fig. 4.6a. The vertical sticks indicate the position of the two Gaussian functions. The symbols reproduce the $Kr_2^+F^-$ emission after F_2 dissociation in Kr and excitation with 260 nm (open squares, ref. [82, 193]) or 248 nm (open circles, ref. [54]). The dashed and dotted lines are fits with the two Gaussians at the indicated positions.

sites are occupied by the immobile Cl. Both bands can be excited with pulses ranging from 278 nm to 248 nm, but the shorter wavelengths preferentially excite the 441 nm fluorescence band (cf. Fig. 5.4).

An emission from Cl^+F^-/Kr could not be observed. It is expected to be shifted to the red with respect to the emission in Ar at 420 nm. This emission would then overlap with the emission from $Kr_2^+F^-$. However, the observed emission grows with irradiation (cf. chapter 4.3.3), implying that it cannot be due to Cl^+F^-/Kr, which should be bleached. Probably the Cl^+F^-/Kr is quenched by nonradiative recombination[1].

5.2.3 Excimer absorption of KrF (probe pulse)

When ClF is dissociated in the matrix, the F and Cl radicals are bound by approximately 100 cm^{-1} due to van-der-Waals interaction with the surrounding Ar and Kr matrix atoms. The van-der-Waals minima of the gas phase potentials of Cl and F to the rare gases are collected in Tab. 5.3 and compared to the nearest neighbor distance (substitutional site) and to the distance from the center of the octahedral O_h site to the rare gas atoms in an undistorted lattice.

For a concise discussion consider Fig. 5.5. The absorption of KrF in Ar matrices shows a sharp onset at 265 nm and a well resolved vibrational progression, indicating absorptions to different vibrational levels in the ionic Kr^+F^- state, $v' \to v''$ from $0 \to 0$ to $0 \to 9$ [82]. The main point is that the transition to the zeroth vibrational level in Kr^+F^- is observed with the highest intensity. This can be explained by the fact that in an octahedral O_h site in Ar with one Kr atom, the $Kr - F$ distance will be approx. 0.266 nm, which is so close to the minimum $R_e = 0.25$ nm of the Kr^+F^- potential, that the overlap of the vibrational ground state wave functions in the valence and ionic state is very large. The same configuration in Ne matrix leads to a $Kr - F$ bond confined to a distance of only 0.224 nm, and the $0 \to 0$ transition has only a weak intensity, whereas the maximum occurs around $0 \to 9$ [82]. Again, this can be explained by a projection onto the repulsive wall of the Kr^+F^- potential at 0.224 nm.

In contrast, the absorption spectrum of KrF in Kr matrix (Fig. 4.9) lacks vibrational structure. In the center of the octahedral site (cf. Fig. 2.5) of an undistorted Kr matrix, the F atom has a distance of 0.286 nm to six Kr atoms. This distance happens to be exactly the van-der-Waals bond

---

[1] Note that the difference in ionization potentials $E^+(Kr) - E^+(Cl) = 1eV$ is on the order of the binding energy of $Kr_2^+F^-$ with respect to Kr^+F^- of 0.66 eV [47] and the binding energy of Kr_2^+ of 1.15 eV [48].

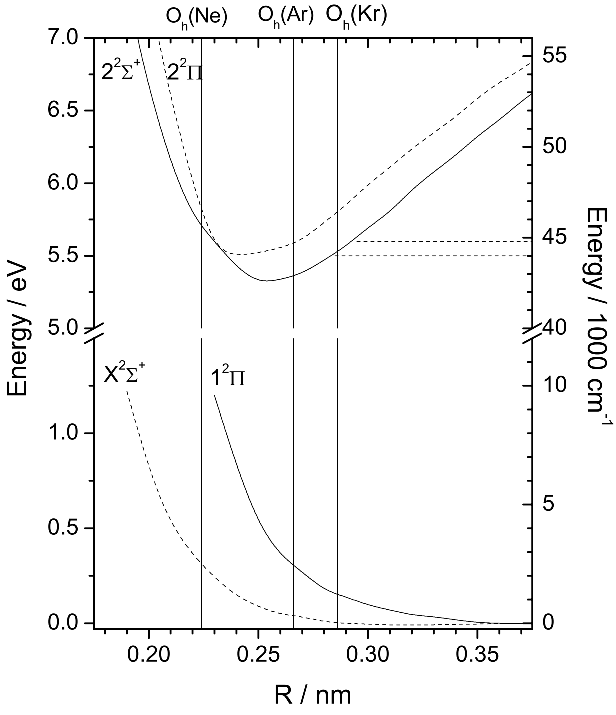

Figure 5.5: KrF potential calculated by Dunning and Hay [51]. Vertical lines indicate the $Kr-F$ distance in an interstitial O_h site of Ne, Ar and Kr in an undistorted lattice. The distance in Kr coincides with the van-der-Waals distance of $Kr-F$. The dashed horizontal lines display the width of the sharp absorption at $\lambda = 275$ nm of KrF at 4 K (Fig. 4.9).

Matrix	notation	Ne	Ar	Kr
van der Waals to F [57]	R_{vdW} / nm		0.31	0.285
min of Rg^+F^- [51]	$R_{\min \Delta V}$ / nm	0.201	0.245	0.25
van der Waals to Cl [56]	R_{vdW} / nm		0.388	0.395
nearest neighbor [119]	R_{nn} / nm	0.316	0.376	0.404
octahedral site [119]	R_{os} / nm	0.224	0.266	0.286

Table 5.3: Bond lengths of van-der-Waals RgX molecules and lattice parameters.

length of KrF. Therefore, the F atom will be in the center of the O_h site, and this highly symmetrical configuration gives rise to the sharp absorption at 275 nm [88] at 4K (cf. Fig. 4.9). Upon irradiation more and more F atoms are trapped in the O_h site. At higher temperatures, vibrations of the lattice and of the F fragment within the cage destroy the symmetry, and since the F atom has various distances to the nearest Kr atoms the absorption broadens. For temperatures higher than 15 K, F becomes thermally mobile in the matrix and occupies various sites. This changes the absorption band to the one observed by Bressler, Andrews and in this thesis at high T (Fig. 4.9). The vibrational structure is missing, since different sites inhomogeneously broaden the peaks.

At low temperatures, $\lambda_{probe} = 278$ nm does not lead to recombination of ClF or F_2 by radiative dissociation of $Kr_2^+F^-$, whereas $\lambda_{probe} < 270$ nm does. Bressler observes that the sharp 275 nm absorption grows with photon flux at 275 nm, while it decays when the sample is irradiated with shorter wavelengths. Also the relative weight of the emissions at 441 and 480 nm depends on the excitation wavelength (Fig. 5.4). These observations together support the following hypothesis: the shorter λ_{probe} is, the higher the energy in the ionic manifold will be, and the possibilities for a geometric rearrangement within the ionic state increases. Then the fluorescence may occur in a geometry favoring recombination. If λ_{probe} is kept low, the fluorescence must occur in such a way as to retain F inside the O_h site. The dependence of the relative weight of the two bands on excitation, discussed in the previous chapter, is consistent with this interpretation.

The following implications of the spectroscopy in Kr matrix for the pump-probe experiments with the KrF excimer as the probed species can be inferred. The fluorescence bands at 441 and 481 nm are indicative of KrF formation. If a wavelength $\lambda_{probe} < 270$ nm is used, the F atoms, which have not reached the O_h site, will contribute little to the signal. Warm matrices enforce thermal recombination but at the same time greatly reduce the static fluorescence intensity induced by $\lambda_{probe} \approx 275$ nm.

The interpretation of both the spectroscopic results and the interpretation of pump-probe spectra will greatly profit from a detailed theoretical investigation of the ionic species. The calculation of precise ion-pair states by the DIIS method is a complicated task and has not been accomplished for F in rare gases, but is investigated in the groups of Prof. Gerber and Prof. Manz.

5.3 Potential energy surface for ClF in Ar matrix

A.B. Alekseyev kindly provided us with the numerical data for the potentials of ClF in the gas phase [121]. The calculation of DIM potentials for ClF in Ar are in progress[2]. Throughout this thesis gas phase potentials are used, with the ion-pair states shifted according to the results from chapter 4.2.3 which are collected in Tab. 5.1.

5.3.1 Difference potentials for ClF

Difference potentials ΔV are needed for the evaluation of the pump-probe spectra. Fig. 5.6c shows the bound triplet states $^3\Pi$, the first excited singlet $^1\Pi$ and an exemplary repulsive triplet state. The thick line emphasizes the $B(^3\Pi_0)$ state, which is excited in most of the pump-probe experiments discussed below. Panel b) displays the shifted difference potentials for all triplet-triplet transitions which obey the propensity rule $\Delta\Omega = 0$. The lowest transition from the singlet state has its minimum around 41000 cm^{-1}, above the scale of this plot. The thick lines indicate the $B \rightarrow E$ (solid) and $B \rightarrow f$ (dash-dot) transitions. The transitions from other bound states have similar difference potentials. The transitions from the repulsive triplet state are plotted as dashed lines. They have not been observed in this thesis, as the longest probe wavelength that resulted in a pump-probe signal was 320 nm, and the ionic potentials where shifted to have the $B \rightarrow E$ resonance at this wavelength.

The square of the transition moments for the $B \rightarrow E$ and $B \rightarrow f$ transitions is plotted in the upper panel of Fig. 5.6. The transition to f dominates for short bond distances and probe wavelengths. For bond distances $R > 6$ a$_0$ the transition moment is negligible, prohibiting probe windows at these large distances. The transition probabilities for the other bound triplet states are similar [158] and the ones for repulsive triplets are weaker [121]. If the repulsive triplets were significantly populated, a pump-probe signal with $\lambda_{probe} > 320$ nm should be observed.

5.3.2 Difference potential of Cl_2

Fig. 5.7a displays the difference potentials for the $B \rightarrow E$ (solid) and $B \rightarrow f$ (dash dot) transitions in Cl_2/Ar, shifted in the same way as for ClF, namely as to match the excitation threshold for the Cl^+Cl^-/Ar emission at 286 nm. Panel b) shows the potential energy curves for the relevant states of Cl_2. The ground state X, the B state (solid) as a representative of the bound triplets, the $^1\Pi$ state (dash) and two states from the repulsive manifold (dotted) are displayed. The E (solid) and the f state (dash dot) are indicated.

5.4 Photochemistry of ClF in Ar and Kr

Cl atoms (and all larger compounds formed by it) are spatially fixed in Ar and Kr matrices. F atoms become thermally mobile at $T = 25$ K in Ar and at $T = 15$ K in Kr [81]. At temperatures below this threshold, they are fixed but can move, if they receive enough kinetic energy in a photodissociation event. These photo-mobilized F atoms travel a certain distance in the crystal until they have lost their

---

[2] PhD thesis by Maike Schröder in the cooperating group of Prof. Manz, Theoretical Chemistry Department

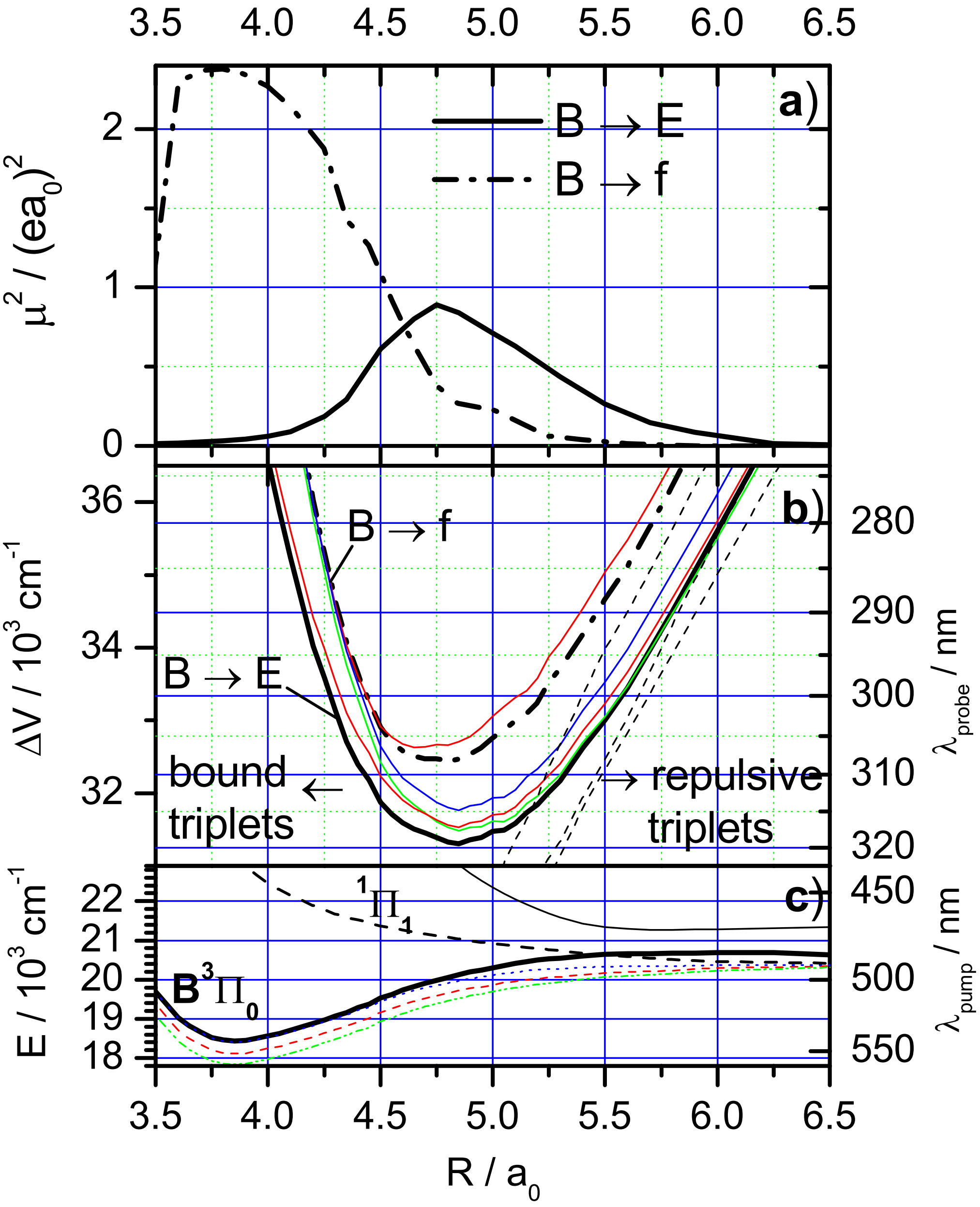

Figure 5.6: Results obtained in the CI calculations for ClF from ref. [121]. a) Square of the transition dipole moment μ^2. The transitions with $\Delta\Omega \neq 0$ have weak dipole moments, and their μ^2 is two orders of magnitude smaller. b) Difference potential ΔV red shifted by 4500 cm^{-1}. The thick solid line corresponds to the $B \rightarrow E$ transition and the thick dash-dotted line to $B \rightarrow f$. c) Potential energies for some valence states.

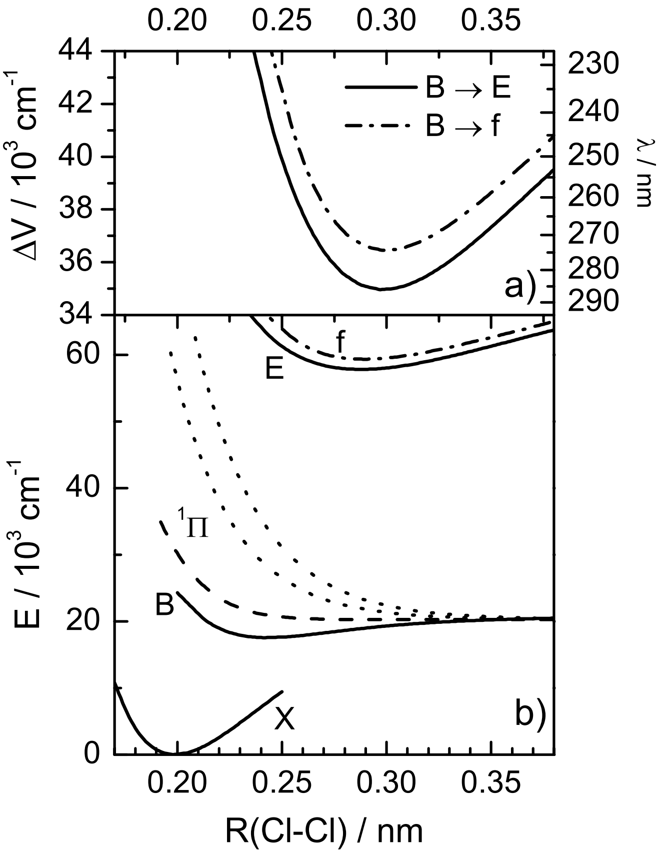

Figure 5.7: a) Difference potential for Cl_2 shifted by 3760 cm^{-1} for the $B \rightarrow E$ (solid) and $B \rightarrow f$ transition (dash dot). b) Unshifted potential surfaces of Cl_2. Ground state X, B (solid), $^1\Pi$ (dash) and two repulsive triplet states (dotted). At higher energies E (solid) and f (dash dot).

energy. Then they are trapped, either in a rare gas cage or by a center with which they react. In Ar they travel on average about 2.1 nm upon photoexcitation with 3 eV excess energy [203]. Traps for F fragments are ClF itself, Cl and F from previous dissociation events and also molecular products like F_2, ClF_2 and ClF_3 formed by previous fragmentations. At the excitation wavelength of 308 nm the products ClF_2 and F_2 are known to absorb much more strongly, approximately by a factor of 4, than ClF itself [152, 173]. Nongeminate recombination should become rare at concentrations as low as 1 : 100,000, since the average distance traveled by photomobilized F fragments has been shown to be around 8-9 lattice constants [203]. The mean distance between two ClF molecules deposited at a concentration of 1 : 100,000 is 46 lattice constants.

The objective of this thesis is to investigate the ultrafast photodynamics in the primary dissociation event by fs-pump-probe spectroscopy. A more detailed study of the static photochemical experiments is deferred.

5.4.1 Dissociation quantum efficiency

ClF/Ar

Here the evaluation will restricted to exponential fits, which should indicate within a factor of two the dissociation efficiency and its dependence on temperature and wavelength. The dissociation efficiencies ϕ_d are calculated from $\sigma\phi_d$ derived in chapter 4.3. The absorption cross sections σ are taken from Tab 5.4. This yields dissociation efficiencies at 308 nm in argon of $\phi_{d,308} = 4.4\%$ at 5 K and 5.0% at 19 K using the lowest concentration (see Table 5.4). The dissociation quantum yield of $\phi_{d,387} \approx 4.8\%$ for excitation at 387 nm measured at 19 K has to be used with care, since the large uncertainty in the value for σ_{387} enters.

		F_2			ClF					units
atom 1	m	19			19					amu
atom 2	M	19			35					amu
diss. energy	D_0	12820			20930					cm^{-1}
excitation wavel.	λ	360	450		308			387		nm
photon energy	$h\nu$	27780	22222		32468			25840		cm^{-1}
energy of F	E_{kin}	7430	4650		7370			3070		cm^{-1}
absorpt. x-section	σ	5.16 ^{a}	0.23 ^{a}		3.5			0.44		10^{-21}cm^2
diss. x-section	$\sigma\phi_d$	1.86	0.081	0.028	0.15	0.18	1.8	0.021	0.22	10^{-21}cm^2
diss. quant. yield	ϕ_d	36 ^{b}	35 ^{c}	12 ^{c}	4.4	5.0	50	4.8	50	%
temperature	T	12	4.5	12	5	19	28	19	20	K
host		Ar	Kr		Ar		Kr	Ar	Kr	

a) Ref. [152], b) Ref. [81], c) Ref. [53]

Table 5.4: Summary of dissociation efficiencies for ClF determined in this work by bleaching of the A' emission. Earlier results for F_2 are included for comparison.

The values for the dissociation efficiencies of $4.4 - 5\%$ reported here are low considering the excess energy of 0.9 eV for the F fragment and the fact that excitation at 387 nm with a lower excess energy of 0.4 eV still leads to photodissociation. One has to keep in mind, though, that these values for the efficiency for permanent dissociation are determined by the cage exit probability *minus* the probability for geminate and nongeminate recombination.

The results for ClF are compared to the dissociation efficiencies obtained for F_2 [53, 81] at the same kinetic energies E_{kin} of the F fragments in Tab. 5.4. The excess energy E_e given by the difference between the photon energy $h\nu$ and the dissociation energy D_0 is shared among the fragments according to momentum conservation. This leads to a kinetic energy E_{kin} of the lighter F fragment of $E_{kin} = (h\nu - D_0) \times M/(M + m)$ with $m = 19$ amu for F and $M = 35$ amu for Cl. The results show the expected trend of decreasing dissociation probability going from 5% to 4.8% when lowering the kinetic energy of the F fragment from 0.91 eV (7370 cm^{-1}) to 0.38 eV (3070 cm^{-1}). However, one might expect a larger change as in the case of F_2 [53, 81] (cf. Tab. 5.4). The ClF results for ϕ_d are significantly lower than those reported in [53, 81] for F_2 dissociation. A possible explanation may be found in the orientation of the F orbital. Calculations of the transmission coefficient of an F atom through the triangular window shown in Fig. 2.5c showed [68] that the barrier for an F atom with the singly occupied F orbital aligned parallel to the direction of motion is 2.1 eV, with a saddle point in the center of the triangle. For the P-orbital orientation perpendicular to the motion, the saddle point is in the line connecting two nearest neighbor Ar atoms with a barrier height of only 0.7 eV. For symmetry reasons, and from the considerations on the molecular orbitals in Fig. 2.14, it is evident that a dissociating F_2 molecule will have parallel and perpendicular P-orbital orientation on both F fragments with equal probability. For ClF, the singly occupied P-orbital on the F fragment is always aligned with the direction of motion and thus it experiences the higher barrier, if the orbital is not tilted on the timescale of dissociation. Simulations on the orbital orientation of F atoms in matrices suggest [70] that the timescale of orbital alignment will be on the order 60 fs. This point deserves further experimental and theoretical attention.

Clearly, detailed studies of the reaction mechanism and the dissociation efficiency are required to elucidate pathways and cage exit probabilities. However, even the preliminary results given here have important implications. Since the kinetic energy of the F fragment is lower in the case of excitation of ClF at 387 nm than for F_2 at 450 nm the observation of permanent cage exit sets a new upper bound for the barrier height for F in Ar of 0.4 eV.

ClF/Kr

The yields for Kr are calculated in the same way (Tab. 5.4). They are on the order of 50% in warm matrices and at relatively high concentrations of $1 : 5000$. The mobility of F fragments is very high and repeated re-excitation can expel the F fragments from the laser focus.

In this system not only the bleaching of the educts ClF, but also the accumulation of the products can be measured by inducing the KrF excimer transition and measuring the $Kr_2^+F^-$ emission. If the early rise in Fig. 4.14a is fitted with an exponential growth curve, as it was done in the Apkarian group [88] for the F_2 dissociation in Kr, a dissociation efficiency beyond 100% is calculated. This result is unphysical. It can be explained in terms of a saturation value induced by secondary processes and back reaction, i.e. the concentration of ClF does not decrease to zero. This is consistent with the finding of nonexponential decay or background in the ClF bleaching experiments. Obviously, the cage exit probability and mobility of F fragments in Kr is very high. In the future it will be helpful to detect the ClF educt and the KrF product of the dissociation simultaneously in order to find quantitative solutions of the rate equations. This can be done for example by exciting ClF with $\lambda_{diss} = 387$ nm, which dissociates ClF and induces the $A' \rightarrow X$ of the remaining ClF educts. A weak probe laser at $\lambda_{probe} = 270$ nm then records the KrF products. Experiments employing these pulses were reported in chapter 4.3.3. However, the $A' \rightarrow X$ emission was not monitored there, as this study aimed at preparing the femtosecond experiments. The results are discussed in the following chapter.

5.4.2 Control of F motion: Shuttling F from Cl to Kr

Fig. 4.14 demonstrates that there are two ways to control the concentration of F fragments with laser pulses. The dissociation laser $\lambda_{diss} = 387$ nm can drive the ClF dissociation to completion and the probe laser $\lambda_{probe} = 270$ nm induces recombination of the ClF fragments, because the fluorescence of $Kr_2^+F^-$ mobilizes the F atoms. In other words, the F atoms can be shuttled from Kr to Cl much in the same way as was previously demonstrated for multiply doped Ar matrices, where F atoms are shuttled from Xe to Kr and back [81].

A second, more sophisticated way to shift the equilibrium uses a sequence of pulses on the fs timescale. This is demonstrated in Fig. 4.14b between 400 and 580 s. After the dissociation with λ_{diss}, the F fragments are not in thermal equilibrium for several ps, i.e. they move within the Kr crystal. The detection efficiency at λ_{probe} for these hot F atoms is enlarged and therefore the observed signal is higher for the sequence B, where $\lambda_{probe} = 270$ nm comes 100 fs after $\lambda_{diss} = 387$ nm. In sequence A (λ_{diss} 1 ps after λ_{probe}), almost 1 ms passes between λ_{diss} and λ_{probe}, because the repetition rate of the laser is 1 kHz, and after this time all F fragments have thermalized in the Kr lattice. The signal alternates from equilibrium A to B in a stepwise manner, when the time delay is changed accordingly. A closer look at the step function shows that after the step up there is some additional rise, and after the step down there is a decay, indicating that in addition to the altered detection efficiency, also the equilibrium concentration changes. Consider the decay from B to A between 400 and 420 s in Fig. 4.14b. λ_{probe} comes 1 ms after λ_{diss} during this time and thus only thermally equilibrated F fragments are probed. The decay must originate from a decay of the F concentration. The reason for the higher F concentration produced by the sequence B is that the recombination of ClF induced by λ_{probe} is completed before the dissociation with λ_{diss} and thus there are more ClF molecules to dissociate.

Rate equations

This chapter gives a description of the photochemical equilibria by rate equations, that may become important in future investigations. This thesis focuses on the fs-pump-probe experiments and here only the shape of the observed rise and decay functions of Fig. 4.14 shall be explained. The full rate diagram

$$ClF + Kr \underset{k_2}{\overset{k_1}{\rightleftharpoons}} Cl + KrF \overset{k_3}{\rightarrow} Cl + Kr + XF$$

can be described by the a system of differential equations for the concentrations N_i

$$\begin{aligned} dN_1 &= -k_1N_1 + k_2N_2 \\ dN_2 &= +k_1N_1 - k_2N_2 - k_3N_2 \\ dN_3 &= k_3N_2 \end{aligned}$$

with $N_1 = N_{ClF}$, $N_2 = N_{KrF}$, $N_3 = N_{XF}$, and XF denotes any of the species such as Cl_2F, ClF_2 etc., or F atoms that have left the laser focus.

The solution for the KrF concentration, which is measured in the experiment by λ_{probe}, is[3] $N_2(t) = C_0 + C_1 \exp((-\kappa_1 - \kappa_2)t) + C_2 \exp((-\kappa_1 + \kappa_2)t)$. This function describes the fast initial rise and slow decay of the entire signal, i.e. when pulse sequences are not changed.

In order to determine the individual rates from the experiment, the rate k_3 can be neglected (at least for weak pulses as used for figure 4.14a). The solution for this reduced system is $N_2(t) = N_{eq} + (N_0 - N_{eq}) \exp(-(k_1 + k_2)t)$, which describes all rise- and decay functions in Fig. 4.14. N_0 is the starting value and N_{eq} is the equilibrium value. Since $\lambda_{probe} = 270$ nm dissociates ClF and also drives the recombination, the rate constants must be rewritten as $k_1 = k_{387} + k_{270}$ and $k_2 = k_{probe}$. The rise and decay rates are the sum of the three rates k_{387}, k_{270} and k_{probe}. Three equations are needed to obtain the rates. Two are determined by the rates for the rise $k_r = k_{387} + k_{270} + k_{probe}$ and decay $k = k_{270} + k_{probe}$. A third equation can be derived from the steady state concentration N_2^{eq} and the total number of available F fragments N_{allF}, which is measured in the highest spike in Fig. 4.14, when λ_{diss} has driven the ClF dissociation to completion: $\frac{k_{270}+k_{387}}{k_{probe}} = \frac{N_2^{eq}}{N_{allF}-N_2^{eq}}$.

---

[3] using the definitions $\kappa_1 = \frac{1}{2}k_1 + \frac{1}{2}k_2 + \frac{1}{2}k_3$ and $\kappa_2 = \frac{1}{2}\sqrt{(k_1^2 + 2k_1k_2 - 2k_1k_3 + k_2^2 + 2k_3k_2 + k_3^2)}$,

Part II

Ultrafast dynamics from pump-probe spectra

The fs-pump-probe spectra are the center of this thesis. The experimental results are given first, ordered by the molecules examined, i.e. I_2*,* ClF and Cl_2*. Their interpretation is discussed in chapter 7, ordered by topic. Some additional spectra are shown there that demonstrate a special effect in detail. The discussions include DIM-simulations from the cooperating theory group of Prof. Gerber on the closely related system* F_2/Ar_{54}*, and the good agreement of experimental and theoretical results support the interpretations. In some cases, as for the solvent induced spin-flip (chapter 7.6), the prediction by theory was given before the experimental evidence. In the case of depolarization and angular reorientation (chapter 2.3.5), it is evident that the process is contained in the simulations, but they have to be evaluated accordingly. The 2-D-quantum mechanical wave packet simulations by M. Korolkov are discussed in chapter 2.1.5 together with the energy loss. This shows the beautiful mutual stimulation of theory and experiment that emerges from the cooperation within the SfB 450. In the discussion (chapter 7), the input from the theoretical collaborations will be clearly delimited from the fruits of this thesis. In future, the experiments will be compared to a detailed theoretical study the system* ClF/Ar *itself. The DIM-simulations are currently pursued in the PhD thesis of Maike Schröder in the group of Prof. Manz.*

Chapter 6

Results

Before experiments on the basically unknown system ClF/Rg were started, the concepts for ultrafast spectroscopy in condensed phase were advanced in the similar and well characterized system I_2/Kr (chapter 2.3.6). Iodine is much heavier than ClF and the dynamics can be measured very accurately to obtain detailed information. This thesis presents the first nearly complete set of pump-probe spectra with systematic variation of pump and probe wavelengths. An evaluation scheme is developed, which allows for interpretation of the experimental data without the aid of simulations. It is transferred to ClF by analogy and results on Cl_2 are reported for completeness.

6.1 Systematic pump-probe spectra on I_2 in Kr

This chapter presents selected results obtained from the fs-pump-probe experiments with systematically varied pump and probe wavelength. The potential diagram is presented in Fig. 6.1 and shows the $X \rightarrow B$ transition (pump), which was tuned from 600 nm to 480 nm, and the $B \rightarrow E$ transition (probe), tuned from 550 nm to 387 nm[1]. Nonradiative relaxation to the states $D'(2_u)$ and δ or

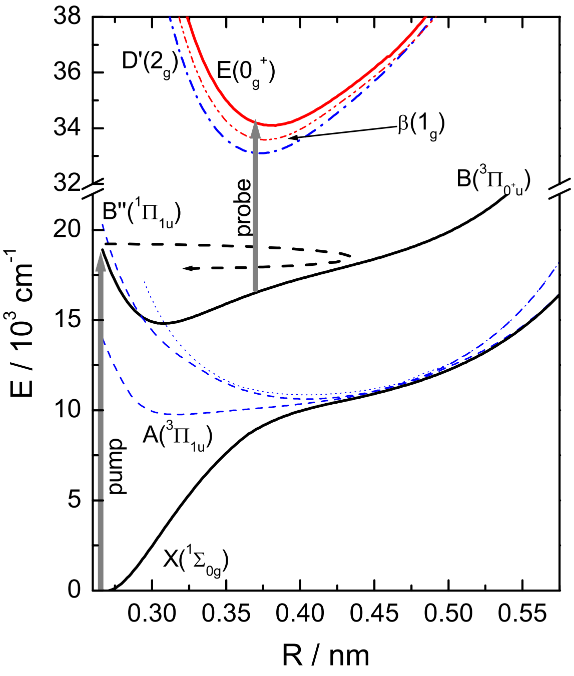

Figure 6.1: Simplified potential diagram for I_2/Kr [204]. The wave function in the ground state X is excited to the B state to create a wave packet (vertical arrow pump). The wave packet is recorded by the probe pulse (vertical arrow probe). After nonradiative relaxation to D' and β, the LIF from these states is detected. The dashed lines indicate the A and B'' states, which can be pumped alternatively. The dotted line indicates the repulsive a state that crosses the B state and causes predissociation [27, 115].

---

[1] Probe transitions to the f state are not used within this thesis. They can be spectroscopically seperated from transitions to E [115, 116].

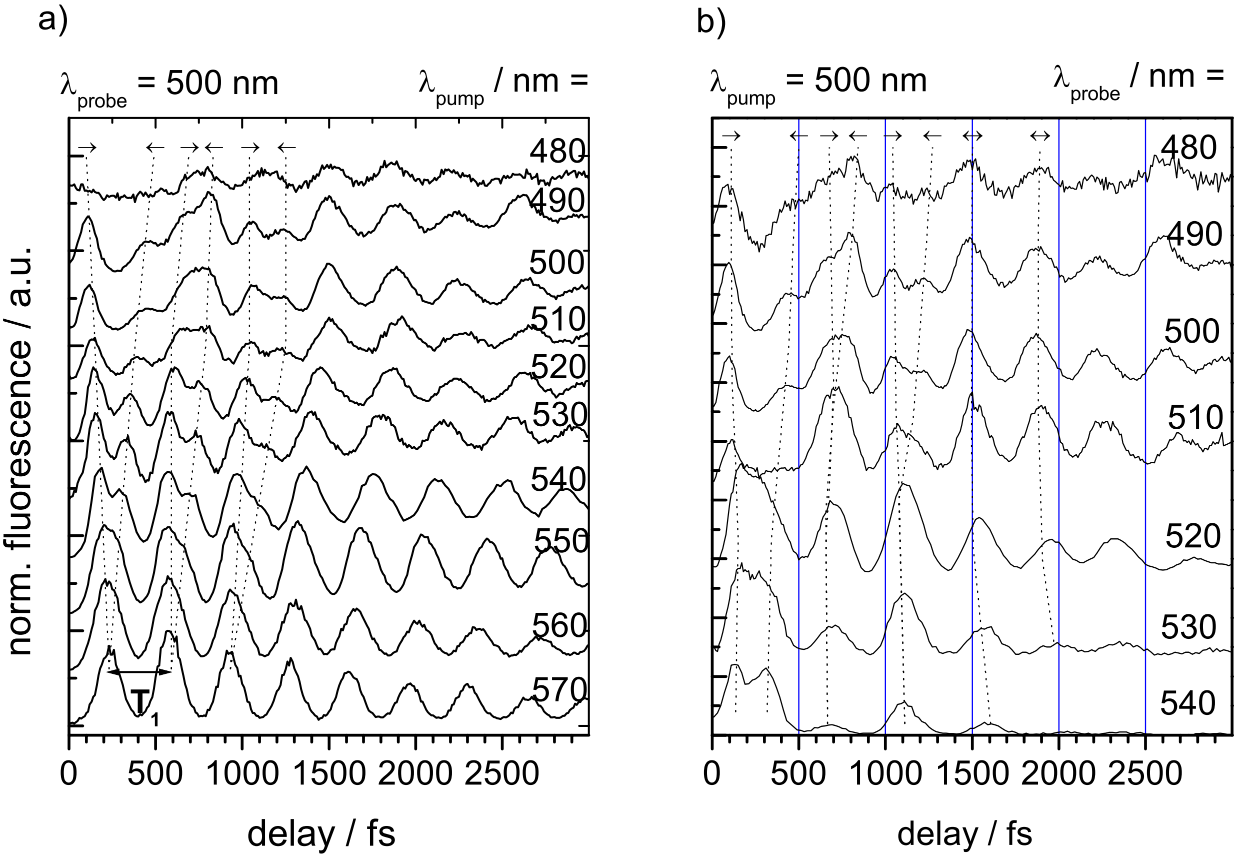

Figure 6.2: Pump-probe spectra for a) $\lambda_{probe} = 500$ nm and $\lambda_{pump} = 570$ to 480 nm and b) $\lambda_{pump} = 500$ and $\lambda_{probe} = 540$ to 480 nm. Dashed lines connect the times for passage through the respective probe windows and the arrows indicate $\rightarrow$ outward and $\leftarrow$ inward motion. T_1 : First round-trip time. Note that strikingly similar trends are observed for variation of a) probe wavelength and b) pump wavelength.

$\beta(1_u)$ results in the recorded LIF signal. The entire collection of the B state spectra is given in the Appendix. These systematic measurements are completed by pump-probe spectra for $A(^3\Pi_1)$ and $B''(^1\Pi_1)$ excitation. All spectra are recorded in I_2/Kr samples with a concentration of $1 : 1000$ at the temperature $T = 15$ K.

6.1.1 Typical B state spectra

Pump-probe spectra for excitation energies which range from deep in the B state well at 570 nm, to the gas phase dissociation limit at 500 nm and even above the dissociation limit (490 and 480 nm) are collected in Fig. 6.2a with a typical probe wavelength $\lambda_{probe} = 500$ nm. For an explanation consider the trace for $\lambda_{probe} = 520$ nm. The thick arrow (pump) in Fig. 6.1 prepares a wave packet on the B state. The first peak in the spectrum corresponds to the first outward passage (dashed arrow) of the wave packet through the probe window (vertical arrow at $R_{win} = 0.376$ nm in Fig. 6.1). The wave packet returns back and passes the probe window a second time, giving rise to the second peak. The periodic motion of the wave packet in the B state potential continues and produces the oscillations in the pump-probe spectrum.

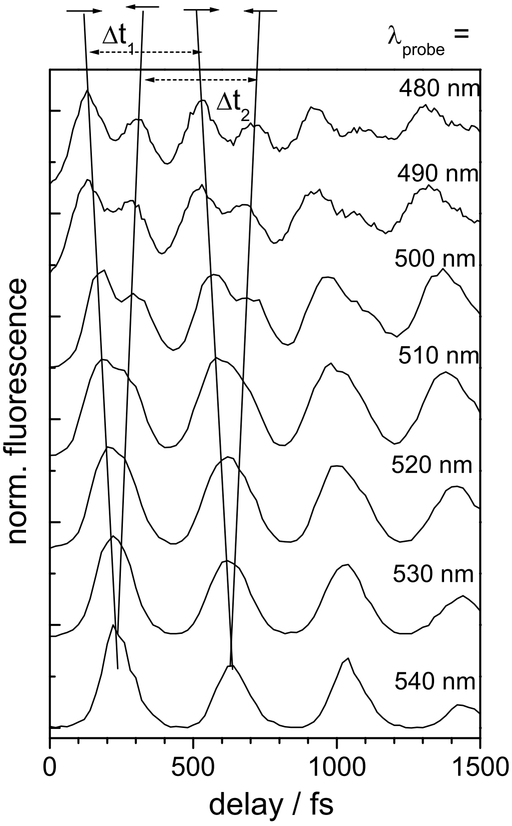

Figure 6.3: Pump-probe spectra with fixed pump wavelength that demonstrate the influence of the probe window. $\lambda_{pump} = 540$ nm: decreasing λ_{probe} from 540 to 480 nm yields an increased splitting between the inward and outward motion of the wave packet indicated by the arrows. The time between two outward passes (Δt_1) and two inward passes (Δt_2) seems to be constant at first sight (cf. Fig 7.3).

In essence, for excitation beyond the probe window the wave packet passes the probe window twice in each complete period, which results in the splitting indicated by the inward and outward pointing arrows in Fig. 6.2a. The wave packet passes the window on the outward motion ($\rightarrow$) for the first time, on the inward motion ($\leftarrow$) for the second time and – after one full period – it shows up a third time in the outward and a fourth time on the inward motion. Obviously, one full period corresponds to the time difference between two outward or two inward passes which are connected in Fig. 6.2a by dotted lines as a guide to the eye. For $\lambda_{pump} = 540$ nm the wave packet is excited slightly above the window and the inward/outward splitting occurs for the first time. Qualitatively, it is immediately evident from Fig. 6.2a, that the difference between the first two outward passes indicated by T_1 increases with pump energy E_{pump} as expected by the anharmonicity in a Morse-like potential.

The origin of the inward/outward splitting can be confirmed by tuning λ_{probe} and keeping λ_{pump} fixed at, for example, 540 nm (Fig. 6.3). Taking $\lambda_{probe} = 540$ nm, the wave packet is caught just at the turning point, and the splitting disappears. Shortening λ_{probe} shifts R_{win} inwards, according to the $B - E$ difference potential. For $\lambda_{probe} < 510$ nm the wave packet passes the window twice; it spends a longer and longer time in the region from the window to the outer turning point and back, which results in the increased splitting in Fig. 6.3. Similar trends can be observed for the fixed pump-wavelength $\lambda_{pump} = 500$ nm in Fig. 6.2 b). At this high excitation energy the influence of the matrix is more important and the peak structures are less regular.

In essence, the first complete oscillation period $T_1(E)$ in Fig. 6.2a is the round-trip time of the wave packet at the energy E_{pump}, prepared by the pump pulse. T_1 is taken directly from the spectra and converted to the vibrational frequency $\nu(E) = 1/T_1(E)$, which is plotted in Fig. 7.1.

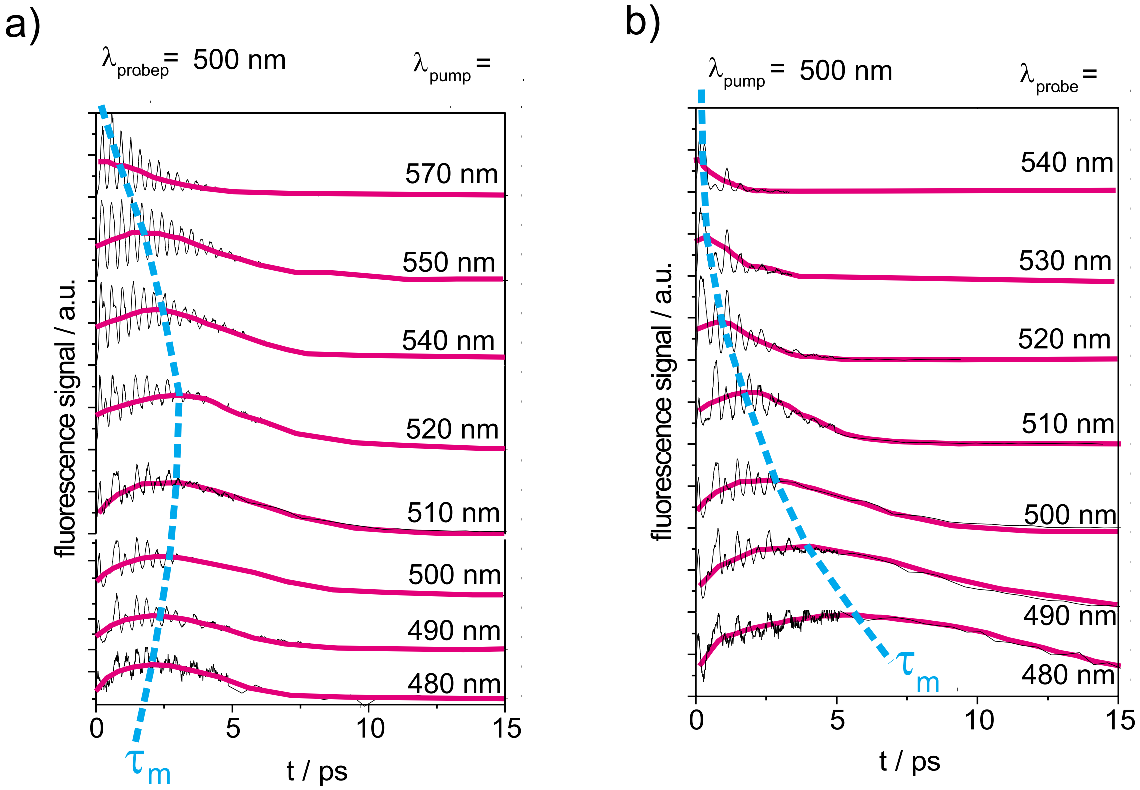

Figure 6.4: Pump-probe spectra from Fig. 6.2 on a stretched timescale. a) $\lambda_{probe} = 500$ nm and $\lambda_{pump} = 570$ to 480 nm and b) $\lambda_{pump} = 500$ and $\lambda_{probe} = 540$ to 480 nm. The dashed lines connect the maxima of the envelopes and indicate τ_m.

Fig. 6.4a shows the spectra from 6.2 on a longer timescale up to 15 ps. The time at which the envelope of the pump-probe spectra is maximal is indicated by τ_m and the dashed line guides the eye. The spectra with fixed $\lambda_{probe} = 500$ nm in panel a) have the longest τ_m for an intermediate pump wavelength $\lambda_{pump} = 520$ nm. Excitation with higher and lower energy leads to a smaller τ_m, i.e. to an earlier maximum of the pump-probe spectrum. For fixed pump wavelengths the time τ_m increases monotonically with decreasing probe wavelength. In chapter 7.4.1 it will be shown that the maximum of the pump-probe envelope occurs, when the vibrational population has relaxed down to the probe window energy E_{win}. The shorter wavelengths probe population deeper in the potential and it takes longer for the wave packet to relax down to this energy. This explains the observed trend in panel b). The explanation for the trend in panel a) lies in the nonlinearly increasing energy dissipation that is displayed in Fig. 7.11 and will be discussed in chapter 7.4.2. The energy dissipation is connected to the loss of coherence (chapter 2.3.3), which smears out the oscillatory structure after several ps in addition to the dispersion effects.

6.1.2 Polarization analysis of pump-probe spectra

Since I_2 occupies a double substitutional site in the Kr lattice and since the size of I atoms is similar to Kr, it is expected that the bond direction will be sterically fixed by the axially symmetric surrounding (sketch of geometry in Fig. 7.15b). This hypothesis excludes depolarization in pump-probe spectra according to the discussion in chapter 2.3.5. The preserved orientation of the molecule is confirmed in the following experiment by changing the relative polarization of the pump and probe pulse.

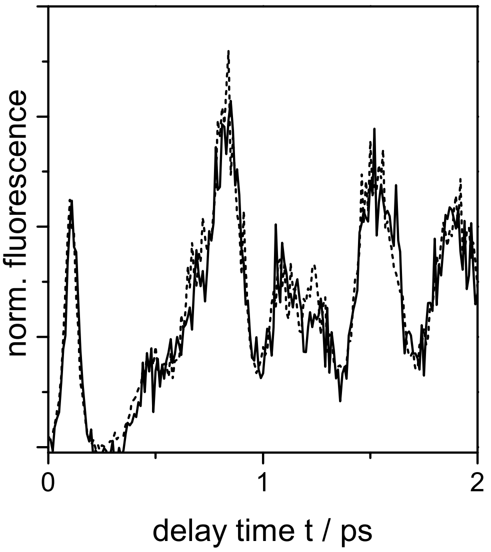

Figure 6.5: Pump-probe spectra with $\lambda_{pump} = 486$ nm and $\lambda_{probe} = 486$ nm for I_2 in Kr. The spectrum for $\|$ pump-probe excitation has been multiplied by a factor of 1/3 and agrees perfectly with $\perp$ excitation. The ratio of $I_{\perp}/I_{\|} = 1/3$ is maintained throughout the entire spectrum, indicating negligible angular reorientation of the I_2 molecule.

Fig 6.5 shows the results for excitation of I_2/Kr above the gas phase dissociation limit[2]. The fluorescence intensity is plotted versus time delay between the pump pulse ($\lambda_{pump} = 486$ nm) and the probe pulse ($\lambda_{probe} = 486$ nm) with probe polarization parallel ($\|$) and perpendicular ($\perp$) to the pump. The $\|$ - spectrum is multiplied by the factor of $I_{\perp}/I_{\|} = 1/3$ (cf. Tab 2.3.5) corresponding to preserved photoselection and it shows perfect agreement with the $\perp$ - spectrum. This proves that on the timescale of 2 ps no depolarization, i.e. no reorientation of the molecular bond occurs.

To check the conservation of the initial alignment on a longer timescale, the polarization of the laser induced fluorescence (LIF) from D' after $\|$-pump $\|$-probe excitation was recorded by introducing a polarization analyzer just in front of the monochromator. Again the ratio for preserved photoselection (cf. Tab. 2.3.5) of $I_{LIF\perp}/I_{LIF\|} = 1/5$ is found for LIF polarization $\perp$ / $\|$ with respect to the polarization of the pump and probe beams. This indicates that the D' state of I_2 in Kr matrix does not depolarize, i.e. angular reorientation is negligible, on the timescale of the fluorescence lifetime of about 5 ns.

6.1.3 A and B'' state spectra

Fig. 6.6 compares pump-probe spectra for excitation to the A and B'' states. The broken lines display spectra with excitation to the A state with $\lambda_{pump} = 670$ nm and two different probe wavelengths, $\lambda_{probe} = 387$ nm (dashed line) and $\lambda_{probe} = 400$ nm (dotted line)[3]. The first peak ~ 200 fs corresponds to the first outward pass ($\rightarrow$) of the wave packet in the A state through the probe window at $R_{win} \approx 0.38$ nm (Fig. 6.1). The second peak after ~ 1100 fs catches the wave packet on the way back ($\leftarrow$). In the first collision with the Kr matrix, the wave packet has lost so much energy that for all subsequent oscillations the probe window is just reached and the wave packet is only observed once per period ($\leftrightarrow$). The probe wavelength $\lambda_{probe} = 400$ nm is just at the threshold for reaching the ion-pair states according to eq. 2.6. The super-elevated peak at 1.5 ps is a consequence of the response of the Kr lattice. The contracting Kr cage increases the shift of the ion-pair states, moving them into resonance with the probe pulse.

---

[2] The polarization sensitive pump-probe spectra on I_2/Kr presented in this chapter were taken by Markus Gühr.

[3] The 400 nm beam is the second harmonic of the older Ti:Sa laser system (CPA 1 from Clark), which had a fundamental wavelength around 800 nm.

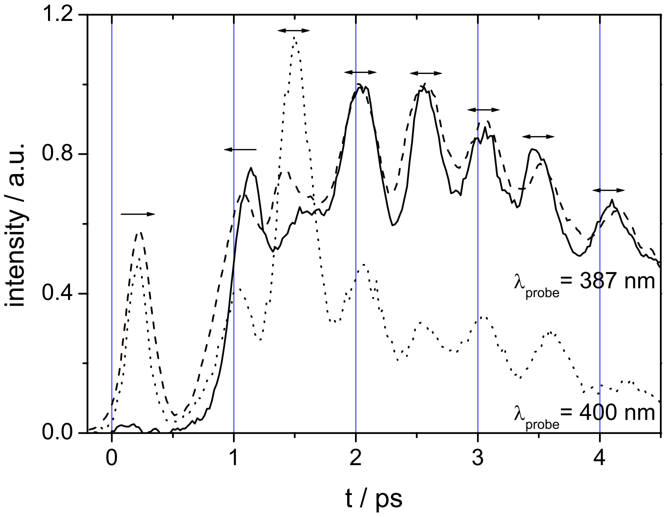

Figure 6.6: Pump-probe spectra on I_2/Kr with a fixed excitation to the A state with a pump wavelength $\lambda_{pump} = 670$ nm and differing probe wavelengths $\lambda_{probe} = 400$ nm (dotted) and 387 nm (dashed). For comparison, the solid line displays excitation to the $^1\Pi_1$ state at $\lambda_{pump} = 480$ nm with $\lambda_{probe} = 387$ nm. Except for the missing peak at 200 fs, this spectrum is almost identical to the A state spectrum recorded with $\lambda_{probe} = 387$ nm. The same effect is seen in the cases of Cl_2/Ar (Fig. 6.17) and ClF/Ar (Fig. 6.11).

The spectrum with $\lambda_{probe} = 387$ nm has a much larger background than the one for $\lambda_{probe} = 400$ nm. The probe window for the shorter wavelength is located deeper in the A state. Thus it probes longer lasting relaxed population than the higher lying probe window (cf. Fig. 2.2). For even shorter probe wavelengths the background keeps increasing [29]. This is equivalent to the signals for B state excitation (Fig. 6.4b).

The solid line in Fig 6.6 shows a spectrum for excitation to the $B''(^1\Pi_1)$ state, recorded with $\lambda_{probe} = 387$ nm, as well. It is generated with $\lambda_{pump} = 480$ nm (solid line), while the $A^3\Pi_1$ state is prepared with $\lambda_{pump} = 670$ nm (dashed line). The spectra are nearly identical after 1 ps, demonstrating that the B'' population nonadiabatically relaxes down to the A state during this time. The higher excess energy is quickly dissipated in the first ps. The main difference of the two spectra is the peak at 200 fs, which is not present for $B''(^1\Pi_1)$ excitation, since there is no probe window in that state. The crossing to the A state occurs at large R in the first round-trip, analogous to the case of ClF/Ar and Cl_2/Ar.

6.2 Road map for condensed phase pump-probe spectra

From the preceding chapter, together with all other pump-probe spectra on I_2/Kr that are collected in the Appendix, a compact diagram can be distilled. It is a useful road map for pump-probe spectra of diatomics in the condensed phase in general and will prove helpful in the discussion of ClF and Cl_2 spectra. In this sense I_2/Kr can be used as a model system to guide the experiments and the interpretation of the pump-probe spectra on similar systems that are less well understood. The diatomics, that are the topic of the present thesis, all have qualitatively similar potentials. The final state of the probe transition has a larger equilibrium distance than the state where the dynamics take place.

Fig. 6.7a shows a typical potential diagram. The wave function in the ground state X is promoted to the excited B state, creating a wave packet in the vibrational levels around the energy $E_{pump.}$ The outer turning point is indicated as $R_{pump.}$ The probe pulse defines the probe window location R_{win} to the E state by the resonance condition $\hbar\omega_{probe} = \Delta V(R_{win})$. The minimum $R_{\min\Delta V}$ of the difference potential $\Delta V = E_E - E_B$ is often quite close to the minimum of the final E state.

Fig. 6.7b) is a diagram summarizing the properties of pump-probe spectra as a function of λ_{pump} on the vertical axis (energy in excited state) and of λ_{probe} on the horizontal axis, defining the location of the probe window R_{win}. The highest possible pump wavelength (640 nm for I_2) is defined by the minimum T_e of the B state. The corresponding probe window (387 nm) lies on the left border of

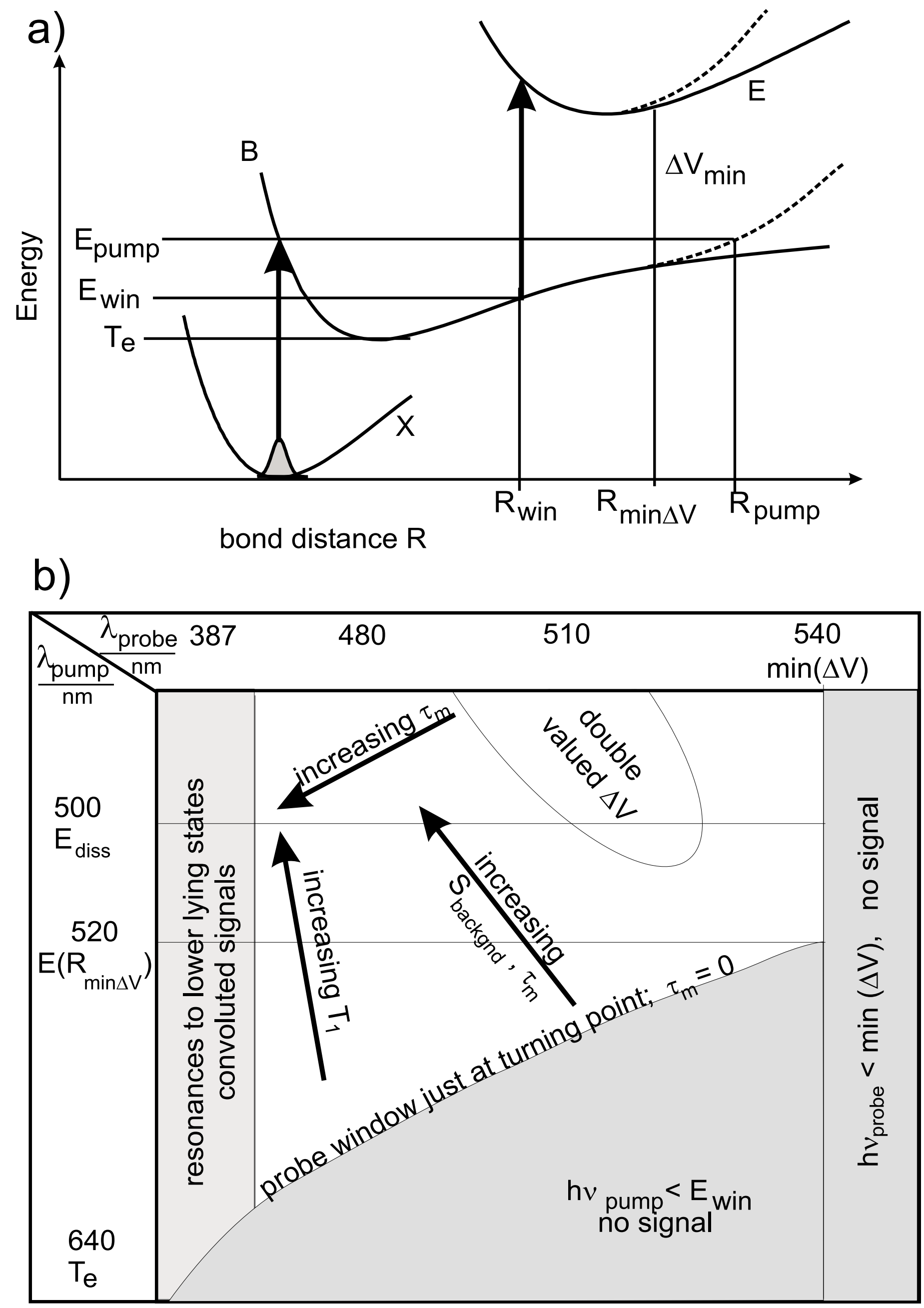

Figure 6.7: a) Schematic potential energy diagram for diatomics in condensed phase with the notation introduced in Fig. 2.9. b) Road map for the systematic set of pump-probe spectra for the B state of I_2/Kr (see Appendix) summarizing the observed trends. The pump wavelength is indicated vertically since it specifies the energy of the wave packet. The probe wavelength is varied on the horizontal axis, as this corresponds to a variation of the probe window (cf. panel a). In the light grey region the signal is a convolution with lower lying electronic states. In the dark grey region, no signal can be observed, and at its border the probe window R_{win} is just at the turning point R_{pump}. The arrows indicate trends in the pump-probe spectra when pump and probe wavelengths are tuned. T_1 is the first oscillatory period, τ_m is the maximum of the envelope and $S_{backgnd}$ indicates the background from smeared out oscillations.

the diagram, although in general, shorter probe wavelengths are possible for probing the inner limb of the B state. At shorter wavelengths, however, resonances to lower potential energy surfaces (e.g. A state) start to play a role and the pump-probe spectra are a convolution of contributions from both states, which is indicated by the light-grey shaded area. The right border of the diagram is given by the minimum of the difference potential. For $\lambda_{probe} < \min(\Delta V)$ (540 nm) no signal is observed. This is marked by the dark grey shaded area, as well as the region where $h\nu_{pump} < E_{win}$. At the borderline of the dark area, the probe window R_{win} is just at the turning point R_{pump}. The condition $E_E(R_{pump}) = h\nu_{pump} + h\nu_{probe}$ is fulfilled, which will be used in chapter 7.1.3 to construct the E state from the systematic spectra. Above the horizontal line for $E(R_{\min\Delta V})$ (520 nm) the wave packet can access two probe windows to the E state, since the difference potential is double-valued. However, the region in which the outer window is observed, is limited since the probe wavelength must not be too short.

The arrows indicate the trends observed in pump-probe spectra. The first period T_1 increases with decreasing pump wavelength and slightly with decreasing probe wavelength. The background signal $S_{backgnd}$ from relaxed and dephased population increases, together with the time τ_m for the maximum of the pump-probe envelope, with decreasing λ_{pump} and $\lambda_{probe.}$ Near the gas phase dissociation limit E_{diss} (500 nm) and upwards, this trend continues for $S_{backgnd}$, but here τ_m is reduced with higher pump energy due to the nonlinear dissipation of energy (cf. Fig. 6.4 and chapter 7.4.2).

6.3 Pump-probe spectra for ClF in Ar and Kr

The bleaching experiments for ClF in Ar and Kr demonstrated, that the dissociation quantum efficiency in Ar is low (~ 5 %), while in Kr it is very large (~ 50 %) (chapter 5.4.1). In Ar the fluorescence of Cl^+F^- at $\lambda_{LIF} = 420$ nm was identified (Fig. 4.5), and probing to these ion-pair states can be used to monitor the recombination dynamics of ClF. In Kr this fluorescence is missing but instead the dominant fluorescence originates from $Kr_2^+F^-$ at $\lambda_{LIF} = 460$ nm (Fig. 4.6), which can be used to monitor the F fragments after ClF dissociation.

6.3.1 B state excitation

ClF/Ar is excited to the B state above the dissociation limit, since the focus of this study is on dissociation-recombination dynamics and on strong interaction of the molecule with the solvent. The spectra are recorded with the fixed pump wavelength of the second harmonic of the Ti:Sa at $\lambda_{pump} = 387$ nm, i.e. 0.6 eV above the gas phase dissociation limit[4]. This is the maximum of the B state absorption. The location of the probe window R_{win} is varied by scanning the probe wavelength. This corresponds to a horizontal line in the "Road map of condensed phase pump-probe spectroscopy" (Fig. 6.7).

Overview and envelope

The pump-probe spectra for ClF/Ar are recorded in the same scheme as for I_2/Kr. The femtosecond pump pulse at $\lambda_{pump} = 387$ nm prepares a vibrational wave packet on the weakly bound B ($^3\Pi_0$)-state above the gas-phase dissociation limit (Fig. 4.1). A probe pulse with $\lambda_{probe} < 322$ nm promotes the population to the ionic E state in the Cl^+F^- manifold (cf. chapter 4.2.1). This is indicated by the solid arrow $h\nu_1$ in Fig. 4.1. After relaxation within the Cl^+F^- ionic manifold the fluorescence from the lowest state, D', is observed (Fig. 4.5) [205]. The signal intensity is recorded as a function of time delay between the two pulses. Fig. 6.8 shows pump-probe spectra with systematic variation of the probe wavelengths from 322 to 282 nm, keeping the pump wavelength fixed at $\lambda_{pump} = 387$ nm.

For $\lambda_{probe} > 322$ nm the probe resonance is lost. Hence this wavelength corresponds to the minimum of the difference potential $\Delta V = V_E - V_B$ between the B and the E state (chapter 2.3.2).

---

[4] In the present setup the laser cannot be spectrally tuned in this wavelength region.

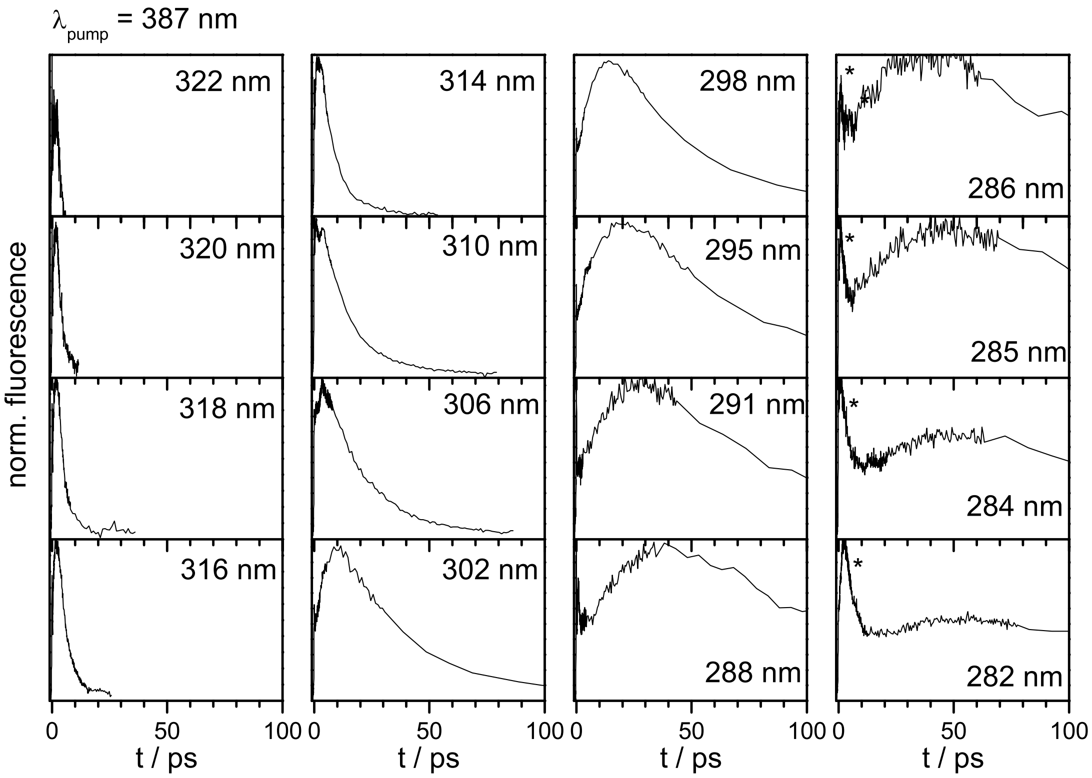

Figure 6.8: Pump-probe spectra with $\lambda_{pump} = 387$ nm, where λ_{probe} is varied from 322 to 282 nm. The fluorescence is detected at $\lambda_{LIF} = 420$ nm. Therefore ClF and Cl_2 population is observed (cf. Fig. 4.8). The maxima of the pump-probe envelope correspond to the delay time τ_m at which the vibrational population of ClF passes E_{win} (see Tab. 7.3). The early maxima in the last column, marked with an asterisk (*), correspond to Cl_2 as discussed in chapter 6.4. The assignment of the latter dynamics to Cl_2 was tested by preparation of pure Cl_2/Ar samples without ClF impurities. Consistently, the ClF contributions are then absent (cf. Fig 6.15).

The shifted difference potential ΔV of ClF in Ar matrix (Fig. 5.6) is derived from this value. The same trend as for I_2/Kr is observed when tuning the probe wavelength. Shorter wavelengths probe deeper parts of the B state potential and the maximum of the envelope τ_m shifts to later times. A more detailed examination of the envelopes for $\lambda_{probe} = 314$ to 306 nm shows the presence of two maxima, which are due to absorptions to two different states, E and f, respectively (cf. Fig. 5.6). The interpretation of spectra with $\lambda_{probe} > 310$ nm is more straight forward, since only the E state resonance can be reached.

For $\lambda_{probe} < 288$ nm an additional maximum near $t = 0$ marked with an asterisk (*) appears, which is due to the Cl_2 molecules present in the sample. The spectra are shown and discussed below.

Oscillations

Fig. 6.9 displays on an enlarged scale the first 3 ps of pump-probe signals of ClF/Ar for the first three rows from Fig. 6.8. In the first row, the probe pulse terminates only in the E state and those spectra show oscillations in the first 1.5 ps due to several passes of the wave packet through the probe window. All other spectra have the early peak near $t = 40$ fs in common, which can be attributed to the first passage of the wave packet through the probe window. The last two spectra for $\lambda_{probe} = 291$ and 288 nm represent a superposition of ClF and Cl_2 contributions, which results in the super-elevated early maximum. The deconvolution is discussed in chapter 7.8. Again, as for I_2/Kr it is evident that the modulation depth decreases on probing deeper in the potential well and hence no oscillations could be detected for $\lambda_{probe} < 314$ nm. The assignment of the oscillations will be given in chapter 7.3.2, after the dynamics of the analog model system I_2/Kr has exemplified the peak-structure.

6.3.2 Polarization dependent pump-probe spectra

ClF/Ar, excited above the gas phase dissociation limit, shows a significant depolarization in contrast to the sterically fixed I_2/Kr. The emission from D' (50 ns lifetime) after $\|$-pump $\|$-probe excitation is completely depolarized, i.e. the fluorescence is isotropic and unpolarized. Therefore, the direction of the fluorescence detection is irrelevant and a $90°$ configuration is chosen to reduce the stray light. In order to observe reorientation on the timescale of the wave packet dynamics, the probe wavelength should be long, since short probe wavelengths delay the highest sensitivity τ_m to later times (cf. Fig 6.8). Fig. 6.10 shows spectra ($\lambda_{pump} = 387$ nm and $\lambda_{probe} = 317$ nm) with parallel ($\|$ solid line) and perpendicular ($\perp$ dotted line) pump-probe polarization, as well as pump-probe polarization close to the magic angle (dashed), all on the same intensity scale.

The magic angle configuration produces a spectrum intermediate between parallel and crossed polarization. It is insensitive to angular dynamics by definition of the magic angle and will therefore be used to characterize the vibrational wave packet dynamics in chapter 7.3.2. The parallel and magic angle spectra both show a pronounced dip at 300 fs, which will be attributed in part to breathing motion of the cage in chapter 7.3.2. In the perpendicular ($\perp$) configuration, a broad minimum with a small maximum is observed after 300 fs. The $\perp$ polarization is sensitive especially to molecules that are tilted 90° with respect to the pump geometry and this suggests that this peak is due to scattering events that produce this geometry after the first encounter. All signals coincide for delay times longer than 2 ps, indicating that the anisotropy prepared by the pump pulse decays on this timescale.

In ClF/Ar nonradiative relaxation to A' is fast and the only observed $A' \rightarrow X$ emission has a lifetime of 141 ms. It is completely depolarized after excitation with 387 nm since it is a $\Delta\Omega = 2$ transition and in addition the orientation of the molecule is randomized within 1.2 ps. This was tested by introducing a polarization analyzer as discussed in chapter 6.1.2.

6.3.3 $^1\Pi$ state excitation

Pump wavelengths in the range from 310 to 260 nm excite ClF/Ar to the repulsive $^1\Pi$ state. Spectra for three different probe wavelengths between 318 and 302 nm are plotted in Fig. 6.11 as dashed

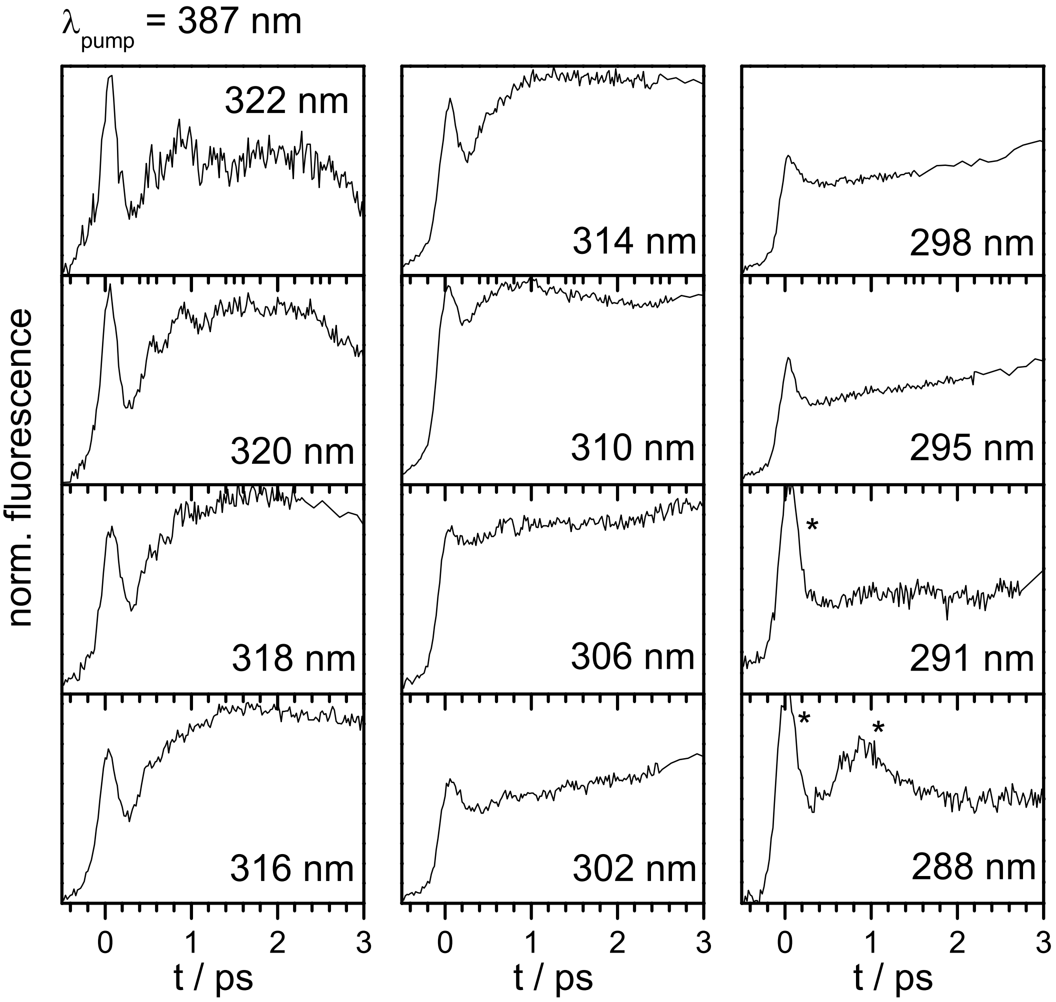

Figure 6.9: Pump-probe spectra with $\lambda_{pump} = 387$ nm and probe wavelength tuned from $\lambda_{probe} = 322$ to 288 nm. Wave packet dynamics are clearly visible in the first column with the longest probe wavelengths. The minimum at 200 fs becomes more and more substantial with increasing wavelengths (see text). The asterisk (*) in the last two plots ($\lambda_{probe} = 291$ and 288 nm) indicates contributions from Cl_2.

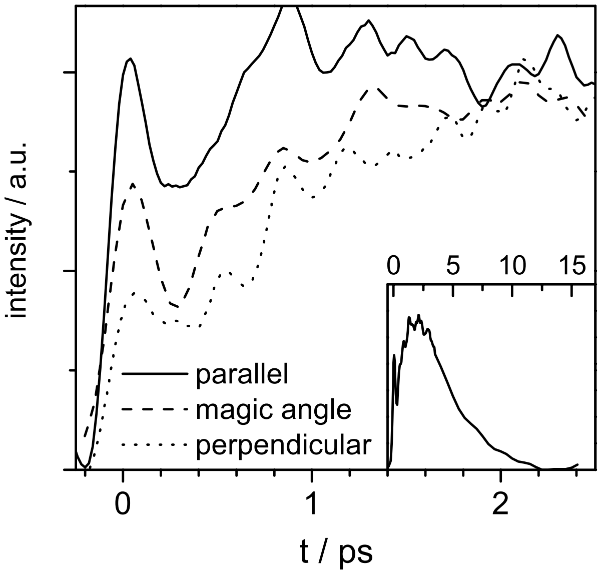

Figure 6.10: fs-pump-probe spectra with $\lambda_{pump} = 387$ nm and $\lambda_{probe} = 317$ nm for ClF in Ar for $\|$, $\perp$ and magic angle configuration of pump and probe polarization. The spectra converge after 2 ps, demonstrating the ultrafast randomization of the initially prepared alignment. The inset displays the spectrum on a longer timescale.

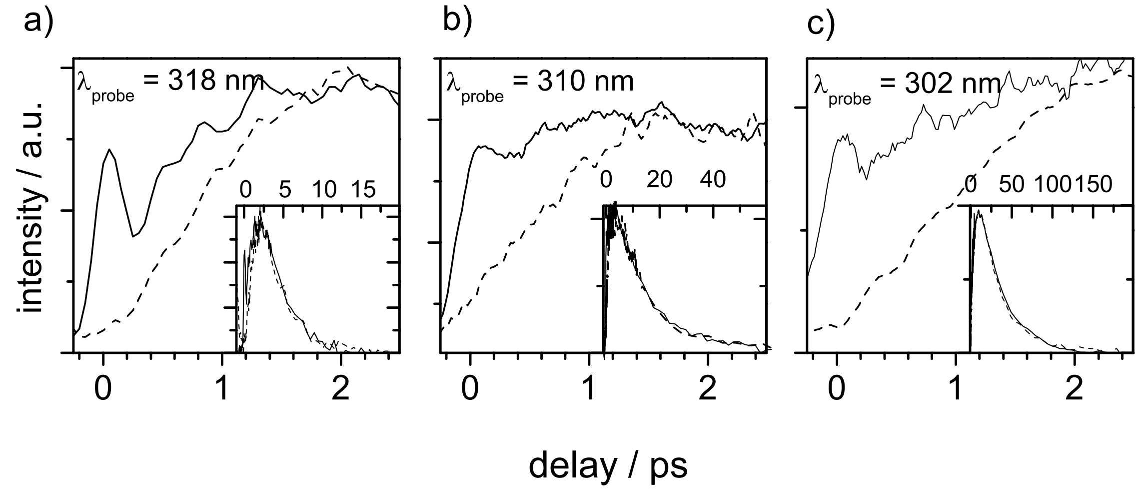

Figure 6.11: Pump-probe spectra that compare singlet excitation (dashed) to triplet excitation (solid). The $B(^3\Pi_0)$ state is pumped with $\lambda_{pump} = 387$ nm and $^1\Pi_1$ state with $\lambda_{pump} = 280$ nm for panel a) and 290 nm for panels b) and c). Three different wavelengths probe the wave packet at different energies a) $\lambda_{probe} = 318$ nm, b) $\lambda_{probe} = 310$ nm and c) $\lambda_{probe} = 302$ nm. All spectra show oscillations due to wave packet dynamics. Note the different timescales in the insets.

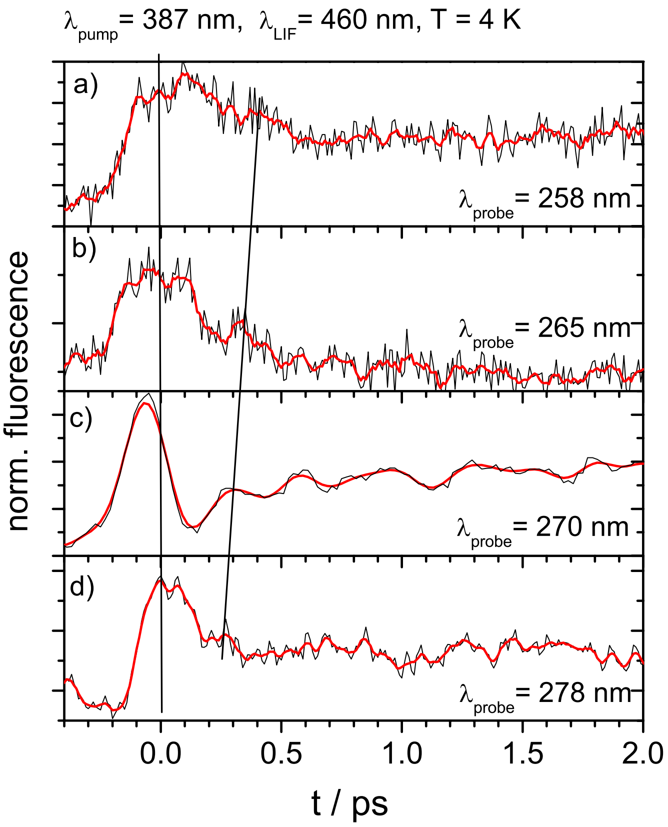

Figure 6.12: Pump-probe spectra on ClF/Kr samples at 4 K with $\lambda_{pump} = 387$ nm and LIF from $Kr_2^+F^-$ recorded at $\lambda_{LIF} = 460$nm. The probe wavelength λ_{probe} is varied: a) 258 nm, b) 265 nm, c) 270 nm and d) 278 nm. The vertical line indicates $t = 0$ and the second line guides the eye to the first maximum around $t = 0.3$ ps.

lines. For the first 2 ps, the signals differ significantly from those after excitation to the $B(^3\Pi_0)$ state at 387 nm. For longer times they coincide perfectly, after normalization to the same intensities, which accounts for the different absorption cross section and photon flux. Shorter probe wavelengths record the B state population with lower vibrational excitation (see above) and the signal can be observed up to 100 ps. For these probe wavelengths, the only allowed transition that are accessible are from $^3\Pi_\Omega$ states to the states with the same quantum numbers in the ionic manifold. All these transitions have difference potentials very close to the $B \rightarrow E$ transition, and a separation seems impossible (Fig. 5.6). That the spectra in Fig. 6.11 agree for times $t > 2$ ps immediately implies, that the molecule nonadiabatically decays from the initially excited $^1\Pi$ state to the bound $^3\Pi$ states on this ultrafast timescale. This surprising result will be further analyzed in chapter 7.6. If the population was transferred to the repulsive $^3\Pi$ states, there should also be a signal for $\lambda_{probe} > 322$ nm, according to the difference potential in Fig. 5.6. This resonance could not be observed up to now.

The signal envelope (insets) of the signals for $^1\Pi$ excitation shows the signature of vibrational relaxation, already observed above for the B state and described in chapter 6.2. First, the signal increases as the wave-packet relaxes into the probe window, improving the Franck-Condon overlap with the ionic states. Then as the wave packet loses energy, it is unable to reach the probe window and the signal decreases towards zero.

6.3.4 Pump-probe spectra with $Kr_2^+F^-$ fluorescence

The F fragments are monitored after ClF dissociation in ClF/Kr samples. The pump-probe spectra presented in this chapter use $\lambda_{pump} = 387$ nm, i.e. $B(^3\Pi_0)$ excitation. The detected fluorescence $\lambda_{LIF} = 460$ nm is indicative of the formation of the $Kr_2^+F^-$ exciplex, as it was shown in chapter 5.2.2. Two different regimes must be distinguished for the probe wavelength. If $\lambda_{probe} < 278$ nm,

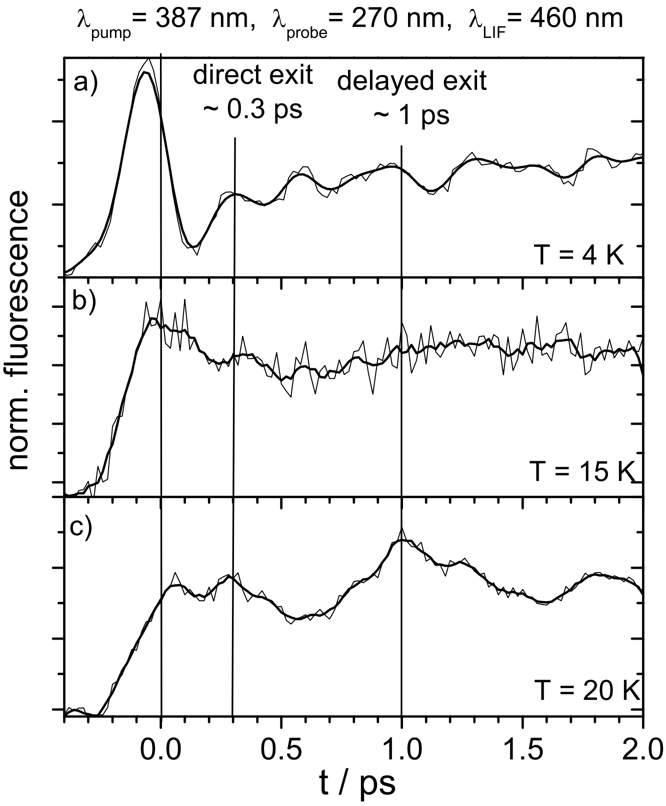

Figure 6.13: Pump-probe spectra with on ClF/Kr samples with $\lambda_{pump} = 387$ nm, $\lambda_{probe} = 270$ nm and LIF from $Kr_2^+F^-$ recorded at $\lambda_{LIF} = 460$ nm. The temperature is varied: a) 4 K (F fragments frozen), b) 15 K (threshold for F mobility) and c) 20 K (F thermally mobile).

besides the escaping F atoms also the isolated cold F atoms in the Kr lattice are probed as in the static experiments. For this reason, the ”lock-in” technique (Appendix) was applied that subtracts this static background and only yields contributions from F atoms that have just been excited. For $\lambda_{probe} > 278$ nm this static background is not present and the pump-probe spectra are recorded as usual.

Fig. 6.12 shows spectra recorded at 4 K with a variation of probe wavelength from $\lambda_{probe} = 278$ nm to 258 nm. Care was taken to accurately measure the zero time delay $t = 0$ by the FROG technique. The best signal to noise ratio is obtained for probing at 270 nm, which is the maximum of the KrF absorption at 4 K and for small irradiation doses (Fig. 4.9). Clearly reproducible features in all spectra are the maximum at negative delay times (approx. -50 fs) and the peak at ~ 300 fs, marked by a line to guide the eye. The exact time t_1, where the peak occurs, depends on the probe wavelength and varies from $t_1 \sim 250$ fs for $\lambda_{probe} = 278$ nm to $t_1 \sim 350$ fs for $\lambda_{probe} = 258$ nm. Since the cage exit probability for ClF in Kr is very high, the concentration of ClF quickly decays (cf. Fig. 4.12). A compromise has to be found concerning the number of pulses used for averaging and the bleaching rate. Most of the spectra are averaged over 500 to 1000 shots per point. For longer averaging the structures observed in the spectra are reduced due to the decaying ClF content. Several runs with 500 to 1000 shots on fresh sample positions are averaged to yield the plotted spectra. The peak at negative time delays, which is most clearly seen in the spectrum for $\lambda_{probe} = 270$ nm, depends quadratically on the intensity I_{387} of the pump pulse ($\lambda_{pump} = 387$ nm), while the spectrum for positive time delay scales linearly with intensity. I_{387} was reduced as much as possible to minimize the contribution at $t = -50$ fs. The bleaching weakens all structures in a similar manner, indicating that they originate from nascent ClF fragments.

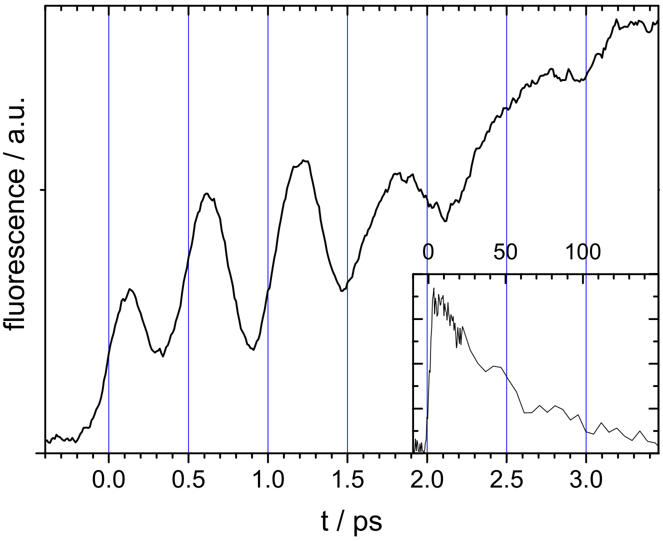

Figure 6.14: Pump-probe spectrum recorded in ClF/Kr samples at 20 K with $\lambda_{pump} = 387$ nm and $\lambda_{probe} = 289$ nm. The fluorescence band that shows the oscillations is centered at $\lambda_{LIF} = 480$ nm with a width of 50 nm and is thus identified as the $Kr_2^+F^-$ fluorescence. In chapter 7.7.3 this will be ascribed to cage dynamics of the Kr lattice around an F fragment.

Fig. 6.13 shows spectra for three different temperatures, $T = 4$, 15 and 20 K, recorded with the probe wavelength $\lambda_{probe} = 270$ nm, which provides the best signal to noise ratio. The peak ~ 300 fs is present in all spectra and the broad feature after 1ps is dominant especially in warm matrices ($T = 20$ K). In Kr the F fragments become mobile at $T = 15$ K. Note that in warm matrices ($T = 20$ K) the thermal motion of F fragments leads to recombination, which changes the bleaching of ClF. Moreover, the F atoms migrate out of the laser focus.

Fig. 6.14 shows a spectrum recorded with $\lambda_{probe} = 289$ nm at the temperature $T = 20$ K. The "lock-in" technique is not needed, since the cold trapped F radicals are not probed at this long wavelength; however, it yields identical results. The spectrum shows very well modulated oscillations. The oscillation period in Fig. 6.14 increases from 550 fs in the beginning to 750 fs around 2.5 ps. The fluorescence in the minima and maxima of the oscillation was measured, to confirm that the deep modulation really corresponds to a coherent motion of F atoms. The fluorescence band that identifies the oscillating species was recorded by subtracting the fluorescence in the second minimum at 900 fs from the one on the second maximum around 650 fs. The resulting band is centered at 480 nm with 50 nm bandwidth. It agrees with the $Kr_2^+F^-$ fluorescence (cf. Fig. 4.6) and thus the oscillations indeed originate from F fragments.

The longest wavelength, that produces a fluorescence signal at $\lambda_{LIF} = 440$ to 510 nm in pump-probe spectra corresponds to $\lambda_{probe} = 310$ nm. All spectra for λ_{probe} between 310 and 278 nm show structures similar to Fig. 6.14 or Fig. 6.13.

6.4 Pump-probe spectra on Cl_2 in Ar

This chapter gives a short account of the new results obtained for Cl_2/Ar, which represent the first ultrafast pump-probe spectra of this molecule. The experiments were necessary to separate the Cl_2 contribution from the ClF signals. However, the results are interesting in themselves and deserve further consideration. The assignment to Cl_2 was checked by growing samples from pure Cl_2 reservoirs.

6.4.1 B state excitation

Fig 6.15 collects the spectra recorded for Cl_2/Ar with LIF detection at 360 nm, indicative of Cl^+Cl^-/Ar fluorescence (Fig. 4.8). The pump wavelength is fixed at $\lambda_{pump} = 387$ nm and the

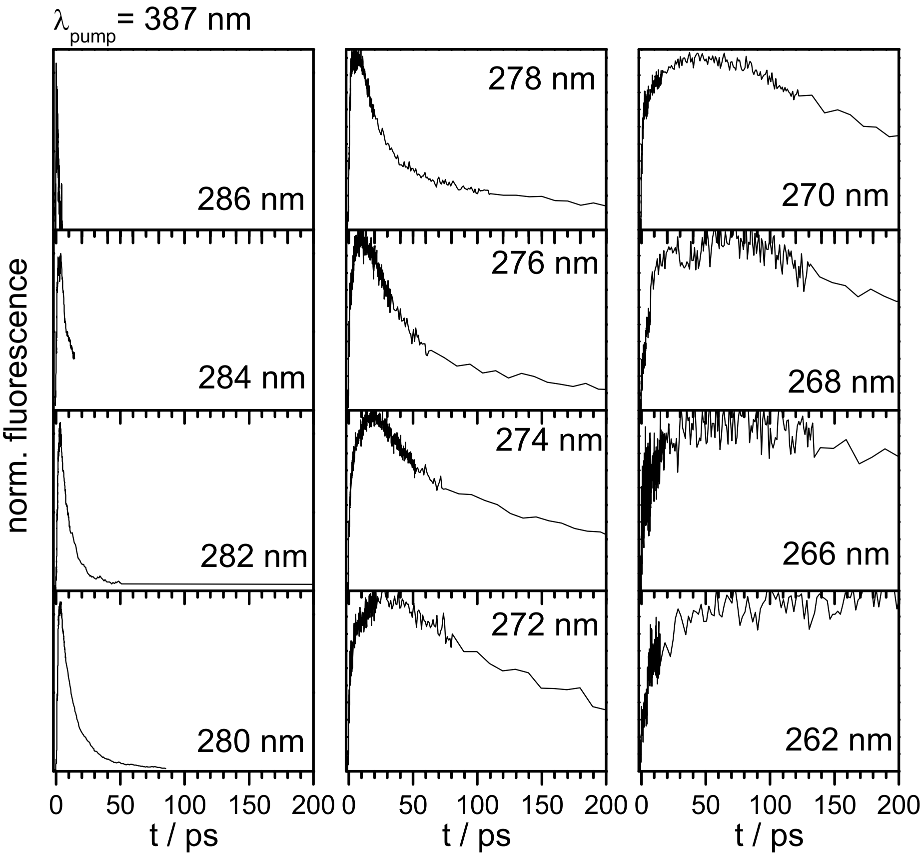

Figure 6.15: Pump-probe spectra with $\lambda_{pump} = 387$ nm. λ_{probe} is varied from 286 to 262 nm. The fluorescence is detected at $\lambda_{LIF} = 360$ nm and therefore only Cl_2 population is observed (see the fluorescence spectra in Fig 4.8). The maxima of the pump-probe envelope correspond to the delay time τ_m at which the vibrational population passes E_{win} (see Fig. 7.13). The early maxima in the first column are identical to those shown in the last column in Fig. 6.8, marked with an asterisk.

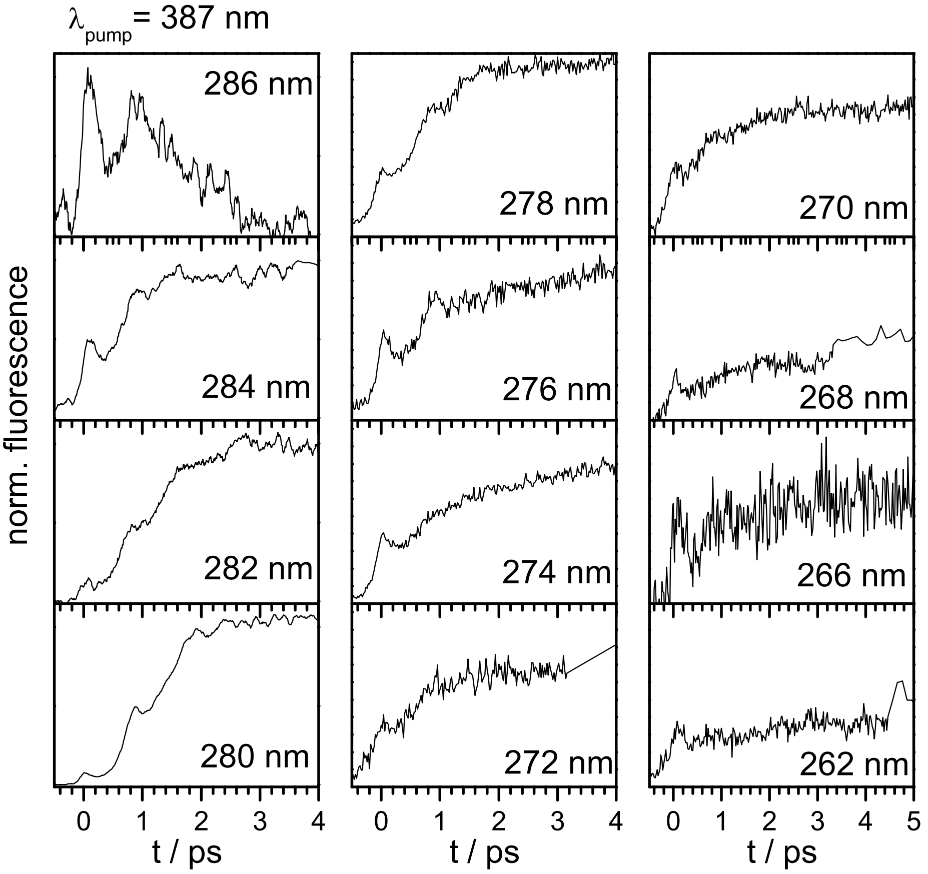

Figure 6.16: Pump-probe spectra Fig. 6.15 on a shorter timescale where $\lambda_{pump} = 387$ nm. λ_{probe} is varied from 286 to 262 nm. The fluorescence is detected at $\lambda_{LIF} = 360$ nm and therefore only Cl_2 population is observed (cf. Fig 4.8).

probe pulse is tuned from $\lambda_{probe} = 286$ to 262 nm. The first column shows spectra for $\lambda_{probe} = 286$, 284 and 282 nm, which have the same pump and probe wavelengths as the last column in Fig. 6.8 but there the LIF was detected at 420 nm, where both Cl^+Cl^-/Ar and Cl^+F^-/Ar emit (see the fluorescence spectra in Fig. 4.8). Therefore these spectra have an early, sharp maximum at $t < 5$ ps, marked with an asterisk (*) in Fig. 6.8, due to Cl_2 and a late maximum ($t > 40$ ps) due to ClF.

In pure Cl_2/Ar samples, identical results are obtained for $\lambda_{LIF} = 360$ nm (Cl^+Cl^-/Ar). However, for $\lambda_{LIF} = 420$ nm only the early peaks due to Cl_2, marked with an asterisk (*) persist, while the late maxima due to ClF are missing in Fig. 6.15. This substantiates the assignment of the 360 nm emission to Cl_2. For probe wavelengths $\lambda_{probe} > 290$ nm, the 420 nm emission is exclusively from ClF, and for shorter wavelengths due to both species. The different temporal shape of the Cl_2 vs. ClF dynamics is exploited for a two-pulse control scenario in chapter 7.8.

Fig 6.16 reproduce the spectra from Fig. 6.15 on an shorter time scale to display the wave packet dynamics. All spectra show an oscillatory period of approx. 800 fs. In some spectra an additional splitting of 150 - 200 fs is observed.

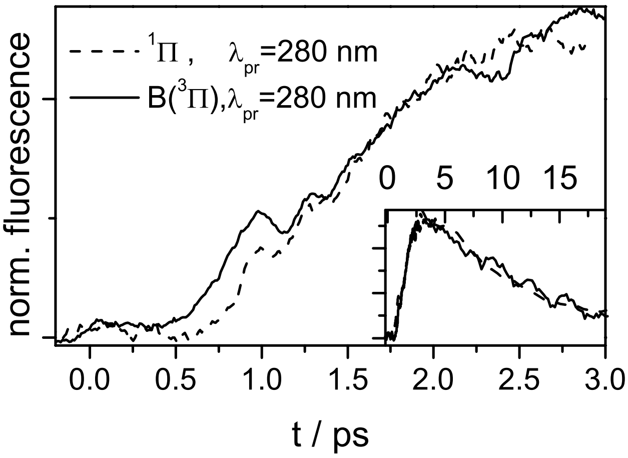

Figure 6.17: Comparison of fs-pump-probe spectra with $\lambda_{pump} =$ 387 nm ($B(^3\Pi_0)$ excitation) and 290 nm ($^1\Pi_1$ excitation) with fixed $\lambda_{probe} = 280$ nm. The fluorescence is detected at $\lambda_{LIF} = 360$ nm and thus only Cl_2 population is observed (cf. Fig 4.8).

6.4.2 $^1\Pi$ state excitation

As in ClF and I_2, the excitation of Cl_2/Ar to its repulsive $^1\Pi_1$ states yields almost identical dynamics as excitation to $^3\Pi_0$. This is demonstrated in Fig. 6.17, which shows fs-pump-probe spectra with $\lambda_{pump} = 387$ and 290 nm and fixed $\lambda_{probe} = 280$ nm. The fluorescence is detected at $\lambda_{LIF} = 360$ nm and therefore only Cl_2 population is observed (cf. Fig 4.8). The assignment of these dynamics was tested by preparation of pure Cl_2/Ar samples without ClF impurities. The potential surfaces of Cl_2/Ar (cf. Fig. 5.7) are very similar to those of ClF/Ar. Transitions from the bound triplet states $^3\Pi$ are - analog to the discussion for ClF - the only candidates for the observed probe transition. Obviously, the wave packet nonadiabatically passes from the excited singlet state to a lower and bound triplet state in the first ps.

Chapter 7

Discussion

The rich experimental results on I_2 in Kr allow for the first time the derivation of the recombination dynamics of a molecule in the condensed phase without the aid of simulations. It is instructive to compare the results obtained purely from experiment with those from DIM-trajectory simulations. The results obtained for I_2/Kr guide the interpretation of the experiments on ClF and Cl_2 by analogy.

Ultrafast energy transfer to the solvent (chapters 7.3 and 7.4) and a strong coupling of potential energy surfaces (chapter 7.6) are observed both in the large and heavy I_2 and in the small and light ClF molecule. Unlike I_2, the small size of the F fragment gives rise to ultrafast reorientation of the molecular bond in recombination dynamics (chapter 7.5) and allows the F atoms to leave the solvent cage (chapter 7.7). The heavy mass of the I_2 fragments and the well defined scattering conditions keep the wave packet much better localized and oscillations in the pump-probe spectra live much longer.

7.1 I_2 in Kr - model data from systematic experiments

A one dimensional representation for the multidimensional potential of excited state surfaces of I_2/Kr is constructed from the pump-probe spectra. In the subsequent chapters experimental snapshots of a wave packet trajectory immediately display the inelastic and nonlinear interaction of the I fragments with the Kr cage. Different signatures of vibrational relaxation in the pump-probe spectra are investigated, and it is demonstrated that the envelope of pump-probe spectra can be exploited to determine vibrational relaxation rates, even if the oscillations are not resolved. The influences of the width of the wave packet and of the probe window are analyzed.

7.1.1 Vibrational frequencies in the B state

Fig. 7.1 shows the observed first periods T_1 as a function of pump energy. The triangles are read from spectra with fixed $\lambda_{probe} = 480$ nm, and the squares for $\lambda_{probe} = 520$ nm (for the original spectra see Appendix). It is evident, that the periods are similar, but they show systematic deviations of up to 10% for the two probe wavelengths. To obtain the correct round-trip times, it is necessary to tune the probe together with the pump wavelength in such a way that the wave packet is probed at its turning point. This consistent variation of pump and probe wavelength yields the solid circles. A discussion of this procedure is presented in chapter 7.1.2.

For pump wavelengths $\lambda_{pump} > 600$ nm the $X \rightarrow A$ transition dominates the absorption spectra, because the Franck-Condon factors of the $X \rightarrow B$ transition decrease rapidly. Unfortunately, every wavelength λ_{probe} that probes the B state near its minimum expected around 640 nm, also probes the A state population. Therefore T_e of the B state could not be measured. Near the minimum, the potential should be only weakly influenced by the matrix and is well described by a Morse potential. The square of the experimental frequencies $\nu^2(E)$ from Fig. 7.1 is linearly extrapolated to estimate T_e, since the frequency of classical vibrations in a Morse potential at energy E is $\nu(E) = \omega_e\sqrt{1 + E/D_e}$. The matrix shifts of ω_e and T_e should be on the order 1 to 2% for valence states (cf. chapter 2.2.3)

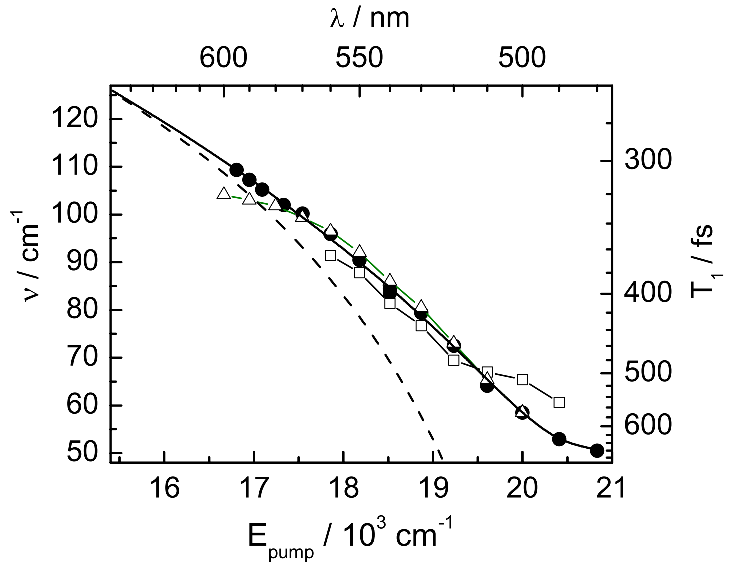

Figure 7.1: First round-trip times T_1 and frequency ν as a function of energy E_{pump}. The solid circles are the correct values determined by probing the wave packet at the turning point via an adjustment of the probe wavelength (see text). Deviations occur if the probe wavelength is kept fixed at 520 nm (squares) or 480 nm (triangles). The dashed line displays the gas phase frequencies corrected for the vertical solvation shift.

and under these constraints the extrapolation yields $\omega_e = 125.9$ cm^{-1} and $T_e = 15420$ cm^{-1} (Tab. 7.1). The function $\nu_f^2(E) = \omega_e(1 + E/D_e) + \exp(-\alpha(E - E_0))$ is fitted to the solid circles, yielding the solid line in Fig. 7.1. $\nu_f^2(E)$ consists of the linear Morse-term and an empirical exponential term, that is negligible below 19500 cm^{-1}. This exponential term describes the deviation of $\nu^2(E)$ from the Morse value at high energies E quite well.

In Fig. 7.1 the $\nu(E)$ curve in Kr is compared to the gas phase (dashed), shifted in T_e by the 350 cm^{-1} due to solvation. The anharmonicity in the matrix is systematically smaller. The repulsive interaction with the cage atoms increases with the elongation R, i.e. with energy E. This bends up the outer wing of the potential in Fig. 7.2. The potential in the matrix for high energies E is closer to the harmonic oscillator, which is expressed in a smaller slope of $\nu(E)$. A Morse-like approximation works well only deep in the well, where the interaction is still relatively weak. Near the dissociation limit the cage walls confine the I fragments and a curvature of $\nu(E)$ with the opposite sign is observed.

7.1.2 Construction of B state potential from pump-probe spectra

The scheme in Fig. 7.2 shows the $X \rightarrow B$ transition induced by the pump beam and the $B \rightarrow E$ transition due to the probe beam. Different X, B and E state surfaces of I_2 in the Kr matrix are derived and explained in the following.

An effective 1-D potential energy surface is constructed from the experimental values (solid circles) for the periods T_1 given in Fig. 7.1. For resolved quantized vibrational levels one would use the RKR (Rydberg-Klein-Rees) [207–209] scheme for the construction of the potential, and here the classical continuum analogue [210] can be applied. If the round-trip times $T(E)$ in a potential $V(r)$ are known for all energies E, the potential can be constructed as follows. The velocity of the classical particle is $v = \sqrt{2(E - V(r))/m}$. Thus an infinitesimal time step is $dt = dr\sqrt{2(E - V(r))/m}$. The potential is constructed successively by going from the potential minimum to higher energies using

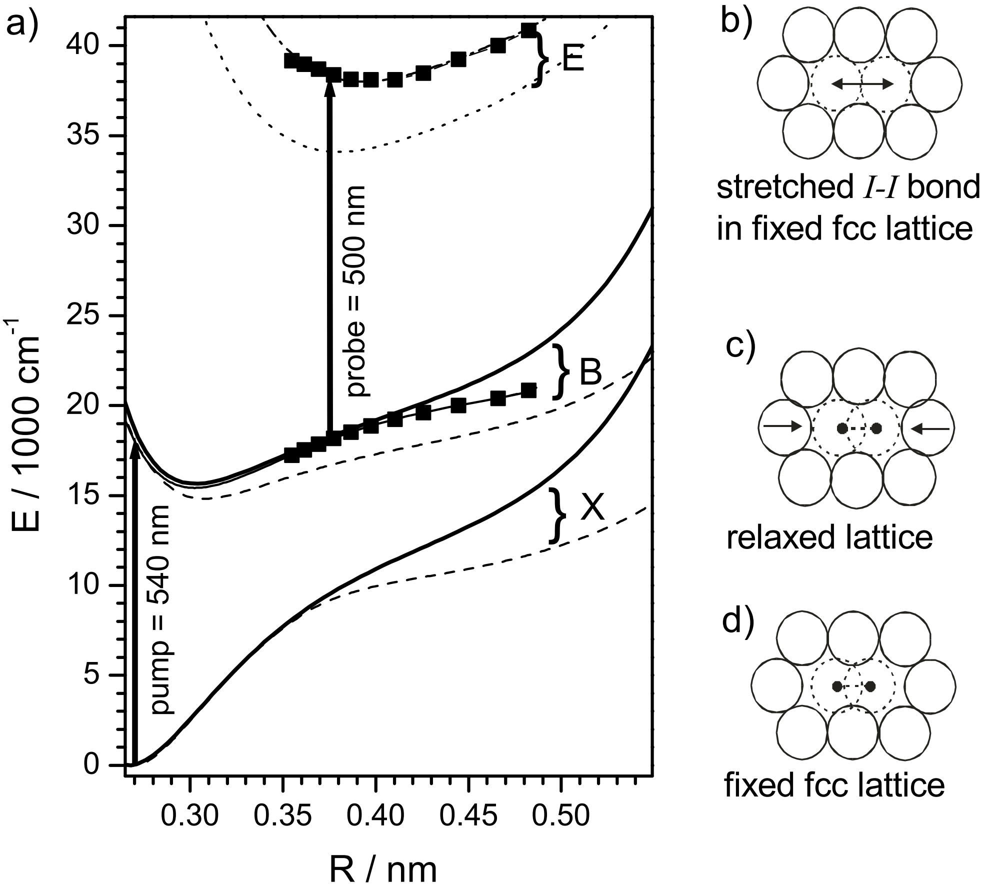

Figure 7.2: a) Potential energy diagram of I_2 in Kr including the ground state X, the valence B state and the ionic E state relevant for the pump-probe spectra. The arrows depict pump and probe transitions. The squares indicate the shape of the potentials as derived from the experiment. Dashed lines correspond to DIM calculations in the fixed Kr fcc lattice (see text and panels b and d) and solid lines to a relaxed cage geometry (see panel c). The dotted line reproduces the E state from ref. [204] for a fixed fcc lattice (see panel b) and the dash-dotted line includes a shift by 0.01 nm outwards and 3900 cm^{-1} up in energy. Panel d) shows I_2 in the ground state surrounded by a fixed fcc lattice. Note the space between I and Kr along the internuclear axis is responsible for the soft potential in this geometry. In panel c) the Kr atoms have relaxed around the molecule, bending the outer limb of the potential up. Fig. 1b shows the I_2 at a bond distance $R = 0.4$ nm typical for a probe transition. Here the fixed fcc lattice approximates a geometry relaxed around the extended $I - I$ bond.

State			I_2/Kr RKR	I_2/Kr DIM	I_2/Kr DIM
		I_2 gas phase[a]	dynamic lattice	relaxed lattice	fixed fcc lattice
		experiment	experiment	theory	theory
B	ω_e / cm^{-1}	125.69	125.9	125.9	116.5
	$\omega_e x_e$ / cm^{-1}	0.764	0.702	0.721	0.783
	T_e / cm^{-1}	15769	15420	15644	14816
E	T_e / cm^{-1}	41411	38000	-	34101[b]

[a] ref. [206], [b] ref. [204]

Table 7.1: Spectroscopic parameters T_e, ω_e and $\omega_e x_e$ for the gas phase, and for I_2 in Kr matrix. Note the RKR method measures a dynamic potential including the lattice response and the DIM calculation is for the relaxed lattice and the fixed fcc lattice, respectively. The parameters for the B-state DIM potential in the relaxed cage agree well with those for the RKR potential within the accuracy of a Morse-fit to the potential. The parameters describe the potential near the minimum and the dynamic potential deviates from the DIM-potential in the relaxed cage only at high energies (cf. Fig. 7.2).

the fitting function $\nu_f^2(E)$. Note that for the construction of the potential by the RKR method, rotational information is needed to find the absolute positions of the inner and outer turning points. In the matrix I_2 does not rotate. Instead, the gas phase Morse potential is kept as the repulsive inner wing of the B-state, since the matrix interaction near the inner turning point is expected to be minimal. Alternatively, one could adopt the inner wing of the calculated DIM potentials. This would shift the outer wing by less the 0.003 nm to larger elongations, which is negligible with respect to the quality of the potential. In essence, the outer wing was determined from $\nu(E)$ by numerical integration and the result is presented in Fig. 7.2 as a solid line with solid squares indicating where experimental points have been measured.

The effective potential incorporates some of the coupling to other modes of the multidimensional system. If classical trajectories are run on this potential, they reproduce the classical frequencies ν_{osc} collected in Fig. 7.1. The frequencies $\nu(E)$ and the derived RKR potential are obtained from the round-trip time T_1 immediately after excitation. The periods are measured for relaxing wave packets. Thus the potential is based on the initial condition of a wave packet prepared on the B-state with the surrounding Kr atoms thermally equilibrated at $T = 15$ K around an I_2 molecule in its ground state $-$ which is the typical situation in pump-probe spectroscopy. However, it should be a good approximation in different situations, as long as the solvent atoms are not too far from this thermal equilibrium. Such a potential is very helpful for quick and precise estimates of the dynamics and to develop an intuitive picture of the multidimensional problem. It also helps to design pump-probe experiments, because the potentials can be directly used to estimate the needed wavelengths and time-resolution.

To give an intuition of the one-dimensional representation of the multidimensional potential and to have a first comparison with experiment, the DIM potential surface for I_2 in Kr was calculated following refs. [63, 64] and including their correct diagonalization of the Hamiltonian matrix. The results are shown in Fig. 7.2a. The dashed lines correspond to calculations of the X and B states where the Kr atoms are kept fixed at the fcc lattice positions (Fig. 7.2d). This is the geometry for which potentials are shown in refs. [63, 64]. For the solid lines, the Kr atoms are relaxed around an I_2 molecule in the X state. In this geometry the two Kr atoms, that are in line with the I_2 axis, move closer to the I atoms (Fig. 7.2c). Stretching the molecular bond of I_2 against this solvent cage, with the Kr atoms fixed at this position, induces a steeper outer limb in the potential. Comparison of the DIM potentials with the experimental RKR potential shows that $-$ not surprisingly $-$ the relaxed cage geometry gives a better agreement. However, close to the dissociation limit the RKR potential is softer, since it includes the cage dynamics. In the course of the $I-I$ stretching motion, the Kr atoms are pushed out, which bends the outer limb of the potential towards the loose fcc cage. This phenomenon is expected to be accurately reproduced by the averaged DIM trajectory calculations, discussed below in chapter 7.3.1. Note that the repulsive interaction between I and Kr shifts the potential minimum of the B state up by 600 cm^{-1} upon cage relaxation (cf. also Fig. 2.6).

The spectroscopic constants that reflect the situation near the minimum are collected in Tab. 7.1. The calculations for a fixed fcc lattice (dashed lines in Fig. 2.6) yields significantly lower T_e and ω_e and an anharmonicity $\omega_e x_e$ closer to the gas-phase value. To get the correct values, the calculations have do be performed in a relaxed geometry (solid lines). These values agree well with the gas phase and the RKR result. At higher excitation, the anharmonicities change and the potentials differ for large R (cf. Fig. 7.2). These deviations would be described by higher orders of the anharmonicity. The DIM potentials in the fcc or relaxed configuration of the cage are calculated for fixed Kr atoms. The RKR potential includes the cage dynamics, which bends the potential down at large $R.$ The shape of the potential near the minimum is only weakly affected and Tab. 7.1 only compares the ”constants” near the minimum. In chapter 7.3.1 , the calculation of a ”trajectory averaged” potential will be proposed which will approximate the measured potential at large $R,$ as well.

A similar analysis for ClF/Ar in the excitation region relevant for this thesis cannot be accomplished. It will be interesting to apply the method again in the bound region of the B state of $ClF.$ These experiments are expected to be rather difficult due to the small Franck-Condon factors in this region; However, it will be interesting to compare the dynamics of the light ClF molecule in the bound region to the very detailed corresponding dynamics of $I_2.$

7.1.3 Construction of E state from pump-probe spectra

The vibrational frequency $\nu(E)$ of the B state was derived in section 7.1.2, without assumptions concerning the shape of the E state or the difference potential ΔV. Having constructed the B state potential $E_B(R)$ in the previous section by tuning the pump wavelength and optimizing the probe wavelength, the dependence of the pump-probe spectra on the probe wavelength can now be exploited in addition to construct the final E state energy surface $E_E(R)$.

To that end the optimal probe photon energy $h\nu_{probe}$ is identified, which records the wave packet just at the outer turning point R_{win}. For $\lambda_{pump} = 540$ nm the corresponding probe wavelength is 520 nm (cf. Fig. 6.3). The first criterion for probing at the turning point is the observation that the double splitting of the oscillation due to inward and outward motion just disappears. The second criterion is vanishing $\tau_m \approx 0,$ i.e. the shortest probe wavelength is chosen, for which the maximum of the envelope is close to time $t = 0$ (cf. Fig. 6.7). $h\nu_{probe}$ determined in this way corresponds to the difference potential, $h\nu_{probe} = \Delta V = E_E(R_{pump}) - E_B(R_{pump}),$ at the turning point R_{pump} in the Franck approximation [104]. Since the B state potential, $E_B(R),$ is known from the preceding chapter, the final state $E_E(R)$ can be obtained by adding $h\nu_{probe}$ to the B state energy in Fig. 7.2 at the position $R = R_{win} = R_{pump}.$ The experimentally determined points (squares) are compared to the surfaces given by Batista and Coker (dotted) [204]. Concerning the shape $E_E(R)$ of the ionic E state surface, the results obtained by Batista and Coker [204] in the fixed fcc cage (Fig. 7.2b) agree very well with the experimentally determined potential (squares), if the potential is shifted by 0.01 nm outward and 3900 cm^{-1} up in energy (dash-dotted line). Here the experiment probes the potential at $I-I$ elongations around 0.4 nm, which is the nearest neighbor distance in Kr (Fig. 7.2b). This renders the fixed fcc lattice, used in the calculations, a good approximation.

The minimum $T_e(E)$ of the ionic E state derived experimentally is compared to the gas phase and the result by Batista and Coker in Tab. 7.1. The large red shift of 3400 cm^{-1} with respect to the gas phase, derived experimentally, is typical for the solvation of ionic states (chapter 2.2.3). The calculation by Batista and Coker yields a red shift of 7300 cm^{-1}, which is more than twice as large.

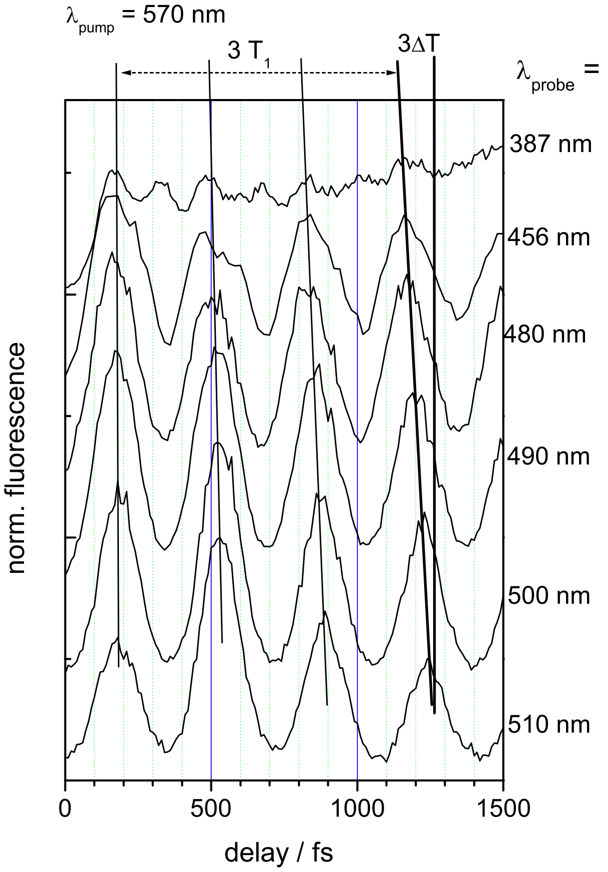

Figure 7.3: Pump-probe spectra with pump wavelength fixed at $\lambda_{pump} = 570$ nm to demonstrate the effect of the probe window. The lines indicate the decrease ΔT of the measured period T_1 with decreasing probe wavelength. After 3 periods the difference for $\lambda_{probe} = 510$ and 456 nm has accumulated to $3T_1 = 70$ fs.

This may originate from the fixed fcc Kr structure used in the calculation or from the empirical shifts introduced in the DIIS formalism.

7.2 Window effects in condensed-phase pump-probe spectra

At first glance, one would assume that it is only the pump pulse which determines the frequency of the oscillations observed in a pump-probe experiment, as it prepares certain vibrational levels. In this case, the differences Δt_1 or Δt_2 between the parallel lines, e.g. in Fig. 6.3, for inward or outward motion correspond to the correct round-trip time T_1. However, this is not the case, and a systematic deviation of T_1 or ν values is obtained in Fig. 7.1, if, for example, probe wavelengths of 480 nm (triangles) or 520 nm (squares) are used.

For a demonstration of this effect consider Fig. 7.3, which displays spectra with a fixed pump wavelength of 570 nm. With $\lambda_{probe} = 480$ nm the wave packet will be recorded just at the turning point (cf. Fig. 7.2). $\lambda_{probe} = 456$ nm already results in a considerable broadening of the peaks.

In order to form a wave packet, it is necessary to coherently excite a superposition of several vibrational levels according to the spectral width of the pump pulse wave packet $\Delta\nu$. Fig. 7.4 schematically shows the projection of the ground state population onto the B state, with a pump pulse of frequency ν_{pump} and bandwidth $\Delta\nu_{pump.}$ The bandwidth determines which part of the Gaussian wave function in the ground state is promoted to the excited state, leaving a hole in the ground state wave function after excitation. On the B state, this gives amplitude to the vibrational levels which lie within the bandwidth. A contour plot of the wave packet moving outwards is indicated. The difference potential ΔV to the E state at R_{win} likewise determines how the spectral bandwidth $\Delta\nu_{probe}$ is transformed to the spacial width of the probe window ΔR_{win}. This in turn defines which vibrational levels are

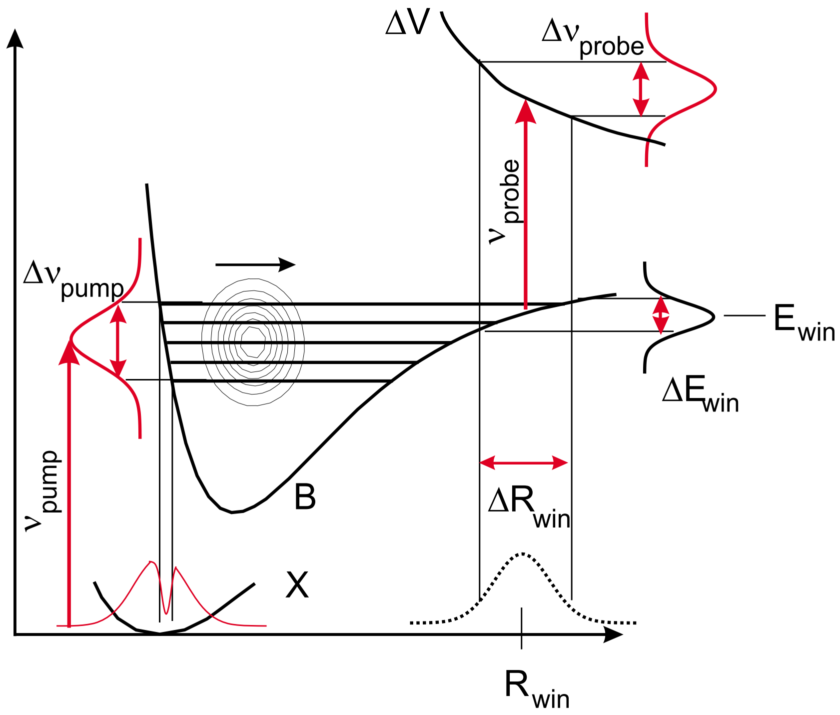

Figure 7.4: Potential diagram showing the ground state X, the excited state B, and the difference potential ΔV to the final state E. The spectral shape of the pump pulse with mean frequency ν_{pump} and bandwidth $\Delta\nu_{pump}$ determines, which vibrational states of the B state are populated. The projection onto the repulsive limb of the B state yields the hole burned into the ground state population. Likewise, the projection of the probe pulse onto the difference potential ΔV yields the probe window R_{win}. The outer limb of the B state then determines which vibrational levels are probed, i.e. the energy of the probe window E_{win} and the probed bandwidth ΔE_{win}.

probed within ΔE_{win}. In the example shown in Fig. 7.4, only the upper two of the excited vibrational levels are probed. The anharmonicity yields a longer apparent vibrational period T_1 compared to the center of the wave packet.

If the probe wavelength λ_{probe} is reduced, the probe window moves spatially inward and to a lower energy E_{win}. Thus the less energetic parts of the wave packet, which have a shorter period according to the anharmonicity, gain in weight and the measured period T_1 is reduced. This effect can be clearly seen in the experimental spectra shown in Fig. 7.3. Although the spatial shift is not large enough to yield a resolved splitting, the differences between the maxima indicate a smaller T_1. In essence, the part of the wave packet at E_{win} gains the highest detection efficiency (chapter 2.3.1). This is the wave packet for which the probe window is at the turning point.

Since the effect accumulates, three periods are displayed in Fig. 7.3 to make it clearly visible. The time difference $3T_1$ for $\lambda_{probe} = 456$ nm corresponds to 990 fs and to 1060 fs for $\lambda_{probe} = 510$ nm. This results in a variation of T_1 from 353 fs for probing above the turning point with 510 nm to 330 fs for probing too deep with 456 nm. This error of $\Delta T_1/T_1 = 0.07$ fully explains the systematic difference between the results with probe wavelength fixed at $\lambda_{probe} = 480$ or 520 nm in Fig. 7.1. A correct determination of T_1 requires a tuning of λ_{probe} just to the turning point for each λ_{pump}. The error in the round-trip times T_1 on the order of 7 % is serious, because the anharmonicity is the derivative $d\nu/dE$ of the $\nu(E)$ curve in Fig. 7.1. The slope of $\nu(E)$ differs by more than 50% for the solid circles and the triangles at low energies. The correct T_1 values given by the circles in Fig. 7.1 were derived by an optimization of λ_{probe} for each value of E_{pump}.

It is instructive to complement this explanation with arguments from the classical MD simulations [26]. If the trajectory travels high above the window, it moves with more kinetic energy and larger velocity through the window. It spends less time in the window, diminishing the detection efficiency. Thus the low energy trajectories with too short periods T_1 dominate the experimental spectrum. If the average energy of the trajectories lies below the window, only the fraction with high energy reaches the probe window, and the apparent T_1 is too long. These classical arguments are in full accord with a quantum mechanical Franck-Condon picture.

Changes of the observed oscillational period with probe wavelength have already been observed in trajectory simulations [27]. There they have been used to estimate the probe window position, since it could not be deduced from the systematic variation of the probe wavelength in the experiments. The position of the probe window has a dramatic influence on the decay of the envelope of the pump-probe spectra in these simulations [27] and thus also on the predissociation time deduced from the simulations. The experimental approach just discussed has the advantage to separate the processes of vibrational energy relaxation and predissociation. This was applied recently to determine predissociation rates and to clarify the interplay of vibrational relaxation and predissociation rates [115, 116]. Thus, tuning both pump and probe wavelength proves to be helpful even when a high level simulation is at hand, i.e. to judge, if systematic errors are introduced by the simulation of the probe process.

In the gas phase, where oscillations in the B state of I_2 can be observed for hundreds of ps, the Fourier transformation yields clearly resolved vibrational levels that are pumped and probed. The spectrum of the probe pulse then changes the intensity of the individual vibrational lines in the observed Fourier transform.

7.3 Wave packet dynamics with strong fragment-cage interaction

7.3.1 Construction of an $I-I$ trajectory from pump-probe spectra

The spectra in Fig. 6.2a show that the time spent between the first outward (→) and inward passage (←) for the fixed probe window ($\lambda_{probe} = 500$ nm, $R_{win} = 0.376$ nm) increases dramatically from 120 fs, for $\lambda_{pump} = 540$ nm, up to 350 fs for $\lambda_{pump} = 490$ nm, whereas that for the second outward/inward passage stays essentially constant at 120 fs. The energy corresponding to $\lambda_{pump} = 500$ nm is close to the gas phase dissociation limit. Obviously, the interaction of an essentially free I atom ($\lambda_{pump} = 490$ nm) with the cage atoms around the outer turning point takes a much longer time than for a bound one ($\lambda_{pump} = 540$ nm). The collision of the free I atom with the Kr cage is connected with such a high energy loss that the bond cannot be stretched as far in the second round-trip. Snapshots of this interaction are recorded now in Fig. 6.2b) by scanning the probe wavelength from $\lambda_{probe} = 540$ nm to 480 nm and therefore the probe position R_{win} from 0.36 nm to 0.45 nm for an excitation at the dissociation limit ($\lambda_{pump} = 500$ nm). The probe window positions R_{win} for the respective wavelengths are plotted as a function of time (open circles in Fig. 7.5a, given by the maxima in the pump-probe spectra of Fig. 6.2b). The positions are connected by a smoothed line to yield the time course $R(t)$ of a mean trajectory (solid line in Fig. 7.5a) for the first three excursions I to III. The circles for the inner turning point near 0.27 nm are estimated from the potential together with the energy loss derived in Fig. 7.11. The wave packet reaches out to 0.43 nm only in the first excursion, and already in the second one it does not go beyond 0.39 nm. The most interesting first excursion is asymmetric. The outward motion is still rather sinusoidal, and from the window at 0.36 nm to the turning point it takes about 100 fs. The return is extremely delayed, and especially around 300 fs the wave packet is not accelerated on the way back to the potential minimum as expected, but it is further slowed down. The return from the turning point to the 0.36 nm window takes more than 250 fs.

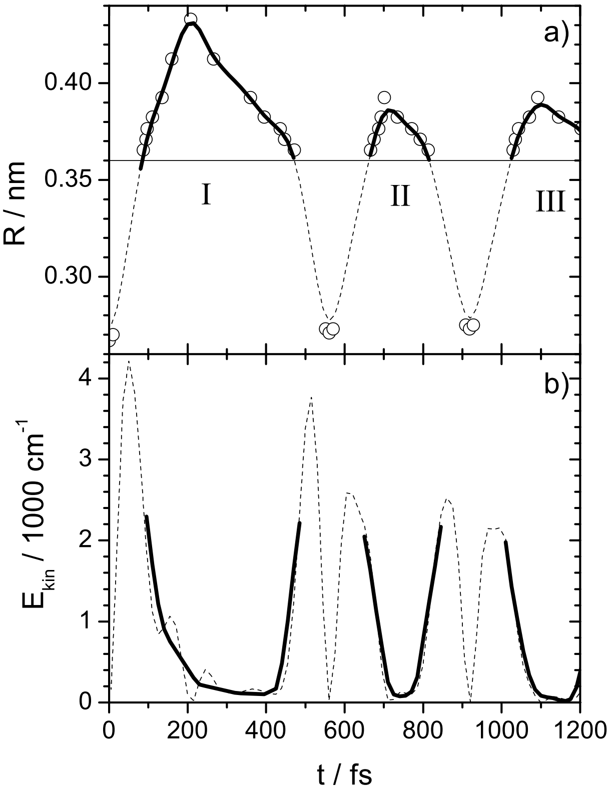

Figure 7.5: a) Trajectory $R(t)$ (solid line) showing $I - I$ separation R versus time t as derived from the maxima in the pump probe spectra for $\lambda_{pump} =$ 500 nm. (Fig. 6.2b). Only the outer bow between 0.36 nm and 0.43 nm is covered by probe windows and I - III indicate the first three excursions. The kinetic energy $E_{kin}(t)$ is obtained from differentiation (weak dashed line) and smoothing (thick dashed line)

Differentiation of $R(t)$ versus time yields the local velocity $v(t)$, presented as kinetic energy $E_{kin}(t) = \frac{1}{2}\mu v^2(t)$ as the dashed line in Fig. 7.5b), where μ is the reduced mass of I_2. The mild undulations may be artifacts due to the differentiation and the kinetic energy only relies on the measured data points in the region of the thick smoothed line. Around the inner turning points, it depends on the interpolation and should be close to a free oscillator. The maximal kinetic energy is consistent with the excitation 4230 cm^{-1} above the minimum of the B state. The snapshots of the oscillation were taken on the relevant outer limb of the potential and the corresponding kinetic energy $E_{kin}(t)$ is emphasized by the thick solid line. It shows a deceleration on the way to the outer turning point as expected for a Morse potential, but the acceleration on the way back is completely different. The trajectory moves extremely slowly for a long time, between 200 and 400 fs with only $E_{kin} \approx 200$ cm^{-1}. On a Morse potential it should have already 2000 cm^{-1} at 300 fs. It seems as if the I atoms stick to the cage wall and move back very slowly together with the cage. This peculiar behavior is demonstrated in Fig. 7.6a on the outer limb of the potential surface of the B state. The energy loss derived from the trajectory is supported by the analysis of the vibrational relaxation rates in chapter 7.4.2. A wave packet excited with $\lambda_{pump} = 520$ nm travels out and returns with an energy loss of 455 cm^{-1}. A wave packet pumped with 500 nm lies significantly higher in energy and reaches much farther out on the soft wing of the potential, then it sticks to the potential energy surface and does not gain kinetic energy. It slides down along the potential surface far below the energy of the 520 nm wave packet until it finally gains kinetic energy.

Comparison to classical trajectory calculations

The dynamics at the dissociation limit (Fig. 7.5) determined for $\lambda_{pump} = 500$ nm can be qualitatively compared to the classical calculation ($\lambda_{pump} = 510$ nm) in ref. [27]. The simulations create a swarm of trajectories. Unfortunately only an ”anecdotal” trajectory is presented [27] instead of an

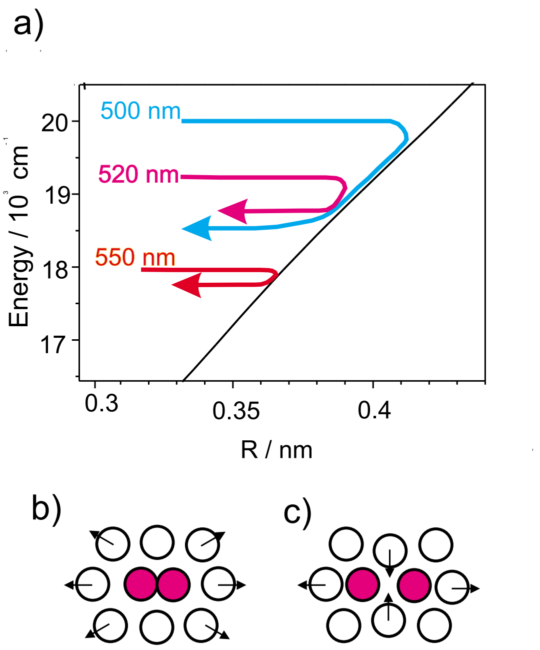

Figure 7.6: a) Sketch of potential and kinetic energy showing the peculiar dynamics of the I_2 molecule for strong fragment cage interaction. In the first collision a wave packet started near the dissociation limit ($\lambda_{pump} = 500$ nm) is scattered below a wave packet that was started at lower energy (i.e. $\lambda_{pump} = 520$ nm). During the interaction the kinetic energy is very small (Fig. 7.5). The energy after the collision is given by the energy relaxation rate (Fig. 7.11). b) Two cage modes according to [37] illustrate the intuitive breathing of the cage and the belt mode that slows down the I fragments in the recombination event (see text).

averaged trajectory with a distribution. In any case, the simulations catch the very strong fragment-cage interaction that allows only one large excursion beyond $R = 0.4$ nm. Similar to the averaged potential discussed above, a comparison of an averaged trajectory with the present experimentally derived trajectory could improve the value of the comparisons and would yield a deeper analysis.

The explanation for the apparent sticking of the I atom to the cage is most evident from a simulation of Cl_2 in Ar near the dissociation limit [37]. Recall from chapter 2.2.1 that Cl_2 in Ar is isolated on double substitutional sites, just like I_2 in Kr. Three modes of deformation are excited with large amplitudes. An expansion of the cage along the $Cl - Cl$ axis excites two modes. The cage breathing, displayed in Fig. 7.6b), is intuitively expected. The second mode (c) contracts a belt of 4 matrix atoms, which lie in a plane perpendicular to and in the center of the $Cl - Cl$ bond. The expansion of the $Cl - Cl$ bond displaces matrix atoms along the bond direction and creates space just around the center of the bond. The atoms in the belt can move inwards and thus compensate the volume change from the $Cl - Cl$ expansion. This picture is valid also for the I_2 in Kr case [29] in accord with the discussion in ref. [37] and with essential features of the simulations on the A state of I_2 in Ar matrix [21]. Now, when the I atoms are stopped at the turning point and try to return, they first have to displace the matrix atoms in the tightened belt, which delays a recombination. The acceleration of these belt atoms takes out kinetic energy from the $I - I$ coordinate. This reduces the I velocity as seen in the sliding down on the potential surface in Fig 7.6a and explains the extremely large energy loss. The usual Morse-like rise in kinetic energy appears only after the belt atoms have been expelled around 400 fs in Fig. 7.5. The experimental trajectory in Fig. 7.5 directly displays this peculiar process.

Comparison to DIM-trajectory calculations

In trajectory calculations using DIM potentials (diatomics in molecules) [108], the potential felt by the I_2 including all Kr atoms is derived (eigenvalues of the Hamiltonian) at each time step for each trajectory.

Fig. 7.7a shows the potential surfaces for the system I_2/Ar as a function of time, as they are usually plotted in publications that report DIM trajectory calculations by Batista and Coker [64]. The data were kindly provided by N. Yu from the group of Coker. Only a selection of 7 states from the 36 valence states is shown. Unfortunately, similar trajectories for Kr are missing and also data for

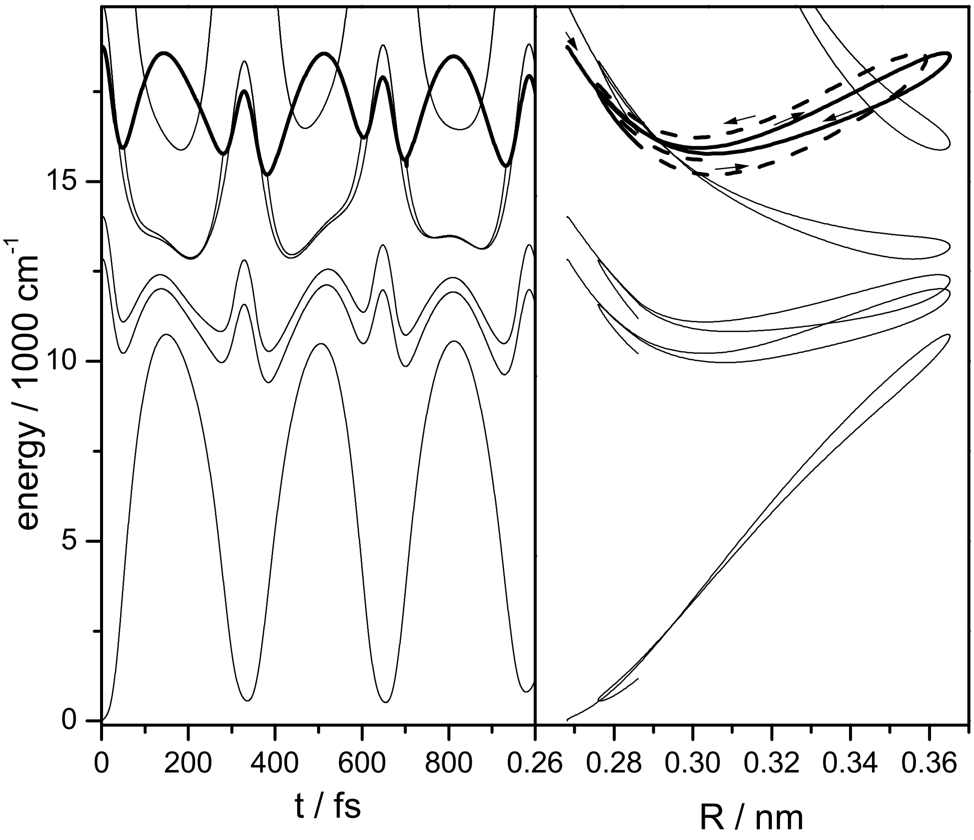

Figure 7.7: a) Potential surfaces of I_2/Ar valence states from a DIM-trajectory as a function of time (data provided by Ning Yu from the group of Coker). The thick line indicates the B state, which is occupied in this trajectory. b) Same trajectory for the first round-trip (up to 350 fs) as a function of R. The potential is higher for the outward motion, than for the return, since the Kr atoms are pushed to the side. The thick solid line indicates the first and the thick dashed line the second round-trip in the B state.

the ionic states are not available. In Fig. 7.7b the same surfaces are plotted as a function of the bond distance R for the first round-trip ($t = 0$ to 360 fs). For the B state, which is populated in this trajectory, two periods (till $t = 700$ fs) are plotted. The first round-trip is depicted by the thick solid line and the second round-trip by the dashed line. Some qualitative results can already be picked out from this simple approach. The trajectory starts at $R = 0,266$ nm and moves outwards, collides with the Ar atoms, loses energy and travels back at a lower energy. For this reason the inner turning point now is at $R = 0,275$ nm. The trajectory moves back out at even lower energy and at the outer turning point a collision with a hot Ar atom transfers energy back into the $I - I$ coordinate.

The plot represents the collision events of a single trajectory. The pump pulse in the experiment prepares a coherent wave packet with a quantum mechanical uncertainty in phase space. Therefore, an ensemble average over many trajectories is required. The mean value of the potential for these trajectories corresponds to an average 1-D potential seen by a wave packet ”on the fly” and it should be compared to the surface (Fig. 7.2a) constructed from the experiment. However, such ”trajectory averaged” potentials are not available, even though it is a much better approximation than any potential calculated for a fixed lattice. The outward and inward motions are not symmetrical due to the energy loss from the $I - I$ coordinate. In the DIM trajectory calculation, one could even get rid of this problem by constructing two potentials - one for outward and one for inward motion.

Up to now, only simulated signals for special pump-probe combinations have been compared to experiment, and sometimes errors in the simulation compensate each other. One example for such an error compensation can be found in the earliest simulations [64]. It explains the entire pump-probe signal with $\lambda_{probe} = 400$ nm by probe transitions from the A state, and very good agreement is obtained. From the experiment it is obvious, however, that the signal originates from probing B and this is proved by the experimental determination of the time zero, which was not known at the time of the simulations. The error has now been corrected [66], resulting now in a much weaker nonadiabatic coupling of the B state to the predissociating states.

The potential constructed entirely from the experiment (Fig. 7.2a) may advance the understanding of the ultrafast manybody dynamics, since a detailed theoretical modeling of the probe process to the ionic surfaces is circumvented and the simulations are compared to the experiment at an earlier stage. It imposes a test onto the simulation in a systematic way. The computation of the ionic surfaces is very tedious work and therefore it is only accomplished rarely in trajectory simulations. In the theoretical support for the ClF experiments this task is still out of reach.

7.3.2 Recombination dynamics of ClF in Ar

The pump-probe spectra for ClF in Ar are not as well modulated as the I_2/Kr spectra. Nevertheless, the oscillations due to wave packet motion can be used to determine the ultrafast dissipative dynamics. The early wave packet motion after excitation with $\lambda_{pump} = 387$ nm above the dissociation limit can best be displayed for a probe window near this limit, i.e. at $\lambda_{probe} = 319$ nm. The recombination dynamics can be seen and the population that relaxes further down in the potential well is not probed and thus does not contribute to an unwanted background signal. The first 3 ps of the spectrum are shown on an enlarged scale in Fig. 7.8b. The following interpretation of the spectrum is analogous to the I_2 system discussed in the preceding chapter.

The first strong maximum after 50 fs catches the wave packet when it moves outwards (→) through the probe window for the first time. The minimum around 250 fs corresponds to the time when it is beyond the probe window. There it smashes into the cage and loses most of its energy, which forces the wave packet to travel back. Thus the shoulder after 500 fs displays the wave packet, when it passes the probe window for a second time on the inward motion (←). Next, it reaches the inner turning point and subsequently passes the probe window a third time, about 850 fs after the first peak. Due to the strong collision in the first excursion it has already lost most of its kinetic energy. The

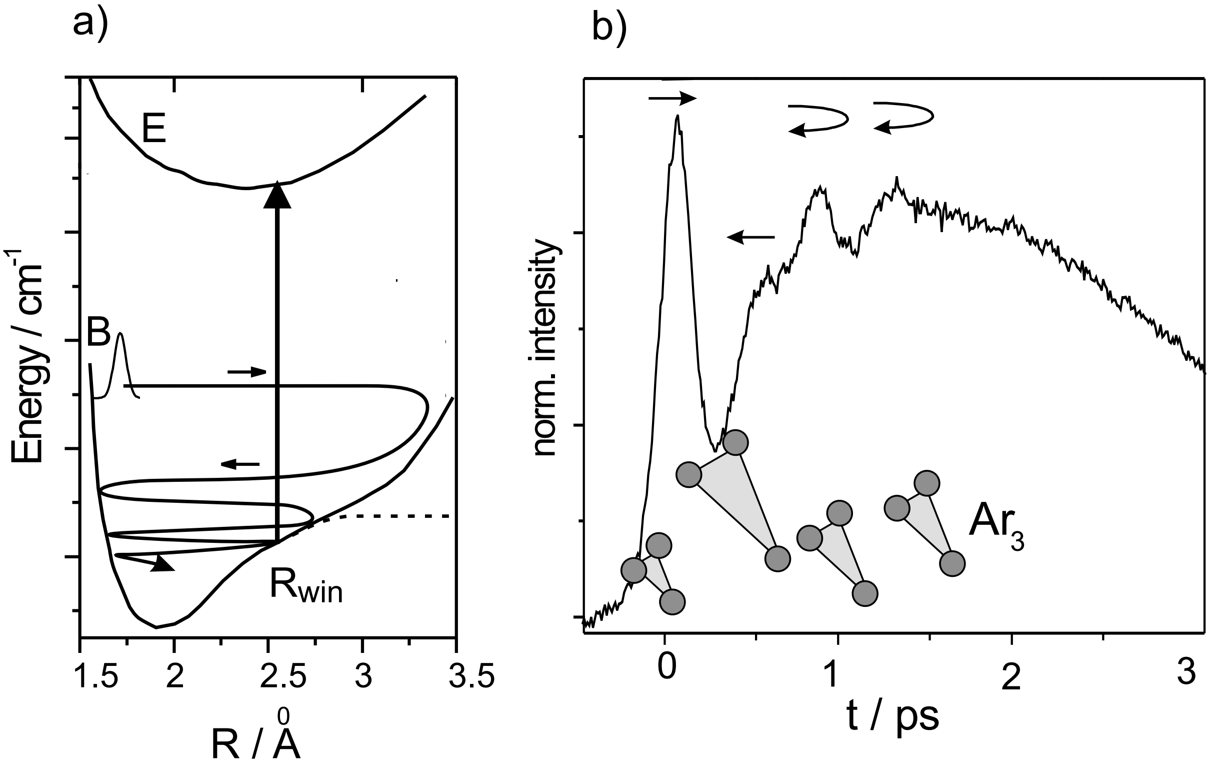

Figure 7.8: a) Scheme of the wave packet dynamics observed in the pump-probe spectrum (panel b) with the probe window at R_{win}. The wave packet is excited (vertical arrow) above the gas phase dissociation limit (dashed) and loses energy in the B state due to interaction with the cage. b) fs-pump-probe spectrum with $\lambda_{pump} = 387$ nm and $\lambda_{probe} = 319$ nm. The arrows above the peaks indicate, how the wave packet passes through the window. The Ar_3 breathing mode is sketched below (see text).

turning point and the probe window in the third passage lie closer together, and the wave packet is only probed once on its outward and inward motion. Finally, after 1250 fs it shows up once more at the turning point. Thus three periods are resolved (cf. Fig. 7.8), and the first one is doubled due to a separated detection of outward and inward motion. The dynamics are sketched in the left panel of Fig. 7.8 in analogy to the trajectory derived for $I_{2,}$ and consistently with the peaks in the fs-pump-probe spectrum and the relaxation time analysis (chapter 7.4.3). The wave packet rides on a background increasing with time, because of dispersion [32], caused by the anharmonicity and because the first strong collision induces decoherence [211]. The latter forces the wave packet dynamics to enter the regime of population relaxation. The main conclusion of the dramatic energy loss in the first collision is substantiated by the analysis of vibrational relaxation in chapter 7.4.3 and supported by DIM-trajectory simulations [71].

From the second to the third period, a round-trip time of about 400 fs is derived, as expected according to the simulation of an F_2 molecule oscillating in the cage structure discussed below. The difference of 350 fs between the shoulder and the second maximum is shorter, because it does not correspond to a full round-trip. The time of 450 fs, spent on the outer bow from the first peak to the shoulder is remarkably long, similar to the corresponding dynamics of I_2/Kr (chapter 7.3.1). These experiments show that the velocities are especially slowed down just after the collision due to the details of the deformation of the cage and the energy losses involved in it. The question deserves some consideration, whether the recombination dynamics of the heavy $I - I$ molecule in the lighter Kr surrounding is comparable to the recombination dynamics of the asymmetric ClF molecule in

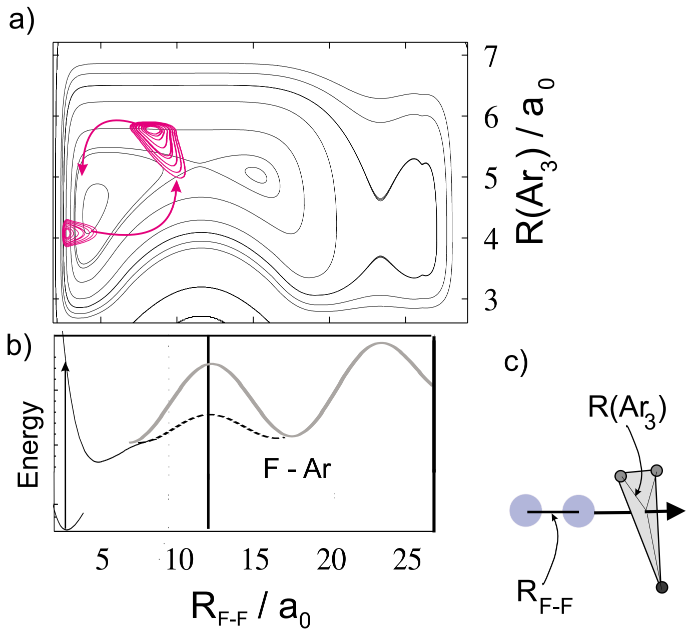

Figure 7.9: a) 2-D potential energy surface of F_2/Ar calculated by G. Chaban [73]. The horizontal axis is the $F-F$ distance and the vertical coordinate is the breathing of the Ar_3 triangle. The geometry is fixed with the $F-F$ coordinate perpendicular to the triangles. b) 1-D representation of the potential surface. The first barrier is greatly suppressed (dashed) when the Ar_3 window is expanded. c) Geometry that defines the F_2 bond distance R_{F-F} and $R(Ar_3)$ as the distance of one Ar to the center of mass of the three Ar.

Ar, where the F fragment has only half of the mass of an Ar atom. The I fragments are heavier than Kr and undergo head-on collisions with one Kr atom and the belt of four Kr atoms moves inward. In contrast, the dissociation of ClF leads to a symmetric collision of the Cl and the F atom each with a triangle of Ar atoms (Fig. 2.5c). A plausible consideration is to take all atoms as hard spheres with van-der-Waals radii, which yields kinetic energy losses of 54 % and 67 % for Cl and F respectively. The deformation will enhance the losses.

A characteristic feature of the spectra in Fig. 7.8b) is the first sharp maximum and a minimum around 250 fs. Both signatures are emphasized near the threshold of $\lambda_{probe} = 320$ nm for the probe resonance and attenuate at shorter probe wavelengths (cf. Fig. 6.9)[1]. The analog phenomenon shows up also in the I_2/Kr spectra (Appendix, e.g. $\lambda_{pump} = 500$, $\lambda_{probe} = 540$ nm) when the probe wavelength is just at the threshold. In the minimum energy configuration of F_2 in Ar at 5 K the molecule is located in a single substitutional site with each F atom pointing at a symmetric triangle of Ar atoms [68] and a similar geometry is likely for ClF (Fig. 2.5c). The collision of the F atom with the triangle leads to cage expansion and breathing. The ionic E state is significantly red shifted in the matrix by solvation of the dipole [205]. The solvation is reduced on expansion of the Ar cage and the E state moves up in energy. The probe wavelength of 319 nm is just at the threshold for reaching the E state (Fig. 7.8a) and the probe window will be lost in the expanded cage. Cage expansion starts with the first collision occurring just after the first maximum in Fig. 7.8b. The sensitivity decreases during the expansion leading to the reduced intensity of the subsequent shoulder. Full sensitivity will be reached again after a period of the Ar breathing mode which appears in Fig. 7.8b around the second maximum and after 800 fs delay. Such a period of the Ar breathing mode is in good accordance with simulations and experiments for doped Ar matrices [212–215].

Support from theory

The interplay of the dissociation of the diatomic with the cage breathing is investigated in a 2-D wave packet simulation on the symmetric F_2 molecule in the fcc argon lattice [72, 73]. One coordinate is the $F-F$ stretch and the other coordinate is the breathing mode of the Ar_3 triangles, at which the F atoms are pointing. All other Ar atoms are frozen and enforce a cage potential. The potential energy surface is shown in Fig. 7.9. The barrier due to the nearest Ar triangle is located at an $F-F$

---

[1] From 291 nm on the peak increases again due to excitation of Cl_2.

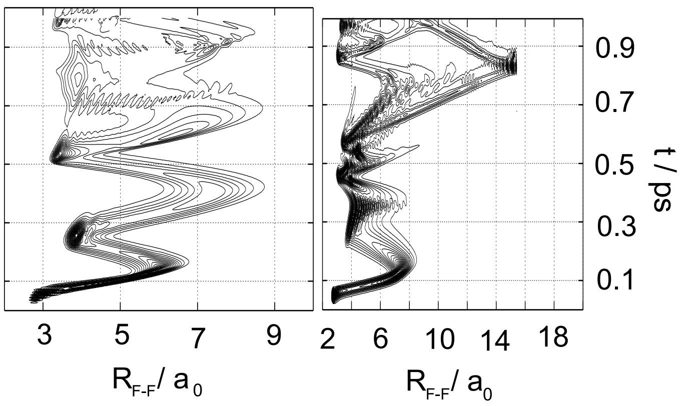

Figure 7.10: Projections of the 2-D wave packets of F_2/Ar onto the $F-F$ coordinate as a function of time, kindly provided by M. Korolkov. Panel a) demonstrates the spreading of the wave packet due to dispersion for the initial condition of a cold window. Panel b) presents the same dynamics for a pre-excited Ar_3 window, leading to partial cage exit of the wave packet at 700 fs.

separation of 11.5 a_0 and the second triangle at 22.9 a_0 and both barriers are saddle points in the 2-D surface (Bohr radius $a_0 = 0.0529$ nm).

The pump pulse prepares the 2-D wave packet on this excited state surface at $R_{FF} = 2.66\ a_0$ and $R_{ArAr} = 4.14\ a_o$ in the well localized ground state configuration. The wave packet moves according to the gradient of the potential surface. It was demonstrated in ref. [72] that the wave packet follows the principle of relief reflection, i.e. the wave packet is reflected by the 2-D walls of the potential (Fig. 7.9a).

Fig. 7.10a shows the projection of the 2-D wave packet onto the $F-F$ coordinate as a function of time for the initial condition of an unexcited Ar_3 window. The originally well localized packet smears out quickly within 1ps. The wave packet is dispersed on the anharmonic potential and the higher dimensionality amplifies the dispersion. In addition, the wave packet will be dephased due to the random encounters with the solvent, which is not considered in the simulation. This explains why oscillations in the pump probe spectra with such pump energies are not observed for longer times. The period in this calculation (~ 250 fs) is significantly shorter than the one derived in the experiment. This is a consequence of the smaller reduced mass of the F_2 compared to ClF, the higher excitation energy used in the simulation and the fact that dissipation to other modes of the Ar lattice is neglected. Fig. 7.10b demonstrates the enhancement of cage exit ($R > 11.5$ a$_0$) for a pre-excitation of the Ar_3 window into its 6th vibrational level. At 700 fs, the additional cage breathing allows part of the wave packet to exit the original cage, which ends at 11.5 a$_0$ on the $F-F$ axis.

There are several drawbacks in this simulation, some of which are discussed in the original work [72, 73]. In addition the P-orbital alignment [68] is not properly taken into account, because of the fixed symmetry in this simulation. As detailed at the end of chapter 5.4.1, the minimum for an aligned orbital is in the center between two and not three nearest neighbor atoms, as assumed in the simulations. Moreover, energy dissipation and coupling to other electronic surfaces is not included and - as will be discussed in chapter 7.5 - the angular reorientation of the fragment is neglected. Nonetheless, the simulations give a good estimate of how the anharmonicity disperses the wave packet and the lower barrier for cage exit when the Ar mode is excited.

7.3.3 Recombination dynamics of Cl_2 in Ar

For Cl_2 the 387 nm pump pulse excites a wave packet with a large excess energy of 8270 cm^{-1}, comparable to the case of ClF in the previous chapter. The expected rapid energy loss is evident from the spectrum at $\lambda_{probe} = 286$ nm (Fig. 6.16), which is the longest probe wavelength, just at the threshold for the $B \rightarrow E$ transition. Here only the first two peaks from the first oscillation period are observed and the spectrum rapidly decays after 1 ps. In the spirit of the discussion in chapters 7.4.1 and 6.2, this indicates that after 1 ps the wave packet has relaxed to the probe window, i.e. it has lost 7000 cm^{-1}. The systematics of this evaluation is given in chapter 7.4.3. The only published

MD simulation [37] on Cl_2 in Ar reports excitation just at the dissociation limit. The first period is 550 fs, which is much faster than the 800 fs seen in the experiment. However, the excitation energy in the experiment is 0.7 eV higher and the deformation of the cage is expected to be larger. The double substitutional site again implies head-on collisions of Cl with Ar. Since the mass of both particles is nearly identical, a complete energy transfer to the Ar atom is expected for a head on collision from classical mechanics. The simulations predicted the generation of shock waves. The dynamics of the belt and breathing modes were already discussed in the context of I_2/Kr (chapter 7.3.1). In the present case the energy transfer to the matrix is even more efficient and coupling of energy back into the Cl_2 mode probably has a significant effect on the dynamics. It would be very helpful to perform MD simulations in the right excitation regime to assign the peaks with certainty. By analogy, the 800 fs period should correspond to the motion in the Cl_2 coordinate and not to the cage breathing, as the signal displays the expected rise of the envelope due to vibrational relaxation. However, the strong modulation in the 286 nm spectrum with the dip at 300 fs probably originates from the cage breathing, as this probe wavelength is just at the threshold.

7.4 Vibrational relaxation kinetics of $I_{2,}$ ClF and Cl_2 in rare gases

7.4.1 Signatures of vibrational relaxation

One unequivocal feature of condensed phase dynamics is dissipation of energy to the bath, which leads to vibrational relaxation of the excited molecule. This process can be displayed by femtosecond pump-probe spectroscopy in several ways. If wave packet oscillations are well resolved and the potential is anharmonic, then the vibrational period is indicative of the mean energy of the wave packet *(method α)*. Thus the relaxation can be monitored by recording the increase of vibrational frequency, while the wave packet is relaxing in the potential well.

A second signature, which is suited also for pump-probe signals in which no oscillations are observed, is the envelope of the pump-probe spectrum *(method β)*. The maximum of the envelope indicates the time, when the vibrational population is relaxed from the initial energy E_{pump} to the energy of the probe window E_{probe}. This is obvious from the classical expression $S \sim 1/v(R_{win})$, which states that the observed signal intensity S is inversely proportional to the velocity v of the wave packet at the probe window R_{win} [27, 45]. The classical expression diverges at the turning point. Similar to the discussion in chapter 2.3.1, this classical expression has its quantum mechanical counterpart in the Franck-Condon overlap of the stationary vibrational wave functions, which remain finite, but are maximal at the turning point. The high probability (large $|\psi(R,t)|^2$) of finding the particle near the turning point in a potential reflects the slow classical motion of a particle in this potential. If the probe window is at the turning point of the wave packet, the packet has zero velocity when it is probed. This corresponds to the antinodes of the vibrational wave functions. Since the wave packet has to continue on the final electronic state with zero velocity, the vertical transition also terminates in an antinode of the final state vibrational wave functions, yielding a large overlap (cf. chapter 5.2.3).

If the wave packet is started at $E_{pump} >\acute{}E_{win}$, i.e. above the energy of the probe window (Fig. 2.9), the signal is small initially, because it passes with high velocity v through the window. Vibrational relaxation populates lower levels and the velocity at the window becomes smaller. At the delay time $t = \tau_m$, when the average energy of the wave packet has arrived in the probe window at E_{win}, it is probed at its turning point with zero velocity, and the maximum in the pump-probe signal is observed. The population relaxes further down in the well and the signal decreases, as the wave packet does not reach the probe window anymore [45].

The envelope of the pump-probe spectrum (method β) pictures vibrational population relaxation. It is not sensitive to the coherence of the levels and independent of the question, whether the wave packet is dispersed, destroyed by collisions, or simply not resolved due to experimental limitations. The disadvantage of method β is that additional information is needed if the excited electronic state is coupled to another state. Then the decay of the signal is a convolution of the population losses to the other state and the vibrational population relaxation. Both methods are compared in chapter 7.4.3 for the example I_2 in Kr and applied to the case of ClF in Ar.

7.4.2 Vibrational relaxation in B state of I_2/Kr from oscillations (method α)

A careful inspection of successive periods in a pump-probe spectrum shows that the period length T_n decreases systematically from the first to the n^{th} oscillation.. For example the pump wavelength $\lambda_{pump} = 520$ nm in Fig. 6.2a yields the successive periods $T_1 = 460$ fs, $T_2 = 410$ fs, $T_2 = 390$ fs, $T_2 = 380$ fs and $T_5 = 370$ fs. The analysis for different pump wavelengths can be found in refs. [32, 144]. A wave packet prepared high up in the B state with a long T_1 falls down in energy by vibrational relaxation. In the time course of relaxation, it passes regions in the B state with increasingly shorter T_n due to the anharmonicity displayed in Fig. 7.1. Thus the change of T_n with delay time can be directly traced to a change of energy E of the wave packet with delay time. For high excitation energies the change in T_n is large enough to read it from the maxima of successive periods in the pump-probe spectrum. For lower excitation, the vibrational relaxation rate decreases (cf. Fig. 7.11) and several periods have to be averaged to obtain high accuracy. The method of a windowed Fourier transformation, introduced by us in ref. [32] to obtain the relaxation rates at low energies, yields the same results. More details are presented in my diploma thesis [144].

The measured rates $k_{rel} = dE/dt$ in cm^{-1} per ps and per period are displayed in Fig. 7.11 (left hand scale). The data set covers a broad range of energies in the B state. A nearly exponential increase is observed, from very low rates with dissipation of only a fraction of a vibrational quantum per period deep in the well ($\lambda_{pump} = 580$ nm) over energy losses of about one quantum per period at $\lambda_{pump} = 540$ nm and to losses of more than 10 quanta per period at and above the gas phase dissociation limit ($\lambda_{pump} = 500$ nm). The smooth change over three orders of magnitude hides that something exceptional happens in the region of the dissociation limit. Fig. 7.11 displays the energy E_1 (dashed line, energy scale to the right) after the first round-trip versus the initial excitation energy E_{pump}. The rise of E_1 with E_{pump} is sublinear, which reflects that the losses per round-trip increase with E_{pump}. Around the dissociation limit, the smooth rise is interrupted, and E_1 falls with E_{pump}. Thus a wave packet that started with a lower energy E_{pump} returns with a larger energy E_1 than a packet that started with initially higher energy. This is not compatible with simple energy and momentum conservation in an elastic scattering event with a cage atom. It indicates that the tremendous losses above the dissociation limit of up to 30 vibrational energies in the first collision are also connected with severe distortions of the cage. These losses are in full accord with the trajectories in chapter 7.3.1.

This evaluation demonstrates that detailed information on potentials and dynamics of a condensed phase system with strong relaxation may be obtained directly from femtosecond pump-probe spectra via method α. The required accuracy for measuring the round-trip time changes considerably with the energy in the B state. Near the bottom of the potential, i.e. for $\lambda_{pump} = 580$ nm, the round-trip time changes by only 4 fs between successive vibrational levels due to the small anharmonicity. In addition it takes about 5 periods to dissipate the energy of one vibrational quantum due to the low relaxation rate. Thus a variation of 4 fs distributed over 5 round-trips has to be resolved and this limits the applicability of the method in this range. However for the interesting case of strong fragment-cage interaction around $\lambda_{pump} = 500$ nm the energy loss per round-trip exceeds 1000 cm^{-1}. The related change of the period on the order of 100 fs is easily resolved.

The consistency of the resulting rates displayed in Fig. 7.11 was checked by comparing a spectrum for E_{pump} with one at the corresponding E_1 (Fig. 7.11), i.e. the energy after one round-trip.. Indeed,

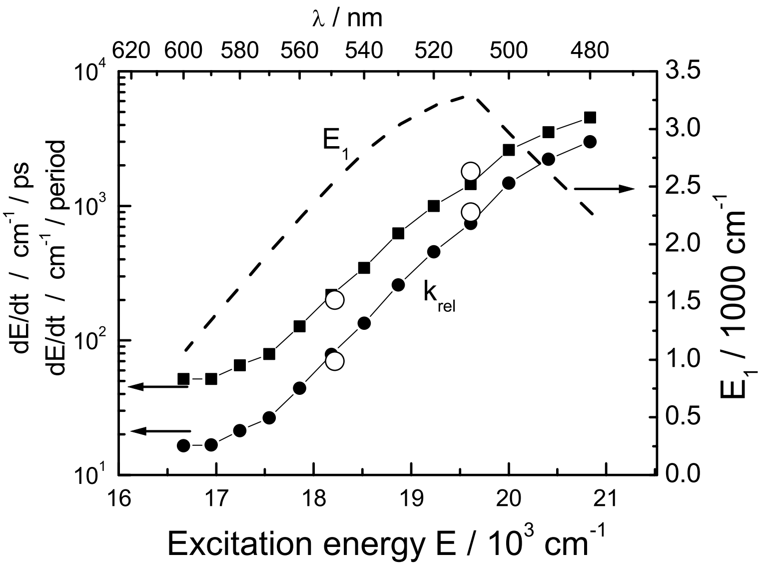

Figure 7.11: Energy relaxation rate $k_{rel} = dE/dt$ of I_2/Kr in the first oscillation as a function of energy in the B state measured in units of cm^{-1}/ps (solid squares) and cm^{-1}/period (solid circles). For comparison the values from ref. [27] are shown as open symbols. To demonstrate that near the dissociation limit the behavior of the system qualitatively changes, the energy E_1 of the wave packet after the first collision (dashed line) is plotted as a function of the initial excitation energy E_{pump}. It shows a maximum around $E = 19500$ cm^{-1}.

perfect agreement is obtained, if the E_1 spectrum is shifted by the period T_1 with respect to the E_{pump} spectrum.

Fig. 7.11 presents the vibrational relaxation rate versus E with a systematic variation over three orders of magnitude. The results are in excellent agreement with the values of the classical simulation in ref. [27] for dE/dt in Kr which are shown as hollow symbols in Fig. 7.11. The values must be read from the graphs in Fig. 6 of ref. [27], because the values given in the text correspond to a rate dE/dt averaged over 1 ps and the present results are averaged over one period only. The small rates near the bottom show up also in the calculations.

7.4.3 Energy dissipation from pump-probe envelope (method β)

B state of I_2/Kr

An alternative signature of the vibrational relaxation is found in the envelope of the pump probe signal (method β). It is discussed first for I_2 and subsequently applied to ClF/Ar and Cl_2/Ar. As it was mentioned above, the maximum of the pump-probe envelope occurs at time τ_m, when the wave packet is probed at its turning point. The difference potential $\Delta V = V_E - V_B$ between the E and the B state (Fig. 7.2) maps the probe wavelength λ_{probe} onto the bond distance R_{win} and the energy E_{win} of the probe window, as it was described in Fig. 7.4. E_{win} is decreased from near the dissociation limit down into the minimum of the B state well by shortening the probe wavelength, i.e. increasing $h\nu_{probe}$. Thus the wave packet is followed during the relaxation and in Fig. 7.12 its energy E_{win} is

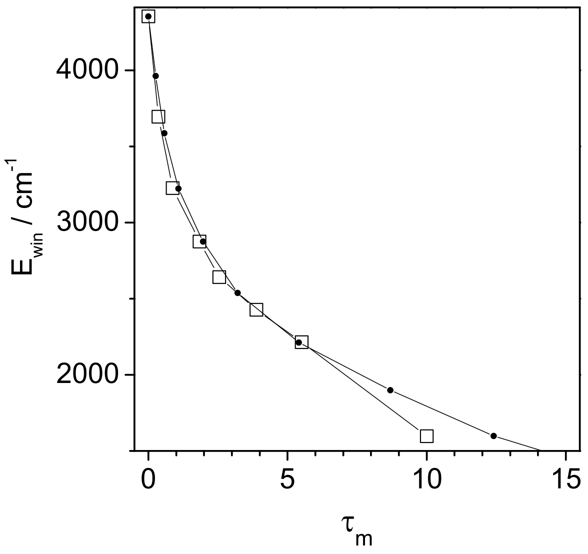

Figure 7.12: The open squares show the energy relaxation as derived from the τ_m values, which are read from the spectra in Fig. 6.4b and collected in Tab. 7.2. Solid dots depict the relaxation as derived numerically from the rates in Fig. 7.11.

plotted as a function of time τ_m. Tab. 7.2 collects $\tau_{m,}$ E_{win} and λ_{probe} for the pump-probe spectra displayed in Fig. 6.4b for a fixed pump wavelength $\lambda_{pump} = 500$ nm. The probe wavelength is varied from $\lambda_{probe} = 530$ nm to 456 nm. The energy of the packet at time $\tau_m = 0$ is taken from the pump wavelength λ_{pump} and the know B state potential[2].

λ_{probe} / nm	τ_m / ps	E_{win} / cm^{-1}
	0	4356
530	0.35	3696
520	0.85	3226
510	1.8	2876
500	2.5	2641
490	3.8	2427
480	5.3	2214
456	10	1597

Table 7.2: Vibrational relaxation of I_2/Kr. Probe wavelength λ_{probe} / nm with the corresponding energy E_{win} in the B state and the related delay time τ_m of maximal intensity in the pump probe spectrum. The excitation at $\lambda_{probe} = 500$ nm corresponds to 20000 cm^{-1} (4356 cm^{-1} above the B state minimum) directly after excitation ($\tau = 0$).

This result can be compared with the relaxation derived from method α. The rates dE/dt in Fig. 7.11 determine the amount of energy $\Delta E_i = t_i dE/dt$,that a wave packet at energy E_i will lose in a time step t_i. The discreteness given by the energies E_i, for which the rates $k_i = dE/dt(E_i)$ have been determined (Fig. 7.11), is used to calculate $t_i(E_i)$ recursively via $t_i = t_{i-1} + (E_{i-1} - E_i)/k_i$. The initial energy is given by $E_0 = E_{pump} = 4356$ cm^{-1} (for $\lambda_{pump} = 500$ nm). The inverse function $E_i(t_i)$ is plotted in Fig. 7.12 as dots, and shows the mean energy of the wave packet starting at E_{pump}. The agreement with the energy relaxation derived with method β (open squares) is excellent . For large delay times, $t > 10$ ps, method β yields times τ_m that are too short. The population losses

---

[2] $\lambda_{probe} = 540$ nm is not considered in this evaluation, since it lies below the classical resonance, and thus the energy E_{win} is not well defined.

from the B state due to predissociation reduce the signal in addition to the vibrational relaxation. The predissociation time for the B state is larger than 10 ps in this energy region, rendering the envelope a good criterion for energy relaxation at shorter times [115, 116].

A state of I_2/Kr

The A state of I_2/Kr was not studied with systematic variation of the probe wavelength. However, the spectra plotted in Fig. 6.6 already give an estimate for the strong vibrational relaxation in the A state. This state is much more weakly bound than the B state and thus the matrix cage gains importance. The maximum in the dotted curve after $\tau_m = 1.5$ ps indicates that the wave packet has relaxed down to the probe window within this time. $\lambda_{pump} = 670$ nm provides the initial energy $E_{pump} = 3390$ cm^{-1} above the minimum $T_e = 11538$ cm^{-1} of the A state and the probe window for $\lambda_{probe} = 400$ nm is located around $E_{win} = 500$ cm^{-1} above the minimum. Thus the packet loses energy at a rate of approx. 1900 cm^{-1}/ps or 2280 cm^{-1} in the first period of 1200 fs. This loss of $\Delta E/E_{vib} = \Delta E/E_{pump} = 67$ % is included in Tab. 7.4. The energy loss derived here is in excellent agreement with the results of the classical MD simulations presented in Fig. 2.2.

Evaluation for ClF/Ar and Cl_2/Ar

Method β will be used now to derive the energy relaxation in the B state of ClF in Ar from τ_m. The errors due to population losses will be even smaller than in the I_2/Kr case, since the $^3\Pi$ states energetically decouple from all other states for low energies (cf. Fig. 7.19) and the population losses are small. The pump pulse at 387 nm (25840 cm^{-1}) creates a wave packet with an energy of 7400 cm^{-1} above the B state minimum and approx. 5000 cm^{-1} above the gas phase B state dissociation limit. Momentum conservation yields a kinetic energy of about 3000 cm^{-1} in the F fragment [205].

In Figs. 6.8 and 6.9 the Cl^+F^- fluorescence intensity is plotted versus time delay between the pump pulse at 387 nm and probe pulses with wavelengths varying from 322 to 282 nm. The τ_m values are taken from the maxima and are collected in Tab. 7.3. The window location R_{win} and energy E_{win} follow from the difference potential ΔV in Fig. 5.6. $\lambda_{probe} = 320$ nm corresponds to the minimum in ΔV and according to Tab. 7.3 to the probe window position $R_{win} = 0.261$ nm, which lies energetically close to the dissociation limit[3]. Besides the sharp feature near $t = 0$ due to the outward moving wave packet a maximum after a delay time $\tau_m = 1.64$ ps is found (Fig. 6.9). Thus an excess energy of 5780 cm^{-1} is dissipated by strong collisions with the Ar cage during this time and the population has reached the probe energy of 20062.4 cm^{-1} with respect to the X state minimum and 1624.0 cm^{-1} above the B-state minimum (cf. Tab. 7.3).

Dissociation is prevented only by these collisions with the cage and the severe energy loss. The containment of the fragments by the cage is effective and at this energy a cage exit probability of only 4.8 % was derived (chapter 5.4.1). Probing deeper in the well by decreasing λ_{probe} leads to larger τ_m values (arrows in Fig. 6.8 and Tab. 7.3), because it takes longer for the population to reach the energy E_{win} by vibrational relaxation[4]. This flow down in energy of the population versus time τ_m is displayed in Fig. 7.13 by solid squares on a logarithmic scale. The rate of vibrational relaxation is

---

[3] $\lambda_{probe} = 322$ nm is not considered in this evaluation, since it lies below the classical resonance, and thus the energy E_{win} is not well defined.

[4] A more detailed examination of the envelopes for $\lambda_{probe} = 310$ and 306 nm shows the presence of two maxima, which are due to absorptions to E and f, respectively. In the present evaluation of the vibrational relaxation, only the transitions to the E state were considered. However, the result is not affected much, if for each spectrum the difference potential is used, which has higher weight according to the transition probabilities. Since this change would affect only the evaluation for short wavelengths, where f would be dominant, the determined relaxation rate would be somewhat smaller deep in the minimum, i.e. closer to the Cl_2 result plotted in the same graph (Fig. 7.13 open circles). For Cl_2 no transition moments are available and thus the evaluation can only be made with the E state. The same evaluation has been made for ClF in order have a consistent comparison in Fig. 7.13.

λ_{probe} / nm	R_{win} / nm	τ_m / ps	E_{win} / cm^{-1}
		0	7402.2
320	0.261	1.6	1624.4
318	0.249	1.7	1472.1
316	0.242	1.9	1244.8
314	0.238	2.2	1112.8
310	0.234	3.0	905.0
306	0.230	5.5	735.3
302	0.228	8.9	641.7
298	0.225	13.5	546.1
295	0.223	19.0	468.1
291	0.221	28.0	390.9
288	0.219	35.0	340.2
286	0.218	39.0.	305.8
285	0.218	43.0	288.4
284	0.217	45.0	270.9
282	0.216	54.0	241.4

Table 7.3: Vibrational relaxation of ClF/Ar. Probe wavelength λ_{probe} nm with the corresponding probe window location R_{win} and energy E_{win} in the B state and the related delay time τ_m (Fig. 6.8) of maximal intensity in the pump probe spectrum. The excitation at $\lambda_{probe} = 387$ nm corresponds to 25840 cm^{-1} or 7400 cm^{-1} above the B state minimum directly after excitation ($\tau = 0$).

the slope of the graph in Fig. 7.13. Two distinct regimes of energy dissipation are observed. A large relaxation rate of ~ 3500 cm^{-1}/ps is determined in the early dynamics (inset in Fig. 7.13), when the wave packet is above or close to the dissociation limit and the fragment is only bound by the solvent cage. When the molecule has recombined and is bound by the molecular potential, the relaxation rate has decreased to 10 cm^{-1}/ps.

The same evaluation scheme (method β) is employed for Cl_2/Ar, using the difference potential from Fig. 5.7. The resulting $E(t)$ curve is displayed in Fig. 7.13 by open circles. The Cl_2 molecule initially loses the energy in early dynamics even faster than ClF (inset in Fig. 7.13). The energy loss is $dE/dt \approx 7000$ cm^{-1}/ps. The masses of Cl and Ar are 39 and 40 amu, respectively, and from classical billiards it is evident that this leads to a very effective energy transfer in a head-on collision, which Cl fragments experience when dissociated on a double substitutional site (chapter 2.2.1). This corresponds nicely with the discussion in chapter 7.3.3, where the same rapid relaxation is also evident from the oscillation pattern.

Comparison of ClF/Ar, Cl_2/Ar and I_2/Kr

If the results for the energy relaxation in the B state of ClF/Ar and Cl_2/Ar (Fig. 7.13) are compared to those in the B state of I_2/Kr (Fig. 7.11), it catches the eye that the decay is much smoother in the latter case (a logarithmic energy scale would even decrease the curvature). The main reason is that I_2/Kr is excited just at the gas phase dissociation limit, whereas ClF/Ar and Cl_2/Ar are pumped far beyond. The energy loss in the first ps is large and the wave packet quickly drops below this limit. Within the bound part of the molecular potential the interaction with the matrix is much smaller.

Fig. 7.14 shows a comparison of the relaxation rates dE/dt for ClF/Ar, Cl_2/Ar and I_2/Kr as a function of the excess energy E_{excess} above the gas phase dissociation limit. The rates for ClF/Ar (open circles) and Cl_2/Ar (open squares) are the derivative of the $E(t)$ curves from Fig. 7.13 (method β). For I_2/Kr (solid squares) they are reproduced from Fig. 7.11, where they are derived from the

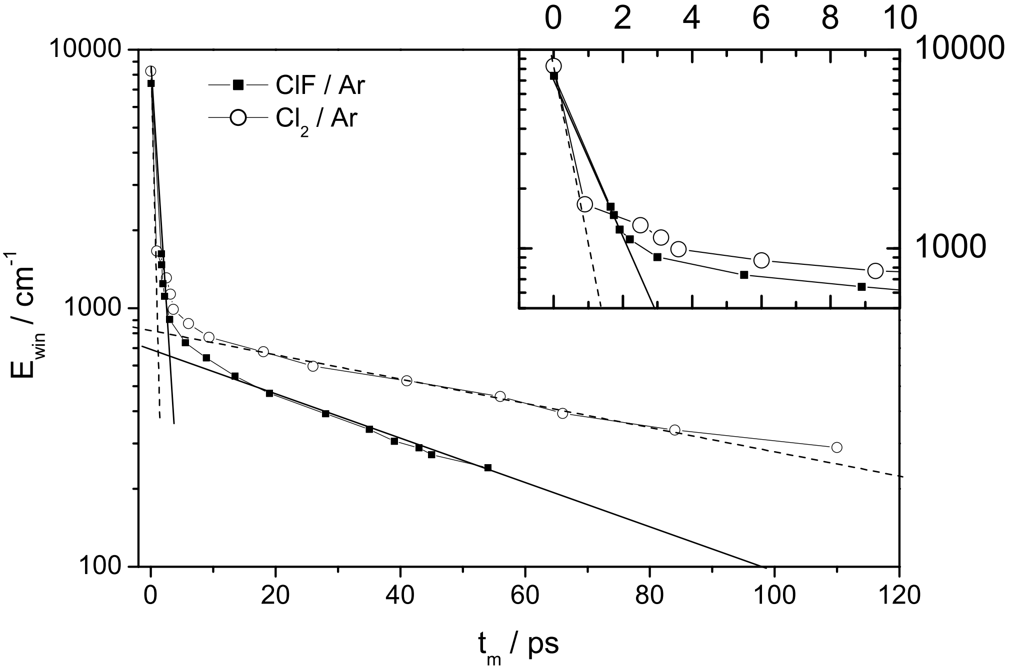

Figure 7.13: Vibrational energy E_{win} in the B state versus delay time τ_m, obtained from the maxima of the pump-probe spectra in Fig. 6.8 for ClF/Ar (solid square) and in Fig. 6.15 for Cl_2/Ar (open clircles).

vibrational periods (method α). The equivalence of the two methods was shown in chapter 7.4.3. For negative excess energies E_{excess} in Fig. 7.14, the molecules are bound in the molecular potential. The horizontal lines near $E_{excess} = 0$ correspond to an energy loss of 100% of the energy above the potential minimum E_{vib} in one collision for I_2/Kr (dash) and ClF/Ar (solid)[5]. This is the maximal rate in the picture of an oscillating wave packet. The measured rates indeed approach this limit exponentially and turn over to the limiting slower increase near the dissociation limit $E_{excess} = 0$.

The nonlinear increase of the relaxation rates is related to the soft anharmonic potential, which allows large bond extensions at high vibrational energy E_{vib} of the molecule. At the gas-phase dissociation limit ($E_{excess} = 0$) the bond length would already reach far beyond the size of the matrix cage, if the molecules were not confined by the forces imposed by the surrounding rare gas atoms. Therefore, the coupling of the molecule to the matrix cage becomes very strong.

The high rates for the energy loss per picosecond have to be used with care. The periods are shorter than 1ps, and the microscopic picture suggests that the energy loss takes place per collision rather than in a continuous way. Recall the peculiar consequence of the nonlinear increase of the energy dissipation that was derived for I_2/Kr (Fig. 7.11). There it was demonstrated that excitation at higher energy E_{pump} may lead to a lower energy E_1 after the first collision (cf. 7.6). Fig. 7.14 shows that for I_2/Kr at the dissociation limit ($E_{excess} = 0$), the rate is $dE/dt = 2600$ cm^{-1}/ps. Since one oscillation takes 570 fs, the energy loss in the first round-trip is 1480 cm^{-1}. In the collision the rate will be only $dE/dt = 400$ cm^{-1}/ps for the lower $E_{excess} = -1480$ cm^{-1}.

As a survey, Tab. 7.4 displays the fraction (percentage) of energy $\Delta E/E_{vib}$ lost in one period T for selected excess energies E_{vib} and for several electronic states. The periods are taken from the wave packet dynamics in chapter 7.3, except the values for ClF and Cl_2 near the minimum, which

---

[5] For Cl_2/Ar this limit is intermediate between ClF/Ar and I_2/Kr.

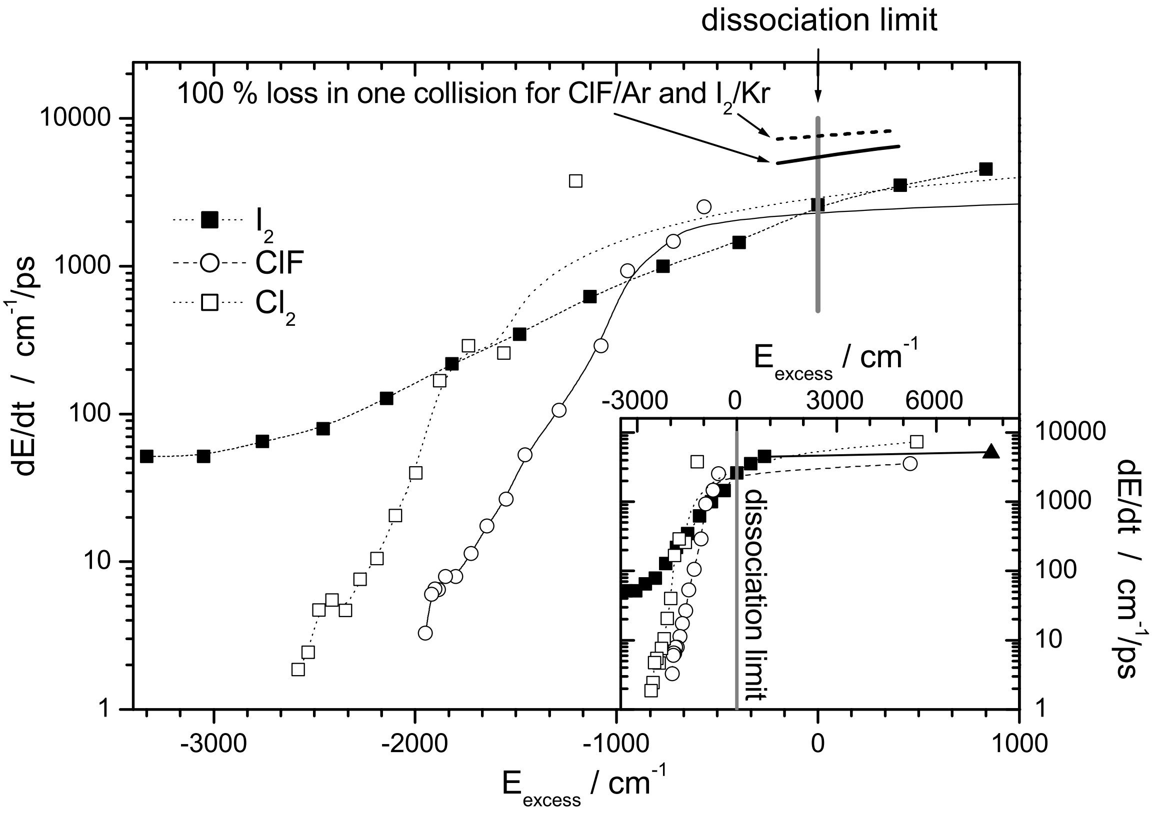

Figure 7.14: Relaxation rates dE/dt for I_2/Kr (solid squares), ClF/Ar (open circles) and Cl_2/Ar (open squares) as a function of the excess energy E_{excess} above the gas phase dissociation limit. For all three molecules the rates increase exponentially in the bound region ($E_{excess} < 0$). They approach the maximal rate of 100% loss per period (solid line for ClF/Ar, dashed for I_2/Kr) near the dissociation limit. The inset includes the large rates far beyond the limit. The solid triangle corresponds excitation of I_2/Kr to its B'' state.

	I_2/Kr			ClF/Ar		Cl_2/Ar		units
state	B	A	B''	B	$^1\Pi$	B	$^1\Pi$	
D_0	4350	1650	0	2190	0	2870	0	cm^{-1}
High vibrational energy								
$\Delta E/E_{vib}$	**57**±5	**67**±20	**70**±20	**35**±10	**55**±20	**60**±20	**60**±20	**%**
E_{excess}	830	1750	7650	5210	17200	5410	18080	cm^{-1}
E_{vib}	5180	3400		7400		8280		cm^{-1}
$T(E_{vib})$	660	1200	1200	675	675	800	800	fs
Low vibrational energy								
$\Delta E/E_{vib}$	**1**$\pm.5$			**0.2**$\pm.1$		**0.1**$\pm.1$		**%**
E_{excess}	-3050			-1890		-2470		cm^{-1}
E_{vib}	1300			300		400		cm^{-1}
$T(E_{vib})$	315			100		130		fs

Table 7.4: Vibrational relaxation in ClF/Ar, Cl_2/Ar and I_2/Kr for excitation to different electronic states. The energy loss $\Delta E/E_{vib}$ in percent is given for high and low vibrational energies. The confidence intervals are estimated from the uncertainty of the vibrational period and energy loss. If the excess energy E_{excess} is negative, the molecule is bound by its own potential and the rate is very small. For excitation above the gas phase dissociation limit, about half of the energy is lost in the first period.

are from the spectroscopic data for the gas phase from ref. [206]. Intermediate relaxation rates can be read from Fig. 7.14

7.5 Depolarization and angular reorientation

This chapter presents one of the few examples where ultrafast angular reorientation of molecules in the condensed phase has been detected with femtosecond pump-probe spectroscopy. It offers for the first time the possibility to compare the ultrafast decay of the polarization anisotropy to the sophisticated DIM-trajectory calculations.

7.5.1 Ultrafast reorientation of molecules measured by polarization dependent pump-probe spectroscopy

In the ultrafast dissociation-recombination events examined in this thesis, the scattering of the fragments off the solvent cage atoms may be asymmetric and lead to recombination in a tilted geometry (Fig. 7.15a). Polarization dependent femtosecond pump-probe spectroscopy is exploited to measure this reorientation[6] of the recombining fragments in time during the first encounters on the ultrafast timescale, which is dictated by the kinetic energy of the fragments and the fast dissipation of rotational and vibrational energy in condensed media. Starting from a sample with randomly oriented molecules, a linearly polarized pump pulse prepares an anisotropic ensemble of excited state molecules (photoselection) [140] and dissociates them. The anisotropy is probed during the recombination process with a second linearly polarized pulse by recording the laser induced fluorescence.

Although it is well known that such polarization sensitive measurements yield information on the rotational motion of molecules according to the selection rules for electronic transitions, only few experiments used this method on an ultrafast timescale. The rotation of free molecules and the coherent vs. random rotation of I_2 in liquid rare gases [216, 217] has been displayed by this method and it was proposed to measure the fragment rotation for ICN in liquid Xe [218]. Often these polarization effects are neglected or unwanted and the experiment is performed in the magic angle

---

[6] In this chapter the words "reorientation" and "orientation" are used as the colloquial form of the word alignment. It does *not* imply orientation of an arrow, i.e. with direction.

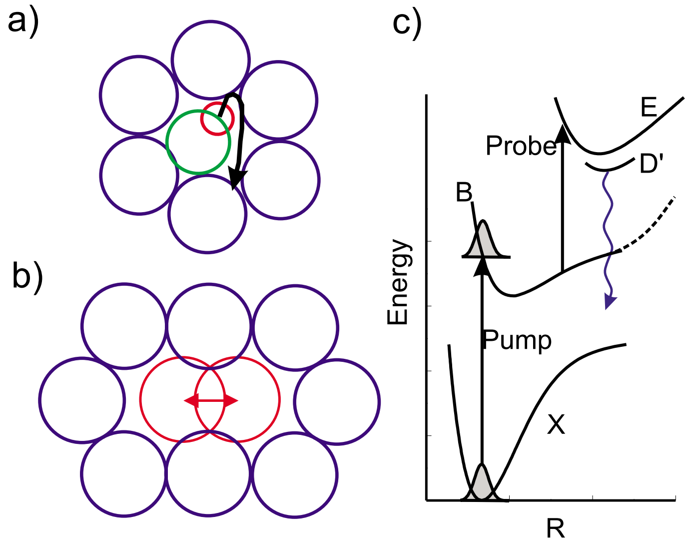

Figure 7.15: a) Scheme for a ClF molecule on a single substitutional site in an Ar matrix. After photodissociation the F fragment can be scattered into a new orientation with respect to Cl, depending on the scattering parameters. b) Scheme for an I_2 molecule on a double substitutional site in a Kr matrix. The geometry suggests that tilting the molecule is strongly inhibited. Dissociation leads to vibrational motion after recombination. c) Pump-probe scheme for both molecules with the relevant electronic potential curves.

configuration to be sensitive to vibrational wave packet dynamics only [21]. A different approach uses polarization effects in the third order polarizability with techniques like CARS or Kerr-effect [22,219].

For the polarization sensitive measurements in chapters 6.1.2 and 6.3.2 the following scheme was used and the first five lines of Tab. 2.3.5 are relevant. Starting from the vibrational ground state $X(^1\Sigma_0)$ in both cases (Fig. 7.15c), the $B(^3\Pi_0)$ state $(\Delta\Omega = 0)$ is excited with the linearly polarized pump pulse, creating a $\cos^2(\Theta)$ distribution of excited molecules aligned with the laser polarization. The time delayed probe pulse transfers population to the $E(^3\Pi_0)$ state and after relaxation within the ion-pair manifold, emission from the $D'(^3\Pi_2)$ state is observed [80, 115, 205]. The transitions between valence and ion-pair states obey the selection rule $\Delta\Omega = 0$ favoring an electric field parallel to the internuclear axis. The probe pulse has horizontal polarization in all experiments and the pump pulse is polarized either parallel ($\|$) or perpendicular $(\perp)$ with respect to the probe polarization. In the pump-probe experiments, the fluorescence from D' is collected in forward direction without polarization sensitive optics (first three lines in Tab. 2.3.5). To check the results, a polarization analyzer is introduced (lines four and five in Tab. 2.3.5).

Tab. 2.3.5 summarizes the intensity ratios for the probe absorption of an ensemble photoselected by the pump. $I_\|$ and $I_\perp$ in the last column are the ratios for completely preserved photoselection parallel and perpendicular to the probe polarization. I_d denotes probing a depolarized (random) distribution with linearly polarized light. If the laser induced fluorescence (LIF) is detected without polarization sensitive optics, it is proportional to these ratios. lines four and five indicate the intensity ratios observed, if a photoselected ensemble is probed with polarization parallel to the selected axis and the LIF is detected with a parallel $(I_{LIF\|})$ or perpendicular $(I_{LIF\perp})$ polarization analyzer. An interchange of analyzer and probe polarization yields the same ratio for symmetry reasons.

The classical trajectory calculations summarized in chapter 2.1 show that scattering of F fragments in the Ar cage can lead to recombination of F_2 with a tilted bond direction (Fig. 2.4). The fragments are small enough to move inside the nearly isotropic cage (Fig. 7.15a). These skewed scattering events also appear in nonadiabatic trajectory calculations (Fig. 7.17 [71]). However, for I_2/Kr such events are not expected because of the geometry of the double substitutional site, occupied by the I_2 molecule (Fig. 7.15b). Accordingly, reorientation of the bond is not observed in the corresponding classical and semiclassical simulations of I_2/Kr. To demonstrate the different behavior of I_2/Kr vs. ClF/Ar, the same set of experiments is performed on both systems in the way described above. Both molecules have similar electronic structure. The nonadiabatic dynamics on several electronic states are discussed in chapter 7.6, which deals with the dynamics of spin-flips. The method of polarization dependent pump-probe spectroscopy applied in the following separates out the geometric orientation only.

7.5.2 Sterically fixed molecule: I_2/Kr

The spectra in Fig. 6.5 for I_2/Kr and $\lambda_{pump} = \lambda_{probe} = 486$ nm with parallel (solid) and crossed (dashed) pump-probe polarization show an oscillatory structure from the vibrational wave packet dynamics. The I_2 wave packet prepared 0.08 eV above the dissociation limit dissipates 0.44 eV within 1 ps according to the rates in Fig. 7.11, leading to the increasing envelope function. The fact that both spectra in Fig. 6.5 coincide perfectly after multiplication of the parallel spectrum by the factor $1/3$ for preserved photoselection (cf. Tab. 2.3.5) implies that the I_2 molecule is indeed fixed in space as expected from the axial symmetry of the tight Kr cage around the double vacancy. This is indicated in Fig. 7.15b.

The results confirm that unlike the results for I_2 in liquid Kr [216, 217], the angular reorientation (randomization) of the I_2 molecule embedded in a solid Kr matrix is negligible, since it is inhibited by the rigid matrix cage despite the large amount of energy deposited locally. In high pressure Ar at room temperature, on the contrary, the anisotropy depicts the coherent rotational motion of I_2, that leads to a dip after 2 ps, and a constant asymptotic anisotropy of 0.1 at low pressures [217]. For high pressures approaching liquid phase densities, the random collision time becomes faster and faster, until the rotational coherence is destroyed and the anisotropy decays to zero.

At $\lambda_{pump} = 486$ nm the B'' state is also populated and this transition ($\Delta\Omega = 1$) selects an ensemble perpendicular to the polarization. However, only the B state is probed in this experiment and the small portion of the wave packet crossing from B'' to B is negligible according to experimental observation in ref. [115, 116]. For low excitation, it may suffice to perform an experiment with a single linearly polarized pulse that excites the B state and to measure the polarization of the $B \rightarrow X$ fluorescence [33], to prove the preserved alignment. If I_2 is excited above 500 nm, the $B \rightarrow X$ fluorescence originates from both ${}^1\Pi_1$ and $B({}^3\Pi_0)$ excitation. In that case one can *assume* that the molecule is not tilted and use the polarization of the fluorescence to separate ${}^1\Pi_1$ and $B({}^3\Pi_0)$ as it was done for ICl in Ar [220]. Moreover, in order to compare to ClF/Ar, the pump-probe experiment is required to be sensitive to angular reorientation of the molecule in the excited state on the fs-timescale.

7.5.3 Random scattering in cage: ClF/Ar

Fig. 7.16a reproduces the spectra from Fig. 6.10 ($\lambda_{pump} = 387$ nm and $\lambda_{probe} = 317$ nm) with parallel ($\parallel$ solid line) and perpendicular ($\perp$ dashed line) pump-probe polarization. Directly after excitation ($t = 0$) the ratio of the recorded fluorescence intensities is close to the expected ratio of $I_\perp/I_\parallel = 1/3$ for preserved photoselection. After 2 ps both spectra coincide, indicating complete depolarization. The oscillatory structure reflects the wave packet dynamics. $I_\parallel$ at $\tau = 0$ is scaled to the value 0.6. Then $I_\perp(t = 0)$ is close to the 0.2 in accordance with Tab. 2.3.5 for preserved photoselection. For the complete depolarization, reached after 2 ps, one would expect $I_\parallel = I_\perp = 0.33$. However, the observed signals converge to the value of 0.5. The reason for the difference is ultrafast vibrational relaxation of ClF in Ar. The ClF wave packet prepared 0.6 eV above the dissociation limit relaxes below the dissociation limit within 1 ps. The larger probe efficiency yields the increase of the signal for both polarizations (chapter 7.4.3). To eliminate the changes due to the probe efficiency, the anisotropy $r = (I_\parallel - I_\perp)/(I_\parallel + 2I_\perp)$ is calculated. Fig. 7.16b shows the anisotropy $r(t)$ together with an exponential fit $r(t) = r_0 \exp(t/\tau_r)$ with the time constant $\tau_r = 1.2$ ps and an initial value of $r_0 = 0.35$, close to the expected value of 0.4. The exponential decay to $r(t > 2ps) = 0$ indicates complete depolarization. Thus τ_r is the timescale for randomization of the molecule's orientation induced by dissociation, scattering of fragments off the cage and subsequent recombination.

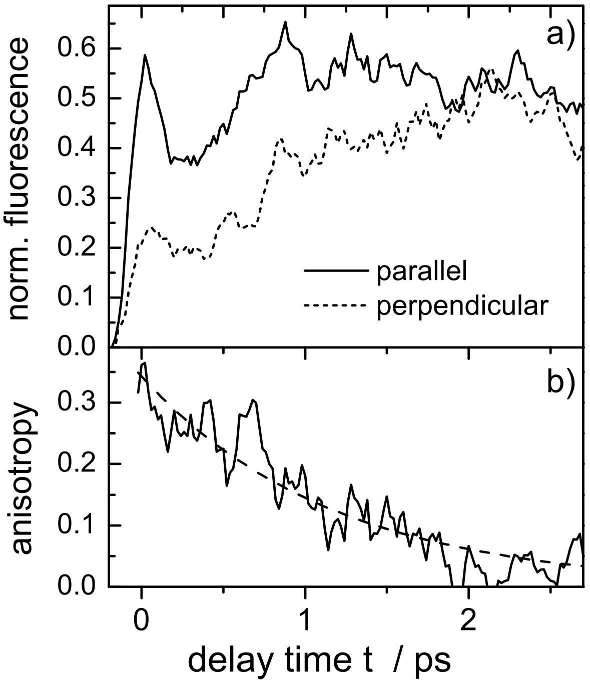

Figure 7.16: a) fs-pump-probe spectra with $\lambda_{pump} = 387$ nm and $\lambda_{probe} = 317$ nm for ClF in Ar from Fig. 6.10. The spectra for $||$ and $\perp$ pump-probe excitation converge after 2 ps but show a ratio of nearly $I_\perp/I_{||} = 1/3$ directely after excitation. b) The anisotropy $r = (I_{||} - I_\perp)/(I_{||} + 2I_\perp)$ is shown together with an exponential decay with the time constant $\tau_r = 1.2$ ps. The depolarization proves the ultrafast statistical angular reorientation of the ClF molecule.

The time $\tau_r = 1.2$ ps should be related to the vibrational period (400 fs) of ClF and the Ar-cage-breathing mode (800 fs) discussed previously (chapter 7.3.2) [205]. The first fragment-cage collision leads to a dramatic loss of kinetic energy in the ClF. From this point of view, it is surprising that the angular randomization in the first 500 fs is rather small (cf. Fig. 7.16b). The anisotropy decreases from $r_0 = 0.35$ to 0.25. The data suggest that the cage breathing which is induced by the impulsive first collision enforces the tilting of the molecular bond after 800 fs.

The results discussed above have several important implications. It is demonstrated experimentally for the first time that fs-pump-probe spectra of small molecules in condensed phases $-$ even in a rigid matrix cage $-$ display fast depolarization. In the future this method can be used to measure molecular alignment on the femtosecond timescale induced by strong non-resonant IR pulses. These experiments are in preparation. It is confirmed that the validity of reduced dimensionality approaches [72,73], which keep the internuclear bond orientation fixed and propagate 2-D wave packets quantum mechanically, is limited to the first oscillation. The experimentally determined decay of the anisotropy can be compared to the statistics of trajectory simulations, once the averaging of the trajectories is accomplished. Again this signature is very useful, since the tedious calculation of the ion-pair potentials is circumvented, and the pump-probe spectrum itself need not be simulated.

Mechanism

The timescale of angular reorientation can be compared to high level trajectory simulations in the spirit of the DIM formalism [71]. In this way predictions for the scattering of open-shell fragments [68, 70] and recombination onto excited molecular states can be verified experimentally. The information on depolarization is contained in the calculations [71] (Fig. 7.17). An evaluation presenting an average over the trajectories like for the spin-flip transitions (see below) is missing, although highly desirable.

The mechanism that induces angular randomization can be deduced from the simulations, which were carried out for the similar situation of F_2 dissociation at different levels of sophistication. The classical molecular dynamics calculations that used isotropic $F - Ar$ potentials [67] were improved

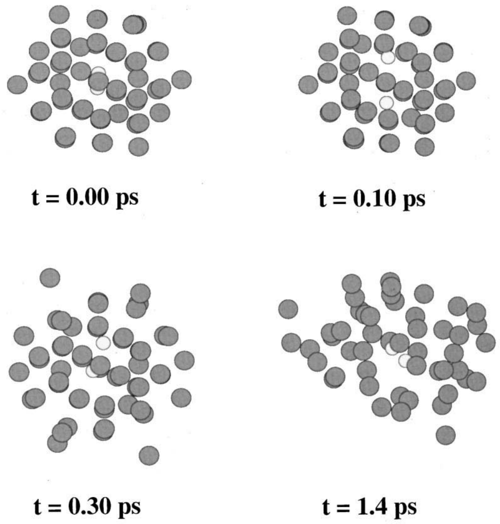

Figure 7.17: Snapshots of the molecular dynamics of F_2/Ar_{54} from ref. [71]. The balls represent F atoms (white) and Ar atoms (grey). In the first 300 fs, the molecular bond is broken and recombined again in the initial orientation. After 1.4 ps the bond is tilted by more than 50°.

by explicitly taking into account the open-shell nature of the fragments [68, 70] and by a full DIM-simulation[7] including nonadiabatic effects [71]. For illustration consider Fig. 7.17 taken from ref. [71], which shows snapshots of a typical trajectory of F_2 in an Ar_{54} cluster with excitation parameters close to our experiment. In the first 300 fs, the $F - F$ bond is broken and formed again in the original orientation. After 1.4 ps, however, the bond is tilted by more than $50°$. Obviously, a time dependent orientation averaged over all trajectories would be more informative than this single trajectory.

A more detailed discussion of the microscopic structure shall be given, that describes important features of the problem. The ClF molecule is supposed to be aligned in the way depicted in Fig. 2.5, i.e. with the fragments pointing symmetrically at the triangular windows. The discussion of the molecular orbitals in chapter 2.4.5 showed, that the P-orbital of the dissociating F atom will be aligned with the direction of motion (Fig. 2.14). As already mentioned, ref. [68] showed that in this geometry the barrier for dissociation is 2.1 eV with the saddle point in the center of the Ar_3 triangle, symmetrical to the dissociation. The P-orbital will align with the plane of the Ar_3 triangle after dissociation, because then the barrier is lowered to 0.7 eV. The saddle point now lies in the center between two Ar atoms, i.e. asymmetrical to the direction in which the F fragment was dissociated. It is evident that the corresponding potential surface will enforce a skewed scattering event. On the other hand, since there are three saddle points which are symmetrically ordered around the axis of dissociation and correspond to different alignments of the orbital, the problem remains symmetrical until the symmetry is broken and the Jahn-Teller effect is established. It will be a challenge to future experimental and theoretical studies to decide how fast the P-orbital is aligned by the cage forces [68–70].

7.6 Solvent induced spin-flip

This chapter presents the perhaps most surprising result of these studies. Pump-probe signals evidence the ultrafast spin-flip in ClF induced by the presence of the solvent. Cl and F are light atomic fragments, and in the gas phase the intersystem crossing is forbidden on a nanosecond timescale.

Great effort is taken to investigate the non-adiabatic coupling in molecules, i.e. the interplay of the dynamics of electrons and nuclei in the presence of the solvent. The spin-selection rule in molecules composed of light atoms is strict and intersystem crossing is intuitively considered to be slow.

---

[7] Similar calculations on ClF/Ar are currently pursued in the group of Prof. Manz.

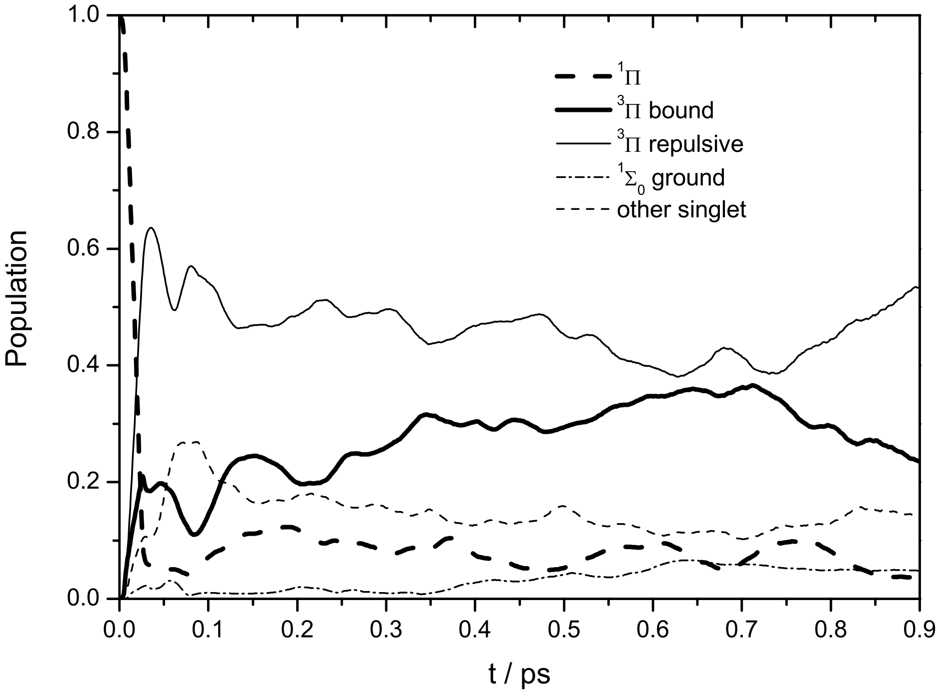

Figure 7.18: Populations of electronic states after excitation to the singlet state $(^1\Pi)$ of F_2/Ar_{54} ensemble averaged over many trajectories in ref. [71]. The lines indicate the populations in the initially excited singlet state $(^1\Pi)$ (thick dashed), the bound triplet states $(^3\Pi)$ (thick solid), all repulsive triplet states (thin solid), the ground state (thin dash-dot) and all other singlet states (thin dashed). After 60 fs, the population in all triplet states is 0.8, which is the statistical weight of the triplet states. The growing population in the bound triplet states (thick solid) is observed in the experiment (cf. Fig. 7.21).

Strong transitions are observed in light diatomics from the ground state $^1\Sigma_0$ only to the singlet states, e.g. $^1\Pi_1$. The absorption cross section to the triplet states is much smaller according to the spin selection rule. The $B(^3\Pi_0)$ state can be accessed in the experiment by appropriate spectral selection (cf. Fig. 5.2).

Recent simulations of nonadiabatic dynamics in the excited states of F_2 in Ar clusters predicted that ultrafast spin-flips play an important role in the dynamics and occur on the 100 fs timescale [71]. The same has been calculated for HCl in Ar [221, 222]. The second important prediction is the rapid recombination of the molecule into different excited electronic states as opposed to recombination into the original state or into electronic ground state. These non-adiabatic transitions have been investigated in detail for the similar system of I_2 in rare gas both theoretically [63, 64, 66] and experimentally [27, 46, 115]. Strong spin-orbit coupling in I_2 already weakens the spin selection rule in the free molecule. The small spin-orbit interaction in the case of ClF or F_2 molecules simplifies the potential diagram, and the solvent contribution to the spin-flip can be demonstrated more clearly. It is important to keep in mind that non-adiabatic coupling between a pair of electronic states is bidirectional, i.e. the wave packet hops back and forth with equal probability. In the following discussion it will be shown that in the condensed phase it is the energy dissipation to the surrounding that directs the process towards lower energy [115].

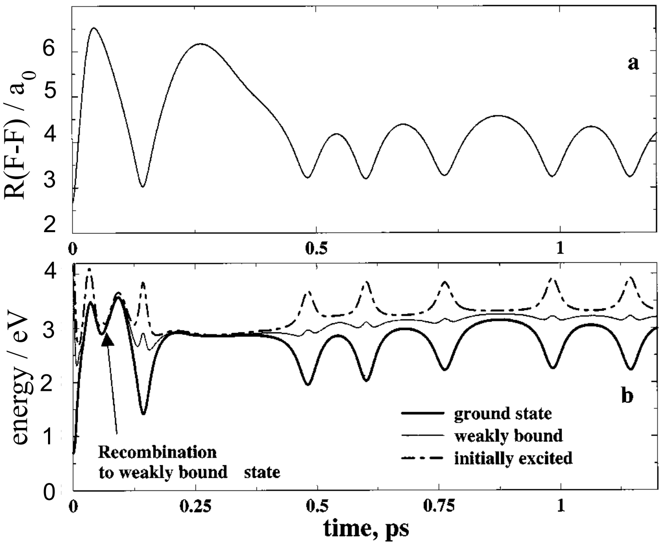

Figure 7.19: Single DIM-trajectory demonstrating the mechanism of spin-flip from ref. [71]. After 60 fs, the trajectory hops from the initially excited $^1\Pi$ to a bound triplet state. In the next excursion it loses so much energy to the solvent that the electronic states decouple, i.e. the trajectory does not reach the region at large R where the states overlap. It is trapped in the bound triplet state.

7.6.1 Spin-flip in F_2 (theory)

First the theoretical findings that stimulated the measurements shall be summarized. In the simulations [71] of F_2 in Ar_{54} clusters the electronic states were described by the valence bond approach for the $F(^2P) + F(^2P)$ interaction. The spin-orbit and non-adiabatic coupling was included and the anisotropic interactions between $F(^2P)$ and Ar are described by the diatomics-in-molecules approach (DIM). This basis was used throughout to construct the 36 electronic valence states. The dynamical simulations use the surface hopping method. The study analyzed photodissociation and recombination dynamics. The present investigation focuses on the ultrafast spin-flip in the recombination dynamics of ClF in Ar. Hence only the main results concerning the recombination of F_2 in Ar with comparable photoexcitation at 4.6 eV are summarized Fig. 7.18. The data were kindly provided by M. Niv.

The molecule is excited into the $^1\Pi_1$ state by an ultrafast laser pulse. The trajectories move outwards, and preferentially at large bond distances, surface hopping to other electronic states occurs. The population of the initially excited singlet state $^1\Pi$ (thick dashed line), drops from unity to 0.1 within less than 40 fs and subsequently remains nearly constant within the simulated time of 1 ps. The population is transferred to the bound (thick solid line) and repulsive (thin solid line) triplet state in the first 40 fs. Slightly later $\sim$ 60 fs, the other singlet states gain some weight (thin dashed line). Subsequently, the main process is transfer of population from the repulsive triplet and singlet states to the bound triplet states $^3\Pi_u$. 40% of the population accumulate in the bound triplet states in the first 700 fs, and subsequently population is partially transferred back to the repulsive triplets. The interpretation in ref. [71] is that after 60 fs the trajectories are distributed among the triplet and singlet states with the statistical weight of 3:1. A reason for the accumulation in the bound triplet states is found in the corresponding trajectories. Fig. 7.19, reproduced from ref. [71], shows a trajectory that hops to the bound triplet state after 100 fs. The bound triplet state is depicted by the thin solid line. In the subsequent excursion of the trajectory to large $F - F$ distances (upper panel), a lot of energy is dissipated to the Ar atoms, and the bound triplet states "decouple" from all other states, since the trajectories no longer reach the region where the states cross.

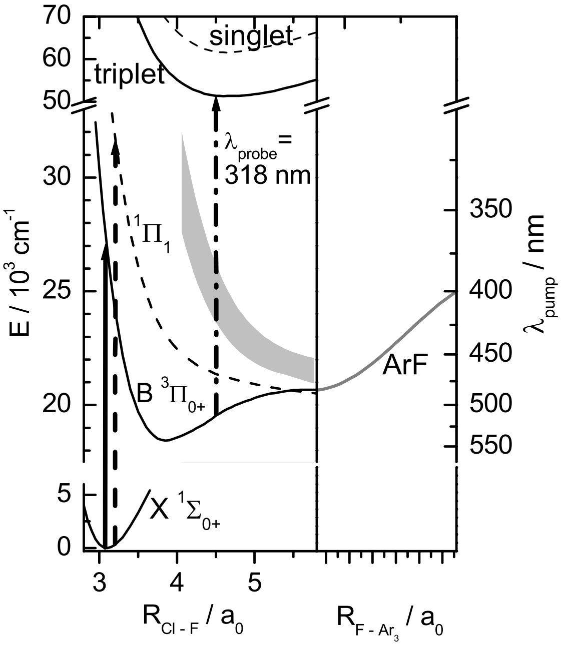

Figure 7.20: One dimensional potential diagram of the ClF molecule embedded in an Ar matrix. The left panel reproduces the gas phase potential energy curves for ClF taken from ref. [121]. The right panel schematically shows the cage-effect of the surrounding Ar crystal, that imposes a binding force on the fragments, here represented by the ArF potential. The following valence states of the ClF molecule are shown: Ground state $X(^1\Sigma_{0^+})$, the $B(^3\Pi_{0^+})$ state as a representative of all four bound $^3\Pi$ states which coincide within 500 cm^{-1}, the repulsive singlet $^1\Pi_1$, and the gray shaded area covering all other valence states. The ion-pair manifold contains the closely spaced triplet states $^3\Pi$ and $^3\Sigma$. The singlet states lie 10000 cm^{-1} higher in energy and cannot be accessed with the wavelenghts used in this experiment.

7.6.2 Spin-flip in ClF (experiment)

In the following these theoretical studies are compared to experimental findings derived from fs-pump-probe spectra on ClF/Ar. The discussion will show that there is good agreement on the fact that population accumulates in the bound triplet states shortly after singlet excitation. The ultrafast spin-flip and the large amount of recombination onto bound excited states are verified.

The bound triplet states $^3\Pi_\Omega$ are probed via the strong charge transfer transitions to the ion-pair states $^3\Pi_\Omega$, and for the chosen probe wavelength $\lambda_{probe} = 318$ nm these are the only energetically accessible transitions (cf. Fig. 7.20). The fluorescence intensity at 420 nm is recorded versus time delay. The states with $\Omega = 0, 1$ and 2 are very closely spaced due to the weak spin-orbit interaction and we do not attempt to separate them. In the F_2 molecule they correspond to the $^3\Pi_u$ manifold. Two different pump laser beams ($\lambda_{pump} = 280$ nm and $\lambda_{pump} = 387$ nm) are overlapped on a dichroic mirror and focused together with the probe beam onto the sample (chapter 6.3.3 and Fig. 6.11). By blocking one of the two pump beams one can now choose to excite the ClF molecule either to the singlet state $^1\Pi_1$ (280 nm) or to the triplet $B(^3\Pi_0)$ (387 nm). Fig. 7.21a shows the pump-probe spectra obtained by delaying the probe pulse by the time t with respect to the pump. Direct excitation to the $B(^3\Pi_0)$ state (solid curve), produces the oscillations due to vibrational dynamics of the wave packet discussed in chapter 2.1.5. The first maximum at $t = 50$ fs corresponds to probing the wave packet on the outward stretch motion (→) of the $Cl - F$ bond. The peak at $t = 500$ fs indicates the return of the wave packet (←) into the probe window after it has lost almost half its kinetic energy (~ 0.6 eV) with respect to the minimum of the B state [195]. In the next two maxima the packet is probed near its turning point (↔) with the vibrational period of 300 to 400 fs, typical of ClF in the B state near the dissociation limit.

If on the other hand, the molecule is excited into the singlet state $^1\Pi_1$ (dashed curve), the pump-probe signal is close to zero at time $t = 0$, since only the triplet states $^3\Pi$ are probed. However, the spectrum rises, indicating population transfer to $^3\Pi$, i.e. spin-flip, and it converges to the pump-probe spectrum for direct excitation into $B(^3\Pi_0)$ within 1.5 ps. The wave packet dynamics, displayed by the oscillations in the signal, are similar and interpreted in the same way, except for a larger energy loss than for triplet excitation. This energy loss, qualitatively compatible with the simulations [71], is on the order of 1.5 eV due to the higher kinetic energy that the Cl and F fragments attain by excitation with $\lambda_{pump} = 290$ nm. In the preceding chapters it was shown that energy dissipation increases nonlinearly with excitation energy in ClF and in the analog system, I_2 in Kr solid [27,46]. The inset in Fig. 7.21 shows that the spectra agree for all delay times longer than 2 ps within the reproducibility. Shorter probe wavelengths displayed in Fig. 6.11 display the B state population deeper in the well with lower vibrational excitation and the signal can be observed up to 100 ps. At these long time delays the spectra for excitation to singlet $^1\Pi_1$ or to triplet $B(^3\Pi_0)$ coincide perfectly and the spectra are normalized accordingly. The normalization constant accounts for the different absorption coefficient and photon flux. The oscillations in the early part of the signals display the wave packet dynamics as described before and the envelope shows the signature of vibrational relaxation. At first the signal increases, as the wave-packet relaxes into the probe window, improving the Franck-Condon overlap with the ionic states. Then the intensity decreases as the wave packet energetically falls out of the probe window.

As a measure of the spin-flip, the ratio of the dashed ($I_{\sin glet}$) and the solid ($I_{triplet}$) curve from Fig. 7.21a, i.e. $I_{\sin glet}/I_{triplet}$ is plotted in Fig. 7.21b as the solid line. It represents the triplet population after singlet excitation normalized to that for triplet excitation. The division by $I_{triplet}$ removes most of the variation of the detection sensitivity with delay time caused by vibrational relaxation. To derive the spin-flip rate from the experimental data, the increasing population is fitted with an exponential growth (dotted line), $I_{flip}(t) = 1 - \exp(-t/\tau_f)$, with a time constant $\tau_f = 500$ fs as the only adjustable parameter. However, the spin-flip seems to occur preferentially at times when the ClF bond is stretched, according to the step in the experimental solid line between 250 and 400 fs. At time $t = 0$ the triplet population must be zero, and the small finite value measured in the experiment is due to the finite duration (100 fs) of the laser pulses. The chosen scale in Fig. 7.21b agrees with the fraction of molecules predicted to cross to the bound triplet states in the simulation [71]. In the simulations, there are also dissociated molecules with fragments that left the cage and large $Cl - F$ distance, which are not included in the present count. The triplet state population accumulated according to the simulation is displayed in Fig. 7.21b as open circles[8]. The agreement of experiment and theory is excellent. The scatter in the theoretical data reflects the statistics of the trajectories, while the bleaching of the sample limits the time to accumulate experimental data.

A correction of the spectra has to be considered because the vibrational relaxation and thus the changes of the probe sensitivity, are not identical for both excitations. Prepared in the $^1\Pi_1$ state, the wave packet has higher kinetic energy at $t = 0$ and thus the sensitivity is reduced. The energy loss increases with kinetic energy and the sensitivity rises quickly to the final value. The vibrational relaxation and sensitivity for times $t > 2$ ps are very similar in both cases according to the same shape of the envelopes. The correction will enlarge the signal (solid line) near $t = 0$ and thus bring the experimental values even closer to the theoretical data (Fig. 7.21b). To estimate the correction, the kinetic energy of the wave packet at the probe window is calculated for the first excursion. It is $E_{kin} = 6000$ cm^{-1} and 15800 cm^{-1} for B state and $^1\Pi$ excitation, respectively. Taking the sensitivity S as inversely proportional to the velocity [45] $S \sim 1/v \sim 1/\sqrt{E_{kin}}$ yields the correction factor $c = S_{triplet}/S_{\sin glet} = 1.6$ before the first collision with the matrix. At later times the correction is very close to 1.

The excitation to $B(^3\Pi_0)$ is a parallel transition [138, 140] ($\Delta\Omega = 0$), whereas to $^1\Pi_1$ it is perpendicular ($\Delta\Omega = 1$). The pump beams are chosen to have polarization parallel and perpendicular to the probe polarization, respectively, to avoid differences due to depolarization. The intensity ratio

---

[8] In Fig. 7.18 this is the thick solid line.

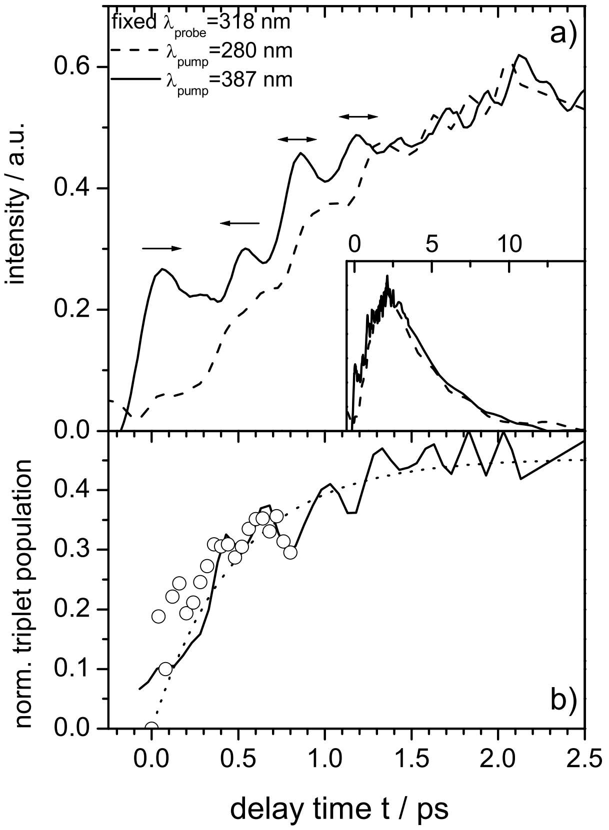

Figure 7.21: a) Pump-probe spectra with $\lambda_{probe} = 317$ nm, probing only the bound $^3\Pi$ states. The solid curve corresponds to excitation into the $B(^3\Pi_0)$ state with $\lambda_{pump} = 387$ nm and the dashed curve to $^1\Pi_1$ with $\lambda_{pump} = 280$ nm from Fig. 6.11. Both spectra show oscillations due to wave packet dynamics. b) Ratio of the two spectra, displaying the spin-flip from $^1\Pi$ into $^3\Pi$ (solid line). The dashed line is an exponential fit to the solid line with time constant $\tau_{pump} = 500$ fs. The open circles are taken from the simulation in ref. [71]

for probing the torus prepared with a $\Delta\Omega = 1$ transition on the $^1\Pi$ state by a cos$^2\theta$ lobe ($\Delta\Omega = 0$) is 1/5 for parallel ($||$) and 2/5 for perpendicular ($\perp$) pump probe polarization according to the last two lines of table 2.3.5. When probing the $\Delta\Omega = 0$ transition to the B state with another $\Delta\Omega = 0$ transition, the intensities are 3/5 for parallel ($||$) and 1/5 for perpendicular ($\perp$) pump probe polarization. In order to achieve the same depolarization behavior for B and $^1\Pi$ state the equal ratios of 1/5 must be chosen. Otherwise the time dependence in the spectra from Fig. 7.21a would be different due to the depolarization, since the final value in both cases (after 2 ps) is given by $I_d = 1/3$ for a depolarized ensemble. The results on time dependent depolarization of ClF in Ar are discussed separately in chapter 2.3.5.

7.6.3 Comparison of experiment and theory

This experiment on ClF in solid Ar can be regarded as a test of the predictions of multidimensional semiclassical quantum theory for non-adiabatic transitions. Theory and experiment agree on important aspects in the sense that the experimental data are reproduced by the evolution of a large fraction of the simulated trajectories. Fig. 7.21b shows a nearly quantitative agreement of the timescale for accumulation of population in the bound triplet states for ClF in Ar (experiment: solid line) and F_2 in Ar (theory: open circles). After excitation of the molecule above its gas phase dissociation limit, the Ar surrounding forces ultrafast recombination onto the lowest set of electronically excited states. When the bond is stretched to the region ($R > 4.5\ a_0$) where the splitting of the states is very small (Fig. 7.20), the wave packet can undergo non-adiabatic transitions (surface hopping) to coupled states. Those which are kept on the repulsive states like $^1\Pi_1$ stay above the crossing region will always have the chance to decay non-adiabatically to the lower $^3\Pi$ states when the wave packet is in the interaction region (cf. Fig. 7.20 and Fig. 7.19). Thus substantial population of 40% is accumulated in the bound triplet states within 1 ps and an exponential rise time of $\tau_f = 500$ fs (cf. Fig. 7.21b). τ_f measures the time it takes to dissociate ClF, flip the spin and recombine the molecule. The transition to the triplet state observed in the experiment (solid line) are especially strong between 250 and 400 fs, when the $Cl - F$ bond is stretched and all electronic states are nearly degenerate. The Ar cage confines the Cl and F within the region of high transition probability and at the same time dissipates a large fraction of the excess energy. In this way it directs the non-adiabatic transitions towards electronic states with lower energy. The excellent agreement allows the conclusion that the nonadiabatic molecular dynamics simulations capture the important processes.

The simulations on F_2/Ar derive a spin-flip time of approx. 60 fs (Fig. 7.18). It is the spin-orbit coupling that allows non-adiabatic transitions between singlet and triplet states. The spin-flip processes are very efficient and occur surprisingly rapidly in view of the weakness of the spin-orbit coupling. The F_2 molecule is lighter than ClF and is excited with higher excess energy in the simulations (the dissociation limit of F_2 is lower) and thus the dissociation is faster. After 60 fs the $F - F$ bond is stretched and thus the spin-flip occurs preferentially at large bond distances, in accordance with the experimental finding. All trajectories presented in ref. [71] show large surface hopping probability among the coupled states for bond distances $R > 4.5$ a$_0$. This coincides with the observation that the electronic states are very close to each other in this region (Fig. 7.20).

In the interpretation of the trajectory simulations previously given [71,221,222], it was stated that the ratio between the population of the singlet and triplet states reaches the statistical equilibrium (1 : 3) in the first excursion. The statistical distribution with larger weight on the triplets can explain why recombination on the excited triplet state is preferred to recombination onto the ground state. It will be instructive to disentangle the effects that electrostatic interactions and spin-orbit coupling in the fragments have on the recombining molecular orbital occupation.

The measured rise time of the triplet population ($\tau_f = 500$ fs) in ClF agrees nearly quantitatively with the calculated population rise in F_2 (cf. Fig. 7.21b). In the future, the recombination onto the ground state should be measured as well as the decreasing population in the initially excited singlet state to complement the information on the triplet states. In this way it can be checked, whether the predicted statistical population of singlet vs. triplet states is established very fast within 60 fs, while the bond is stretched, and the relation to the 500 fs feeding time of the triplet states can be clarified. The singlet ion-pair manifold lies very high in energy and probe wavelengths $\lambda_{probe} \sim 240$ nm are required. The potential surfaces for the gas phase predict the minimum of the difference potential at $R_{win} = 4.6$ a$_0$ and $E_{win} = 21200$ cm^{-1}. The outward motion of the wave packet must be observable and the returning wave packet should have sufficient energy to reach the window a second time.

In principle the repulsive triplets can be probed with wavelengths longer than $\lambda_{probe} = 322$ nm, however the transition dipoles decrease at large $Cl - F$ distances [121]. At small internuclear separations the repulsion of these triplet states requires very high energy of the returning wave packet (cf. Fig. 5.6). The strong energy loss in the first encounter probably explains why this transition was never observed, although it was attempted to record pump-probe spectra with $\lambda_{probe} < 322$ nm.

7.6.4 Comparison to I_2 and Cl_2

In the corresponding spectra for Cl_2/Ar (Fig. 6.17) and I_2/Kr (Fig. 6.6), a very similar behavior is observed. These spectra are recorded for probing deeper in the bound state. Therefore the signal intensity in the first ps is weak and the normalization made for ClF, $I_{\sin glet}/I_{triplet}$, is noisy. It is evident that for $t > 1$ ps the spectra for singlet and triplet excitation agree nearly perfectly. Although in the heavier I_2 molecule the intersystem crossing is not surprising, the similarity of the spectra emphasizes the fact, that energy dissipation becomes highly nonlinear in the strong coupling limit. The singlet excitation in the case of I_2/Kr at $\lambda_{pump} = 480$ nm provides the I fragments with an energy of $E_{pump} = 9300$ cm^{-1}. Direct excitation to the triplet $^3\Pi_1$ at $\lambda_{pump} = 670$ nm results in

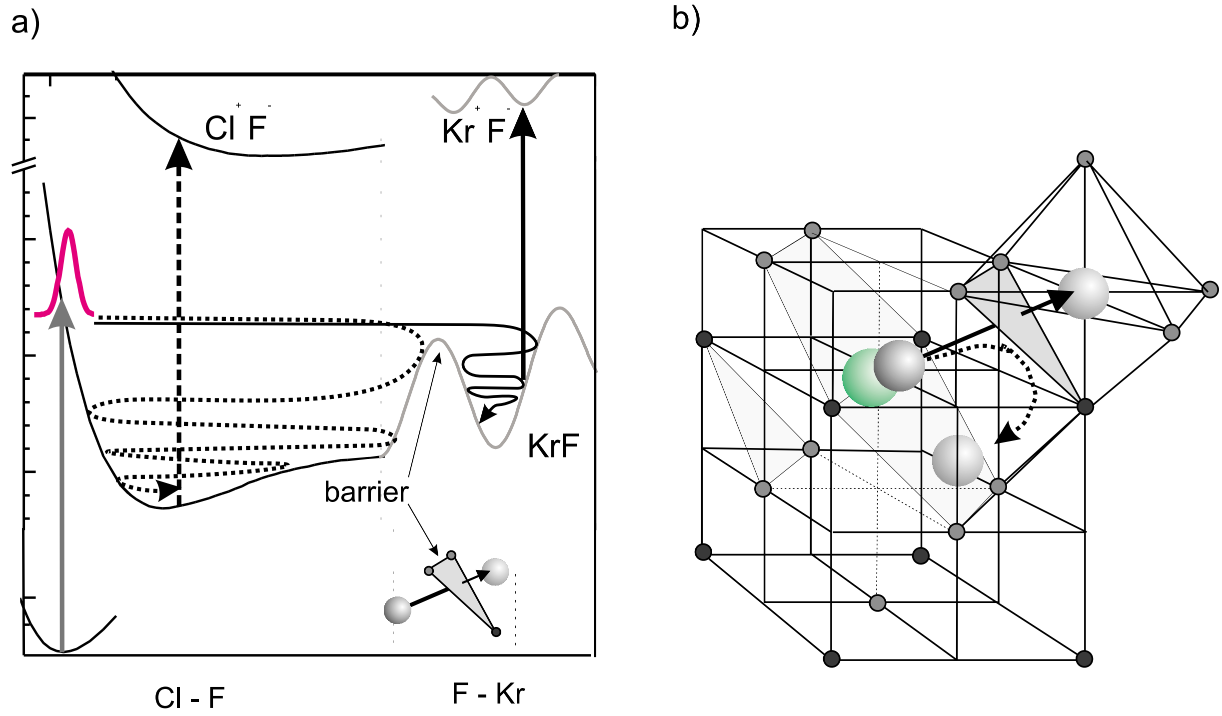

Figure 7.22: a) Potential energy surface of ClF/Kr. The pump pulse excites a $Cl-F$ wave packet, which can either undergo recombination (dashed arrow) in the original cage, or leave the cage by overcoming the barrier (solid arrow). After cage exit the F fragment can be probed by excitation to the Kr^+F^- state. b) Dissociation (solid arrow) vs. recombination (dashed arrow) of ClF in the three dimensional Kr latttice.

$E_{pump} = 3390$ cm^{-1}. Nonetheless both spectra agree for $t > 1$ ps. Obviously the three times higher excess energy prepared in the singlet state is dissipated just as well by the Kr matrix.

7.7 Cage exit dynamics of ClF in Kr

Until this chapter, femtosecond pump-probe spectra of ClF/Ar were analyzed with probe windows in the molecular $Cl-F$ coordinate, which are sensitive to the rich recombination dynamics. This is indicated in Fig. 7.22 by the dashed arrows. From the static experiments on photodissociation of ClF in Kr, it is evident that a large fraction of molecules is permanently dissociated (chapter 5.4.1). The F fragments can be probed via the Kr^+F^- excimer (chapter 4.2.4), i.e. in the $Kr-F$ coordinate. Fig. 7.22a sketches the potential energy surface, and the solid arrows display the cage exit dynamics. For a dissociation of ClF with cage exit of the F fragment, the wave packet prepared by the pump pulse has to overcome the barrier imposed by the gray shaded triangle of Kr atoms. Behind the barrier, the F fragment is surrounded by Kr atoms, and it can be detected by a probe pulse to the Kr^+F^- states. Fig. 7.22b displays the competition of recombination and the cage exit in the three dimensional Kr lattice.

7.7.1 Direct versus delayed exit

The simulations [67, 71] show two ways in which the dissociation of F_2 in Ar can proceed on the fs timescale, and this behavior is more generally observed for photodynamics of molecules in solid rare gases [36]. A direct dissociation proceeds with cage exit after 250 fs, and in the delayed dissociation events the F fragments leave the cage after one or two collisions with the surrounding, e.g. after 1 ps. Trajectories displaying these dynamics from ref. [71] are reproduced in Fig. 7.23.

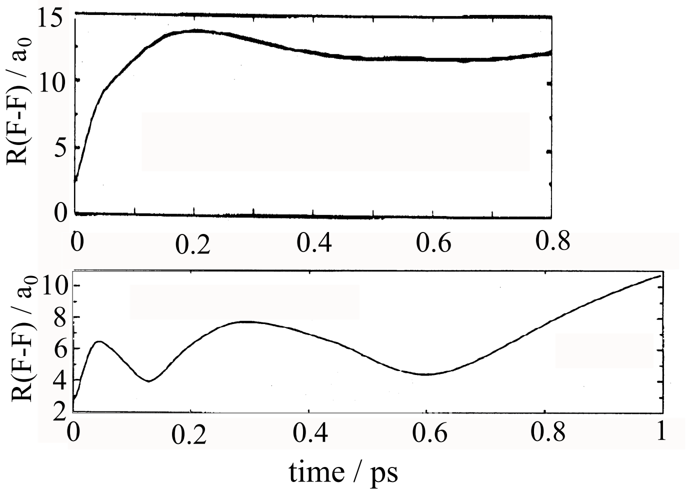

Figure 7.23: Trajectories $R(t)$ taken from the DIM simulations on F_2/Ar in ref. [71]. Panel a) shows a trajectory with direct cage exit after 200 fs. Panel b) demonstrates the delayed cage exit after 1ps. In this trajectory two collisions with the cage walls (at 100 and 300 fs) occur before dissociation.

Figs. 6.12 and 6.13 show pump-probe spectra for ClF/Kr with $\lambda_{pump} = 387$ nm. The ClF dissociation provides the F fragment with a kinetic energy of $E_{kin} = 3070$ cm^{-1}. All spectra have a peak around 300 fs, which is predicted for the direct cage exit. In the spectrum for $\lambda_{probe} = 270$ nm at $T = 4$ K (Fig. 6.13a), for example, the interpretation is straight forward. 270 nm probe F atoms in the center of the O_h site after they escaped from the original substitutional site of the ClF molecule. If the peak at negative time delay (discussed below) is subtracted, the signal is zero at the time origin and rises after 150 fs to reach the first maximum at 300 fs, when the F atoms have reached the center of the O_h site. This corresponds to a straight flight of the F fragment from the initial substitutional site to the O_h site through the Ar_3 triangle, as indicated in Fig. 7.22b. In an estimate that assumes free motion of F with a kinetic energy of $E_{kin} = 3000$ cm^{-1}, it takes 250 fs to travel the distance of 0.49 nm. This time imposes a lower limit, since the fragment will lose some of its energy and move more slowly. In the calculated trajectory for F_2/Ar displayed in Fig. 7.23a, the cage exit is faster than 200 fs, because the molecule is prepared with more than twice the kinetic energy.

The subsequent dynamics cannot be unambiguously assigned at the moment. The peaks at 600 fs and 1 ps may originate either from delayed cage exit (Fig. 7.23b) or from further migration of the F atoms to more remote sites. However, the broad feature at 1 ps that is clearly seen for probing with $\lambda_{probe} = 270$ nm at $T = 20$ K (Fig. 6.13c) most likely corresponds to the delayed cage exit. The time for delayed exit is not as well defined as for the direct cage exit and the broad peak at 1 ps corresponds to the broad distribution of different scattering parameters. Statistics on the trajectories displaying delayed cage exit like Fig. 7.23b are missing but are in preparation in the collaborating theory groups. Fig. 7.10b shows the 2-D quantum simulation for F_2/Ar with pre-excitation of the Ar_3 mode to the 6th vibrational level. While the cage exit without pre-excitation is zero within the simulated 1 ps, a high probability for delayed cage exit is observed after 0.7 ps, where the Ar_3 triangle is pre-excited. This corroborates the assignment of the broad peak around 1 ps to the delayed cage exit, which occurs preferentially in warm samples (20 K), with an excited lattice.

7.7.2 Two ultrafast pathways to $Kr_2^+F^-$

It was mentioned in chapter 6.3.4 that the peak at $t = -50$ fs depends quadratically on the intensity I_{387} of the pulse at 387 nm. This suggests an explanation of this feature in terms of process b) sketched in Fig. 7.24. A pump pulse at 270 nm excites ClF to its $^1\Pi$ state. A two photon resonance with 387 nm leads high into the ion-pair manifold of Cl^+F^-. A wave packet is prepared in the ionic states which corresponds to an F^- ion with sufficient energy to overcome the barrier to the next Kr cage within the ionic manifold. The F^- ion exits the solvent cage and subsequent structural rearrangement leads to formation of the $Kr_2^+F^-$ exciplex. This process occurs for the inverted pulse sequence with

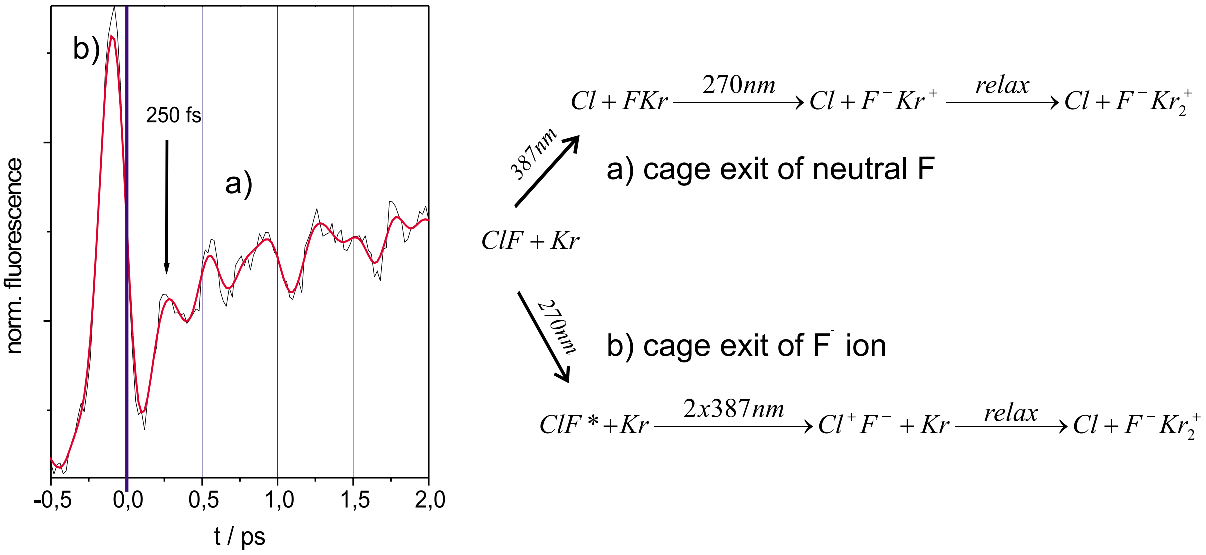

Figure 7.24: Pump-probe spectrum demonstrating cage exit of F in Kr. For positive time delays, the cage exit proceeds via the neural F fragment (process a). The arrival time of the F fragment in the nearest site is 250 fs. For negative time delays the cage exit of the F^- ion is observed (process b).

negative time delay. The peak at $t = -50$ fs suggests that the two photon resonance occurs on the repulsive inner limb of the ClF potential This is supported by the difference potential for the singlet states (Fig. 2.11).

For positive time delay, the pump-pulse $\lambda_{pump} = 387$ nm dissociates ClF and the neutral F fragment leaves the cage as described in chapter 7.7.1. After ~ 250 fs, the F fragment has reached the nearest O_h site and the 270 nm pulse excites the excimer Kr^+F^-. Again structural rearrangement leads to the formation of the fluorescing $Kr_2^+F^-$ exciplex.

7.7.3 Vibration of the Kr cage around F fragments

The pump-probe spectrum in Fig. 6.14 is surprisingly well modulated and the oscillational period increases from 550 fs to 750 fs in the first 4 periods. The assignment of the fluorescence to the $Kr_2^+F^-$ exciplex suggests that this oscillation corresponds to a vibrational mode of the Kr cage around an F fragment. In an anharmonic Morse like molecular potential, the vibrational relaxation would lead to a decreasing period of the vibration, when the harmonic part of the potential is approached (cf. chapter 7.4.2). This is contrary to the observation. On the other hand, the steep van-der-Waals potentials, that govern the $Kr - Kr$ interaction, give rise to potentials with a broad flat minimum and steep walls, that resemble the a square well. In these potentials, higher excitation results in higher frequencies and this would explain the observed slowing down of the vibration in Fig. 6.14 in the course of vibrational relaxation. Moreover, periods around 650 fs are typical for modes of the Kr lattice and are also observed in spectra of I_2/Kr after the dominant I_2 oscillation has decayed [29]. These solvent modes show up in the pump-probe spectra, when the probe wavelength is reduced below the excitation threshold for the resonance of the molecule isolated in the static lattice (e.g. spectra with $\lambda_{probe} = 540$ nm in the Appendix). As was detailed at the end of chapter 7.3.2, the solvent breathing shifts the strongly solvated ionic potentials and thus leads to modulation of the observed spectra.

A microscopic view of the process is suggested from the geometry of the cage exit shown in Fig. 7.22. The F atom points at a triangle of Kr atoms. After photodissociation of ClF, the F atom kicks this triangular window and traverses it. The interaction time of F with the three Kr atoms is well

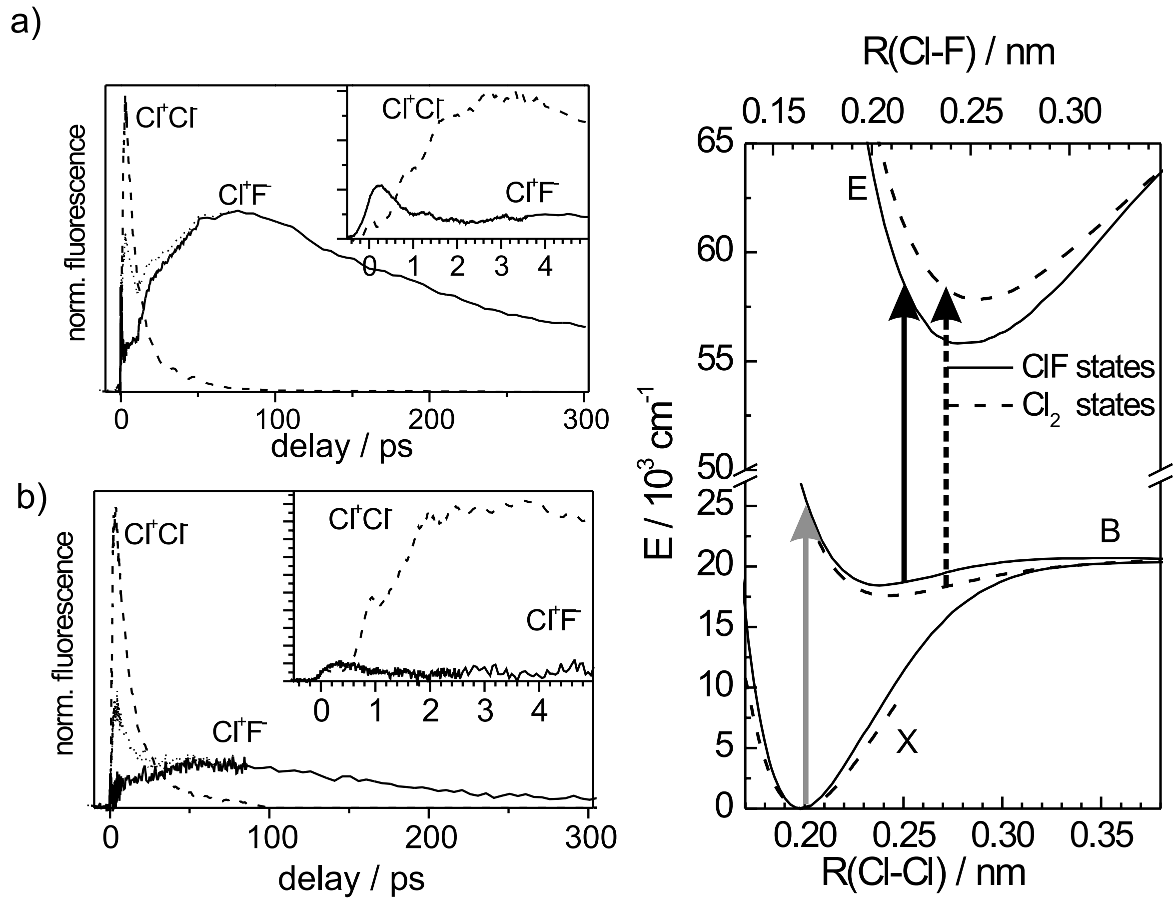

Figure 7.25: Control of $Cl^{+}Cl^{-}$ vs. $Cl^{+}F^{-}$ population demonstrated by pump-probe spectra on $Cl_2 : ClF : Ar$ samples at the concentration $1 : 100 : 100,000$. Both species are excited with $\lambda_{pump} = 387$ nm. The fluorescence $\lambda_{LIF} = 420$ nm monitors Cl_2 and ClF (dotted), $\lambda_{LIF} = 360$ nm monitors Cl_2 only (dashed). From these traces the ClF signal is calculated (solid). a) $\lambda_{probe} = \lambda_{control} = 282$ nm, b) $\lambda_{probe} = \lambda_{control} = 282$ nm. c) Unshifted potential surfaces for ClF and Cl_2. The bond distance of ClF (top scale) is calibrated to obtain the same equilibrium position as for Cl_2 (bottom scale). The potentials are very similar. The dashed and the solid arrow indicate the probe window for Cl_2 and ClF, respectively.

defined and this will trigger coherent motion of the Kr atoms. The F is now in the interstitial O_h site (Fig. 7.22b) and vibrationally relaxes. The coherent modulation of the Kr cage size shifts the ionic $Kr^{+}F^{-}$ states, formed by the F fragment with either of the Kr cage atoms, up and down and this produces the observed oscillations. The rise and decay of the signal envelope shown in the inset is a signature of vibrational relaxation of the F atom within the cage and energy loss from the Kr mode.

This interpretation should be confirmed in the future by MD simulations on ClF/Kr. Trajectory calculations can be found on the related system NO in Ar [215]. NO is isolated on a substitutional site of an Ar lattice. Excitation to a Rydberg state of NO leads to an impulsive cage breathing. The simulations corroborate the slowing down of the cage vibration.

7.8 Relaxation-time-control of Cl_2 vs. ClF

Recent experiments aim at an extension of coherent control or quantum control strategies to molecules in condensed phases, i.e. to systems with dissipation. In the Gerber group evolutionary strategies are used to find the optimal pulse sequence to steer the fluorescence of two substances with nearly identical absorptions in the liquid phase [223] and a contrast ratio of $1:1.5$ is obtained. Based on the fact that shaped laser pulses can control the relative fluorescence from the two molecules, the authors conclude that coherences must survive at least for the timescale of 100 fs.

This chapter treats the experiments on a solid Ar sample, doped with $Cl_2 : ClF : Ar$ at a relative concentration of $1 : 1000 : 100,000$, in the spirit of control with ultrafast laser pulses in a double pulse scenario (Tannor-Kosloff-Rice scheme [15, 16, 20]). $\lambda_{pump} = 387$ nm excites Cl_2 and ClF with nearly equal probability as can be judged from the $A' \rightarrow X$ fluorescence intensities (Fig. 4.2)[9]. The wavelengths $\lambda_{probe} = 280$ and 282 nm probe Cl_2 and ClF to their ionic states Cl^+Cl^- and Cl^+F^- (Fig. 7.25a and b). The fluorescence intensity from these ion-pair states is proportional to the number of these ion-pair species produced in the double pulse sequence. Now, the control target is to maximize the yield of one of the two ion-pair species, i.e. its fluorescence. The only parameter varied in this control scheme is the time delay between $\lambda_{pump} = 387$ nm and $\lambda_{control} = 280$ or 282 nm.

When the fluorescence is detected at $\lambda_{LIF} = 420$ nm (dotted line in Fig. 7.25a), both molecules contribute to the signal (cf. Fig. 4.8a and b). Fluorescence at $\lambda_{LIF} = 360$ nm is exclusively due to Cl_2 (cf. Fig. 4.8). The pump-probe spectrum for $\lambda_{control} = 282$ nm with $\lambda_{LIF} = 360$ nm is indicated by a dashed line in Fig. 7.25a. The dashed spectrum is used to decompose the dotted spectrum ($\lambda_{LIF} = 420$ nm) into a signal for Cl_2 and ClF. The resulting ClF contribution is shown in Fig. 7.25a as a solid line.

The inset in Fig. 7.25a shows the decomposed fluorescence intensities I_{ClF} (solid) and I_{Cl_2} (dashed), and therefore the number of excited ion-pair species Cl^+F^- vs. Cl^+Cl^- on a shorter timescale. In the maximum of the Cl^+Cl^- signal at time $t = 3$ ps, the ratio of the excited molecules is $I_{ClF}/I_{Cl_2} = 1/5$. For times $t > 70$ ps I_{Cl_2} almost vanishes and I_{ClF} has a maximum at $t = 70$ ps. The contrast ratio at this time is better than $I_{ClF}/I_{Cl_2} = 50/1$. Thus by varying the time delay from 3 ps to 70 ps the ratio between ClF and Cl_2 fluorescence can be switched by a factor 250 in this one parameter control scheme. In view of the similarity of the two PES for Cl_2 and ClF (Fig. 5.7) the contrast ratios obtained are excellent. For a $Cl_2 : ClF$ concentration of $1 : 1$, the contrast at $t = 3$ ps in favor of Cl_2 would improve to $500 : 1$.

Fig. 7.25b shows the same procedure for a different control wavelength $\lambda_{control} = 280$ nm and an even better switching between ClF and Cl_2 ion-pair species is obtained. Again ClF dominates for $t > 100$ ps, while the Cl_2 fluorescence is zero. At $t = 3$ ps on the other hand, $I_{ClF}/I_{Cl_2} = 1/10$.

Besides the control on the ps timescale, control on the femtosecond timescale can be seen in Fig. 7.25a in the early peak at 50 fs, which belongs to Cl^+F^- (solid line), whereas from 1 ps onwards the Cl^+Cl^- signal (dashed) dominates. In chapter 7.3.2 the early peak is identified as the outward moving ClF wave packet. This demonstrates the selective excitation of Cl_2 vs. ClF on the femtosecond timescale as wave packet timing control with a contrast ratio of $1 : 3.4$. For an optimized control wavelength this can be improved.

The maxima in Fig. 7.25a at $t = 3$ ps for Cl^+Cl^- and at $t = 100$ ps for Cl^+F^- are due to vibrational relaxation (cf. chapter 7.4). Therefore the term relaxation-time control may be adequate. Fig. 7.25c reproduces the potential surfaces of ClF and Cl_2 and shows the probe window for ClF by the solid arrow and for Cl_2 by the dotted arrow. The relaxation-time control scheme delivers excellent contrast ratios. The population in high vibrational levels of Cl_2 quickly decays below the probe window and the resonance to Cl^+Cl^- is lost. Obviously, this control scheme is entirely incoherent, as it makes use of vibrationally relaxed population in the intermediate state. The wave packet timing control around 50 fs exploits the wave packet motion in a Tannor-Kosloff-Rice scheme [15, 16, 20]. However, a quantum mechanical coherence is not necessary in this scheme either.

---

[9] The much larger absorption of Cl_2 compared to ClF balances the lower concentration.

7.9 Dissipation and vibrational coherence

In chapter 7.3, the spectra for I_2/Kr and ClF/Ar were analyzed in terms of wave packet dynamics. The wave packet is initially prepared in the molecular $I-I$ or $Cl-F$ coordinate. In the first oscillation of the molecule, a substantial fraction of the energy is already transferred to the solvent by collisions of the molecular fragments with the cage. Despite the dramatic energy loss, the pump-probe transients show oscillations due to vibrational coherence. Moreover, the collision induces vibrational motion of the cage atoms. This in turn appears in the pump-probe spectra, since changing the size of the solvent cavity shifts the strongly solvated ion-pair states of the molecule up and down with the coherent oscillations of the cage breathing [29]. If a probe wavelength close to the threshold is chosen, the probe transition is shifted into and out of resonance periodically..

Energy dissipation is intimately connected to decoherence, since the interaction of the originally excited molecule with the ”bath” of atoms induces both processes. The results of this thesis demonstrate that a strong dissipation of energy can take place in a way that preserves the vibrational coherence of the wave packet to a large extent. Even after the strongest collisions at high energy (e.g. Fig. 6.2), the oscillations survive for several ps. Inspection of the spectra on a longer timescale (Fig. 6.4a) reveals that the contributions from an unmodulated background increase with the interaction energy, since the modulations decay faster for shorter pump wavelength. This background is a signature of the decoherence of the wave packet, which is induced by the random distribution of scattering conditions. However, the detection of the coherence with the probe pulse must be considered, as well. The spectra in Fig. 6.2b and 6.4b, that probe a wave packet excited at the dissociation limit of I_2 at $\lambda_{pump} = 500$ nm with different λ_{probe}, demonstrate that the background increases with shorter $\lambda_{probe,}$ as the probe window moves to lower energies E_{win}. The background disappears entirely if the wave packet is probed with a window below resonance ($\lambda_{probe} = 530$ and 540 nm). The reason for this is closely related to the effect of the probe window on the apparent vibrational period discussed in chapter 7.2. If the probe window energy E_{win} is above the energy of the wave packet, then only the highest fraction of vibrational levels that make up the wave packet are recorded. The population in these levels has not yet suffered the energy loss and the decoherence is negligible. A probe window in the potential minimum, on the other hand, monitors all parts of the wave packet. The energy of the wave packet determines the detection sensitivity, which scales with the velocity as $1/v$ or with the energy E of the vibrational level as $1/\sqrt{E}$. Thus the wave packet is probed over a broad range of energies and thus different scattering parameters with comparable sensitivity. This blurs the modulations in the spectra. The trend, that the modulation depth decreases with shorter probe wavelength is observed as well in ClF/Ar.

The theoretical description of wave packets that experience dissipation still in its infancy. The loss of coherence has to be implemented in the density matrix formalism by empirical parameters. In reduced dimensionality approaches the problem is manifest in the somewhat arbitrary definition of the quantum mechanical ”system” and the ”bath”. The detailed experimental results in the model systems presented here will allow testing further predictions from theory.

The preserved vibrational coherence observed even in the regime of strong system-bath coupling demonstrates that there is good prospect to coherent control in condensed phase reactions.

Chapter 8

Summary

Ultrafast spectroscopy of I_2 in solid Kr

The model system I_2 in Kr matrix is examined with femtosecond pump-probe spectroscopy to develop appropriate strategies for the strong system-bath coupling in the condensed phase. A novel evaluation scheme is presented that allows the extraction of information on potentials and dynamics directly from the experiment without the aid of simulations. The vibrational frequency ω_e and the anharmonicity $\omega_e x_e$ of the excited B state are measured over a wide energy range, although the absorption spectrum itself is structureless and contains no information except the Franck-Condon envelope. A one dimensional (1-D) representation of the multidimensional excited state potential is constructed.

It is shown that both pump and probe wavelength have to be optimized when vibrational frequencies are deduced from femtosecond-pump-probe spectra. The effect of the probe window on the measured frequency can exceed 7% in the case of I_2/Kr, which is on the order of the anharmonicity itself. In systems with even stronger interactions, where the wave packet is substantially broadened in energy space (e.g. in liquids with large fluctuations), the question of which part of the wave packet is probed will gain importance.

Snapshots of a wave packet trajectory near the dissociation limit are taken, which directly display the inelastic and nonlinear fragment cage ($I - Kr$) interaction. Vibrational relaxation rates that vary over three orders of magnitude are derived. In the strongest interactions, more than 50 phonons of the Kr lattice are created in a single collision. This is equivalent to 3000 cm^{-1} or 57% of the initial energy. Near the potential minimum the energy loss is only 1 phonon in 5 periods. Despite the strong interactions, vibrational coherences survive up to 10 ps. The interplay of vibrational relaxation and predissociation was further investigated in the diploma thesis of Markus Gühr. This work [115, 116] relies on the good knowledge of the energy dissipation rates derived here.

The experimental findings are compared to calculated potential energy surfaces (PES) and molecular dynamics (MD) simulations. The experiments suggest the use of multiple trajectories in order to derive an averaged 1-D potential that goes beyond the approximation of a frozen solvent cage.

Ultrafast photodynamics of ClF in solid rare gases

The molecule ClF isolated in solid rare gases Ar and Kr is established as a new model system that allows for analysis and control of the interplay of dissociation and recombination dynamics. On the spectroscopic side, the $A' \to X$ emission of ClF is analyzed and found to be a convenient measure of the concentration of recombining ClF molecules. The energetics of the ion-pair state Cl^+F^- in Ar is clarified in absorption and emission, which is essential for monitoring the recombination dynamics by fs-pump-probe spectroscopy with LIF detection. The spectroscopic characteristics of the F fragment after photodissociation of ClF in Ar and Kr and the respective quantum yields are compared to previous experiments on F_2 dissociation. A laser control scheme is demonstrated, which reversibly shuttles F atoms from ClF to interstitial Kr sites and back to the Cl radical.

The evaluation scheme to derive vibrational relaxation rates from fs-pump-probe spectra is applied to ClF/Ar and Cl_2/Ar. Two different regimes of energy dissipation are found. The rate for high excitation energies of ClF/Ar in the B state exceeds 35% (2600 cm^{-1}) per period, and 40 phonons of the Ar lattice are created in one collision. Above the gas phase dissociation limit the interaction of the fragments with the cage is strong and the exponentially increasing dissipation rate displays the nonlinear nature of the interaction. Wave packets excited to the repulsive $^1\Pi$ state lose more than 50% of the energy in the first period. If the molecule is recombined and bound in the molecular potential, the vibrational relaxation is slow ($\sim$ 6 cm^{-1} or 0.2% per period). For Cl_2/Ar the rapid energy loss in the first collision is even stronger (60% per period), because Cl and Ar have nearly equal masses. The MD simulations predict shock-waves that quickly remove the energy from the excited molecule.

The ultrafast coupling of energy into the solvent modes shows up also in the oscillatory structure of the pump-probe spectra of the vibrational wave packets of ClF in Ar or Cl_2 in Ar. This is verified by molecular dynamics (MD) and two dimensional quantum simulations. The vibration of the Kr cage around an F fragment driven by ClF dissociation is observed. As a general result it is confirmed that the vibrational coherence is preserved over several periods when the energy from the initially excited molecule (”chromophore”) is transferred to the solvent on an ultrafast timescale. The solvent cage is excited impulsively and performs coherent vibrations. A well defined geometry and timing of the interactions seem essential for preserved coherence. This may in future offer a route to coherent control in dissipative systems.

Ultrafast tilting of the molecular $Cl-F$ bond ($\tau_r = 1.2$ ps) in dissociation-recombination dynamics in Ar is monitored by polarization sensitive fs-pump-probe spectroscopy. The small fragment size and the isotropic cage (substitutional site) allow for skewed scattering events of F atoms with the cage atoms. The evaluation in terms of the ultrafast decay of the anisotropy is valuable for comparison with simulations, since the difficult calculation of ion-pair states is circumvented. It is verified that the $I-I$ bond experiences no angular reorientation in its axially symmetric double substitutional site. This situation in solid Kr differs from previous experiments in liquid Kr, where I_2 was found to rotate.

Excitation to the singlet state $^1\Pi$ and probing the bound triplet states $^3\Pi$ evidences the ultrafast nonadiabatic transition to the lowest excited electronic states, unequivocally for ClF/Ar, Cl_2/Ar and I_2/Kr. This transition involves an ultrafast spin-flip. It is surprising that it occurs on the femtosecond timescale also in small molecules like ClF, although the intramolecular spin-orbit interaction is weak. The effect was predicted for F_2/Ar by nonadiabatic MD simulations. The accumulation of population in the bound triplet state within $\tau_f = 500,$ fs observed in the experiment, is in quantitative agreement with these simulations. It is an upper limit for the spin-flip time, since it measures the time for dissociation plus spin-flip plus recombination.

The cage exit of F fragments after excitation of ClF/Kr is monitored in real time. The time to reach the nearest interstitial O_h site is $\tau_{exit} = 250$ fs, and an indirect cage exit after 1 ps is observed especially for warm Kr matrices. These results are in excellent agreement with the simulations of F_2/Ar.

A double-pulse control scenario is demonstrated in mixed $Cl_2/ClF/Ar$ solids. Variation of the time delay between a pump and a control pulse switches between the fluorescences of Cl^+Cl^-/Ar and Cl^+F^-/Ar with a very good contrast ratio of 1:250. In these experiments the excited state population of the ion-pair species is controlled. The mechanism exploited in this scheme is ultrafast vibrational relaxation. A wave-packet-timing control in a Tannor-Kosloff-Rice scheme is also demonstrated on a timescale of 50 fs.

Setup for ultrafast spectroscopy

In the experimental setup two major achievements were made. Two non-collinear optical parametric amplifiers (NOPAs) were built for the generation of tunable sub 30 fs pulses. Their efficiency was doubled in comparison to the commercially available ones. With this improvement two experiments with four independently tunable femtosecond pulses can run simultaneously, while a considerable fraction of laser power is retained for a third experiment.

The characterization of the femtosecond pulses was extended in a flexible setup that can be used to characterize pulses from the infrared to the ultraviolet spectral region by Frequency Resolved Optical Gating (FROG). The cross-correlations can be taken in situ, simultaneously with the pump-probe experiment.

Future Prospects

Cage exit dynamics

The cage exit dynamics of F fragments deserve further experimental investigation on the femtosecond timescale. Two directions of investigation are very promising. First, experiments on the cage exit after excitation to the $^1\Pi$ state should be performed. Up to now, experiments with this excitation were accomplished only in Ar and with a probe laser that records the recombination dynamics. They were analyzed in chapter 7.6 with focus on the spin flip. It was shown that the 1.5 eV higher excess energy is absorbed by the matrix within one or two periods. The 2-D quantum simulations presented in Fig. 7.10 demonstrate a greatly enhanced exit probability, if the Ar is pre-excited. This implies that a large effect of the excess energy on the cage exit dynamics can be expected, as this leads to large amplitude motion of the rare gas atoms. These experiments should be carried out in $Kr.$

The second direction that should be pursued is cage exit in multiply doped Ar matrices. The ArF excimer states lie too far in the UV but co-doping with Kr or Xe can be used to detect the F fragments. Then the shuttling of the F atom from Cl to the co-dopand (e.g. Xe) and back can be followed on the femtosecond timescale. It will be interesting to compare the results of ultrafast experiments in different matrices, since already the static bleaching experiments showed an increase of the permanent dissociation efficiency by an order of magnitude on going from Ar to $Kr.$

New Molecules

The molecule $ClXeF$ was observed after photolysis of ClF in Xe matrices [95]. The same experiments that tried to produce $ClKrF$ were unsuccessful. However, calculations show that this molecule is bound by 0.4 eV in the linear configuration and there is a barrier to the formation of $ClF + Kr$ [97]. Since the bleaching experiments show that ClF is effectively dissociated, it is expected that the $ClKrF$ molecule can be generated with properly chosen pulse parameters. In any case it will be very interesting to analyze the formation of either $ClKrF$ or $ClXeF$ in real time with femtosecond pulses.

Active control of molecular dynamics

The active control of molecular dynamics in these model systems will be pursued in several ways. Strong infrared laser pulses will be used to align molecules with the polarization vector of the light field [224]. The feasibility has been demonstrated in the gas phase [225, 226], and the experiments on the statistical reorientation of the ClF bond (chapter 7.5.3) show a way to measure the ultrafast alignment of molecules also in the condensed phase.

The use of double pulses or tailored pulses from a pulse-shaper will be used to actively control the interplay of solute-solvent-solute interaction that was demonstrated in this thesis. The idea is to prepare wave packets with appropriate timing that exploit the coherence of the molecular vibration and the cage motion, e.g. to enhance the cage exit.

Bibliography

[1] A. Zewail and R. Bernstein, “Real-time laser femtochemistry: Viewing the transition from reagents to products,” in *The Chemical Bond*, A. Zewail, ed., (Academic Press, Inc., Boston, 1992), pp. 223–279.

[2] A. Zewail, *Femtochemistry – Ultrafast Dynamics of the Chemical Bond, Vols. I and II* (World Scientific, Singapore, 1994).

[3] M. El-Sayed, I. Tanaka, and Y. Molin, *Ultrafast Processes in Chemistry and Photobiology – Chemistry for the 21st century* (IUPAC, Blackwell Scientific, Oxford, 1994).

[4] D. Wiersma, *Femtosecond Reaction Dynamics* (Royal Academiy of Arts and Sciences, North Holland, Amsterdam, 1994).

[5] J. Manz and A. Castleman, Jr., “special issue on femtochemistry,” J. Phys. Chem. **97,** 12423–12644 (1993).

[6] *Femtosecond Chemistry*, J. Manz and L. Wöste, eds., (VCH, Weinheim, 1995), Vol. 1 and 2.

[7] M. Chergui, *Femtochemistry – Ultrafast Chemical and Physical Processes in Molecular Systems* (World Scientific, Singapore, 1996).

[8] *Ultrafast Phenomena XI*, T. Elsässer, J. Fujimoto, D. A. Wiersma, and W. Zinth, eds., (Springer, Berlin, 1998).

[9] A. H. Zewail, “Femtochemistry,” J. Phys. Chem. A **104,** 5660–5694 (2000).

[10] M. Shapiro and P. Brumer, “The equivalence of unimolecular decay product yields in pulsed and cw laser excitation,” J. Chem. Phys. **84,** 540–541 (1986).

[11] P. Brumer and M. Shapiro, “Control of unimolecular reactions using coherent light,” Chem. Phys. Lett. **126,** 541–546 (1986).

[12] P. Brumer and M. Shapiro, “Laser control of molecular processes,” Ann. Rev. Phys. Chem. **43,** 257–282 (1992).

[13] M. Shapiro, C. Zhidang, and P. Brumer, “Simultaneous control of selectivity and yield of molecular dissociation: pulsed incoherent interference control,” Chem. Phys. **217,** 325–340 (1997).

[14] B. Sheehy, B. Walker, and L. F. DiMauro, “Phase control in the two-color photodissociation of HD^+,” Phys. Rev. Lett. **74,** 4799–4802 (1995).

[15] D. J.Tannor and S. A. Rice, “Control of selectivity of chemical reaction via control of wave packet evolution,” J. Chem. Phys. **83,** 5013–5018 (1985).

[16] R. I. Gordon and S. A. Rice, “Active control of the dynamics of atoms and molecules,” Am. Rev. Phys. Chem. **48,** 601–641 (1987).

[17] A. P. Peirce, M. A. Dahleh, and H. Rabiz, “Optimal control of quantum-mechanical systems: existence, numerical approximation, and applications,” Phys. Rev. A **37,** 4950–4964 (1988).

[18] R. I. Cukier, C. Denk, and M. Morillo, “Control of tunneling processes with an external field in a four-level system: an analytic approach,” Chem. Phys. **217,** 179–199 (1997).

[19] J. Cao and K. R. Wilson, “A simple physical picture for quantum control of wave packet localization,” J. Chem. Phys. **107,** 1441–1450 (1997).

[20] A. Rice and M. Zhao, *Optical control of molecular dynamics* (Wiley, New York, 2000).

[21] Z. Li, R. Zadoyan, A. V. Apkarian, and C. C. Martens, “Femtosecond many-body dynamics of caging: Experiment and simulation of I_2 photodissociation-recombination in solid Ar,” J. Phys. Chem. **99,** 7453–7465 (1995).

[22] N. F. Scherer, D. M. Jonas, and G. R. Fleming, “Femtosecond wave packet and chemical reaction dynamics of iodine in solution: Tunable probe study of motion along the reaction coordinate,” J. Chem. Phys. **99,** 153–168 (1993).

[23] M. Sterling, R. Zadoyan, and V. A. Apkarian, “Interrogation and control of condensed phase chemical dynamics with linearly chirped pulses: I_2 in solid Kr,” J. Chem. Phys. **104,** 6497–6506 (1996).

[24] J. Xu, N. Schwentner, S. Hennig, and M. Chergui, “Ultrafast Intramolecular and Caging Dynamics of I_2 in CCl_4 from Resonance Raman Spectroscopy,” J. Raman Spectr. **28,** 433–443 (1997).

[25] R. Zadoyan, Z. Li, P. Ashjian, C. C. Martens, and V. A. Apkarian, “Femtosecond dynamics of coherent photodissociation-recombination of I_2 isolated in matrix Ar,” Chem. Phys. Lett. **218,** 504–514 (1994).

[26] R. Zadoyan, Z. Li, C. C. Martens, and V. A. Apkarian, “The breaking and remaking of a bond: Caging of I_2 in solid Kr,” J. Chem. Phys. **101,** 6648–6657 (1994).

[27] R. Zadoyan, M. Sterling, and V. A. Apkarian, “Dynamical spectroscopy of many-body interactions: Coherent vibrations and predissociation of I_2(B) in solid Kr,” J. Chem. Soc., Faraday Trans. **92,** 1821–1829 (1996).

[28] R. Zadoyan, M. Sterling, M. Ovchinnikov, and V. A. Apkarian, “Predissociation Dynamics of I_2(B) in Liquid CCl_4 Observed Through Femtosecond Pump-Probe Measurements: Electronic Caging Through Solvent Symmetry,” J. Chem. Phys. **107,** 8446–8460 (1997).

[29] R. Zadoyan, J. Almy, and V. A. Apkarian, “Lattice dynamics from the "eyes" of the chromophore - Real-time studies of I_2 isolated in rare gas matrices,” J. Chem. Soc., Faraday Trans. **108,** 255–269 (1997).

[30] A. V. Benderskii, R. Zadoyan, and V. A. Apkarian, “Caged Spin-Orbit Excited I*($^2P_{1/2}$) + I*($^2\mathrm{P}_{1/2}$) Atom Pairs in Liquids and in Cryogenic Matrices: Spectroscopy and Dipolar Quenching,” J. Chem. Phys. **107,** 8437–8445 (1997).

[31] C. F. Bardeen, J. Che, K. R. Wilson, V. V. Yakovlev, V. A. Apkarian, C. C. Martens, R. Zadoyan, B. Kohler, and M. Messina, “Quantum control of I_2 in the gas phase and in condensed phase solid Kr matrix,” J. Chem. Phys. **106,** 8486–8503 (1997).

[32] M. Bargheer, K. Donovang, P. Dietrich, and N. Schwentner, “Extraction of potentials and dynamics from condensed-phase pump-probe spectra: Application to I_2 in Kr matrices,” J. Chem. Phys. **111,** 8556–8564 (1999).

[33] I. Almy, K. Kizer, R. Zadoyan, and V. Apkarian, “Resonant Raman, Hot, and Cold Luminescence of Iodine in Rare Gas Matrixes,” J. Phys. Chem. A **104,** 3508–3520 (2000).

[34] T. Kobayashi and A. Shirakawa, “Tunable visible and near-infrared pulse generator in a 5 fs regime,” Appl. Phys. B **70,** 239–246 (2000).

[35] E. Riedle, M. Beutter, S. Lochbrunner, J. Piel, S. Schenkl, S. Sporlein, and W. Zinth, “Generation of 10 to 50 fs pulses tunable through all of the visible and the NIR,” Appl. Phys. B **71,** 457–465 (2000).

[36] V. A. Apkarian and N. Schwentner, “Molecular Photodynamics in Rare Gas Solids,” Chem. Rev. **99,** 1481 – 1514 (1999).

[37] M. Ovchinikov and V. Apkarian, “Mixed-order semiclassical dynamics in coherent state representation: The connection between phonon sidebands and guest-host dynamics,” J. Chem. Phys. **108,** 2277–2284 (1998).

[38] R. B. Gerber, A. B. McCoy, and A. B. Garcia-Vela, “Photochemical reactions in weakly bound clusters,” Annu. Rev. Phys. Chem. **45,** 275–314 (1994).

[39] M. Gruebele, G. Roberts, M. Dantus, R. M. Bowman, and A. H. Zewail, “Femtosecond Temporal Spectroscopy and Direct Inversion to the Potential: Application to Iodine,” Chem. Phys. Lett. **166,** 459–469 (1990).

[40] C. Wan, M. Gupta, J. Baskin, Z. Kim, and A. Zewail, “Caging phenomena in reactions: Femtosecond observation of coherent, collisional confinement,” J. Chem. Phys. **106,** 4353–4356 (1997).

[41] Q. Liu, J.-K. Wang, and A. Zewail, “Femtosecond dynamics of dissociation and recombination in solvent cages,” Nature **364,** 427–430 (1993).

[42] C. Lienau and A. H. Zewail, “Femtochemistry at high pressures. Solvent effect in the gas-to liquid transition region,” Chem. Phys. Lett. **222,** 224–232 (1994).

[43] C. Lienau, J. C. Williamson, and A. H. Zewail, “Femtochemistry at high pressures. The dynamics of an elementary reaction in the gas-liquid transition region,” Chem. Phys. Lett. **213,** 289–296 (1993).

[44] Q. Liu, C. Wan, and A. H. Zewail, “Femtosecond reaction dynamics in the gas-to-liquid transition region: Observation of a three-phase density dependence,” J. Chem. Phys. **105,** 5294–5297 (1996).

[45] R. Zadoyan, N. Schwentner, and V. A. Apkarian, “Wavepacket diagnosis with chirped probe pulses,” Chem. Phys. **233,** 353 – 363 (1998).

[46] M. Bargheer, M. Gühr, P. Dietrich, and N. Schwentner, “Femtosecond spectroscopy of fragment cage dynamics: I_2 in Kr,” Phys. Chem. Chem. Phys. **4,** 75–81 (2002).

[47] D. L. Huestis and N. E. Schlotter, “Diatomics-in-molecules potential surfaces for the triatomic rare gas halides: Rg_2X,” J. Chem. Phys. **69,** 3100–3107 (1978).

[48] W. R. Wadt and P. Hay, “The low-lying electronic states of Ar_2F,” Appl. Phys. Lett. **30,** 573–575 (1977).

[49] W. R. Wadt and P. J. Hay, “Electronic states of Ar_2F and Kr_2F,” J. Chem. Phys. **68,** 3850–3886 (1978).

[50] G. Hoffman and M. Colletto, “An ab initio study of some noble gas monohalides,” J. Chem. Phys. **114,** 2219–2227 (2001).

[51] T. H. Dunning, Jr. and P. J. Hay, “The covalent and ionic states of the rare gas monofluorides,” J. Chem. Phys. **69,** 134–149 (1978).

[52] *Excimer Lasers*, C. Rhodes, ed., (Springer-Verlag, Berlin Heidelberg, 1984).

[53] H. Kunttu and V. Apkarian, “Photodissociation of F_2 in crystalline krypton: effect of molecule-lattice prealignment,” Chem. Phys. Lett. **171,** 423–429 (1990).

[54] H. Kunttu, J. Feld, R. Alimi, A. Becker, and V. Apkarian, “Charge transfer and radiative dissociation dynamics in fluorine-doped solid krypton and argon,” J. Chem. Phys. **92,** 4856–4875 (1990).

[55] R. Sauerbrey, Y. Zhu, F. K. Tittel, and W. L. Wilson, “Optical emission and kinetic reactions of four-atomic rare gas halide exciplex Ar_3F,” J. Chem. Phys. **85,** 1299–1302 (1986).

[56] V. Aquilanti, D. Cappelletti, V. Lorent, E. Luzzatti, and F. Pirani, “Molecular beam studies of weak interactions of open-shell atoms: The ground and lowest excited states of rare-gas halides,” J. Phys. Chem. **97,** 2063–2071 (1993).

[57] V. Aquilanti, E. Luyyatti, F. Pirani, and G. G. Volpi, “Molecular beam studies of weak interactions for openßshell systems: The ground and lowest excited states of ArF, KrF and XeF,” J. Chem. Phys. **89,** 6165–6175 (1988).

[58] M. Ovchinnikov and V. A. Apkarian, “Quantum interference in resonant Raman spectra of I_2 in condensed media,” J. Chem. Phys. **106,** 5775–5778 (1997).

[59] A. A. Buchachenko and N. F. Stepanov, “Ar-I_2 interactions: The models based on the diatomics-in-molecule approach,” J. Chem. Phys. **104,** 9913–9925 (1996).

[60] M. Ben-Nun, R. D. Levine, and G. R. Fleming, “Solvent-induced nonadiabatic transitions in iodine: An ultrafast pump-probe computational study,” J. Chem. Phys. **105,** 3035–3056 (1996).

[61] M. Ben-Nun, R. D. Levine, D. M. Jonas, and G. R. Fleming, “Prompt solvent-induced electronic predissociation of femtosecond pumped iodine. A computational study,” Chem. Phys. Lett. **245,** 629–638 (1995).

[62] M. Ovchinnikov and V. A. Apkarian, “Condensed phase spectroscopy from mixed-order semiclassical molecular dynamics: Absorption, emission, and resonant Raman spectra of I_2 isolated in solid Kr,” J. Chem. Phys. **105,** 10312–10331 (1996).

[63] V. S. Batista and D. F. Coker, “Nonadiabatic molecular dynamics simulation of photodissociation and geminate recombination of I_2 liquid xenon,” J. Chem. Phys. **105,** 4033–4054 (1996).

[64] V. S. Batista and D. F. Coker, “Nonadiabatic molecular dynamics simulation of ultrafast pump-probe experiments on I_2 in solid rare gases,” J. Chem. Phys. **106,** 6923–6941 (1997).

[65] V. S. Batista and D. F. Coker, “Nonadiabatic molecular dynamics simulations of the photofragmentation and geminate recombination dynamics in size-selected $I_2^- Ar_n$ cluster ions,” J. Chem. Phys. **106,** 7102–7116 (1997), erratum: J. Chem. Phys. 110, 6583-6584 (1999).

[66] N. Yu, C. J. Margulis, and D. F. Coker, “Influence of solvation environment on excited state avoided crossings and photodissociation dynamics,” J. Phys. Chem. B **105,** 6728–6737 (2001).

[67] R. Alimi, R. B. Gerber, and V. A. Apkarian, “Dynamics of molecular reactions in solids: Photodissociation of F_2 in crystalline Ar,” J. Chem. Phys. **92,** 3551–3558 (1990).

[68] K. S. Kizer and V. A. Apkarian, “Orbital alignment during cage-exit of open-shell photofragments: F in solid Ar and Kr,” J. Chem. Phys. **103,** 4945–4952 (1995).

[69] A. Krylov, R. Gerber, and V. Apkarian, “Adiabatic approximation and non-adiabatic effects for open-shell atoms in an inert solvent: F atoms in solid Kr,” Chem. Phys. **189,** 261–272 (1994).

[70] A. Krylov and R. Gerber, “Reorientation dynamics of electronic orbitals in condensed phases: Simulations of the $F(^2P)$ atoms in solid Kr,” Chem. Phys. Lett. **231,** 395 (1994).

[71] M. Y. Niv, M. Bargheer, and R. B. Gerber, “Photodissociation and recombination of F_2 molecule in Ar_54 cluster: Nonadiabatic molecular dynamics simulations,” J. Chem. Phys. **113,** 6660–6672 (2000).

[72] R. B. Gerber, M. V. Korolkov, J. Manz, M. Y. Niv, and B. Schmidt, “A reflection principle for the control of molecular photodissociation in solids: model simulation for F_2 in Ar,” Chem. Phys. Lett. **327,** 76–84 (2000).

[73] G. Chaban, R. Gerber, M. Korolkov, J. Manz, M. Niv, and B. Schmidt, “Photodissociation dynamics of molecular fluorine in an argon matrix induced by ultrashort laser pulses,” J. Phys. Chem. A **105,** 2770–2782 (2001).

[74] M. Jacox, “Comparison of the electronic energy levels of diatomic molecules in the gas-phase and in inert solid matrices,” J. Mol. Struct. **157,** 43–59 (1987).

[75] M. Chergui and N. Schwentner, “Cage Effect on the Photodissociation of Small Molecules in Van der Waals Clusters and Crystals,” In *Trends in Chemical Physics*, D. J. Menon, ed.,**2,** 89–113 (Trivandum, India, 1992).

[76] M. E. Jacox, “The vibrational energy levels of small transient molecules isolated in neon and argon matrices,” Chem. Phys. **189,** 149–170 (1994).

[77] V. Apkarian and V. Bondybey, “Special issue on: Photophysics of matrix isolated molecules,”, 1994.

[78] V. E. Bondybey, A. M. Smith, and J. Agreiter, “New Developments in Matrix Isolation Spectroscopy,” Chem. Rev. **96,** 2113–2134 (1996).

[79] M. Macler and M. C. Heaven, “Spectroscopy and relaxation dynamics of metastable electronically excited states of iodine in rare gas matrices,” Chem. Phys. **151,** 219–232 (1991).

[80] J. Helbing and M. Chergui, “Solvation of ion-pair states in non-polar media: I_2 in solid neon, argon and krypton,” J. Chem. Phys. **115,** 6158–6172 (2001).

[81] H. K. J. Feld and V. A. Apkarian, “Photodissociation of F_2 and mobility of F atoms in crystalline argon,” J. Chem. Phys. **93,** 1009 – 1020 (1990).

[82] C. Bressler, *Spektroskopie und Photomobilität von Fluor in Edelgasmatrizen* (Wissenschaft und Technik Verlag, Berlin, 1995), iSBN 3-928943-24-3.

[83] C. Bressler, W. G. Lawrence, and N. Schwentner, “Spectroscopy of F_2 in Ne matrices,” J. Chem. Phys. **105,** 1318–1329 (1996).

[84] M. H. Hill and V. A. Apkarian, “Photodynamics of charge transfer and ion-pair states of Cl_2Xe complexes in liquid Ar,” J. Chem. Phys. **105,** 4023–4032 (1996).

[85] P. Beeken, E. A. Hanson, and G. J. Flynn, “Photochemical and photophysical dynamics of diatomic iodine isolated in a rare gas cage,” J. Chem. Phys. **78,** 5892–5899 (1983).

[86] R. Perutz, “Photochemical Reactions Involving Matrix-Isolated Atoms,” Chem. Rev. **85,** 77–96 (1985).

[87] R. Alimi, R. B. Gerber, and V. A. Apkarian, “Photodissociation dynamics of F_2 in solid Kr: Theory versus experiment,” Phys. Rev. Lett. **66,** 1295–1297 (1991).

[88] H. Kunttu, E. Sekreta, and V. A. Apkarian, “Photodissociation and charge transfer photodynamics in crystalline krypton doped with F_2 and Xe,” J. Chem. Phys. **94,** 7819–7831 (1991).

[89] C. Bressler and N. Schwentner, “Penetration depths of photomobilized F atoms from a sandwich experiment,” Phys. Rev. Lett. **76,** 648–651 (1996).

[90] M. Dickgießer and N. Schwentner, “Penetration depth of energetic F atoms from F_2 dissociation in layered rare gas samples,” J. Chem. Phys. **113,** 8260–8265 (2000).

[91] A. Holleman and E. Wiberg, *Lehrbuch der Anorganischen Chemie* (Walter de Gruyter, Berlin, New York, 1985).

[92] F. Schreiner, J. Malm, and J. Hindman, “The preparation and nuclear magnetic resonance of krypton difluoride,” J. Am. Chem. Soc. **87,** 25–28 (1965).

[93] J. J. Turner and G. C. Pimentel, “Krypton fluoride: preparation by the matrix isolation technique,” Science **140,** 974–975 (1963).

[94] N. Bartlett and F. Sladky, “The chemistry of krypton, xenon and radon,” University of California Radiation Laboratory Report 19658 (June 1970).

[95] W. F. Howard, Jr. and L. Andrews, “Synthesis of noble-gas dihalides by laser photolysis of matrix-isolated halogens,” J. Am. Chem. Soc. **96,** 7864–7868 (1974).

[96] L. Khriachtchev, M. Petterson, N. Runeberg, J. Lundell, and M. Rasanen, “A stable argon compound,” Nature **406,** 874–876 (2000).

[97] R. Gerber, “private communication,”, 2001.

[98] J.-C. Diels and W. Rudolph, *Ultrashort laser pulse phenomena* (Academic Press, New York, 1996).

[99] J. Manz, “Molecular Wavepacket Dynamics: Theory For Experiments 1926-1996,” In *Femtochemistry and Femtobiology,* V. Sundström, ed., pp. 1–222 (World Scientific, Singapore, 1997).

[100] D. Tannor, *Introduction to Quantum Mechanics: A Time Dependent Perspective* (University Science Press, Sausalito, 2001).

[101] P. Ehrenfest, “Bemerkung über die angenäherte Gültigkeit der klassischen Mechanik innerhalb der Quantenmechanik,” Z. Phys. **45,** 455–457 (1927).

[102] K. Thompson and N. Makri, “Rigorous forward-backward semiclassical formulation of many-body dynamics,” Rhys. Rev. E. **59,** 4729–4732 (1999).

[103] A. Donoso and C. Martens, “Quantum Tunneling Using Entangled Classical Trajectories,” Phys. Rev. Lett. **87,** 223202 (2001).

[104] J. Franck, “Elementary processes of photochemical reactions,” Trans. Faraday Soc. **21,** 536–542 (1925).

[105] L. LAndau and E. Lifschitz, *Lehrbuch der theoretischen Physik* (Verlag Harri Deutsch, 1990), Vol. III, Quantenmechanik.

[106] C. Zener, “Non-adiabatic crossing of energy levels,” Proc. R. Soc. **137,** 696–702 (1932).

[107] A. Arthurs and A. Dalgarno, “The theory of scattering by a rigid rotator,” Proc. R. Soc. A **256,** 540–551 (1960).

[108] F. O. Ellison, “A Method of Diatomics in Molecule. I. General Theory and Application to H_2O,” J. Am. Chem. Soc. **69,** 3540–3544 (1963).

[109] F. Naumkin, “The ArClF van der Waals complex as an example of how atoms inside a molecule interact with those outside,” Chem. Phys. **213,** 33–43 (1996).

[110] I. Last and T. George, “Semiempirical study of polyatomic rare gas halides: application to the Xe_nCl systems,” J. Chem. Phys. **87,** 1183–1193 (1987).

[111] I. Last and T. George, “Interaction of Xe^+ and Cl^- ions and their formed molecules with a Xe solid,” J. Chem. Phys. **86,** 3787–3794 (1987).

[112] *The Diatomics-in-Molecules Method and the Chemical Bond*, Z. Maksic, ed., (Springer, New York, 1990).

[113] J. Tully and R. Preston, “Trajectory surface hopping approach to nonadiabatic molecular collisions: The reaction of H^+ with D_2,” J. Chem. Phys. **55,** 562–572 (1971).

[114] J. Tully, “Molecular dynamics with electronic transitions,” J. Chem. Phys. **93,** 1061–1071 (1990).

[115] M. Gühr, M. Bargheer, P. Dietrich, and N. Schwentner, “Predissociation and Vibrational Relaxation in the B state of I_2 in Kr Matrix,” J. Phys. Chem. submitted (2002).

[116] M. Gühr, “Schwingungsrelaxation und Prädissoziation von Jodmolekülen in Edelgasmatrizen,”, Diploma Thesis, Institut für Experimentalphysik, FU-Berlin, 2001.

[117] B. Garraway and K.-A. Suominen, “Wave packet dynamics: New physics and chemistry in femto time,” Rep. Prog. Phys. **58,** 365–419 (1995).

[118] C. Cohen-Tannoudji, *Quantum Mechanics* (John Wiley and Sons, New York, 1977).

[119] M. Klein and J. Venables, *Rare gas solids* (Academic Press, London, 1976).

[120] M. Dickgiesser and N. Schwentner, “Optimization of Exciton-Induced Detection of Atoms at Interfaces,” J. Phys. Chem. A **104,** 3743–3749 (2000).

[121] A. B. Alekseyev, H. Liebermann, R. J. Buenker, and D. B. Kokh, “Relativistic configuration interaction study of the ClF molecule and its emission spectra from 0^+ ion-pair states,” J. Chem. Phys. **112,** 2274–2284 (2000).

[122] M. E. Fajardo, V. A. Apkarian, A. Moustakas, H. Krueger, and E. Weitz, “Absorption Spectra of Intermolecular Charge-Transfer Transitions between Xenon and Halogen Molecules (F_2, Cl_2, Br_2) in liquid xenon,” J. Phys. Chem. **92,** 357–360 (1988).

[123] H. Kuzmany, *Festkörperspektroskopie* (Springer Verlag, Berlin, Heidelberg, 1990).

[124] W. Fowler and W. Beall, *Physics of Color Centers* (Academic Press, New York, 1986), (eds.).

[125] N. Schwentner, “Dynamics of localized excitations from energy and time resolved spectroscopy,” Appl. Opt. **19,** 4104–4114 (1980).

[126] K. Huang and A. Rhys, “A theory of light-absorption and non-radiative transitions in F-centers,” Proc. Roy. Soc. London A **204,** 406–423 (1950).

[127] D. Halliday, M. Potter, J. Mullins, and A. Brinkman, “Photoluminescence study of a bulk vapour grown CdTe crystal,” Journal of Crystal Growth **220,** 30–38 (2000).

[128] V. E. Bondybey and C. Fletcher, “Photophysics of Cl_2 in rare gas solids,” J. Chem. Phys. **64,** 3615–3620 (1976).

[129] H. H. Mohammed, A. M. Taleb, and J. Fournier, “Rare-gas matrix shift calculations of CO Cameron bands,” Chem. Phys. **91,** 267–272 (1984).

[130] N. Schwentner, C. Bressler, W. Lawrence, J. Xu, and M. Chergui, “Environmental effects on the energetics and photo-induced dynamics of molecular states,” Chem. Phys. **189,** 205–216 (1994).

[131] C. Bressler, W. Lawrence, and N. Schwentner, “Rydberg and charge transfer states of F atoms in neon matrices,” J. Chem. Phys. **102,** 48–56 (1995).

[132] B. Ault and L. Andrews, “Absorption and emission spectra of matrix-isolated XeF, KrF, $XeCl$ and $XeBr$,” J. Chem. Phys. **65,** 4192–4201 (1976).

[133] V. A. Alekseev and D. W. Setser, “Optical-optical double-resonance spectroscopic study of four ion-pair states of ClF and identification of the ClF$(A^3\Pi_1)$ valence state,” J. Chem. Phys. **107,** 4771–4782 (1997).

[134] P. Gürtler, H. Kunz, and J. LeCalvé, “VUV spectroscopy of the Cl_2 molecule trapped in pure neon, pure argon or mixed neon-argon matrices,” J. Chem. Phys. **91,** 6020 – 6028 (1989).

[135] E. U. Condon, “A theory of intensity distribution in band systems,” Phys. Rev. **28,** 1182–1201 (1926).

[136] M. Karavitis, R. Zadoyan, and V. Apkarian, “Time resolved coherent anti-Stokes Raman scattering of I_2 isolated in matrix argon: Vibrational dynamics on the ground electronic state,” J. Chem. Phys. **114,** 4131–4140 (2001).

[137] G. Herzberg, *Molecular Spectra and Molecular Structure. I. Spectra of Diatomic Molecules* (Van Nostrand Reinhold Co., New York, 1950).

[138] L. Brus, “Electronic transition dipole moments and excited-state alignment in linear molecules, with application to diatomic rare gas halide,” J. Mol. Spectr. **64,** 376–381 (1977).

[139] H. Haken and H. Wolf, *Molekülphysik und Quantenchemie* (Springer, Berlin, 1998).

[140] A. C. Albrecht, “Polarizations and Assignments of transitions: The method of photoselection,” J. Mol. Spectr. **6,** 84–108 (1961).

[141] J. Michl and E. Thulstrup, *Spectroscopy with polarized light* (VCH Publishers, New York, 1986).

[142] D. S. Kliger, *Polarized Light in Optics and Spectroscopy* (Academic Press, Boston, 1990).

[143] E. Schreiber, *Femtosecond real-time spectroscopy of small molecules and clusters, Springer Tr. Mod. Phys. 143* (Springer Verlag, Berlin, 1998).

[144] M. Bargheer, “Wellenpaketdynamik von Jodmolekülen in Krypton Matrizen,”, Diploma Thesis, Institut für Experimentalphysik, FU-Berlin, 1999.

[145] V. A. Alekseev, D. W. Setser, and J. Tellinghuisen, “The D’ → A’ Transition in ClF,” J. Mol. Spectr. **194,** 61 – 72 (1999).

[146] V. A. Alekseev, D. W. Setser, and J. Tellinghuisen, “The A $(^3\Pi_1)$ state of ClF,” J. Mol. Spectr. **195,** 162 – 171 (1999).

[147] V. A. Alekseev and D. W. Setser, “Electronic Spectroscopy and Structure of ClF,” Bulletin of the Korean Chemical Society **21,** 9 – 22 (2000).

[148] D. B. Kokh, V. A. Alekseev, and D. W. Setser, “Analysis of the bound-free emission spectra from the $E(0^+)$ and $f(0^+)$ ion-pair states of ClF to obtain potentials for the ion-pair and repulsive valence states,” J. Chem. Phys. **109,** 1763–1771 (1998).

[149] D. Pilipovich, H. H. Rogers, and R. D. Wilson, “Chlorine Trifluoride Oxide. II. Photochemical Synthesis,” Inorg. Chem. **11,** 2192–2194 (1972).

[150] G. P. Zhitneva, “Role of the reaction $\mathrm{ClF_2{+}Cl} \rightarrow 2\mathrm{ClF}$ in the photolysis of chlorine monofluoride,” Kinet. Katal. pp. 690–694 (1986).

[151] R. Steunenberg and R. Vogel, “The Absorption Spectrum of Fluorine,” J. Am. Chem. Soc. **78,** 901–902 (1956).

[152] A. L. G. Rees, “Electronic spectrum and dissociation energy of fluorine,” J. Chem. Phys. **26,** 1567–1571 (1957).

[153] J. B. Burkholder and E. J. Bair, “Potential energy parameters and shapes of the vibrational components of the 345 nm system of chlorine,” J. Phys. Chem. **87,** 1859–1863 (1983).

[154] H. Schmitz and H. Schumacher, “Das Absorptionsspektrum von ClF_3,” Z. Naturforschung **2a,** 363 (1947).

[155] T. O. Nelson, D. W. Setser, and J. Qin, “Interpretation of the two-photon, laser-assisted reactions of xenon with $\mathrm{Cl_2}$, $\mathrm{F_2}$, and ClF and krypton with $\mathrm{F_2}$,” J. Phys. Chem. **97,** 2585–2595 (1993).

[156] I. S. McDermid, “Potential-energy curves, Franck-Condon factors and laser excitation spectrum $B^3\Pi(0^+) - X^1\Sigma^+$ system of chlorine monofluoride,” J. Chem. Soc., Faraday Trans. 2 **77,** 519–530 (1981).

[157] R. Coombe, D. Pilipovich, and R. K. Horne, “Chemical Generation of Electronically Excited ClF (B $^3\Pi_{0+}$) and the B $\rightarrow$ X Emission spectrum,” J. Phys. Chem **82,** 2484 – 2489 (1978).

[158] A. Alekseyev, “private communication,”.

[159] A. H. Nielsen and E. A. Jones, “The analysis of the infrared spectrum of clorine monofluoride,” J. Chem. Phys. **19,** 1117 –1121 (1951).

[160] J. A. Coxon, “Dissociation Energies of Diatomic Halogen Fluorides,” Chem. Phys. Lett. **33,** 136 – 140 (1975).

[161] G. Mamantov, E. J. Vasini, M. C. Moulton, D. G. Vickroy, and T. Maekawa, “Chlorine-Fluorine system at low temperatures: Characterization of the ClF_2 radical,” J. Chem. Phys. **54,** 3419–3421 (1971).

[162] L. Andrews, F. Chi, and A. Arkell, “Matrix infrared spectrum and vibrational analysis of the FClO intermediate,” J. Am. Chem. Soc. **96,** 1997 (1974).

[163] C. Naulin, J. Lambard, and R. Bougon, “Vibrational spectra of the chlorine monofluoride ClF in cryogenic solutions,” J. Chem. Phys. **76,** 3371–3377 (1982).

[164] M. Diegelmann, K. Hohla, and K. Kompa, “Interhalogen UV laser on the 285 nm band of ClF,” Opt. Commun. **29,** 334–338 (1979).

[165] M. Diegelmann, H. P. Grieneisen, K. Hohla, X.-Y. Hu, J. Krasinski, and K. L. Kompa, “New TEA-Lasers Based on D’ -> A’ Transitions in Halogen Monofluoride Compounds: ClF, BrF,

IF," Appl. Phys. **23,** 283 – 287 (1980).

[166] M. Diegelmann, K. Hohla, F. Rebentrost, and K. L. Kompa, "Diatomic interhalogen laser molecules: Fluorescence spectroscopy and reaction kinetics," J. Chem. Phys. **76,** 1233 – 1246 (1982).

[167] F. Alberti, K. Huber, and E. Looi, "The lowest Rydberg Complex of ClF: $c^3\Pi$ and $C^1\Pi$," J. Mol. Spectr. **102,** 289–296 (1983).

[168] K. Darvesh, R. Boyd, and S. Peyerimhoff, "Electronically excited states of chlorine monofluoride: a multi-reference configuration interaction study," Chem. Phys. **121,** 361–369 (1988).

[169] F.-M. Tao and W. Klemperer, "The van der Waals potential-energy surfaces and the structures of ArClF and ArCl2," J. Chem. Phys. **97,** 440–451 (1992).

[170] S. Harris, S. Novick, and W. Klemperer, "Intermolecular potential between an atom and a diatomic molecule: The strucure of ArClF," J. Chem. Phys. **61,** 193–197 (1974).

[171] V. Sorokin and A. Chichinin, "The 248 nm photodissociation of ClF_3: quantum yields for F and Cl atoms," Chem. Phys. Lett. **280,** 141–144 (1997).

[172] J. Qin, T. Nelson, and D. Setser, "Two-Photon Laser-Assisted Reaction between Xe and ClF," J. Phys. Chem. **95,** 5374–5378 (1991).

[173] E. S. Prochaska and L. Andrews, "Raman, infrared, and ultraviolet spectra of the chlorine difluoride free radical in solid nitrogen," Inorg. Chem. **16,** 339–343 (1977).

[174] A. Sannigrahi and S. Peyerimhoff, "Ab initio SCF and CI study of the electronic structure of chlorine difluoride cation and anion," Chem. Phys. Lett. **119,** 119–122 (1985).

[175] A. Sannigrahi and S. Peyerimhoff, "Ab initio SCF and CI study of the electronic structure and spectrum of the chlorine difluoride radical," Chem. Phys. Lett. **114,** 6–9 (1985).

[176] E. Prochaska, B. Ault, and L. Andrews, "Infrared, Raman and Ultraviolet Spectra of M^+ClF^- Species in Solid Argon," Inorg. Chem. **16,** 2021–2023 (1977).

[177] B. Ault, "A search for the HF_2 and $HClF$ neutral free radicals isolated in argon matrices," J. Chem. Phys. **68,** 4012–4016 (1978).

[178] L. Andrews, F. Chi, and A. Arkell, "Matrix infrared spectrum and vibrational analysis of the FClO intermediate," J. Am. Chem. Soc. **96,** 1997–2000 (1974).

[179] P. Bagus, B. Liu, and H. S. III, "Electronic structure and properties of krypton difluoride," J. Am. Chem. Soc. **94,** 6635–6641 (1972).

[180] A. Boate, J. Morton, and K. Preston, "EPR spectrum off Kr_2F," Chem. Phys. Lett. **54,** 579–581 (1978).

[181] E. Riedel, *Anorganische Chemie* (de Gruyter, Berlin, 1999).

[182] I. S. McDermid and J. B. Laudenslager, "Perturbations in the $B^3\pi(0^+)$ state of ClF: A new low-lying electronic state," Chem. Phys. Lett. **79,** 370–374 (1981).

[183] T. Wilhelm, J. Piel, and E. Riedle, "Sub-20-fs pulses tunable across the visible from a blue-pumped single-pass noncollinear parametric converter," Opt. Lett. **22,** 1494–1496 (1997).

[184] G. Cerullo, M. Nisoli, S. Stagira, and S. D. Silvestri, "Sub-8-fs pulses from an ultrabroadband optical parametric amplifier in the visible," Opt. Lett. **23,** 1283–1285 (1998).

[185] A. Shirakawa, I. Sakane, and T. Kobayashi, “Pulse-front-matched optical parametric amplification for sub-10-fs pulse generation tunable in the visible and near infrared,” Opt. Lett. **23,** 1292–1294 (1998).

[186] R. Boyd, *Nonlinear Optics* (Academic Press, San Diego, 1992).

[187] E. Riedle, private communication.

[188] D. Kane and R. Trebino, “Characterization of arbitrary femtosecond pulses using frequency-resolved optical gating,” IEEE J. Quant. Electr. **29,** 571–579 (1993).

[189] R. Trebino and D. J. Kane, “Using phase retrieval to measure the intensity and phase of ultrashort pulses: frequency-resolved optical gating,” J. Opt. Soc. Am. A **10,** 1101–1111 (1993).

[190] N. Schmitt, “Phasen- und Amplitudenmessungen an ultrakurzen Lichtpulsen,”, Diploma Thesis, Institut für Experimentalphysik, FU-Berlin, 1996.

[191] J. G. Caffrey, H. Kunz, and N. Schwentner, “Spectroscopy and photodissociation of chlorine monomers and clusters in Ar-matrices,” J. Chem. Phys. **96,** 155 – 164 (1992).

[192] T. Ishiwata, H. Takekawa, and K. Obi, “Measurements of the radiative lifetimes of the Cl_2 ion-pair states by optical-optical double resonance,” Chem. Phys **177,** 303 – 308 (1993).

[193] C. Bressler, W. Lawrence, and N. Schwentner, “Spectroscopy of argon fluoride and krypton fluoride exciplexes in rare gas matrices,” J. Chem. Phys. **105,** 10178–10188 (1996).

[194] H. Kunz, “Photodissoziation von Cl_2 in Edelgasmatrizen und spektroskopische Untersuchung der Dissoziationsfragmente,”, PhD Thesis, Freie Universität Berlin, 1991.

[195] M. Bargheer, J. Pietzner, P. Dietrich, and N. Schwentner, “Ultrafast laser-control of ionic-bond formation: ClF in argon solids,” J. Chem. Phys. **115,** 9827–9834 (2001).

[196] M. Macler, M. Erickson, H.-S. Lin, and M. C. Heaven, “Electronic spectroscopy and fluorescence decay dynamics of matrix isolated IBr,” J. Phys. Chem **96,** 4301–4306 (1992).

[197] V. E. Bondybey and L. E. Brus, “Rigid cage effect on ICl photodissociation and $B\ 0^+$ fluorescence in rare gas matrices,” J. Chem. Phys. **62,** 620–629 (1975).

[198] J.-P. Nicolai and M. C. Heaven, “Laser excitation spectra for matrix isolated IF: observation of new low-lying electronic states,” J. Chem. Phys. **87,** 3304 – 3312 (1987).

[199] C. A. Wight, B. S. Ault, and L. Andrews, “Laser-induced fluorescence and resonance raman spectra of interhalogen diatomics isolated in inert matrices at 12K,” J. Mol. Spectr. **56,** 239–250 (1975).

[200] M. Bargheer, P. Dietrich, K. Donovang, and N. Schwentner, “Extraction of potentials and dynamics from condensed phase pump-probe spectra: Application to I_2 in Kr matrices,” J. Chem. Phys. **111,** 8556–8564 (1999).

[201] G. Zerza, G. Slivinski, N. Schwentner, G. J. Hoffman, D. G. Imre, and V. A. Apkarian, “Spectroscopy of XeF in Ar and Ne Matrices,” J. Chem. Phys. **99,** 8414–8423 (1993).

[202] M. E. Fajardo and V. A. Apkarian, “Cooperative photoabsorption induced charge transfer reaction dynamics in rare gas solids. I. Photodynamics of localized xenon chloride exciplexes,” J. Chem. Phys. **85,** 5660–5681 (1986).

[203] M. Dickgießer and N. Schwentner, “Set-up combining synchrotron radiation-induced photochemistry with IR probing: $(HCl)_n$ in Kr matrix,” Nucl. Instr. Meth. B **168,** 252–267 (2000).

[204] V. S. Batista, C. Margulis, and D. Coker, private communication .

[205] M. Bargheer, P. Dietrich, and N. Schwentner, “Spectroscopy and Photodissociation of ClF in Ar,” J. Chem. Phys. **115,** 149–157 (2001).

[206] K. P. Huber and G. Herzberg, *Molecular Spectra and Molecular Structure. IV. Constants of Diatomic Molecules* (Van Nostrand Reinhold, New York, 1979).

[207] R. Rydberg, “Graphische Darstellung einiger bandenspektroskopischer Ergebnisse,” Z. Phys. **73,** 376–385 (1931).

[208] O. Klein, “Zur Berechnung von Potentialkurven für zweiatomige Moleküle mit Hilfe von Spektraltermen,” Z. Phys. **76,** 226–235 (1932).

[209] A. Rees, “The calculation of potential-energy curves from band-spectroscopic data,” Proc. Phys. Soc. London A **59,** 998–1008 (1947).

[210] L. D. Landau and E. M. Lifschitz, *Lehrbuch der theoretischen Physik* (Akademie-Verlag, Berlin, 1979), Vol. I: Mechanik, Chap. 12.

[211] H. Dietz, G. Knopp, A. Materny, and V. Engel, “The perturbation of coherent wave-packet dynamics by atom-molecule collisions: the NaI + Ar system,” Chem. Phys. Lett. **275,** 519–526 (1997).

[212] A. Heidenreich and J. Jortner, “Pump-Probe spectroscopy of ultrafast structural relaxation of electronically excited rare gas heteroclusters,” J. Electr. Spectr. **106,** 187–197 (2000).

[213] A. Goldberg and J. Jortner, “Structural Relaxation Dynamics of Electronically Excited XeAr_N Clusters,” J. Chem. Phys. **107,** 8994–9017 (1997).

[214] C. Jeannin, M. Portella-Oberli, S. Jimenez, F. Vigliotti, B. Lang, and M. Chergui, “Femtosecond dynamics of electronic ’bubbles’ in solid argon: viewing the inertial response and the bath coherences,” Chem. Phys. Lett. **316,** 51–59 (2000).

[215] S. Jimenez, M. Chergui, G. Rojas-Lorenzo, and J. Rubayo-Soneira, “The medium response to an impulsive redistribution of charge in solid argon: Molecular dynamics simulations and normal mode analysis,” J. Chem. Phys. **114,** 5264–5272 (2001).

[216] J. Baskin, M. Gupta, M. Chachisvilis, and A. Zewail, “Femtosecond dynamics of microscopic friction: nature of coherent versus diffusive motion from gas to liquid density,” Chem. Phys. Lett. **275,** 437–444 (1997).

[217] J. Baskin, M. Chachisvilis, M. Gupta, and A. Zewail, “Femtosecond dynamics of solvation: Microscopic friction and coherent motion in dense fluids,” J. Phys. Chem. A **102,** 4158–4171 (1998).

[218] I. Benjamin and K. Wilson, “Proposed experimental probes of chemical reaction molecular dynamics in solution: ICN photodissociation,” J. Chem. Phys. **90,** 4176–97 (1989).

[219] M. Levenson and S. Kano, *Introduction to Nonlinear Laser Spectroscopy* (Academic Press, Boston, 1988).

[220] V. Bondybey and L. Brus, “Rigid cage photodissociation dynamics: A double minimum problem for ICl in Ne and Ar lattices,” J. Chem. Phys. **64,** 3724–3731 (1976).

[221] A. I. Krylov and R. B. Gerber, “Photodissociation dynamics of HCl in solid Ar: Cage exit, nonadiabatic transitions, and recombination,” J. Chem. Phys. **106,** 6574–6587 (1997).

[222] M. Y. Niv, A. I. Krylov, and R. B. Gerber, “Photodissociation, electronic relaxation and recombination of HCl in Ar_n(HCl) clusters - Non-adiabatic molecular dynamics simulations,”

Faraday Discuss. **108,** 243–254 (1997).

[223] T. Brixner, N. Damrauer, P. Niklaus, and G. Gerber, “Photoselective adaptive femtosecond quantum control in the liquid phase,” Nature **414,** 57–60 (2001).

[224] B. Friedrich and D. Herschbach, “Alignment and trapping of molecules in intense laser fields,” Phys. Rev. Lett. **74,** 4623–4626 (1995).

[225] J. Larsen, I. Wendt-Larsen, and H. Stapelfeldt, “Controlling the Branching Ratio of Photodissociation Using Aligned Molecules,” Phys. Rev. Lett. **83,** 1123–1126 (1999).

[226] J. Larsen, K. Hald, N. Bjerre, and H. Stapelfeldt, “Three dimensional Alignment of Molecules Using Eliptically Polarized Laser Fields,” Phys. Rev. Lett. **85,** 2470–2473 (2000).

Appendix

Comments on the lock-in detection

In chapter 6.3.4, pump-probe experiments on ClF/Kr with the detection of the $Kr_2^+F^-$ emission are presented. Wavelengths $\lambda_{probe} < 278$ nm probe all F atoms in Kr, including the thermally equilibrated fragments. This gives rise to a strong background signal, which is independent of the time delay between pump and probe pulse. In addition, the concentration of F fragments changes at the time delay zero of a pump-probe signal due to the photochemical equilibrium discussed in chapter 5.4.2. The solution to the problem is a ”lock-in” technique, which uses a light beam chopper to block every second pump-pulse $\lambda_{pump} = 387$ nm. The fluorescence, which is recorded when only λ_{probe} is present, measures the entire unwanted background signal at the right equilibrium concentration. The concentration does not change significantly with a single pulse, but rather on a ”timescale” of 1000 pulses. This background is subtracted from the signal measured with λ_{pump} and λ_{probe} present, yielding the desired pump-probe signal that is sensitive only to the wave packet that was triggered with the last pump pulse.

If the signal is measured without the lock-in technique, a pump-probe scan started at negative time delays, i.e. λ_{probe} first, looks as follows. A high signal is measured at negative time delays, which corresponds to the concentration of cold F fragments in the lattice for equilibrium A. When the pump-probe scan passes the time zero, the signal rises since the hot F fragments are detected with higher efficiency and in addition according to the new photochemical equilibrium B. The photochemical equilibrium changes with time delay Δt and the rate of change depends on the number of photons absorbed during a time step of Δt. Therefore, the measured curve depends on the number of shots averaged to obtain one data point, especially near $\Delta t = 0$. In a fast scan, a slow rise with Δt is measured, and in a slow scan the rise with Δt is fast.

The lock-in detection not only greatly improves the signal-to-noise ratio, it also cancels this unwanted change in the signal at $\Delta t = 0$, since the F concentration is equal for the pump-probe sequence and the background measurement with the probe pulse only. Also the dependence of the measured signal on how the time delay Δt is connected to real time cancels out. Note that this lock-in technique locks the signal to an external chopper, i.e. to a function of the repetition rate. It is not the time delay Δt which is varied with a frequency, and therefore, the lock-in signal is not the derivative of the signal without lock-in.

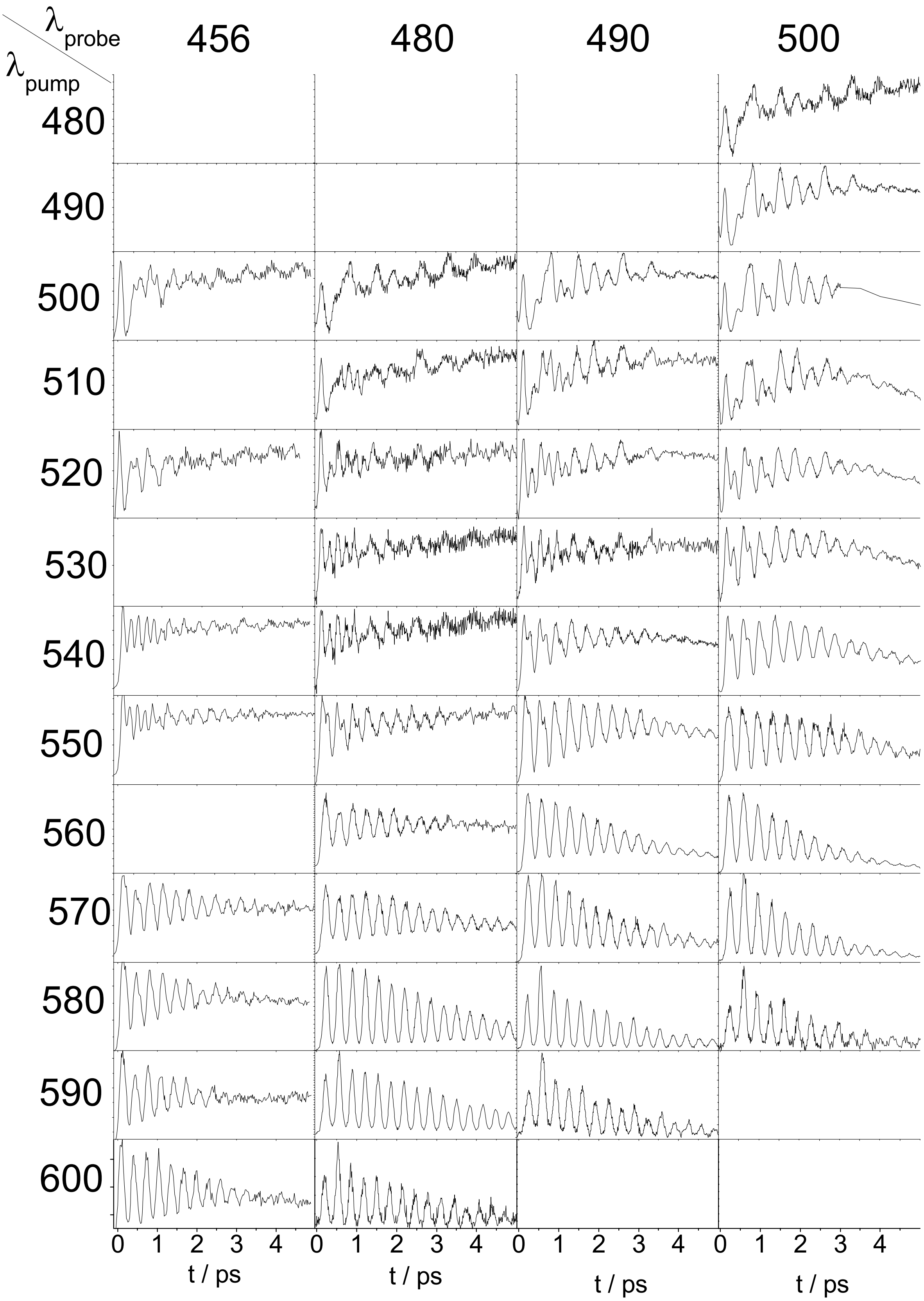

Pump-probe spectra of I_2/Kr summarized in Fig. 6.7

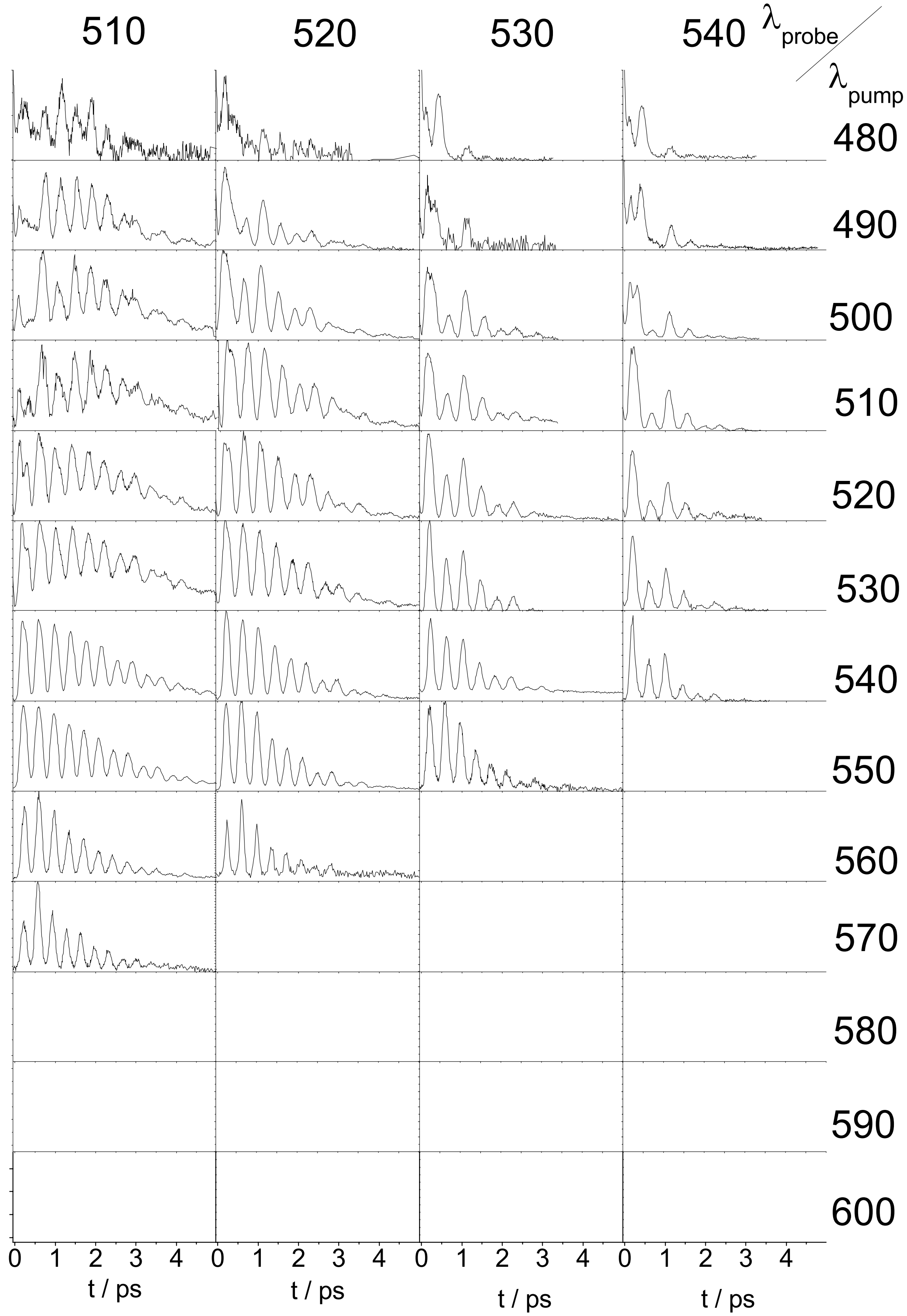

Pump-probe spectra of I_2/Kr summarized in Fig. 6.7

Curriculum vitae

Matias Bargheer

geboren am 24.9.1972	in Münster

Ausbildung

1979-1992	Schulausbildung in Düsseldorf
Mai 1992	Abitur mit der Gesamtnote 1,1
Sept. 1992 - Sept. 1993	Zivildienst bei der Diakonie in Düsseldorf
Okt. 1993 - Sept. 1995	Grundstudium der Physik an der Universität Konstanz
Juli 1995	Vordiplom in Physik mit der Gesamtnote 1,7
Sept. 1995 bis Juni 1996	Physikstudium an der Rutgers University of New Jersey, USA
Okt. 1996 - März 1999	Physikstudium an der Freien Universität Berlin
Okt. 1997 - Juli 1998	Tutor im Fachbereich Mathematik, Leitung einer Übungsgruppe
Okt. 1997 - März 1999	Diplomarbeit in der AG Schwentner ”Wellenpaketdynamik von Iod in Krypton-Matrizen”
März 1999	Diplom in Physik ”mit Auszeichnung” und Preis der Wilhelm und Else Heraeus Stiftung
seit April 1999	Wissenschaftlicher Mitarbeiter in der AG Schwentner

Laborpraktika

Nov. 1995 - Mai 1996	”Research in Physics”-Student im Labor für Tieftemperaturphysik der Rutgers University
Mai 1997	Studentische Hilfskraft im Hahn-Meitner-Institut, Berlin, Bereich Festkörperphysik

Veröffentlichungen

Artikel:

- M. Bargheer, P. Dietrich, K. Donovang and N. Schwentner, ”Extraction of potentials and dynamics from condensed phase pump-probe spectra: Application to I_2 in Kr matrices”, J. Chem. Phys. **111**, 8556-8564 (1999)
- M. Y. Niv, M. Bargheer and R.B. Gerber, ”Photodissociation and recombination of F_2 molecule in Ar_{54} cluster: Nonadiabatic molecular dynamics simulation”, J. Chem. Phys. **113**, 6660-6672 (2000)
- M. Bargheer, P. Dietrich, and N. Schwentner, ”Spectroscopy and photodissociation of ClF in rare gas solids”, J. Chem. Phys. **115**, 149-157 (2001)
- M. Bargheer, J. Pietzner, P. Dietrich, and N. Schwentner, ”Ultrafast laser-control of ionic-bond formation: ClF in Ar solids”, J. Chem. Phys. **115**, 9827-9833 (2001)
- M. Bargheer, M. Gühr, P. Dietrich, and N. Schwentner, ”Femtosecond Spectroscopy of the Fragment-Cage Dynamics: I_2 in Kr”, Phys. Chem. Chem. Phys., **4**, 75-81 (2002)
- M. Bargheer, M. Gühr and N. Schwentner, ”Depolarization as a probe for ultrafast reorientation of diatomics in condensed phase: ClF vs. I_2 in rare gas solids”, J. Chem. Phys., **117**, 5-8 (2002)
- M. Bargheer, M. Y. Niv, R.B. Gerber and N. Schwentner, "Ultrafast Solvent-Induced Spin-Flip and Non-Adiabatic Coupling: ClF in Argon Solids", Phys. Rev. Lett., **89** 108301 (2002)

Conference Proceedings:

- M. Bargheer, P. Dietrich and N. Schwentner, ”Wavepacket Dynamics of Iodine in Kr-Matrices”, in: Advances in energy transfer Processes, Proceedings of the International School of Atomic and MolecularSpectroscopy: 16th Course, edited by B. Di Bartolo & Xuesheng Chen, World Scientific Singapore, 2001
- M. Bargheer, J. Pietzner, P. Dietrich and N. Schwentner, ”Analysis and Control of condensed phase photochemical reactions: ClF in Ar”, in: Femtochemistry and Femtobiology edited by A. Douhal, World Scientific, approx. 2002

Vorträge

- International School of Atomic and Molecular Spectroscopy, 16th Course: ”Advances in energy transfer Processes”, (Erice) Sept. 1999, ”Wavepacket Dynamics of Iodine in Kr-Matrices”
- Symposium on Molecular Spectroscopy (Columbus, Ohio), Juni 2000, ”Dynamics of chlorine monofluoride (ClF) isolated in rare gas matrices”
- Symposium on Molecular Spectroscopy (Columbus, Ohio), Juni 2000, ”Analysis of condensed-phase femtosecond pump-probe spectra: Application to I_2 in Kr matrices”
- ECAMP VII, Seventh European Conference on Atomic and Molecular Physics, (Berlin) April 2001, ”ClF in rare gas matrices: cage exit and recombination dynamics on fs timescale”
- SfB 450 Symposium (Berlin) Nov. 2001, ”Analysis and Control of Bond-Breaking and Bond-Formation in the Condensed Phase”
- 65. Frühjahrstagung (Osnabrück), März 2002, ”Pump-probe spectroscopy in condensed phases: Potentials and dynamics constructed from experiment”
- 65. Frühjahrstagung (Osnabrück), März 2002, ”Ultrafast molecule-solvent interactions in dissociation and recombination dynamics: ClF in rare gas solids”

Poster

- 62. Frühjahrstagung (Konstanz), März 1998, ”fs-Experimente zur Wellenpaketdynamik von I_2 in Edelgasmatrizen”
- SUSSP52 International Summer-School in Laserphysics (St.Andrews), Sept. 1998, ”Control of wave packet dynamics of I_2 in Kr by chirped OPA pulses”
- 63. Frühjahrstagung (Heidelberg), März 1999, ”Wellenpaketdynamik und Prädissoziation von I_2 in Kr-Matrizen”
- 64. Frühjahrstagung (Bonn), April 2000, ”Analyse von Pump-Probe-Spektren in der kondensierten Phase: Dynamik und Potentiale von I_2 in Edelgasmatrizen”
- Gordon Research Summer-School on ”Chemical Physics”, (Rhode-Island), Juni 2000, ”Analysis of femtosecond pump-probe spectra in the condensed phase: Dynamics and potentials of iodine in rare gas matrices”
- ECAMP VII, Seventh European Conference on Atomic and Molecular Physics, (Berlin) April 2001, ”Spectroscopy and photodissociation of ClF in rare gas solids”
- Vth Femtochemistry conference, (Toledo), Sept. 2001, ”Analysis and control of condensed phase photochemical reactions: ClF in Ar”

Danksagung

Die vorliegende Arbeit ist in der Arbeitsgruppe von Prof. Dr. N. Schwentner entstanden. Ihm möchte ich für die freie und freundliche Arbeitsatmosphäre danken, in der wir das noch junge und hochinteressante Gebiet der Femtosekundenspektroskopie bearbeiten. Viele lehrreiche Diskussionen und insbesondere die kritikfreudige Betreuung haben wesentlich zum Gelingen dieser Arbeit beigetragen.

Ich erinnere mich sehr gerne an die erste Hälfte meiner Arbeit, als Dr. habil. Peter Dietrich immer für Probleme und Diskussionen Zeit hatte. Seit der Atlantische Ozean zwischen uns liegt, muß ich auf die wertvollen Beiträge verzichten, die immer eine große Hilfe waren und viele Fortschritte in den Interpretationen der physikalischen Fragestellungen ermöglicht haben. Markus Gühr gilt ein besonderer Dank für die hervorragende Zusammenarbeit im Labor und die erfolgreiche Weiterführung der Experimente an I_2/Kr. Er ist bei jeder Bitte sofort mit mindestens zwei goldenen Händen bei der Sache und hat die erste, noch unfertige Version meiner Arbeit Korrektur gelesen. Bei Jörg Pietzner bedanke ich mich für die tolle Zusammenarbeit und die immer verläßliche Durchführung einiger Experimente an ClF/Ar. Johanna Turk hat mich bei den letzten Messungen an ClF unterstützt und freundlicherweise dafür gesorgt, daß die Arbeit möglichst fehlerfrei in texanischem Englisch erscheint. David Ambrosek, Gunnar Moos und Verena Dietz habe ich weitere Korrekturen an der Arbeit zu verdanken. Bei J. Herbst, Dr. K. Heyne und Dr. habil. R. Diller aus der Arbeitsgruppe Stehlik bedanke ich mich herzlich für die gute Zusammenarbeit am gemeinsamen Lasersystem und bei den anderen Mitgliedern der AG Schwentner für das angenehme Klima: Dr. V. Berghof, Dr. M. Soltwisch und I. Twesten.

Die Kollaborationen mit anderen Arbeitsgruppen im SfB 450 waren sehr wertvoll für die Ergebnisse dieser Arbeit. Hier gilt mein Dank den Mitarbeiten der Gruppe um Prof. J. Manz, Dr. habil. O. Kühn, Dr. M. Korolkov und M. Schröder ebenso wie der Gruppe von Prof. R. B. Gerber: Dr. M. Y. Niv und Dr. G. Chaban. Der Deutschen Forschungsgemeinschaft danke ich für die finanzielle Förderung.

Meine Eltern, die Familie van Kempen/Hoffmann und meine Freunde unterstützen mich mit allen Kräften, und Britta sorgt fleißig dafür, daß wir viel Schönes außerhalb der Physik unternehmen.